PHASE TRANSITIONS IN DISORDERED SPIN-1 FERROMAGNETS

By

SOHELI MUKHERJEE

PHYS11201704024

National Institute of Science Education and Research, Bhubaneswar

A thesis submitted to the

Board of Studies in Physical Sciences

(as applicable)

In partial fulfillment of requirements

for the Degree of

DOCTOR OF PHILOSOPHY

of

HOMI BHABHA NATIONAL INSTITUTE

August , 2022

Homi Bhaba National Institute

Recommendations of the Viva Voce Committee

As members of the Viva Voce Committee, we certify that we have read the dissertation prepared by Soheli Mukherjee entitled " Phase Transitions in Disordered Spin-1 Ferromagnets " and recommend that it may be accepted as fulfilling the thesis requirement for the award of Degree of Doctor of Philosophy.

Chairman - Prof. Sudhakar Panda	06/04/2023
Guide / Convener - Dr. Sumedha	6/4/2023
Examiner - Prof. Sanjay Puri	6/4/2023
Member 1 - Dr. A. V. Anil Kumar	6/4/23
Member 2 - Dr. Nabin Kumar Jana	6/4/2023
Member 3 - Dr. Debashish Chaudhuri	6/4/23

Final approval and acceptance of this thesis is contingent upon the candidate's submission of the final copies of the thesis to HBNI.

I/We hereby certify that I/we have read this thesis prepared under my/our direction and recommend that it may be accepted as fulfilling the thesis requirement.

Date : 06/04/2023

Place : NISER

Signature

Co-guide (if any)

Signature

Guide

i

DECLARATION

I hereby declare that I am the sole author of this thesis in partial fulfillment of the requirements for a postgraduate degree from National Institute of Science Education and Research (NISER). I authorize NISER to lend this thesis to other institutions or individuals for the purpose of scholarly research.

Soheli Mukherjee

Soheli Mukherjee

List of Publications arising from the thesis

Journal

1. "Emergence of a bicritical end point in the random-crystal-field Blume-Capel model", Sumedha and Soheli Mukherjee, Physical Review E, **2020**, 101, 042125.

2. "Phase diagram of the repulsive Blume–Emery–Griffiths model in the presence of an external magnetic field on a complete graph", Soheli Mukherjee, Raj Kumar Sadhu and Sumedha, Journal of Statistical Mechanics : Theory and Experiment, **2021**, 2021, 043209.

3. "Phase transitions in the Blume-Capel model with trimodal and Gaussian random fields", Soheli Mukherjee and Sumedha, Journal of Statistical Physics, **2022**, 188, 22.

4. "Critical behaviour near critical end points and tricritical points in disordered spin-1 ferromagnets", Soheli Mukherjee and Sumedha, Submitted, 2023.

Soheli Mukherjee

To

Ma, Baba, Babai

and

in loving memory of my late grandparents

ACKNOWLEDGEMENTS

ABSTRACT

The effect of disorder on Ising spins has been extensively studied in the last many years. Comparatively, spin-1 systems have been less explored. Pure spin-1 ferromagnetic model with crystal field, the Blume-Capel model has a phase diagram that consists of a second order transition line meeting the line of first order transitions at a tricritical point. This is the simplest model exhibiting tricriticality. We have studied the effect of random magnetic field and random crystal field on the phase diagram of the spin-1 Blume-Capel model for infinite range interactions. We find that even infinitesimal disorder changes the phase diagram. For the random crystal field we found three different topologies of the phase diagram depending on the strength of the disorder. We report the emergence of a bicritical end point in the presence of disorder in this system. We also studied different symmetric distributions of the random magnetic field for the Blume-Capel model. Unlike the spin -1/2 systems, the continuous and discrete symmetric distributions have different phase diagrams for the spin-1 Blume-Capel model. We verified it also by looking at the zero-temperature phase diagrams, where many new phases emerge for discrete disorder distribution. The phase diagrams especially in the case of discrete distribution have many multicritical points and multi-phase coexistence points.

Furthermore, we have studied the effect of biquadratic exchange interaction (K) in the infinite range ferromagnetic spin-1 model, known as the Blume-Emery-Griffiths model. We obtained the phase diagram in both the canonical and the microcanonical ensembles for different values of K. We found ensemble inequivalence in the system by not only looking at the first order transition line, but also at the critical lines in the presence of external field. We observed that the ensemble inequivalence vanishes for $K < -1$. Interestingly, we observed that the presence of repulsive biquadratic interaction changes the phase diagram similarly to the random crystal field disorder.

Contents

Summary

All real systems in nature include some amount of local random inhomogeneities, which breaks the translational symmetry of the system. Such systems are modelled by some frozen or quenched disordered spin models. The disordered spin models are used as a prototype model to study many physical systems in physics, biology as well as in computer science. Study of such systems both using theoretical calculations as well as via simulations are challenging due to the requirement of an additional disorder averaging over the disorder degrees of freedom.

Over the years the effect of quenched disorder on phase transitions and critical phenomena has been extensively studied for spin-1/2 models. It has been well established that, depending on the dimension of the system or type of the disorder system's critical phenomena gets affected. The effect of disorder on first order transitions and multicritical points are more drastic. An infinitesimal random field disorder can make a first order transition gets smeared or can even destroy the transition all together.

The aim of this thesis is to report the effect of different types of field disorder on spin-1 Blume-Capel model. Blume-Capel model is the spin-1 Ising model with an additional crystal field interaction. This crystal field acts like a chemical potential of the system due to which the model exhibits a rich phase diagram. In the two dimensional plane the phase diagram consists of a line of second order transition meeting a line of first order transition at a multicritical point, known as the tricritical point (TCP). In presence of external magnetic field, two more critical lines meet at the TCP. The effect of disorder on spin-1 model has been comparatively studied less. All the previous study has been done mostly on the two dimensional phase diagram. But things become really interesting when we investigate the effect of disorder on the three dimensional phase diagram to understand how the multicritical points get affected.

In this thesis, we study the infinite-range Blume-Capel model in the presence of random crystal field and random field disorder using an approach based on large deviation principle. We find that the effect of these two types of disorder are very different from each other. In presence of random crystal field, we find that disorder is relevant always as soon as we

switch on the disorder. Depending on the strength of disorder we find that there are three different types of phase diagrams. The TCP persists only for very weak strength of the disorder. As disorder increases further, the TCP vanishes and a different multiciritical point known as biciritical end point (BEP) emerge along with a critical end point (CEP). We observe that the BEP is actually a coexistence of two critical phases, which was wrongly reported as a critical line before.

On the other hand, the random field disorder couples with the order parameter of the system. Thus in presence of random field disorder we find that new phases arise in the phase diagram along with multiple number of lines of first order transition, multicritical points and multiphase coexistence points. We consider two symmetric random field distributions : trimodal and Gaussian. We find that the phase diagrams are completely different for different distributions for both in the ground state and finite temperature. This behaviour contradicts the earlier conjecture by Aharony, which states that for N vector models in presence of random field disorder, different symmetric distribution should shows similar phase diagram.

We also investigate the effect of biquadratic exchange interaction (K) on spin-1 Blume-Emery-Griffiths model. We consider both the canonical and microcanonical ensemble. We mainly focus on the repulsive biquadratic exchange interaction ($K < 0$), as we find that $K < 0$ interaction in the pure model creates the similar frustration like the random crystal field disorder. We also observe that the system shows ensemble inequivalence for all $K > -1$ in the three dimensional phase diagram. Remarkably, we observe that for strong repulsive interaction, the phase diagram becomes two dimensional from three dimensional and the ensemble inequivalence vanishes for all $K < -1$.

Finally, we revisit the scaling laws near the multicritical points like the TCP, BEP and CEP to get more insight about these points for spin-1 models.

List of Figures

17

List of Tables

Chapter 1

Introduction

Disordered systems have been widely studied in statistical physics. The ideas and methodologies used to study the disordered systems have huge applications in diverse fields like computer science, neuroscience, quantum information, protein folding etc. This chapter is dedicated to the introduction of disordered systems and its effect on the phase transitions of a pure system. In the first section we will give a brief review of the phase transition and critical phenomena for pure systems and disordered systems. In the second and third sections, we will discuss about two important types of disorder and their effect on the phase transition. In the fourth section, we will discuss about some of the methodologies which are used to study the disordered systems. In the fifth section, we will introduce the spin-1 model we have studied in this thesis. In the last section we will give the outline of the thesis.

1.1 Some overview of the phase transitions and the disordered systems

1.1.1 Phase transitions and critical phenomena

Phase transitions are defined as a singularity or a discontinuity in the thermodynamic properties of a system as the external parameters are changed. A phase transition is characterized by its order parameter. The order parameter is defined as non-zero in the ordered (symmetry broken) phase and zero in the disordered (symmetric) phase. The phase transitions can be categorized into two categories : second order and first order transition. The second order phase transition occurs when the order parameter of the system changes continuously. Depending on the dimension and symmetry of the system, the second order transitions are

classified into different universality classes [1, 2]. Near the critical transition point the correlation length of the system diverges and the transition is associated with no latent heat. Whereas, first order transitions are associated with non-zero latent heat and a finite correlation lengths. This is a type of transition where the order parameter changes abruptly.

One of the examples of the phase transitions is the magnetic phase transition. The basic model for such magnetic systems is the Ising model [3]. The model is described by the following Hamiltonian :

$$\mathcal{H} = -J \sum_{i,j} s_i s_j - h \sum_i s_i \tag{1.1}$$

here J is the exchange interaction between the spins responsible for the magnetic ordering, h is the external magnetic field and the spin variables can take values $s_i = \pm\frac{1}{2}$. For a $J > 0$ and $h = 0$ there is a critical temperature T_c of the system below which ($T < T_c$) the spins align with each other and the phase is ordered ferromagnetic phase. And for temperature $T > T_c$, the spins fluctuate between $\pm\frac{1}{2}$ and thus the phase is disordered paramagnetic phase. The order parameter here is the magnetization m. For $T < T_c$ states with magnetization $m > 0$ and $m < 0$ coexist and in presence of a finite $h \neq 0$, there is a field-driven abrupt jump in the magnetization. Thus the transition is first order for $T < T_c$. At $T = T_c$ the transition becomes second order. Near the T_c, the thermodynamic quantities diverge and follows scaling laws with universal critical exponents, called the Ising universality class.

Apart from these two types of transition there are higher order critical points, known as multicritical points. Multicritical points are the critical points in a multi-dimensional thermodynamic parameter space which can be reached by tuning two or more parameters [4, 5, 6]. These points exhibit some novel features beyond what we observe near an ordinary critical point. Physical systems that exhibits multicritical points are : multicomponent fluid

mixtures [7, 8, 9, 10], binary alloys [11], liquid crystals [12, 13], semiconducting alloys [14], metamagnets [15, 16, 17], super-fluidity [18, 19] etc to name a few.

1.1.2 Disordered systems

The studies of phase transition on the homogeneous matter has been well understood [20]. The presence of disorder is an ubiquitous phenomenon in nature. Some of the important examples are the Anderson localization [21, 22], pinning of vortices in superconductors [23, 24], structural defects in magnetic crystals [25], anomalous conductivity and diffusive transport in porous media [26, 27], nonlinear properties in charge-density-waves in presence of impurities [28, 29]. Study of disordered systems are useful in understanding many optimization problems in computer science [30], quantum systems [31] and non-equilibrium phase transitions [32], as well as in biology like protein folding [33], transport processes in biological cells [34, 35]. Hence a natural question arises that how a presence of random disorder can affect the phase transition of a system and the multicritical points? The study of disordered magnetic systems and the effects of disorder on phases and critical phenomenon are widespread in condensed matter physics [36, 37, 38]. The properties of such systems are richer and more complex than their pure counterpart. In general, there is always some quenched randomness present in real materials in the form of defects, vacancies, impurities, dislocations etc, which in turn breaks the transnational symmetry of the system and also leads to frustration in the system. Therefore, studying a pure model is not sufficient to compare the experimental data of a material with its theoretically expected value [39]. In order to incorporate the disorder in a model some interactions with random variables are considered in the Hamiltonian of a system. If the time scale of the fluctuations of these random variables are smaller than the time of observation, then they are known as *annealed disorder*. As a consequence, the disorder is in thermal equilibrium with the spin degrees of freedom. The other kind of disorder is known as *quenched disorder*. The time scale of

fluctuations of such random impurities are larger than the time of observation which means the disordered variable remains frozen-in or static while the spins fluctuate. There are many different types of quenched randomness that can be taken into account. Some of the widely studied disordered systems are : spin glasses [40, 41], random anisotropic systems [42, 43], dilute systems [44, 45] and magnets under a random field [38, 46].

Presence of quenched disorder in a system can drastically change the properties of the system. The possible changes depend on the type and strength of the disorder [47] and also on the dimension of the system. Even for weak disorder, the phase transition and the critical properties of a system can change [48]. Disorder can affect the critical exponents, smoothen first order transitions, new multicritical points can emerge, or they can be moved lower in temperature [39, 49, 50, 51]. In the next two sections, we will discuss about the random-bond disorder and random field disorder. And how they affect the phase transition and order of the system.

1.2   Random-bond disorder

Random-bond disorder is a quenched disorder when the exchange interaction becomes inhomogeneous and varies from bond to bond. Such disorder arises due to crystal defects or random impurities which in turn effect the bond lengths and thus the exchange coupling changes. For example, we consider the following random-bond Ising Hamiltonian in the absence of external magnetic field

$$\mathcal{H} = -\sum_{i,j} J_{ij} s_i s_j \tag{1.2}$$

here J_{ij} is now a random variable and $J_{ij} > 0$. This disorder does not break the up-down symmetry of the Hamiltonian. Thus it does not change the phases of the system. It simply changes the local tendency towards the ferromagnetism. Which means it affects the

local critical temperature of the system. Depending on the type of the transition, the bond randomness is known to affect the system's behavior significantly [49, 52, 51, 53, 54, 55].

1.2.1 Effect of disorder on second order transition and Harris criterion

The quenched disorder coupling to the local energy density of the system has been extensively studied. For the pure models undergoing continuous transition, Harris argued a criteria for the stability of the universality class of the pure model in presence of uncorrelated or short-range correlated disorder [49]. Harris considered a system at a temperature T which is above the global critical temperature T_c of the system. The system is then divided into blocks of size of the correlation length ξ. The volume of each block in d dimension is thus $V = \xi^d$. As the bond disorder fluctuates the local critical temperature, each block has a critical temperature $T_c(i)$. Near the critical temperature T_c, the correlation length diverges as the following scaling laws

$$\xi \sim |T - T_c|^{-\nu} \tag{1.3}$$

where ν is the correlation length critical exponent. And the fluctuation of the $T_c(i)$ from block to block can be calculated from the central limit theorem. As the $T_c(i)$ is the average of the large number of random variables (J_{ij} in the Hamiltonian Eq. 1.2) in the block of volume V, the variation of the $T_c(i)$ is given by

$$\Delta T_c \sim \xi^{-\frac{d}{2}} \tag{1.4}$$

The central concept of the Harris' idea was to compare the ΔT_c with $T - T_c$ as we approach the transition i.e $\xi \longrightarrow \infty$. In order to keep the critical behavior of the system to be stable, the fluctuations in the critical temperature should follow

$$\Delta T_c < T - T_c \qquad (1.5)$$

$$\Rightarrow \xi^{-\frac{d}{2}} < \xi^{-\frac{1}{\nu}} \qquad (1.6)$$

So the criterion states that the fluctuation generated in the local critical temperature of the system due to the presence of disorder is relevant if the critical exponents of the clean system satisfies the inequality $d\nu < 2$, in other words when the specific heat exponent $\alpha > 0$ (using the hyper-scaling relation $2 - d\nu = \alpha$). This means that if the correlation length near the phase transition is large enough it can average out the inhomogeneities caused by the disorder, then it gives rise to pure-like transition, else the correlations gets blocked by impurities and thus the nature of the transition changes and it belongs to a new universality class. This criterion was proved to be correct for $O(N)$ models using renomalization group and ϵ expansion [56, 57, 58]. For the marginal case $\alpha = 0$ or $d\nu = 2$ more careful analysis are needed to confirm the stability of the critical exponents, an example of such cases is the two dimensional Ising model [59, 60]. For long-range correlated disorder the above inequality gets modified and has been reported [61, 62, 63], which implies that the effect of long-range correlated disorder are more drastic than the uncorrelated or short-range correlated disorder.

1.2.2 Effect of disorder on first order transition

The Harris criterion holds only for second order transitions [49]. Despite being ubiquitous in nature, the effect of quenched disorder on the first order transition has been studied comparatively less in literature. Due to finite correlation length the universal behaviour is not expected near a first order transition. Extending the Harris's argument, it was observed that at a first order transition $\alpha = 1$, which suggests that the disorder is strongly relevant [64]. Using the domain formation argument Imry and Wortis [52] showed that the formation of

finite size domain is favoured even in presence of arbitrary weak quenched disorder when the spatial dimension $d \leq 2$ for systems with discrete symmetry and $d \leq 4$ for systems with continuous symmetry. This destroys the phase coexistence and suppresses the first order transition. After further work based on renormalization group arguments and on the consideration of the fluctuations, this argument was proven to be correct by Aizenman and Wehr [53, 54] and by Hui and Berker [51, 55] by showing that the symmetry breaking first order transition changes to a second order transition in presence of bond randomness. Soon after this using Monte Carlo simulation it was shown for 2D Potts model [65, 66] and 2D Askin-Teller model [67] that the induced second order transition belongs to the Ising universality class. However there are studies on the q-state Potts model using Monte Carlo simulation where it was reported that the disorder-induced second order transition belongs to a new universality class [64, 68, 69, 70]. For $d > 2$ (for discrete systems) and $d > 4$ (for continuous systems), the rounding off of the first order transition to a second order transition still occurs but above a threshold value of the random impurity [51, 55, 68, 71, 72, 73, 74]. This quenched disorder induced transition occurs only if the first order transition involves a symmetry breaking [68]. Otherwise the transition gets destroyed above the threshold mentioned. Using renormalization group and simulations on Potts model, it was shown that for $d > 2$ between the first order and the disorder induced second order transition regime the system exhibits a tricritical point for a finite value of the disorder [51, 53, 69, 68, 64, 72, 75].

As shown above, the presence of bond randomness affects the systems universality class only when the $\alpha > 0$. The presence of field-disorder on the other hand are more drastic than the bond randomness as it always affects the system's critical exponents [76, 77]. The random field disorder can even eliminate the phase transition of the system in lower dimensions [46, 78, 79]. In the next section, we will discuss about the random field disorder in more details.

1.3   Random field disorder

A model with random field (RF) was first introduced in the literature by Larkin to explain the pinning of the vortex lattice in type-II superconductors [23, 24]. The RF disorder couples with the order parameter of the system. Thus the effect of RF disorder is more drastic. The random field disorder do not preserve the symmetry of the system that breaks at the low temperatures (for example for Ising model, the random field disorder locally breaks the up-down symmetry of the system). The fluctuations of the RF can dominate the macroscopic collective behaviour of the system. Spin systems with random field disorder are an important class of models studied extensively as prototypes for collective phenomenon in systems with quenched disorder [80, 81, 82, 83, 84, 85, 86, 87, 88]. They model diluted antiferromagnets like $Fe_x Zn_{1-x} F_2$, $Rb_2 Co_x Mg_{1-x} F_4$ in the presence of a uniform magnetic field [80, 81, 82]. In addition to this, many random systems like prewetting transition on a disordered substrate [83], binary fluid mixtures in random porous media [84], phase transitions and interfaces in random media [85], structural phase transitions in random alloys [86], binary fluids in gels [87], protein folding [89], collective effects induced by imitation and social pressure on society via network models [88] are modelled by ferromagnets in the presence of random field. Geophysical models of marine climate pattern [90], identification of subsurface soil patterns [91], analysis of molecular structures [92], biomedical imaging [93, 94], population genetics [95], data science [96] and many more problems in other disciplines [97] have also been modelled using random fields.

1.3.1   The random field Ising model and Imry-Ma argument

The simplest frustrated system which has been studied for years is the random field Ising model (RFIM) [98, 99, 76, 100, 101, 102, 103, 104, 105, 106]. The Hamiltonian of the RFIM is as follows
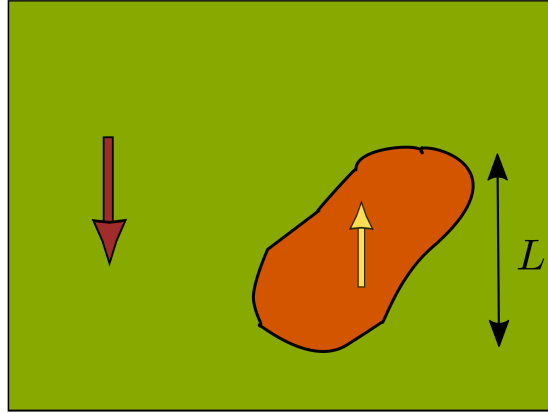
Figure 1.1: Imry-Ma argument derivation by comparing the energy cost due to the domain formation and energy gain due to the alignment of the up spins with the random field. Figure taken from [107].

$$\mathcal{H} = -J \sum_{i,j} s_i s_j - \sum_i h_i s_i \tag{1.7}$$

here h_i is considered as a random variable with zero mean and a finite variance. J is the bilinear exchange interaction term. In spin models, the spins try to align due to the bilinear exchange interaction and the random field tries to align them along the random field direction. Thus the presence of random field disorder creates a frustration in the system. The thermal fluctuations are irrelevant in comparison to the random field fluctuations. That's why the critical properties at finite temperature can be deduced from the study of the zero temperature phase diagrams.

For a long time there has been a confusion about the lower critical dimension of the RFIM model, below which the random field destroys any long-range order. There were arguments based on perturbative renomalization group theory that the lower critical dimension $d_l = 3$ [108, 109, 110]. Later using the phenomenological argument about domain formation it was shown by Imry and Ma [46] that for spatial dimension $d > 2$ there is an ordered phase for low temperature and weak disorder. The basis of the argument of the destruction of the first order transition in presence of bond randomness [52, 53, 51] was

from the adaptation of the Imry-Ma argument on the effect of random fields [46]. The bond randomness couples with the energy density of the system which is different for different coexistence phases. This acts in the similar manner like the random field which couples with the local magnetization of the system [51, 68, 55, 69].

Imry and Ma developed an argument on the stability of the ferromagnetic state against domain formation [46]. They considered one spin-up domain of length L in d dimensions, embedded in a large spin-down region shown in Fig. 1.1. Now the energy cost at the interface of the domain generated due to the domain formation is proportional to the area of the domain L^{d-1}. And each bond at the interface contributes energy $+J$. So the total energy cost is

$$\Delta E_{domain\ wall} \sim JL^{d-1} \tag{1.8}$$

If the random field distribution has a zero mean $\langle h_i \rangle = 0$ and variance σ^2, then the energy gain in the spin-up domain aligning with random field is given by the central limit theorem

$$|\Delta E_{random\ field}| \sim \sigma L^{\frac{d}{2}} \tag{1.9}$$

Imry-Ma argued that, the ferromagnetic state against the domain formation will be stable if $|\Delta E_{random\ field}| < \Delta E_{domain\ wall}$. Which gives $\sigma L^{\frac{d}{2}} < JL^{d-1}$. For $d > 2$, the domain wall interface energy increases with L compared to the random field energy and hence the domain formation becomes unfavourable and the ferromagnetic state remains stable. And the long range order destroys for $d < 2$.

Similar to the bond randomness it was concluded that for systems with composed of $n = 1$ components of spins like Ising model (with $n \geq 2$ components of spins like the XY and Heisenberg model), the random field disorder converts a temperature driven first order

transition into a second order transition for $d \leq 2$ (for $d \leq 4$) if the transition involves a symmetry breaking [51, 53]. And above this dimension the first order transition vanishes for a finite random field disorder [111]. Since this seminal work of Imry-Ma, a lot of studies concluded using renormalization group calculations, perturbations around the upper critical dimension, interface model and also using Monte Carlo simulations that the lower critical dimension of RFIM is $d_l = 2$ [78, 79, 112, 113, 114, 115, 116, 77]. Similar to the Harris criterion, the Imry-Ma argument also gets modified in presence of the long-range correlated random field disorder [117].

Another important topic has been the order of the transition at zero temperature and how they depend on the type of field distribution. There are several probability distribution that have been studied in the literature. Most common are the Gaussian [100] and the bi-modal [76] probability distribution. Earlier, it was conjectured by Aharony [76] using the mean-field theory and renormalization group argument that for $O(N)$ models in presence of random field disorder the phase transition at low temperature is first order (second-order) if the random-field distribution function $p(h_i)$ is symmetric and has a minimum (maximum) at zero field $p''(0) > 0$ $(p''(0) < 0)$. Following this work, Andelman [101] extended the condition based on the number of maxima of the random field distribution function. It showed that if the distribution $p(h_i)$ has n maxima, then for even n, $p''(0) > 0$ and the transition is first order at lower temperature. On the other hand, for odd $n > 1$, $p''(0) < 0$ and the transition is second order if is not take over by a first order transition. Later this criterion for the maxima ($p''(0) < 0$) was modified by Galam and Birman in [102] such that if with $p''(0) < 0$, the random field distribution also satisfies the following conditions for $p^{n'}(0) = \frac{d^n p(H)}{d|H|^n}\Big|_{|H|=0}$:

$$p^{4'}(0) > 0, \quad p^{6'}(0) < 0 \tag{1.10}$$

$$p''(0) > \frac{7}{15} p^{4'}(0)^2 / p^{6'}(0) \tag{1.11}$$

then the transition is first order, otherwise it is second order. Thus the Gaussian and the bimodal field distribution give rise to two different phase diagrams in RFIM. For Gaussian field distribution, there is always a continuous line of transition. Whereas, for bimodal distribution, the transition is continuous at the high temperature and first order at low temperature. These two phase boundaries are separated by a tricritical point (TCP) [76].

There are other distributions also which have been studied for RFIM like the trimodal distribution [105, 106, 118, 119], double Gaussian [120], triple Gaussian [121], asymmetric trimodal distribution [122], asymmetric bimodal distribution [123] and so on. It has been observed that, the phase topologies changes non-trivially with the symmetry of the probability distribution function. The equal peak trimodal distribution has been argued to be a good approximation of the Gaussian distribution in [105]. In [106, 118, 119, 124], for RFIM the trimodal and the Gaussian distributions were found to have similar phase diagram with only continuous transition at all temperatures. The experimental realisation of the RFIM is the diluted antiferromagnetis in presence of uniform magnetic field [80, 82, 81]. It shows the same critical behaviour and belongs to the universality class of RFIM [125, 126, 127]. In three dimensions the nature of the transition is still debated [103, 104, 128, 129]. Most recent numerical studies in three dimensions find the transition to be continuous independent of the nature of the random field distribution [103, 104].

In the next section, we will discuss about some of the analytical methodologies which are used to study the disordered systems.

1.4 Methods to study disordered systems

Since quenched disorder is static during the time of observation, the impurity degrees of freedom are not in thermal equilibrium with the spin degrees of freedom. Due to this nature the free energy and other thermodynamic functions depend on the certain realization of the

quenched variable. For example, for the Hamiltonian given by Eq. 1.2 the partition function for each realization of J_{ij} is given by

$$Z_J = \sum_{\{s\}} e^{-\beta \; \mathcal{H}_J(s)} \tag{1.12}$$

and the free energy becomes

$$f_J = -\frac{1}{\beta} \log Z_J \tag{1.13}$$

Hence to obtain the averaged thermodynamic quantities the free energy is needed to be averaged over the all possible configurations of the quenched random variable. Or equivalently, the logarithmic of the partition function needs to averaged over the different realizations of the quenched disorder variable.

$$F \equiv \langle f_J \rangle_{P(\{J\})} = -\frac{1}{\beta} \langle \log Z_J \rangle_{P(\{J\})} \tag{1.14}$$

This averaging over the logarithmic function makes the problem of disordered system more challenging. Simulations in the finite dimensions are also a difficult task due to the lack of self-averaging [130, 131, 132, 133].

There are some analytical methods which are used to do the disorder averaging. Some of the examples are replica trick [134, 40], cavity method [135], TAP approach [136, 137, 138], the dynamical approach [139, 140], the distributional zeta-function method [141], large deviations technique [142, 143]. In the next subsections we will discuss briefly about two of such methods.

1.4.1 The replica trick

Instead of averaging over the $\log Z$ directly, the replica trick considers n identical and independent copies of the system called *replica* and uses the following logarithmic identity to calculate the disorder averaged free energy :

$$\langle \log Z_J \rangle_{P(\{J\})} = \lim_{n \to 0} \frac{\langle Z_J^n \rangle_{P(\{J\})} - 1}{n} \tag{1.15}$$

It thus calculates the disordered averaged free energy by averaging over the nth power of the partition function Z and then taking the limit $n \to 0$ by analytic continuation.

The replica trick was first introduced by Edward and Anderson [40] for the theory of spin glasses. This method has been highly successful for example in the theory of spin glasses. But there are some drawbacks. For example, Sherrington and Kirkpatrick (SK model) [41] observed that for infinite range Ising spin glass gives unphysical results like negative entropy at low temperatures. This problem happens due to the interchange of the thermodynamic limit ($N \longrightarrow \infty$) and the $n \longrightarrow 0$ limit. To avoid this unphysical results, later a scheme of *replica symmetry breaking* was introduced by Parisi [144, 145, 146].

1.4.2 The TAP approach

There is another approach called TAP, named after Thouless, Anderson and Palmer [136]. It does not first calculate the disorder average partition function. For a given realization of the disordered variable, it constructs a mean-field equation for the local magnetization. For example, for the following Hamiltonian in presence of an external magnetic field h_i

$$\mathcal{H} = -\sum_{i,j} J_{i,j} s_i s_j - \sum_i h_i s_i \tag{1.16}$$

The approach starts by taking a Legendre transformation of the free energy for a given realization of J_{ij}, $f_J(\{h_i\}) = -\frac{1}{\beta} \log Z_J(\{h_i\})$ to obtain a function which only depends on the magnetization m_i [138]

$$\Gamma(\{m_i\}) = \min_{\{h_i\}} \left\{ f_J(\{h_i\}) + \sum_i h_i s_i \right\} \tag{1.17}$$

here h_i fix the value of the magnetization m_i as the thermal expectation value of s_i for site i defined as $m_i \equiv \langle s_i \rangle$. And it obeys the following equation

$$\frac{\partial f_J(\{h_i\})}{\partial h_i} = -m_i \qquad (1.18)$$

Once the $\Gamma(\{m_i\})$ is known the local magnetization is now fixed by the following inverse Legendre transform

$$\frac{\partial \Gamma(\{m_i\})}{\partial m_i} = h_i \qquad (1.19)$$

The Eq. 1.19 is known as the TAP equation and the TAP free energy of the system can be introduced as

$$f_J(\{m_i; h_i\})_{TAP} = \Gamma(\{m_i\}) - \sum_i h_i s_i \qquad (1.20)$$

whose minima is given by Eq. 1.19 and gives the value of stable local magnetization. For example, for SK model [41] the N coupled TAP equations Eq. 1.19 were calculated [138] to be

$$\beta h_i = \tanh^{-1} m_i - \beta \sum_j J_{ij} m_j - \beta^2 \sum_j J_{ij}^2 m_i (1 - m_j^2) \qquad (1.21)$$

which is very similar to the mean-field equations for the local magnetization of the Ising model [1]. For high temperatures, all the N coupled equations only gives a solution $m_i = 0$, which is a paramagnetic state. For lower temperatures, the zero eigenvalues of the Jacobian of Eq. 1.19, $\mathcal{J}_{ij} = \frac{\partial h_i}{\partial m_j}$ (which are related to the eigenvalues of J_{ij}) are used to locate the transition to spin glass state.

In the next section, we will now introduce the spin-1 Blume-Capel model which we have used to study the effect of disorder and it's phase diagram.

1.5   Model used in this thesis : The Blume-Capel model

Blume-Capel model is the extension of spin-1 Ising model with a single-ion crystal field anisotropy. This model was first introduced to explain the first order transition in UO_2 by Blume [147] and Capel [148]. It is the simplest spin model which exhibits higher order critical point, the tricritical point (TCP). The Blume-Capel model has been investigated extensively using various techniques like : mean-field approach [147, 148, 149], renomalization group theory [150], Monte-Carlo simulation [151, 152], series expansion [153] and so on. The Blume-Capel model is used as a prototype model of a wide range of physical systems like : $^3He - ^4He$ mixtures [149], metamagnets [154, 4], phenomena of inverse melting and freezing [155, 156, 157], multicomponent fluid mixture [158, 159], binary alloys [160, 161] and so on.

We have considered the Hamiltonian of an infinite range Blume-Capel model of N spins as the following :

$$\mathcal{H} = -\frac{1}{2N}(\sum_i s_i)^2 + \Delta \sum_i s_i^2 - H \sum_i s_i \qquad (1.22)$$

where s_i can take values $\pm 1, 0$ and every spin is connected to every other spin. The first term is the bilinear exchange interaction, Δ is the crystal field of the system which controls the density of the magnetic and non-magnetic spins, H is the uniform external magnetic field. There are two order parameters of the system. The magnetization $m = \frac{\sum_i s_i}{N}$ and the spin density $q = \frac{\sum_i s_i^2}{N}$. In the limit $\Delta \longrightarrow -\infty$ the non-magnetic spins are suppressed and the model becomes equivalent to Ising model. And for large positive Δ, the $s = 0$ spins dominates. In the ground state it can be straightforwardly shown that for $\Delta < \frac{1}{2}$, the phase is ordered and for $\Delta > \frac{1}{2}$ the phase is disordered. At $\Delta = 0$, the line of continuous transitions cuts the temperature (T) axis at $T = \frac{2}{3}$.

Due to the interplay between the bilinear exchange interaction and the crystal field in-
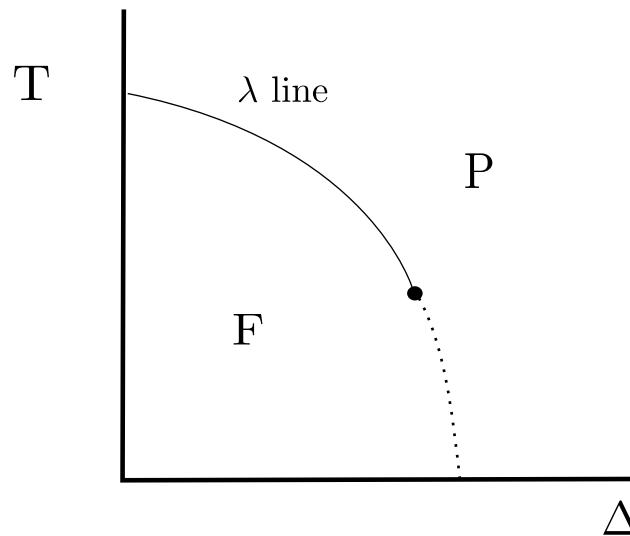
Figure 1.2: Schematic phase diagram of pure Blume-Capel model in the $T - \Delta$ plane. The solid line depicts the line of continuous transition and the dotted line is the line of first order transition. The solid black circle denotes the TCP.

teraction the phase diagram of the Blume-Capel model is very interesting. The mean-field solution of the Blume-Capel model is known to give the correct exponents of the TCP in three dimensions [162]. And also this method predicts the phase diagram of the Blume-Capel model correctly for all dimension $d \geq 2$ [163, 151, 164, 165, 166, 167, 168].

In the next subsection we will discuss about the phase diagram of the pure Blume-Capel model in the $T - \Delta$ and $T - \Delta - H$ plane.

1.5.1 Phase diagram of the Blume-Capel model

The Blume-Capel model even in its pure form has a rich phase diagram. In the absence of any external magnetic field H, the phase diagram of the pure Blume-Capel model in the $T - \Delta$ plane is shown in Fig. 1.22. For high T and lower values of Δ there is a line of continuous transition (shown by continuous line) which separates one ordered phase **F** from a disordered phase **P**. This line is known as λ line. It belongs to the Ising universality class. As Δ increases, for low values of T, the transition changes to a first order transition
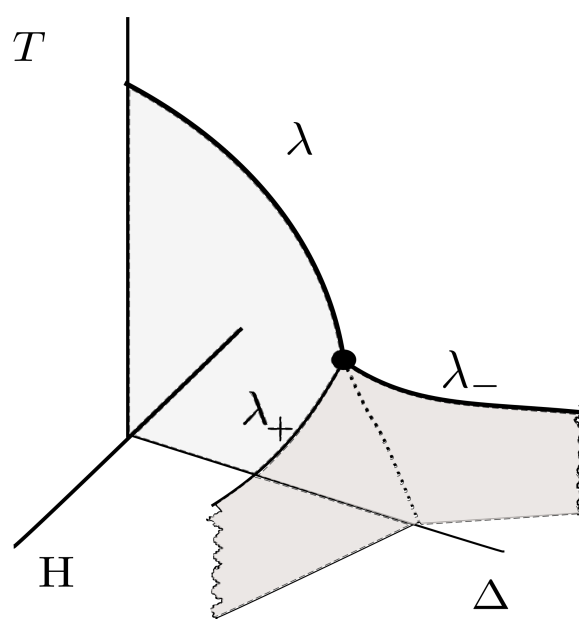
Figure 1.3: Schematic phase diagram of pure Blume-Capel model in $T - \Delta - H$ space. The solid lines depicts the loci of the lines of continuous transition (λ, $\lambda_{\pm}$). The dotted line denotes the triple line. The shaded surfaces in the finite H plane denotes the wings separating an ordered phase from a disordered phase.

(shown by dotted lines). The first order transition line is known as triple line, as this line is a coexistence of three phases : $\pm m$ and $m = 0$. The triple line meets the $T = 0$ axis at $\Delta = \frac{1}{2}$. The two type of transition lines meet at a TCP, shown by a solid circle in Fig. 1.2. The TCP for the mean-field model is located at $\beta = 3$ and $\Delta = \frac{\ln 4}{3}$.

As the external magnetic field H get switched on, the phase diagram looks like Fig. 1.3 in the $T - \Delta - H$ space. Two more lines of continuous transition in the finite $H \neq 0$ plane meets the λ line at $H = 0$ at the TCP, where the first order line meets the λ line. So the TCP is actually a confluence of three lines of continuous transition and thus justifies the name. These two critical lines in the $H \neq 0$ plane bounds two first order surfaces in the $H \neq 0$ plane. These surfaces separates a ferromagnetic phase from a paramagnetic phase (shown by dark shaded surface). These surfaces appear symmetrically about the $H = 0$ plane like the wings of a bird, thus they are referred to as "wings" [169, 149]. The lines of continuous transition which bounds the wings are known as $\lambda_\pm$ lines. They are also from the Ising universality class. The surface in the $H = 0$ on the other hand separates two ferromagnetic phases with opposite magnetization (shown by light shaded surface). The $\lambda_\pm$ lines exists only for the range of $\frac{1}{4} \leq T \leq \frac{1}{3}$ [149]. The wings continues to exist till $T = 0$ and $\Delta \longrightarrow \infty$. This three dimensional phase diagram of the wings has been also experimentally observed in many systems. For example : metamagnets like compounds of UGe_2 [170, 171], $ZrZn_2$ [172], $LaCrGe_3$ [173] to name a few.

The projection of the wings on the $T = 0$ plane is shown in Fig. 1.4. For $H = 0$, until $\Delta = \frac{1}{2}$, there is one first order transition line separating $m = \pm 1$. For $\Delta > \frac{1}{2}$, two more first order line emerges in the finite H plane. These lines can be calculated by comparing the energies of each phases. The $m = 1$ (or $m = -1$) phase is separated from $m = 0$ phase via $H = \Delta - \frac{1}{2}$ (or $H = -\Delta + \frac{1}{2}$) line. These lines continues to exists for $\Delta, H \longrightarrow \infty$.
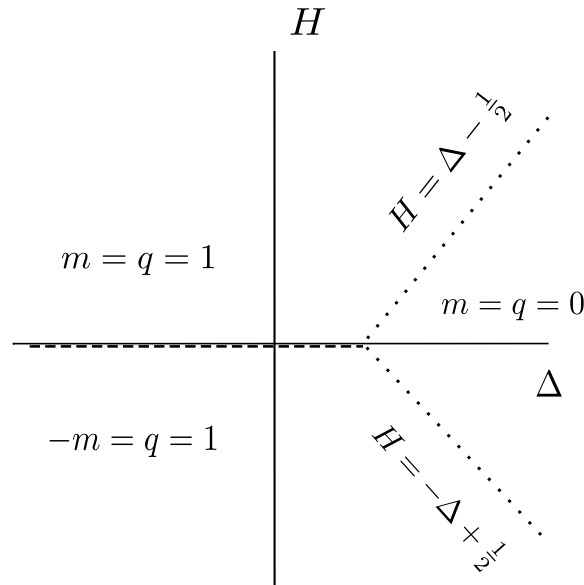
Figure 1.4: Ground state phase diagram of the Blume-Capel model on the $\Delta - H$ plane. Dotted lines represents the lines of first order transition. Until $\Delta = \frac{1}{2}$, the line separates the $m = \pm 1$ spins. For $\Delta > \frac{1}{2}$, the $m = 1$ phase is separated

1.5.2   Tricritical point (TCP)

TCPs are the most widely studied and understood multicritical point. The TCP was first introduced by Griffiths [174] in the context of the phase diagram of the mixtures of $^3He - ^4He$. TCP is actually a point where three phases become identical. TCPs are ubiquitous in nature. Depending on the symmetry of the system the TCPs can either be symmetric TCP or asymmetric TCP. Symmetric TCPs exists for example in metamagnets like Ni $(NO_3)_2$. $2H_2O$ [15], Dy Al garnet [16], $FeCl_2$ [17], ^{3} He - ^{4} He mixture [18]. Whereas, for fluid mixtures like NH_4 Cl [7] the TCPs are asymmetric. There are systems like : alloys of magnetic and non-magnetic materials [11], superconducting films [14], quantum metals [175], polymer collapse [176], polymerized membranes [177], liquid crystal [12], ferroelastic and ferroelectric phase transitions in materials of inorganic fluoro- and oxyfluorometallates [178], piezoelectric materials [179] to name a few which also shows the presence of TCP in the phase diagram. Apart from the Blume-Capel model, there are other solvable

38

models which shows TCP. For example : Potts model [180], Blume-Emery-Griffiths model [149], n-component vector model [181], compressible Ising model [182] and so on.

1.6 Objectives of this thesis

As the discussions from the above sections indicate, the study of the effect of different types of disorder has been studied extensively for spin-$\frac{1}{2}$ Ising model [76, 100, 103, 105]. The effect of disorder on spin-1 models has been studied comparatively less. The pure Blume-Capel model is the simplest spin model which shows a multicritical phase diagram. Thus it becomes a very useful model to verify both the Harris criterion for the second order transition and the criterion for the destruction of the first order transitions in presence of disorder on equal footing. In the existing literature the Blume-Capel model has been mostly studied in presence of random crystal field disorder [183, 184, 185, 186, 187, 188, 189, 190, 191, 192, 193, 194, 195, 196] and random-bond disorder [197, 198, 199, 200, 201, 202, 203, 204, 11]. Comparatively few studies have been done on the Blume-Capel model in presence of random field disorder [205, 206, 207, 208, 209]. All these studies have been done in the two dimensional plane phase diagram. Although the full phase diagram of the Blume-Capel model is three dimensional. Hence it is important to study the effect of disorder on the three dimensional space to understand what happens to the multicritical points.

In our thesis we address two very important questions :

- The crystal field interaction term controls the magnetic and the non-magnetic spins. It is like the external field coupled with the order parameter q, shown in the Hamiltonian of the pure Blume-Capel model (Eq. 1.22). As in presence of disorder destroys the first order transitions and also affects the multicritical points, it is interesting to see what happens to the first order transition line, the TCP and as well as in the $\lambda_\pm$ lines as we introduce randomness in the crystal field interaction?

- The random field disorder is an important class of disorder. It couples with the magnetization of the system and thus affect the phases of the system. The random crystal field, on the other hand couples with the density of the spins which in turn affects the entropy of the system. The effect of random field disorder is very different that of the random crystal field disorder. The spin-1 RFIM has previously been investigated using Monte-Carlo simulations in order to study the solid mixture of $Co_{1-x}(N_2)_x$ [210]. Apart from that there have been study on transverse spin-1 RFIM [211] and bond diluted spin-1 RFIM model [212]. But the role of the crystal field has not been discussed there. The presence of the crystal field interaction acts as a chemical potential due to which the pure Blume-Capel model exhibits a first order transition lines. On the other hand it is well established that presence of random field disorder can destroy or replace a first order transition by a second order transition. So a basic question arises that what happens when the crystal field interaction and the quenched random field disorder interplay?

In this thesis we thus study the effects of random-crystal field [213] and random-field [214] disorder on the spin-1 Blume-Capel model in the three dimensional space. We use an approach based on large deviations methods [215]. This method allows one to calculate the disorder averaged free energy directly from the probability distribution of the magnetization m and the spin desnity q. We mainly focus on the effects of different types of disorder on the first order transition and on the multicritical points. We consider the model on a fully connected graph. We discuss the properties of the new multicritical and multicoexistence points that emerge due to disorder. We also revisit the scaling laws near these points. We also study the effect of higher order interactions on the spin-1 Blume-Capel model and shows some interesting similarity between the effect of disorder and the higher order interactions.

1.7   Outline of the thesis

The plan of the thesis is as follows.

In **Chapter 2** we introduce the method we have used to solve the spin-1 Blume-Capel model in presence of disorder : the large deviations principle. We discuss about the rate function and Gärtner-Ellis theorem. We introduce the titled large deviations principle which we have used throughout in our work.

In **Chapter 3** we introduce the randomness in the crystal field term of the Hamiltonian of the Blume-Capel model. We take a two peak δ distribution for the crystal field randomness. We study the three field space phase diagram depending on the strength of disorder. We then discuss about the effect of disorder on the multicritical points.

In **Chapter 4** we introduce two types of symmetric random magnetic field disorder : discrete and continuous in the infinite-range Blume-Capel model Hamiltonian and study the effect of disorder on the phase diagram and the multicritical points. We study the ground state and finite temperature phase diagrams for both types of disorder in the three-field space depending on the strength of disorder. We then discuss about some interesting features of the phase diagrams that emerge due to disorder.

In **Chapter 5**, we consider the effect of higher order interactions on the generalized infinite range Blume-Capel model, known as the Blume-Emery-Griffiths model. We study the system in two ensembles : canonical and microcanonical in the three dimensional parameter space. We discuss the phase diagrams in both the ensembles. We then discuss about the ensemble inequivalence of the phase diagram in the infinite ranged Blume-Capel model both by looking at the first order as well as second order transition lines.

The nature of the multicritical points are different than an ordinary critical point. In order to understand their nature one must investigate the singularities of the thermodynamic quantities close to these multicritical points. There are well studied scaling hypothesis near

the multicritical points. In **Chapter 6** we show the scaling relations near the multicritical points like tricriitcal point (TCP), critical end point (CEP) and bicritical end point (BEP) that emerges in the disordered Blume-Capel model. We discuss about the earlier scaling hypothesis near these points and revisit those arguments for the disordered spin-1 Blume-Capel model.

Finally in **Chapter 7** we summarize the results of the the thesis and propose some future directions.

Chapter 2

Large deviations theory

In this chapter we will present the theory of large deviations which we have used to study the disordered spin models. The large deviations theory (LDT) deals with the exponential decay of probabilities of large fluctuations in random systems. The theory of large deviations was first developed by Cramér [216] and later by Donsker and Varadhan [217]. Since then it has been found that it has many interesting applications in financial mathematics, statistics, equilibrium and non-equilibrium statistical physics [218, 219, 215, 220, 221]. The LDT gives a complete mathematical framework in which the problems of statistical mechanics can be formulated and solved efficiently. The LDT can be viewed as a mathematical interpretation of the entropy of a system.

To get the central idea of the LDT, we consider the following example. Suppose there are a sequence of n independent and identically distributed (i.i.d.) random variables X_1 ,...,X_n drawn from a probability distribution with mean μ and variance σ^2. Let $S_n = X_1 + X_2 + ... + X_n$ is the sum of the i.i.d. variables. Then according to the Strong Law of Large Numbers (LLN) the sum for $n \longrightarrow \infty$ reduces to

$$\lim_{n \longrightarrow \infty} \frac{1}{n} S_n \longrightarrow \mu \qquad (2.1)$$

So as n grows the probability distribution of the function S_n peaks more and more at the mean μ. The LLN thus gives the description of the most probable state of the system. Similarly, the central limit theorem (CLT) gives the information about the states that differs from the most probable value by an order $\approx \sqrt{n}$. It states that the probability distribution of the quantity $\frac{1}{\sigma \sqrt{n}} (S_n - n\mu)$ converges to a normal distribution with zero mean and variance

43

σ as $n \longrightarrow \infty$:

$$\lim_{n \longrightarrow \infty} P \left(\frac{1}{\sigma \sqrt{n}} \left(S_n - n\mu \right) \in [x, x + dx] \right) = \frac{1}{\sqrt{2\pi\sigma^2}} e^{-\frac{x^2}{2\sigma^2}} dx \qquad (2.2)$$

The CLT is a very important theorem that deals with the small fluctuations of the random variables of order $\sqrt{n}$. But CLT does not hold when the fluctuations from the mean are larger that $\sqrt{N}$. The Gaussian form in Eq. 2.2 becomes a very poor approximation at the extreme tails. The information about the fluctuations of greater order is correctly given by the LDT, which justifies the name large deviations theory. It not only describes the rare events but also describe the typical events. To put it the other way, the LDT is the generalization of the CLT.

In the first section of this chapter, we give the general definition of the large deviation principle (LDP) and the rate function. We give some examples which illustrate the LDP. In section 2, we introduce the Gärtner-Ellis Theorem which gives a systematic way to calculate the rate function of the system. In section 3, we list some of the properties of the rate function. In section 4, we introduce an important theorem: the tilted LDP, which has been used throughout in our work. And finally in section 5, we give an illustrative example of the tilted LDP on the infinite range RFIM.

2.1 General definition of large deviation principle (LDP)

The LDT concerns with the exponential decay of the probability for large system size and the rate at which the probability decays to zero is known as the rate function. Let A_n be a sequence of random variable indexed by integer n, and let $P(A_n \in B)$ be the probability that A_n takes on value from the set B. The probability that $P(A_n \in B)$ satisfies large deviations principle (LDP) with rate function I_B iff the following limit exists.

$$\lim_{n \longrightarrow \infty} -\frac{1}{n} \ln \left[P(A_n \in B) \right] = I(B) \tag{2.3}$$

Here $I(B)$ is called the rate function. The number n is assumed to be large in the condition that $n \, I(B) >> 1$. In statistical mechanics the n is the size of the system. The probability of the occurrence of the event B becomes maximum when the rate function $I_B = 0$. The above expression can be approximated as the following scaling law of the form

$$P(A_n \in B) \approx e^{-n \, I(B)} \tag{2.4}$$

which means that the dominant behaviour of the probability $P(A_n \in B)$ is a decaying exponential in n, which means

$$-\frac{1}{n} \ln P(A_n \in B) = I(B) + o(1) \tag{2.5}$$

and for $n \longrightarrow \infty$, the contribution of the order $o(1)$ is negligible. Thus if $P(A_n \in B)$ satisfies LDP, then the limit given in Eq. 2.3 should exist with a rate function $I(B) \neq 0$. If the limit does not exists then three possibilities might arise

- Either $P(A_n \in B)$ is too singular to have a limit

- $P(A_n \in B)$ decays with n faster than $e^{-n \, a}$ with $a > 0$. In such cases the $P(A_n \in B)$ decays super-exponentially with rate $I(x) = \infty$

- $P(A_n \in B)$ decays with n slower than $e^{-n \, a}$ with $a > 0$. In such cases the $P(A_n \in B)$ decays sub-exponentially with rate $I(x) = 0$

The cases which are relevant to the theory of large deviations are where the limit Eq. 2.3 holds with a non-trivial rate function $I(B)$ which is different from 0 and ∞.
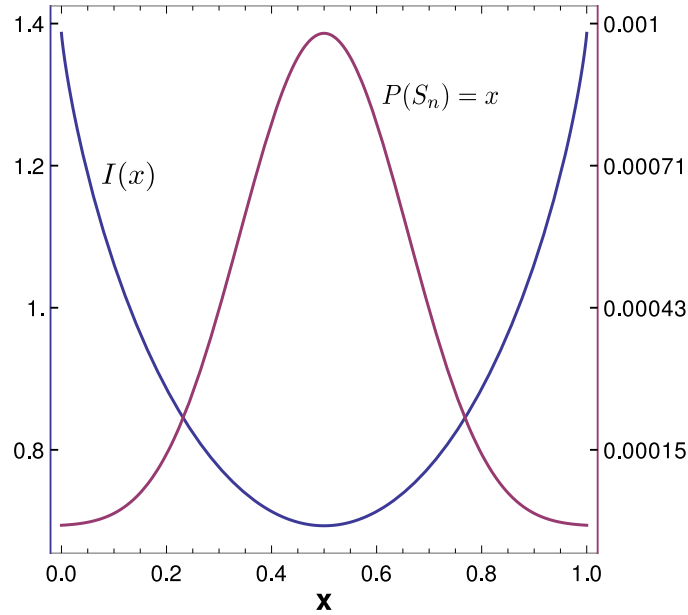
Figure 2.1: Application of the LDT for a coin tossing problem. Plot shows the rate function $I(x)$ and probability distribution $P(S_n = x)$ of r heads for n tosses. The $I(x)$ has a minima at the most probable value which is $x = \frac{1}{2}$.

In the next subsections we will give some examples where the large deviation approximation holds.

2.1.1 Coin toss problem

For a coin toss problem each coin can have two possibilities. We consider a random variable X_i taking two values $P(X_i = 1) = P(X_i = 0) = \frac{1}{2}$. Out of n tosses the probability that the total number of heads are r is :

$$P(S_n = r/n) = \frac{1}{2^n} \frac{n!}{r!(n-r)!} \tag{2.6}$$

Using Stirling's approximation for $n \longrightarrow \infty$ and $r \longrightarrow \infty$, keeping the ratio $x \equiv \frac{r}{n}$ finite we get the asymptomatic behavior of the probability for large n as :

$$P(S_n = x) \approx e^{-nI(x)} \tag{2.7}$$

which thus shows the exponential decaying form of the large deviation approximation with the decay function non-negative $I(x)$ given by

$$I(x) = x \ln x + (1 - x) \ln(1 - x) + 2 \ln 2 \quad 0 \le x \le 1 \tag{2.8}$$

Fig. 2.1 shows the plot of the rate function $I(x)$ as well as the probability $P(S_n = x)$ as a function of x. The probability is maximum (the most likely value) at $x^* = \frac{1}{2}$, the same position where the $I(x)$ is minimum, which reminds us the LLN. So the zeros of the $I(x)$ provides the most probable values.

For fluctuations of order $\sqrt{n}$, we approximate the $I(x)$ upto the first quadratic term as :

$$\begin{aligned} I(x) &\approx& \frac{1}{2} I''(x^*)(x - x^*)^2 \\ &\approx& 2(x - 0.5)^2 \end{aligned} \tag{2.9}$$

and the probability distribution leads to the following Gaussian distribution similar to the CLT :

$$\begin{aligned} P(S_n = x) &\approx& e^{-n\frac{1}{2} I''(x^*)(x - x^*)^2} \\ &\approx& e^{-2n(x - 0.5)^2} \end{aligned} \tag{2.10}$$

2.1.2 Gaussian sample mean

We consider a sample mean of a sequence

$$S_n = \frac{1}{n} \sum_{i=1}^{N} X_i \tag{2.11}$$

and assume that the $\{X_i\}$ are i.i.d random variables drawn from the following Gaussian probability distribution

$$p(X_i = x) = \frac{1}{\sqrt{2\pi\sigma^2}} e^{\frac{-(x-\mu)^2}{2\sigma^2}} \tag{2.12}$$

here μ is the mean and σ^2 is the variance of X_i's.

The probability distribution that $S_n = s$ can be written as

$$P(S_n = s) = \int_{\mathbf{R}^n} \delta(S_n(x) - s) \; p(x) \; dx \tag{2.13}$$

where $p(x) = .p(x_1, x_2, ..., x_n) = p(x_1)p(x_2).....p(x_n)$ for the i.i.d random variables. Thus the integration Eq. 2.13 turns out to be

$$P(S_n = s) = \sqrt{\frac{n}{2\pi\sigma^2}} \; e^{-\frac{n(s-\mu)^2}{2\sigma^2}} = \sqrt{\frac{n}{2\pi\sigma^2}} \; e^{-nI(x)} \tag{2.14}$$

here the rate function is $I(x) = \frac{(s-\mu)^2}{2\sigma^2}$.

2.2 Calculation of the Rate Function

In the previous section we calculated the rate function using Stirling's approximation, it is possible to calculate the rate function straight from the computation of the probability distribution. In general, it could be challenging to obtain LDP using this direct approach. There are other methods like by using **Gärtner-Ellis Theorem** [215] to calculate the rate function. We will describe it briefly in this section.

2.2.1 Gärtner-Ellis Theorem

This theorem states that the rate function $I(x)$ can be calculated from the Legendre-Fenchel transformation of the scaled cumulant generating function (SCGF) of the random variable, if the SCGF is differentiable.

The SCGF or a logarithmic moment generating function $\lambda(k)$ for $k \in \mathbb{R}$ of a random variable A_n is defined by

$$\lambda(k) = \lim_{n \longrightarrow \infty} \frac{1}{n} \ln \; \langle e^{nkA_n} \rangle \tag{2.15}$$
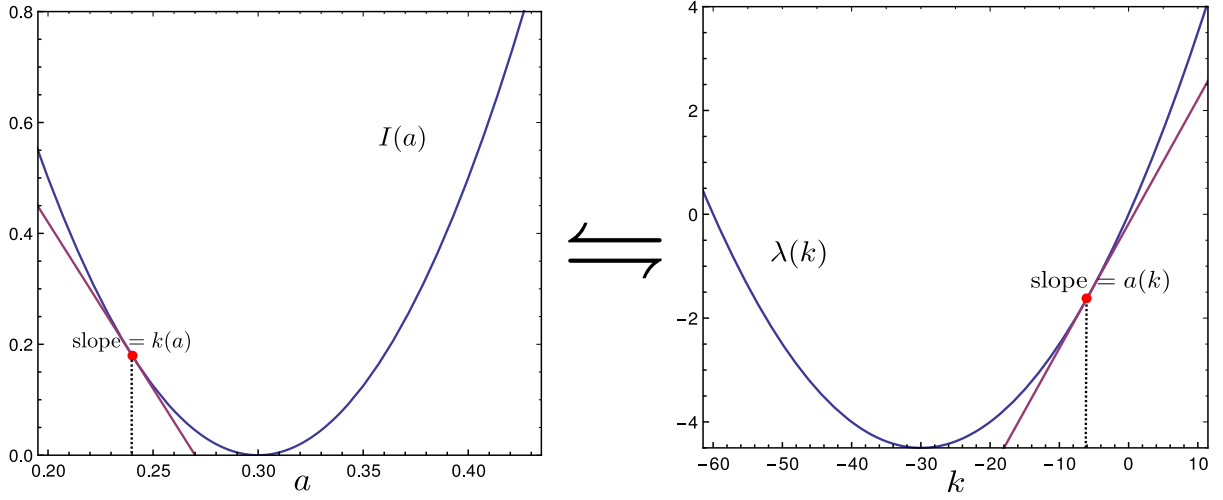
Figure 2.2: Self duality of the Legendre-Fenchel transformation. The slope of the $I(a)$ at a (which is $I'(a) = k(a)$) is the point at which the slope of $\lambda(k)$ is a. This happens when the functions $I(a)$ and $\lambda(k)$ are differentiable and convex.

where the $\langle\rangle$ defines the average w.r.t the probability density of A_n :

$$\langle e^{n\,k\,A_n} \rangle = \int_{\mathbf{R}} e^{n\,k\,a}\ P(A_n\ \in da)$$

Gärtner-Ellis theorem states that, if $\lambda(k)$ exists and is differentiable for all $k \in \mathbf{R}$, then A_n satisfies LDP with a rate function $I(a)$ given by

$$I(a) = \sup_{k\in\mathbf{R}} \{k\,a - \lambda(k)\}$$

The symbol 'sup' stands for the supremum of the function. And the transformation is known as the Legendre-Fenchel transformation [222, 223]. We note that the rate function $I(x)$ is always positive, as the negative $I(x)$ will imply that the probability $P(A_n\ \in da)$ diverges as $n \longrightarrow \infty$.

This theorem can be proven in a heuristic way. If the LDP holds for the random variable A_n, then

$$P(A_n\ \in\ da)\ \approx\ e^{-n\,I(a)}\ da \tag{2.16}$$

Putting this approximation to the expression $\langle e^{n\,k\,A_n}\rangle$ we get

$$
\begin{aligned}
\langle e^{n\,k\,A_n}\rangle &= \int_{\mathbf{R}} e^{n\,k\,a}\, P(A_n \in da) \\
&\approx \int_{\mathbf{R}} e^{n\,(k\,a-I(a))}\, da
\end{aligned}
\tag{2.17}
$$

The integration can be approximated for $n \longrightarrow \infty$ using the saddle-point approximation or Laplace's approximation [224] which is by locating the maximum of the expression $(k\,a - I(a))$. Therefore assuming that the maxima exists and unique, the approximated equation now becomes

$$
\langle e^{n\,k\,A_n}\rangle \approx \exp\left(-n \sup_{a\,\in\,\mathbf{R}} \{k\,a - I(a)\}\right) da
\tag{2.18}
$$

So the SCGF is now can be written as

$$
\lambda(k) = \lim_{n\longrightarrow\infty} \frac{1}{n} \ln \langle e^{nkA_n}\rangle = \sup_{a\,\in\,\mathbf{R}} \{k\,a - I(a)\}
\tag{2.19}
$$

Now to obtain the rate function $I(a)$ from $\lambda(k)$, the Legendre-Fenchel transformation can be inverted as the $\lambda(k)$ is differentiable [222]. Legendre-Fenchel transformation can be self-dual if the rate function $I(a)$ is convex and everywhere differentiable, as shown in Fig. 2.2. In this case the slope of the $I(a)$ at a becomes the point at which the $\lambda(k)$ has slope a. As the expression $(k\,a - I(a))$ has a unique maxima, the transformation now can be self-inverted to

$$
I(a) = \sup_{k\,\in\,\mathbf{R}} \{k\,a - \lambda(k)\}
\tag{2.20}
$$

This points out that the Gärtner-Ellis theorem is actually the consequence of the combination of the LDP and the Laplace's approximation.

We now illustrate the theorem by calculating the rate function using the Gärtner-Ellis theorem for the Gaussian sample mean.

Gaussian sample mean

We consider a sequence of i.i.d random variables $\{X_1, X_2, ...X_n\}$, drawn from the following Gaussian probability distribution

$$P(X_i = x) = \frac{1}{\sqrt{2\pi\sigma^2}} e^{\frac{-(x-\mu)^2}{2\sigma^2}} \tag{2.21}$$

To calculate the rate function for the Gaussian sample mean $S_n = \sum_i \frac{X_i}{n}$ using the Gärtner-Ellis theorem, we first calculate the SCGF as

$$\begin{aligned} \lambda(k) &= \lim_{n\to\infty} \frac{1}{n} \ln\langle e^{k\sum_i X_i}\rangle = \lim_{n\to\infty} \frac{1}{n} \ln\prod_{i=1}^{n}\langle e^{kX_i}\rangle \\ &= \ln\langle e^{kX}\rangle \end{aligned} \tag{2.22}$$

where X is any summands of X_i and $k \in \mathbf{R}$. Using the distribution Eq. 2.21, we get the expression of SCGF as

$$\begin{aligned} \lambda(k) &= \ln\left[\frac{1}{\sqrt{2\pi\sigma^2}} \int_{\mathbf{R}} e^{kX} e^{\frac{-(x-\mu)^2}{2\sigma^2}} \, dx\right] \\ &= \mu k + \frac{1}{2}\sigma^2 k^2 \end{aligned} \tag{2.23}$$

So the $\lambda(k)$ is differentiable everywhere and according to Gärtner-Ellis theorem the rate function $I(x)$ can now be calculated as :

$$I(x) = \sup_k\{kx - \lambda(k)\} \tag{2.24}$$

Minimizing the bracketed quantity, we get the fixed point as $k = \frac{x-\mu}{\sigma}$ and hence the rate function becomes
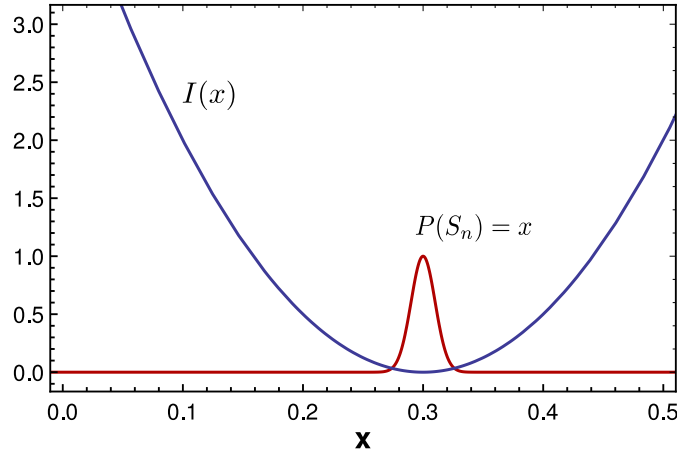
Figure 2.3: Application of the LDT for a Gaussian sample mean. Plot shows the rate function $I(x)$ and probability distribution $P(S_n = x)$ of the sample mean S_n. The $I(x)$ has a minima at the most probable value which is the mean of the Gaussian distribution $x = \mu$.

$$I(x) = \frac{(x - \mu)^2}{2\sigma^2} \tag{2.25}$$

This recovers exactly the rate function calculated for the Gaussian sample mean using Stirling's approximation given by Eq. 2.14 in Subsec. 2.1.2. The rate function of the Gaussian sample mean and the corresponding probability distribution is shown in Fig. 2.3.

2.3 Some properties of the SCGF and the rate function

In this section we will show some of the properties of the SCGF and the rate function which are obtained via the Gärtner-Ellis theorem.

2.3.1 Properties of the SCGF $\lambda(k)$ at $k = 0$

One of the important hypothesis of the Gärtner-Ellis theorem is the differentiability of the SCGF $\lambda(k)$. Since

$$\lambda(k) = \lim_{n \longrightarrow \infty} \frac{1}{n} \ln \langle e^{nkA_n} \rangle \tag{2.26}$$

at $k = 0$, clearly $\lambda(0) = 0$. The first and second derivative of the SCGF at $k = 0$ can be written as

$$\lambda'(0) = \lim_{n \longrightarrow \infty} \frac{\langle A_n \; e^{nkA_n} \rangle}{\langle e^{nkA_n} \rangle} \bigg|_{k=0} = \lim_{n \longrightarrow \infty} \langle A_n \rangle$$

$$\lambda''(0) = \lim_{n \longrightarrow \infty} n \; \frac{\langle A_n^2 \; e^{nkA_n} \rangle - \langle A_n \; e^{nkA_n} \rangle^2}{\langle e^{nkA_n} \rangle^2} \bigg|_{k=0} = \lim_{n \longrightarrow \infty} n \; (\langle A_n^2 \rangle - \langle A_n \rangle^2)$$

$$(2.27)$$

which gives the mean and the variance of the random variable A_n respectively at $k = 0$.

2.3.2 Convexity of $\lambda(k)$

In order to prove the convexity of the SCGF, we consider the following expression with $\alpha \in [0, 1]$

$$
\begin{aligned}
\alpha\lambda(k_1) + (1 - \alpha)\lambda(k_2) &= \lim_{n \longrightarrow \infty} \frac{1}{n} \left(\alpha \; \ln\langle e^{n \, k_1 \, A_n} \rangle + (1 - \alpha) \; \ln\langle e^{n \, k_2 \, A_n} \rangle \right) \\
&= \lim_{n \longrightarrow \infty} \frac{1}{n} \left(\ln\langle e^{n \, k_1 \, A_n} \rangle^\alpha + \ln\langle e^{n \, k_2 \, A_n} \rangle^{(1-\alpha)} \right) \quad (2.28)
\end{aligned}
$$

Now according to the Hölder's inequality

$$\sum_i |y_i z_i| \leq \left(\sum_i |y_i|^{1/p} \right)^p \left(\sum_i |z_i|^{1/q} \right)^q \tag{2.29}$$

with $0 \leq p, \; q \leq 1$ and $p + q = 1$. Applying this inequality in the $\lambda(k)$ it yields

$$\alpha\lambda(k_1) + (1 - \alpha)\lambda(k_2) \geq \lambda(\alpha k_1 + (1 - \alpha)k_2) \tag{2.30}$$

So the SCGF is a convex function which means it is continuous and differentiable everywhere.

2.3.3 Positivity of the rate function

As $\lambda(0) = 0$, and λ can be expressed by the Legendre-Fenchel transformation of the $I(a)$ shown in Eq. 2.19. Hence,

$$\lambda(0) = \sup_{a \in \mathbf{R}} \{-I(a)\} = -\inf_{a \in \mathbf{R}} I(a) = 0 \tag{2.31}$$

So the minima of the rate function is zero and for other x, $I(x) \geq 0$.

2.3.4 Convexity of the rate function

The $I(x)$ obtained from the Gärtner-Ellis theorem are necessarily strictly convex [223, 222]. Because of the Gärtner-Ellis theorem can not always yield a rate function (which are non-convex in nature and in particular having two or more local or global minima) even though $\lambda(k)$ exists.

To prove it we consider $\lambda(k)$ is differentiable and strictly convex which means $\lambda''(k) > 0$. And the Legendre-Fenchel becomes self inverted where the slopes satisfy $I'(a) = k(a)$ and $\lambda'(k(a)) = a$. These two equations then implies

$$I''(a) = k'(a) = \frac{1}{\lambda''(k)} \tag{2.32}$$

Hence the rate function $I(a)$ is also convex with $I''(a) > 0$.

Since Legendre-Fenchel transformation obtain functions which are only convex, the Gärtner-Ellis theorem has the limitation that it cannot calculate non-convex rate functions. In the next section, we will introduce a theorem using which nonconvex rate functions can also be calculated.

2.4 Tilted LDP

The tilted LDP allows one to calculate a new LDP for a new sequence by "tilting" or integrating against an exponential function w.r.t. an old LDP generated by another sequence of probability [225, 220]. The theorem is as follows :

Let P_n is the probability measure on a completely separable metric space X which satisfies LDP with rate n and rate function $I : X \longrightarrow \mathbf{R}$. Let $G : X \longrightarrow \mathbf{R}$ is a continuous function which is bounded above. Then according to Varadhan's lemma [220] the asymptotic behaviour of sequences of integrals holds the following limit

$$\lim_{n \longrightarrow \infty} \frac{1}{n} \ln \int_X e^{n\,G(x)}\, P_n(dx) = \sup_{x \in X}[G(x) - I(x)] \qquad (2.33)$$

We now define $J_n(A) \equiv \int_X e^{n\,G(x)}\, P_n(dx)$, as a sequence of probability measure $P_n^G(A) = \frac{J_n(A)}{J_n(X)}$ for a Borel subset A of X, then according to tilted LDP the probability measure P_n^G on X satisfies LDP with rate n and rate function

$$I^G(x) = I(x) - G(x) - \inf_{y \in X}[I(y) - G(y)] \qquad (2.34)$$

2.5 Calculation of the rate function for the random field spin model using tilted LDP

For random field spin models, along with the spin variables s_i, there are other i.i.d. variables corresponding to the random field disorder. Hence, the magnetization $\frac{\sum_i s_i}{N}$ is not anymore a i.i.d. variable w.r.t the probability distribution of a spin configuration. Thus using directly the Gärtner-Ellis theorem is quite complicated. Also the desired rate function of the disordered models in general are not convex in nature [142] (as will be seen in the later sections), so the Gärtner-Ellis theorem cannot be used to calculate them.

In order to calculate the rate function of a random field spin model Löwe *et al* developed a following method to calculate the rate function of the random field Curie-Weiss model in two steps [142] :

- Prove the LDP w.r.t the probability measure of the non-interacting part of the disordered Hamiltonian.

- Using tilted LDP the rate function of the full Hamiltonian is calculated from the rate function of the non-interacting part of the Hamiltonian.

We will illustrate the tilted LDP in the next subsection by calculating the rate function of the random field Ising model.

2.5.1 Rate function for the random field Ising model

We consider the following random-field Hamiltonian on a fully connected graph

$$\mathcal{H} = -\frac{1}{2N}(\sum_i s_i)^2 - \sum_i (h_i + H)s_i \tag{2.35}$$

where $s_i \in \{-1, 1\}$, h_i is the random field and H is the uniform external magnetic field. The probability of the spin configuration $C_N = (s_1, s_2, ..., s_N)$ for the full Hamiltonian is given by

$$P_{N,\beta} \propto e^{-\beta\,\mathcal{H}(C_N)} \tag{2.36}$$

The non-interacting part of the Hamiltonian is $\mathcal{H}_{ni} = -\sum_i (h_i + H)s_i$. And the probability measure on $\{-1, 1\}^N$ is given by the product measure $Q(\{s_i\}) = \otimes_{i=1}^N Q_i$ for each $i \in N$ with:

$$Q_i(1) = \frac{e^{\beta(H+h_i)}}{2\cosh\beta(H+h_i)} \tag{2.37}$$

$$Q_i(-1) = \frac{e^{-\beta(H+h_i)}}{2\cosh\beta(H+h_i)} \tag{2.38}$$

We first calculate the rate function w.r.t the probability measure $Q(\{s_i\})$ for the sum of the spins $x = \frac{\sum_i s_i}{N}$ (which is the order parameter of the system)

$$Q_{\mathcal{H}_{ni}}(C_N : x = \frac{\sum\limits_i s_i}{N}) \approx e^{-N\ R(x)} \tag{2.39}$$

According to the Gärtner-Ellis theorem the rate function for the non-interacting Hamiltonian part $R(x)$ is calculated using the Lengendre-Fenchel transformation of the SCGF $\lambda(y)$ with $y \in \mathbf{R}$:

$$R(x) = \begin{cases} \sup\limits_{y\in\mathbf{R}}\{xy - \lambda(y)\} & \text{if } 0 \le |x| \le 1 \\ \infty & \text{otherwise} \end{cases}$$

where the SCGF is

$$
\begin{aligned}
\lambda(y) &= \lim_{N\longrightarrow\infty} \frac{1}{N}\ln\langle e^{Nyx}\rangle \\
&= \lim_{N\longrightarrow\infty} \frac{1}{N}\sum_{i=1}^{N}\ln\left(\frac{e^{y+\beta h_i+\beta H} + e^{-y-\beta h_i-\beta H}}{2\cosh\beta(H+h_i)}\right) \\
&= \lim_{N\longrightarrow\infty} \frac{1}{N}\left(\lambda_N(y) - \lambda_N(y)\right)
\end{aligned}
\tag{2.40}
$$

here

$$\lambda_N(y) = \sum_{i=1}^{N}\ln\left(\cosh\left(y + \beta h_i + \beta H\right)\right) \tag{2.41}$$

the limit $\lim\limits_{N\longrightarrow\infty}\frac{1}{N}\lambda_N(y)$ can be approximated using the LLN to it's expectation value w.r.t the random field distribution. For a bimodal distribution of the random field h_i

$$p(h_i) = \frac{1}{2}(\delta(h_i - h) + \delta(h_i + h)) \tag{2.42}$$
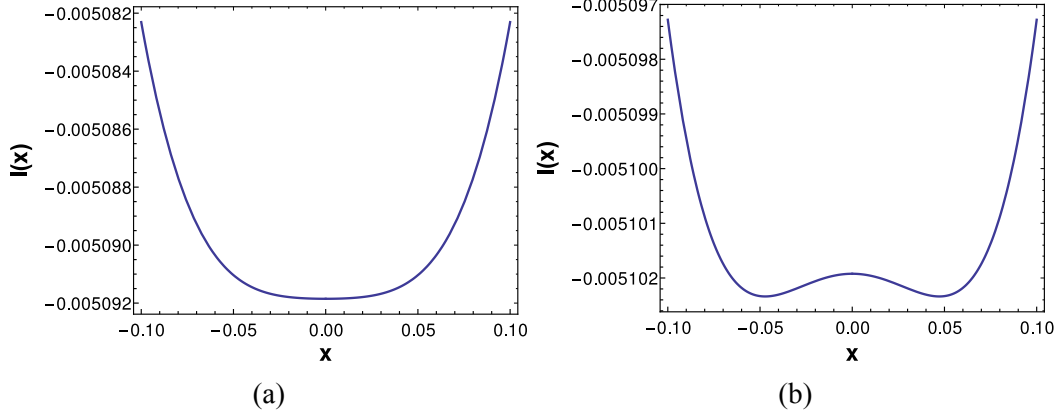
Figure 2.4: The plot of the rate function $I(x)$ for the RFIM in presence of bimodal distributed random field disorder. The plots are for different values of β with fixed $h = 0.1$ and $H = 0$. **(a)** is for $\beta = 1.01$ and, **(b)** is the plot for $\beta = 1.011$.

the SCGF turns out to be

$$
\begin{aligned}
\lambda(y) &= \frac{1}{2}\Big(\ln\left(\cosh\left(x + \beta H + \beta h\right)\right) + \ln\left(\cosh\left(x + \beta H - \beta h\right)\right)\Big) \\
&\quad - \frac{1}{2}\Big(\ln\left(\cosh\left(\beta H + \beta h\right)\right) - \ln\left(\cosh\left(\beta H - \beta h\right)\right)\Big) \\
&= \frac{1}{2}\Big(\ln\cosh 2(y + \beta H) + \ln\cosh 2\beta h\Big)
\end{aligned}
\tag{2.43}
$$

Now in order to calculate $R(x)$, we estimate the supremum of the expression $xy - \lambda(y)$ w.r.t y, which gives

$$
y^* = \frac{1}{2}\sinh^{-1}\left\{\frac{x}{1 - x^2}\left(\cosh 2\beta h + \sqrt{1 + x^2\sinh^2 2\beta h}\right)\right\} - \beta H
\tag{2.44}
$$

and the expression of $R(x)$ at the supresum is given by

$$
R(x) = x\,y^* - \lambda(y^*)
\tag{2.45}
$$

The probability for the full Hamiltonian given by Eq. 2.36 that $x = \dfrac{\sum\limits_i s_i}{N}$ for a given β, h and H can be written in terms of $Q(\{s_i\})$

58

$$P_{N,\beta}(x) = \frac{e^{\beta N x^2 / 2} \ Q(\{s_i\} : x = \frac{\sum_i s_i}{N})}{\sum\limits_{i=-1}^{1} e^{\beta N x^2 / 2} \ Q(\{s_i\} : x = \frac{\sum_i s_i}{N})}$$

We thus note that the probability measure $P_{N,\beta}$ is the tilted version of Q and the continuous and upper bounded function $G(x) : \mathbf{R} \longrightarrow \mathbf{R}$ is now given by

$$G(x) = \begin{cases} \frac{\beta}{2}x^2 & \text{if } 0 \leq |x| \leq 1 \\ \frac{\beta}{2} & \text{otherwise} \end{cases}$$

Now x satisfies LDP w.r.t the measure $P_{N,\beta}$ with rate N and rate function I according to *tilted LDP* as:

$$
\begin{aligned}
I(x) &= R(x) - G(x) - \inf_{y \in \mathbf{R}} \left\{ R(y) - G(y) \right\} \\
&= R(x) - \frac{\beta}{2}x^2 - \inf_{y \in \mathbf{R}} \left\{ R(y) - \frac{\beta}{2}y^2 \right\}
\end{aligned}
\tag{2.46}
$$

Putting the expression of the R(x) from Eq. 2.45, we get the expression for the rate function $I(x)$ as

$$
\begin{aligned}
I(x) &= \ln 2 - \frac{\beta}{2}x^2 - \beta x H + \frac{x}{2}\sinh^{-1}\left\{ \frac{x}{1-x^2}\left(\cosh 2\beta h + \sqrt{1 + x^2 \sinh^2 2\beta h}\right)\right\} \\
&+ \frac{1}{2}\ln\left(\frac{1-x^2}{2}\right) - \frac{1}{2}\ln\left(\cosh 2\beta h + \sqrt{1 + x^2 \sinh^2 2\beta h}\right) - \inf_{y \in \mathbf{R}}\left\{ R(y) - \frac{\beta}{2}y^2 \right\}
\end{aligned}
\tag{2.47}
$$

The plot of the rate function $I(x)$ is shown in Fig. 2.4 for different values of β with $H = 0$ and $h = 0.1$. The minima of the $I(x)$ (where $I'(x) = 0$) gives the value of the stable magnetization x. Below a $\beta_c = 1.01$ the $I(x)$ has one minima shown in Fig. 2.4a which is the paramagnetic phase. Above β_c there are two minimas in the rate function shown in Fig. 2.4b, which is like the ferromagnetic phase.

For Blume-Capel model Hamiltonian given by Eq. 1.22, there are two order parameters $x_1 = \frac{\sum_i s_i}{N}$ and $x_2 = \frac{\sum_i s_i^2}{N}$ and the state space becomes $\{-1, 0, 1\}^N$. For the random field or random crystal field disorder the variables H and Δ becomes site dependent respectively : $H = (H_i)_{i \in N}$ and $\Delta = (\Delta_i)_{i \in N}$. The sequence of probability measures on $\{-1, 0, 1\}^N$ can be written for each $i \in N$ as

$$Q_i(1) = \frac{e^{\beta(H_i - \Delta_i)}}{1 + 2e^{-\beta\Delta_i} \cosh \beta H_i} \tag{2.48}$$

$$Q_i(-1) = \frac{e^{-\beta(H_i + \Delta_i)}}{1 + 2e^{-\beta\Delta_i} \cosh \beta H_i} \tag{2.49}$$

$$Qi(0) = \frac{1}{1 + 2e^{-\beta\Delta_i} \cosh \beta H_i} \tag{2.50}$$

the rate functions $R(x_1, x_2)$ and $I(x_1, x_2)$ are calculated in similar way [194].

This method has been used to solve the random field Curie-Weiss model [142] and the random field $p-$spin Ising model [143]. It has been shown [143] that the full rate function $I(\{x_i\})$ is like the generalized free energy functional, the minima of which gives the free energy of the system. This method relies on the fact that the disorder average can be done on the non-interacting part of the Hamiltonian as the disorder couples with the order parameter, which makes it easier to do the disorder averaging and thus this method can be extended to any other spin models where the disorder couples with the non-interacting part of the Hamiltonian.

In the next chapters we will apply the *tilted LDP* in order to calculate the free energy functional of the disordered spin-1 Blume-Capel model.

Chapter 3

Blume-Capel model with random crystal field disorder

In this chapter we introduce the disorder in the crystal field interaction of the Blume-Capel model mentioned in the previous chapter. We consider a double peak delta function distribution. We calculate the free energy functional using the tilted LDP, mentioned in Chapter 2. We discuss the ground state phase diagram of the system. Next we study the finite temperature phase diagram depending on the strength of disorder in the three dimensional space. We also discuss about the multicritical points that emerge due to the presence of disorder.

3.1 Random crystal field Blume-Capel model (RCFBC)

Random crystal field effect on the Blume-Capel model is not only theoretically interesting, but also has experimental realizations. There are systems like aerogels i.e ^{3} He - ^{4}He mixtures in random porous media [226, 190] which can be modelled using the RCFBC model. The phase diagram of the model is known to change under the effect of disorder. In particular, random crystal field Blume-Capel model (RCFBC) has been studied extensively for different bimodal distributions using mean-field method [183, 184, 185, 186], effective field theory [187, 188, 189], cluster variation method [190], renormalization group study [191], pair approximation method [192], Bethe lattice [193] and large deviations [194]. Also for Gaussian distribution [195] and double Gaussian distribution [196]. All these work have focused on the (T, Δ) plane. These different methods do not agree with each fully in the prediction of the phase-diagram, most of them report that the first order line and

hence the TCP disappears for higher strengths of disorder. Some of them predicted different topologies of the phase-diagram depending on the strength and the type of disorder, with multicritical points like critical end points, ordered critical point and double critical point [183, 185, 187, 184, 196].

Since TCP is a point of confluence of three critical lines, it is important to look at the effect of disorder on the other two lines meeting at the TCP. Hence, we revisit the problem and obtain the phase diagram in the space of three fields, on a fully connected graph by solving the model exactly, using large deviation theory [215]. We study the Blume-Capel model with random crystal field disorder in the presence of external field on a fully connected graph. The Hamiltonian can be written for N spins as :

$$H(C_N) = -\frac{1}{2N}(\sum_i s_i)^2 - \sum_i \Delta_i s_i^2 - H \sum_i s_i \qquad (3.1)$$

where Δ_i represent quenched random crystal field at each site, H is the external field and s_i are spin-1 random variables which can take $\pm 1, 0$ values. We draw random crystal fields from bimodal distribution of the kind:

$$P(\Delta_i) = p\delta(\Delta_i - \Delta) + (1 - p)\delta(\Delta_i + \Delta) \qquad (3.2)$$

Since $p = 0$ or 1 will imply no disorder and $p = 1/2$ would be the most random case, it is enough to look for $0 \leq p \leq 0.5$. We now solve the Hamiltonian Eq. 3.1 of the system using the tilted LDP discussed in Chapter 2.

In the next section, we will show the detailed calculation of the rate function of the RCFBC model.
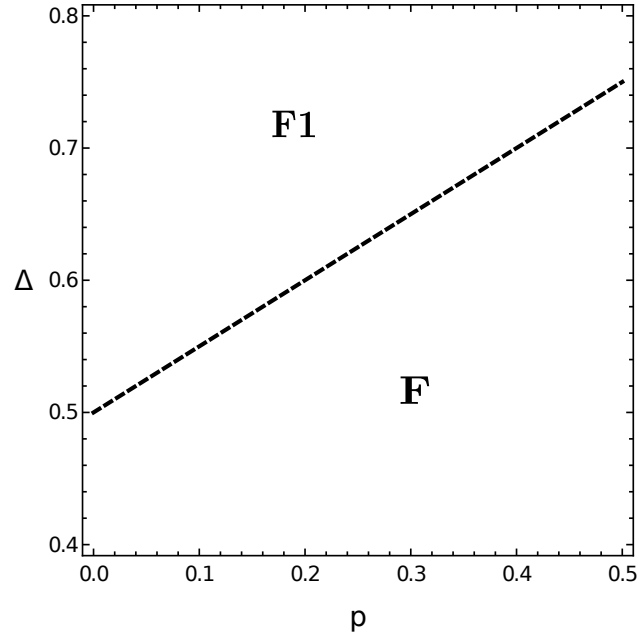
Figure 3.1: Ground state phase diagram of the RCFBC model in presence of the bimodal distribution in the $\Delta - p$ plane. Two ordered phases exists for all $0 < p < 1$. Those are denoted by **F** with $m = q = 1$ and **F1** with $m = q = p$. The **F- F1** phases are separated by the first order line denoted as black dashed line.

3.2 Calculation of the rate function

The rate function $I(x_1, x_2)$ for bimodal random crystal field disorder in the absence of external field was calculated using tilted LDP [194], discussed in Chapter 2. In this section we will show the detailed calculation of the $I(x_1, x_2)$ in presence of external magnetic field. We start with the probability of a spin configuration C_N with magnetization $x_1 = \frac{\sum_i s_i}{N}$ and quadruple moment $x_2 = \frac{\sum_i s_i^2}{N}$, which is proportional to $e^{-\beta\mathcal{H}}$, where $\mathcal{H}$ is the Hamiltonian given in Eq. 3.1. This via large deviation principle (LDP) can be shown that [218, 215, 194] in the limit of $N \to \infty$ goes to

$$P(C_N : \sum_i s_i = x_1 N; \sum_i s_i^2 = x_2 N) \sim \exp(-NI(x_1, x_2)) \tag{3.3}$$

the function $I(x_1, x_2)$ here is the rate function which is like the generalized free energy functional. To calculate $I(x_1, x_2)$ we use two steps, as discussed in Chapter 2 :

1. We first start with the non-interacting part of the Hamiltonian. We calculate the rate function $R(x_1, x_2)$ corresponding to the probability $P_{\mathcal{H}_{ni}}(C_N) \sim e^{-NR(x_1, x_2)}$. Here $\mathcal{H}_{ni}$ is the non-interacting part of the Hamiltonian i.e $\mathcal{H}_{ni} = -\sum_i \Delta_i s_i^2 - H \sum_i s_i$. The function $R(x_1, x_2)$ is calculated using the Gärtner-Ellis (GE) theorem [215]. The expression of $R(x_1, x_2)$ is

$$R(x_1, x_2) = \sup_{k_1, k_2} \left[x_1 k_1 + x_2 k_2 - \lambda(k_1, k_2) \right]$$

(3.4)

Where the SCGF $\lambda(k_1, k_2)$ for the random variables x_1 and x_2 is given by

$$\begin{aligned}
\lambda(k_1, k_2) &= (1-p) \log\left(1 + 2e^{k_2 - \beta\Delta} \cosh(k_1 + \beta H)\right) \\
&+ p \log\left(1 + 2e^{k_2 + \beta\Delta} \cosh(k_1 + \beta H)\right)
\end{aligned}$$

(3.5)

Minimization of the expression $x_1 k_1 + x_2 k_2 - \lambda(k_1, k_2)$ in w.r.t k_1 and k_2 gives the following equations for the supremum (k_1^*, k_2^*) as a function of x_1 and x_2

$$x_1 = 2e^{k_2^*} \sinh(k_1^* + \beta H) \left(\frac{pe^{\beta\Delta}}{1 + 2e^{k_2^* + \beta\Delta} \cosh(\beta H + k_1^*)} + \frac{(1-p)e^{-\beta\Delta}}{1 + 2e^{k_2^* + \beta\Delta} \cosh(\beta H + k_1^*)} \right)$$

(3.6)

$$x_2 = 2e^{k_2^*} \cosh(k_1^* + \beta H) \left(\frac{pe^{\beta\Delta}}{1 + 2e^{k_2^* + \beta\Delta} \cosh(\beta H + k_1^*)} + \frac{(1-p)e^{-\beta\Delta}}{1 + 2e^{k_2^* + \beta\Delta} \cosh(\beta H + k_1^*)} \right)$$

(3.7)

2. We then calculate the full rate function of the interacting Hamiltonian via tilted LDP. Using this principle we calculate the rate function $I(x_1, x_2)$ from the old rate function $(R(x_1, x_2))$ using a change in measure by integrating against an exponential of a continuous function $G(x_1, x_2)$ which in our case is the interacting part of the Hamiltonian, $G = \frac{\beta x_1^2}{2}$. The full rate function $I(x_1, x_2)$ is given by

$$I(x_1, x_2) = R(x_1, x_2) - \frac{\beta x_1^2}{2} - \inf_{y_1, y_2} \left(R(y_1, y_2) - \frac{\beta y_1^2}{2} \right) \tag{3.8}$$

After substituting $R(x_1, x_2)$ and using a new variable $z = 2e^{k_2^*} \cosh(k_1^*)$ as was done in [194], we get the rate function of the system to be

$$
\begin{aligned}
I(x_1, x_2) &= x_1 \tanh^{-1}\left(\frac{x_1}{x_2}\right) + x_2 \left[\ln \frac{z}{2\cosh\left(\tanh^{-1}\frac{x_1}{x_2}\right)} \right] - \frac{\beta x_1^2}{2} - \beta H x_1 \\
&\quad - p\ln\left(1 + ze^{\beta \triangle}\right) - (1-p)\ln\left(1 + ze^{-\beta \triangle}\right) + p\ln\left(1 + 2e^{\beta \triangle}\right) \\
&\quad + (1-p)\ln\left(1 + 2e^{-\beta \triangle}\right)
\end{aligned}
$$

$$\tag{3.9}$$

where z is the solution of the equation:

$$\frac{x_2}{z} = \frac{pe^{\beta \Delta}}{1 + ze^{\beta \Delta}} + \frac{(1-p)e^{-\beta \Delta}}{1 + ze^{-\beta \Delta}} \tag{3.10}$$

In the limit, $N \to \infty$, for a given β, Δ and H, the value of x_1 and x_2 that minimise $I(x_1, x_2)$ will give the value of magnetisation (m) and density(q). The minima of the rate function in (x_1, x_2) plane gives the free energy for a given $\beta(= 1/T), \Delta$ and H. Hence the values of x_1 and x_2 which minimise $I(x_1, x_2)$ are the value of m and q respectively for a given set of thermodynamic variables. Minimising $I(x_1, x_2)$ with respect to x_1 and x_2 results in the following equations for m and q:

$$\tanh(\beta(m + H)) = \frac{m}{q} \tag{3.11}$$

$$z = \frac{2}{\sqrt{1 - m^2/q^2}} \tag{3.12}$$

where z is related to q via the Eq. 3.10, i.e:

$$\frac{q}{z} = \frac{pe^{\beta\Delta}}{1 + ze^{\beta\Delta}} + \frac{(1-p)e^{-\beta\Delta}}{1 + ze^{-\beta\Delta}} \tag{3.13}$$

On substituting the above relations we get the free energy functional to be

$$\tilde{f}(m) = \frac{\beta m^2}{2} \quad -(1-p)\log\big(1 + 2e^{-\beta\Delta}\cosh\beta(m+H)\big)$$

$$-p\log\big(1 + 2e^{\beta\Delta}\cosh\beta(m+H)\big) \tag{3.14}$$

In the next part we solve the ground state phase diagram of the RCFBC model.

3.3 Ground state phase diagram

For the ground state phase diagram, we take the limit $\beta \longrightarrow \infty$ in the free energy functional given by Eq. 3.14. We get the ground state rate function as $\phi(m) = \lim\limits_{\beta\to\infty} \frac{1}{\beta}\tilde{f}(m)$

$$\phi(m) = \frac{m^2}{2} - p\,(\Delta + m) - (1-p)\,\Theta(|m - \Delta|) \tag{3.15}$$

where the $\Theta(x)$ is the Heaviside theta function with $\Theta(x) = 1$ for $x > 0$, $\Theta(x) = 0$ otherwise.

The minima of $\phi(m)$ w.r.t the m gives the ground state energy E of the system. We found that there are two ordered phases for any $0 < p < 1$. The first one is the **F** phase with $m = q = 1$ and ground state energy $E = -\frac{1}{2}$ - $(1 + 2p)\,\Delta$. This phase is stable for $\Delta < \frac{1}{2}\,(p + 1)$. And the other phase is **F1** with $m = q = p$ and energy $E = -\frac{p^2}{2}$ - $p\,\Delta$. The **F1** phase appears due to the presence of the disorder and it is stable for $\Delta > \frac{1}{2}\,(p+1)$. For $\Delta > \frac{1}{2}\,(p + 1)$ the $s = \pm 1$ spins compete with the $s = 0$ spins and thus p fraction of $s = \pm 1$ spins contribute in the magnetization and we get the **F1** phase. The ground state

phase diagram in the $\Delta - p$ plane is shown in Fig. 3.1. The two phases are separated by the first order line $\Delta = \frac{1}{2}(p - 1)$, shown by the dashed line. Due to the symmetry of the distribution, we plot the phase diagram only for $0 < p \leq \frac{1}{2}$.

In the next section, we will show the finite temperature phase diagram of the RCFBC model.

3.4 Finite temperature phase diagram

In subsection 3.4.1 we will recap the results in the absence of external field which was shown in [194] and then build the equations for phase diagram in (T, Δ, H) space in subsection 3.4.2

3.4.1 Two field phase diagram in the (T, Δ) plane

For $H = 0$, the phase diagram has been studied earlier [194, 185]. We will briefly recap those results here: Assuming m to be small the fixed point equations, Eq. 3.11 and 3.12 can be linearized around $m = 0$. This gives $q = 1/\beta$ and $z = 2$ at the critical point. Substituting these values in Eq. 3.13, gives the equation for a line of continuous transition in the $H = 0$ plane. The line of continuous transition in $H = 0$ plane is known as the λ-line and satisfies the following equation

$$5 - 4\beta = 2(\beta p - 1)e^{\beta \Delta} + 2(\beta - \beta p - 1)e^{-\beta \Delta} \tag{3.16}$$

This is valid only when the higher order terms in the expansion can be ignored. Taking $q = (1 + \epsilon)/\beta$ and expanding in powers of ϵ we find that the coefficient of linear term in ϵ becomes zero when

$$12\beta - 17 + (3\beta - 10)\cosh(\beta \Delta) - 3\beta(1 - 2p)\sinh(\beta \Delta) = 0 \tag{3.17}$$
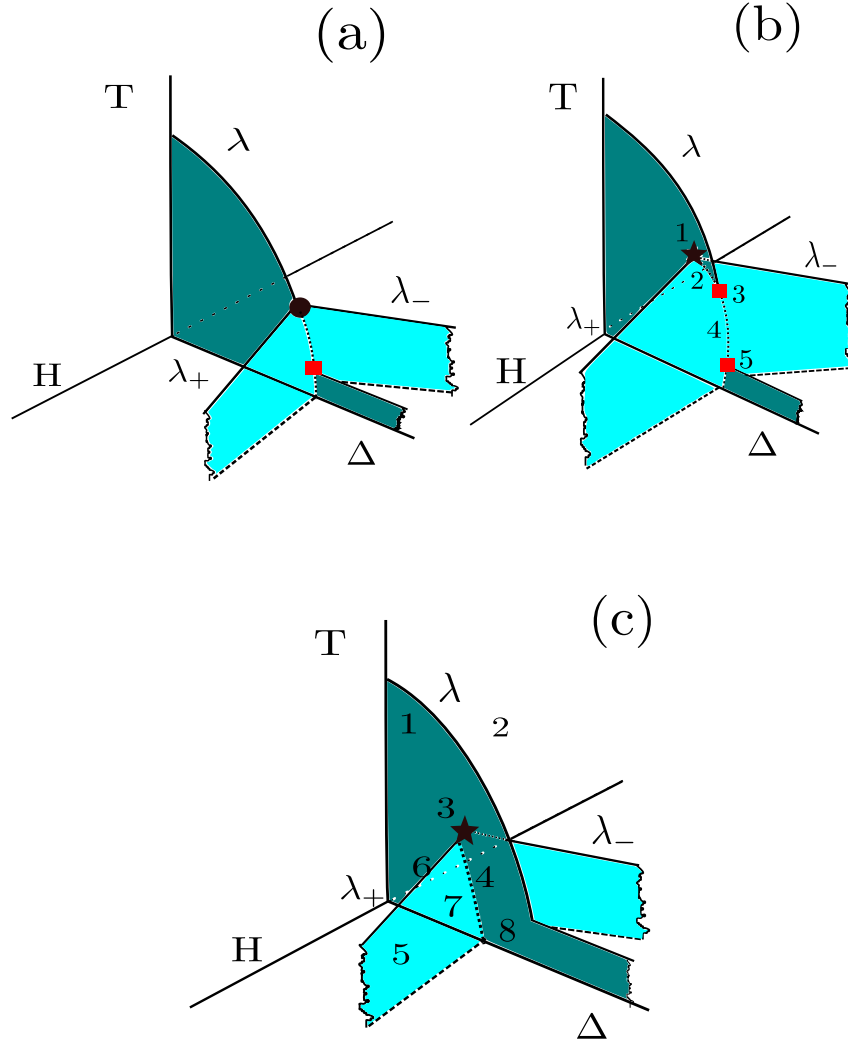
Figure 3.2: Schematic phase diagram for different strengths of disorder. The value of p represents the strength of disorder(there is no disorder for $p = 0$ and the disorder is maximum for p=0.5). Solid lines represent lines of critical points and dotted lines represent first order transition lines. Solid dot represents TCP, solid square represents CEP and star represents BEP. Wiggled lines are to show the infinite length of wings. λ represents the line of critical points in $H = 0$ plane and λ_+ and λ_- represent the critical lines for $H > 0$ and $H < 0$ respectively. The value of $p_1 = 0.022$ and $p_2 = 0.107875$ for the model studied in this paper

Solving Eq. 3.16 and 3.17 together we get the condition for break down of linear approximation as

$$\cosh(\beta\Delta) = \frac{12\beta - 19}{8} \qquad (3.18)$$

Hence for a given Δ, there will be either no transition or a first order transition, beyond the value of β that satisfy Eq. 3.18.

The value of (β, Δ)(or equivalently (T, Δ)) which satisfy Eqs. 3.16 and Eq. 3.18 simultaneously gives the location of TCP for a given p. It was found in [194] that beyond $p_c = 0.0454$ the two equations cannot be satisfied simultaneously and hence there is no TCP, and the λ line in the (T, Δ) plane extends to $\Delta \to \infty$. This treatment is equivalent to Taylor expanding the rate function to get an equivalent Landau free energy functional, which we will discuss in Sec. 3.6.

3.4.2   Three field phase diagram in (T, Δ, H) space

Let us now take $H \neq 0$ and look for the critical points in the full (T, Δ, H) space. We know that at the TCP there are two other continuous lines with $H \neq 0$ which meet the λ line. We call these, depending on the value of H, as λ_+ and λ_-.

We wish to understand the effect of disorder on the two critical lines λ_+ and λ_-. We will focus on the effect of disorder on these two critical lines in this paper. Along these lines, $m \neq 0$ and one cannot look for continuous transition by expanding the free energy functional like we did in the section 3.4.1.

Note that at the fixed point the value of m and q are related via Eq. 3.11. At the fixed point, the free energy functional is given by the Eq. 3.14 and the self-consistent equation for m comes out to be :

$$m = 2\sinh\beta(m + H)\left[\frac{pe^{\beta\Delta}}{1 + 2e^{\beta\Delta}\cosh\beta(m + H)} + \frac{(1 - p)e^{-\beta\Delta}}{1 + 2e^{-\beta\Delta}\cosh\beta(m + H)}\right] \quad (3.19)$$

Since $m \neq 0$ along the λ_+ and λ_- lines, expanding $\tilde{f}(m)$ in powers of m to get a Landau

free energy functional will not give the correct critical behaviour. But, in general along a critical line, the first three derivatives of the free energy functional with respect to the order parameter should be zero. This is because between two successive minimas, there must exist two points of inflexion, i.e $f'' = 0$ and hence also a point where $f''' = 0$. Hence at the continuous transition, all three derivatives should vanish simultaneously. Hence to study λ_+ and λ_- critical lines we equate the first three derivatives of $\tilde{f}(m)$ w.r.t m to zero [162] (and fourth derivative should be greater than zero). This is true also for the λ line, as for $H = 0$ and $m = 0$ the third derivative is trivially zero and second derivative gives the same condition as Eq. 3.16.

In general, equating second and third derivative of $\tilde{f}(m)$ to zero we get the following two conditions respectively:

$$\frac{p(2x^2 + xy)}{(1 + 2xy)^2} + \frac{(1 - p)(2 + xy)}{(x + 2y)^2} = \frac{1}{2\beta} \tag{3.20}$$

$$\frac{p(x - 8x^3 - 2x^2y)}{(1 + 2xy)^3} + \frac{(1 - p)(x^2 - 8 - 2xy)}{(x + 2y)^3} = 0 \tag{3.21}$$

here $x = \exp(\beta\Delta)$ and $y = \cosh\beta(m + H)$. For $p \neq 0$, the two equations are quartic and hexic in x.

For $p = 0$ (pure Blume-Capel model), the equations reduce to the following simpler equations :

$$\frac{2 + xy}{[x + 2y]^2} = \frac{1}{2\beta} \tag{3.22}$$

$$\frac{x^2 - 8 - 2xy}{[x + 2y]^3} = 0 \tag{3.23}$$

Solving these equations we get

$$y = \cosh\beta(m + H) = \frac{\beta - 2}{\sqrt{4 - \beta}} \tag{3.24}$$

$$x = e^{\beta\Delta} = \frac{4}{\sqrt{4 - \beta}} \tag{3.25}$$
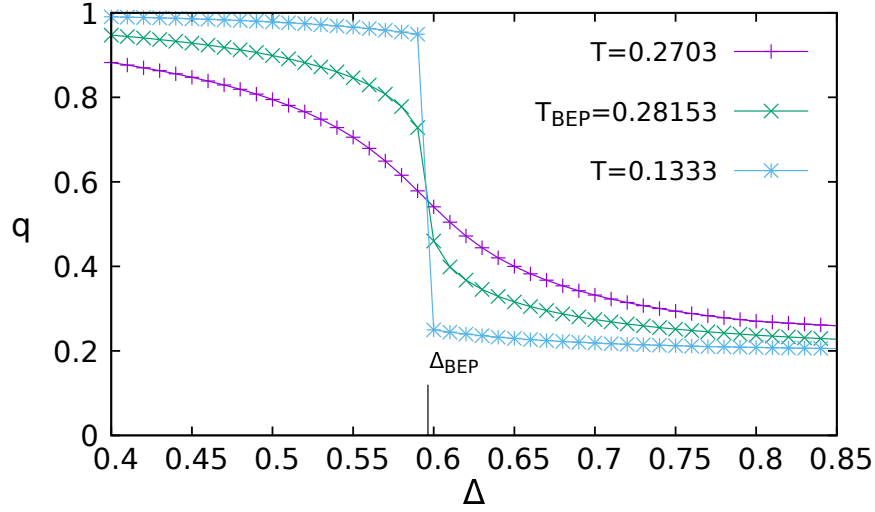
Figure 3.3: Concentration(q) vs Δ plot for $p = 0.2$ for different values of T

Hence, we reproduce the classic results of Blume, Emery and Griffiths [149] already mentioned in Chapter 1 : The $\lambda_{\pm}$ lines that exists for $4 \geq \beta \geq 3$ for $H \neq 0$. Above $\beta = 4$ there is no value of x and y that can satisfy Eqs. 3.22 and 3.23 simultaneously. The magnetisation along these two critical lines is not zero and is equal to

$$m = \pm\sqrt{\frac{\beta - 3}{\beta}} \tag{3.26}$$

This can be used to get the value of H along the critical lines, which comes out to be

$$H = \pm\frac{1}{\beta} \log\left(\frac{\beta - 2 + \sqrt{\beta^2 - 3\beta}}{\sqrt{4 - \beta}}\right) - m \tag{3.27}$$

These $\lambda_{\pm}$ lines meet in the $H = 0$ plane at the TCP co-ordinate of the pure Blume-Capel model : $T_{TCP} = \frac{1}{3}$ and $\Delta_{TCP} = 0.462098$. This is the well known TCP in (T, Δ) plane for $p = 0$ (can be obtained by solving Eq. 3.16 and 3.18 simultaneously for $p = 0$).

For $p \neq 0$, we use Mathematica [227] to solve Eq (3.20) and Eq. 3.21 simultaneously to get the two critical lines numerically. To solve the equations for any arbitrary p, we scan different values of β and Δ and hence x and solve Eq. 3.20 (corresponding to $\tilde{f}''(m) = 0$) exactly to get the corresponding value of y. Then we substitute the value of x and y in Eq. 3.21 to check if (x, y) satisfy the condition, $\tilde{f}'''(m) = 0$.

71

For each set of (x, y) that satisfy Eq. 3.20 and Eq. 3.21 simultaneously, we can calculate m using the equation:

$$m = \pm 2\sqrt{y^2 - 1}\Big[\frac{px}{1 + 2xy} + \frac{(1 - p)}{y + 2x}\Big] \tag{3.28}$$

The above equation is derived from Eq. 3.19 by taking $\cosh \beta(m + H) = y$ and $\exp(\beta\Delta) = x$. The corresponding value of H along the critical lines can then be calculated by inverting $y = \cosh \beta(m + H)$.

For a TCP to exist the two critical lines in the $H \neq 0$ plane should meet in $H = 0$ plane at the point where second order line ends in a first order transition line in the (T, Δ) plane. We can put $H = 0$ and $m = 0$ in Eqs. 3.20 and 3.21 to directly look for this point. Hence, we separately solve the two equations for $y = 1$. Interestingly, we find that for $y = 1$, the two equations can be solved simultaneously only for $p \leq p_c(= 0.0454)$. This is also the value of p beyond which linear stability analysis breaks down and Eq. 3.16 is not valid anymore. More interestingly even though the two equations can be solved for $H = 0$ till $p \leq 0.0454$, we find that for $p > 0.022$, one more solution shows up, with $m \neq 0$ and $H = 0$. For $p > 0.0454$, all possible solutions have $m \neq 0$.

We thus observed that the TCP persists only for very weak strength of the disorder. As disorder increases, the TCP vanishes and instead different multicritical points : bicritical end point (BEP) and critical end point (CEP) emerges. Depending on the values of p, we found that there are three different phase topologies for the range $0 < p \leq 0.5$. We call it strong $(0.1078 < p \leq 0.5)$, intermediate $(0.022 < p \leq 0.1078)$ and weak $(0 < p < 0.022)$ disorder regime. In the next subsections, we discuss the phase topologies for the different disorder regimes separately.
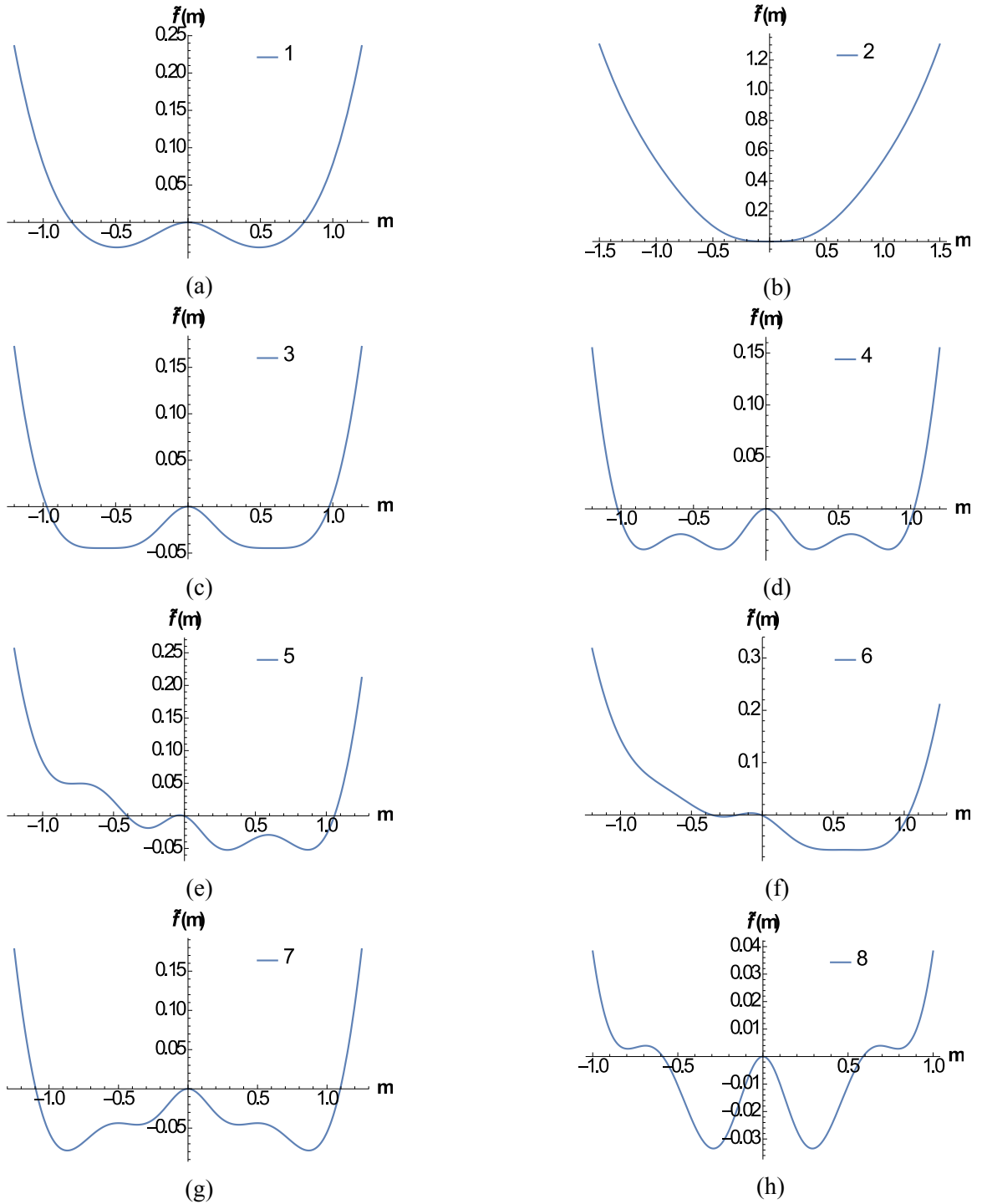
Figure 3.4: Free energy functional($\tilde{f}(m)$) as a function of m in different regions of the phase diagram(see Fig. 3.2(c)). We have taken $p = 0.2$ for which BEP is at $\Delta = 0.596376$ and $T = 0.2058$. The numbers on the plots refer to the numbers in Fig. 3.2(c). In (a) we plot $\tilde{f}(m)$ in $H = 0$ plane just below the λ-line, in (b) just above the λ line. In (c) we show $\tilde{f}(m)$ at the BEP and one can see the coexistence of two critical phases and (d) shows the $\tilde{f}(m)$ along the quadruple coexistence line. In (e) we show the functional along the first order wing surface for positive H and (f) shows the functional along the critical line enclosing the wing. Figs (g) and (h) show the $\tilde{f}(m)$ on two sides of the first order line in $H = 0$ plane.

3.4.3 Strong disorder regime : $0.1078 < p \leq 0.5$

We found that for all values of $0.022 < p \leq 0.5$, the $\lambda_\pm$ lines do not meet at the potential TCP point as given by simultaneous solution of Eq 3.16 and 3.18. Instead they meet inside the ordered plane i.e at a point where $m \neq 0$. This point hence is not a TCP, but a BEP. BEP is a multicritical point where only two of the three critical lines end on a first order surface. We will discuss about this emerging multicritical point in details in Section 3.5.

Furthermore, we find that for $p > 0.022$ there are two different kinds of phase diagrams possible. The range $0.1078 < p \leq 0.5$ is the strong disorder regime. For this range of p along the first order line in $H = 0$ plane there is a four phase coexistence, which ends in a BEP (see Fig. 3.2(c)) shown by a solid star. This line is a first order transition line between two ordered states with different values of magnetizations (**F** and **F1**). These two different ordered states are a result of disorder and are not present in the pure system. At low temperatures, the system prefers ± 1 spin states when Δ is small. As Δ increases, due to disorder, states with finite fraction of zero spins compete with the states with only ± 1 spins. This can be seen by looking at the order parameter q as a function of Δ, as shown in Fig. 3.3.

One can see all the transitions clearly by plotting $\tilde{f}(m)$ in different regions of the phase diagram as shown in Fig. 3.4 for $p = 0.2$. From the plots we can see that the $H = 0$ line separates the two ordered phases. Along the first order transition line there is a coexistence of four phases (see Fig. 3.4d). Along the $\lambda_\pm$ lines, two of these phases become critical, shown in Fig. 3.4f. And at the BEP the two critical phases coexist shown in Fig. 3.4c.

As p increases we find that the critical lines enclosing the wings become flatter and the temperature at which they meet in $H = 0$ plane decreases. We have tabulated the range of T for different p in Table 3.1.
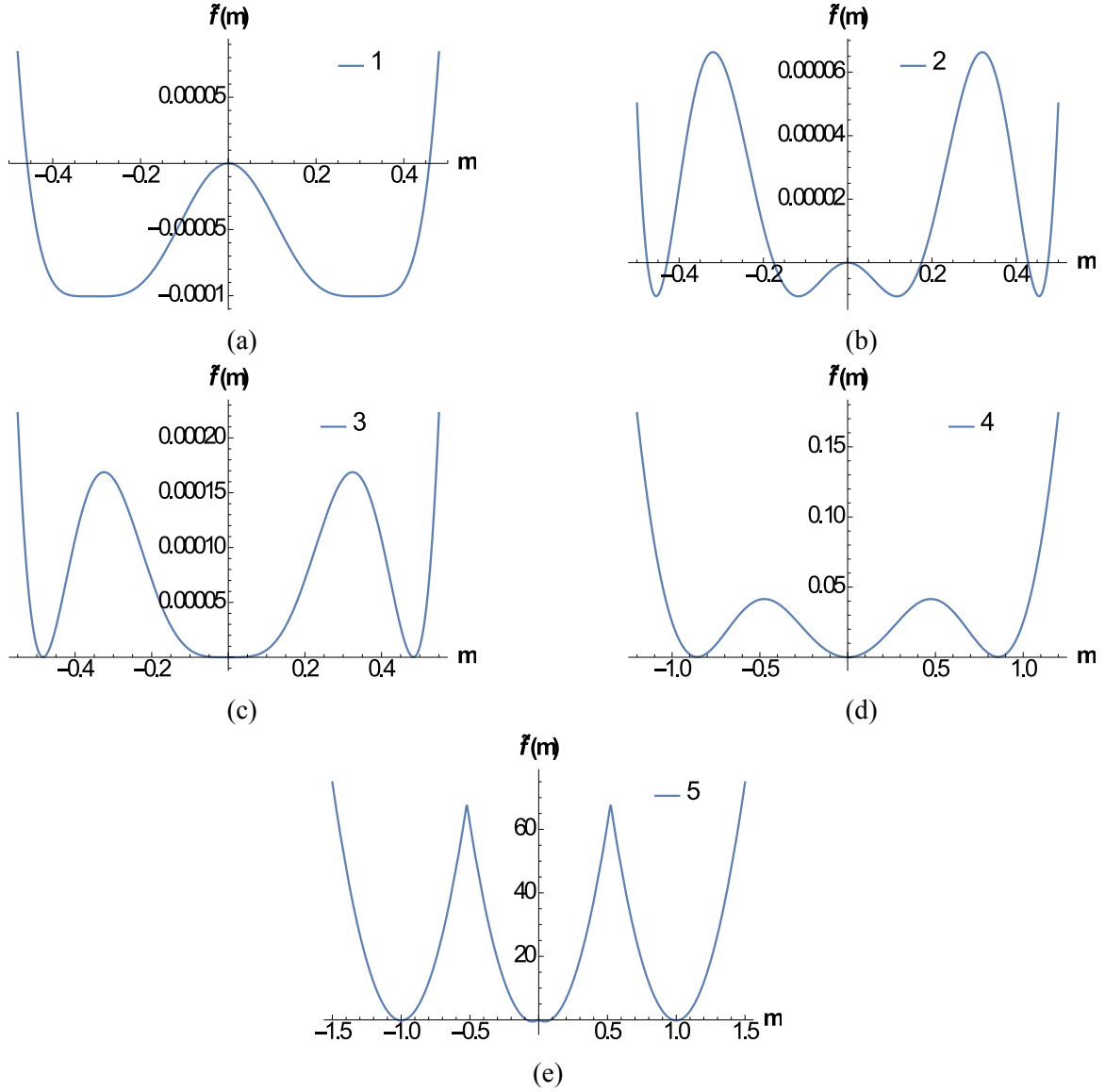
Figure 3.5: Free energy functional $\tilde{f}(m)$ plots for $p = 0.0044$. (a) $\tilde{f}(m)$ at the BEP with $T = 0.281532, \Delta = 0.500195, H = 0$;(b) $\tilde{f}(m)$ along the first order line between BEP and CEP1. (c) $\tilde{f}(m)$ at the CEP1 with $T = 0.27585, \Delta = 0.500186$, d) shows the functional along the first order line from CEP1 to CEP2, e) shows functional along the first order line from CEP2 at $T = 0.02$ to $T = 0$

$0.022 < p \leq 0.5$				
p	T_{lc}	Δ_{lc}	T_{uc}	δT
0.0453	0.28043	0.501175	0.23866	0.0417665
0.05	0.276396	0.50468	0.237473	0.038923
0.07	0.26185	0.518896	0.23245	0.029399
0.1	0.2451	0.538417	0.224972	0.020128
0.2	0.2058	0.596376	0.2	0.0058
0.3	0.17643	0.6490843	0.174978	0.001452
0.4	0.15024	0.69968	0.1499	0.000248
0.5	0.125016	0.7499884	0.12498	0.000036

Table 3.1: Width of the wing lines for different p. T_{lc} and Δ_{lc} represent the values of T and Δ for $H = 0$ where the λ_+ and λ_- lines meet and T_{uc} is the value along the critical line as $\Delta \to \infty$ and $H \to \infty$.

3.4.4   Intermediate disorder regime : $0.022 < p \leq 0.1078$

For $0.022 < p \leq 0.1078$ the wings meet at BEP as mentioned in the previous section. Apart from the BEP we also found that the model exhibits another multiciritcal point, known as CEP. This is also a point where a first order and a second order line of transition meets. But the difference between a TCP and a CEP is that, at the CEP the line of second order transition abruptly terminates on the first order line. We will discuss more the CEP in Section 3.5.

In this region the the λ-line truncates on the first order quadruple line at CEP (we will call this as CEP1). Below this temperature, the first order line becomes a line of triple point (see Fig. 3.2 (b)). At low temperature the ferromagnetic phase **F1** appears which is bounded by another line of continuous transition. This continuous transition line truncates on the triple line at a another CEP (we call as CEP2). The ferromagnetic phase that appears in the higher temperature is due to the re-entrance phenomenon. This phase has a different origin unlike the the ferromagnetic phase **F1** at low temperature. At higher temperature few $s = \pm 1$ spins become more entropically stable and gives rise to a ordered phase. The details of such inverse phenomenon has been discussed in Chapter 4
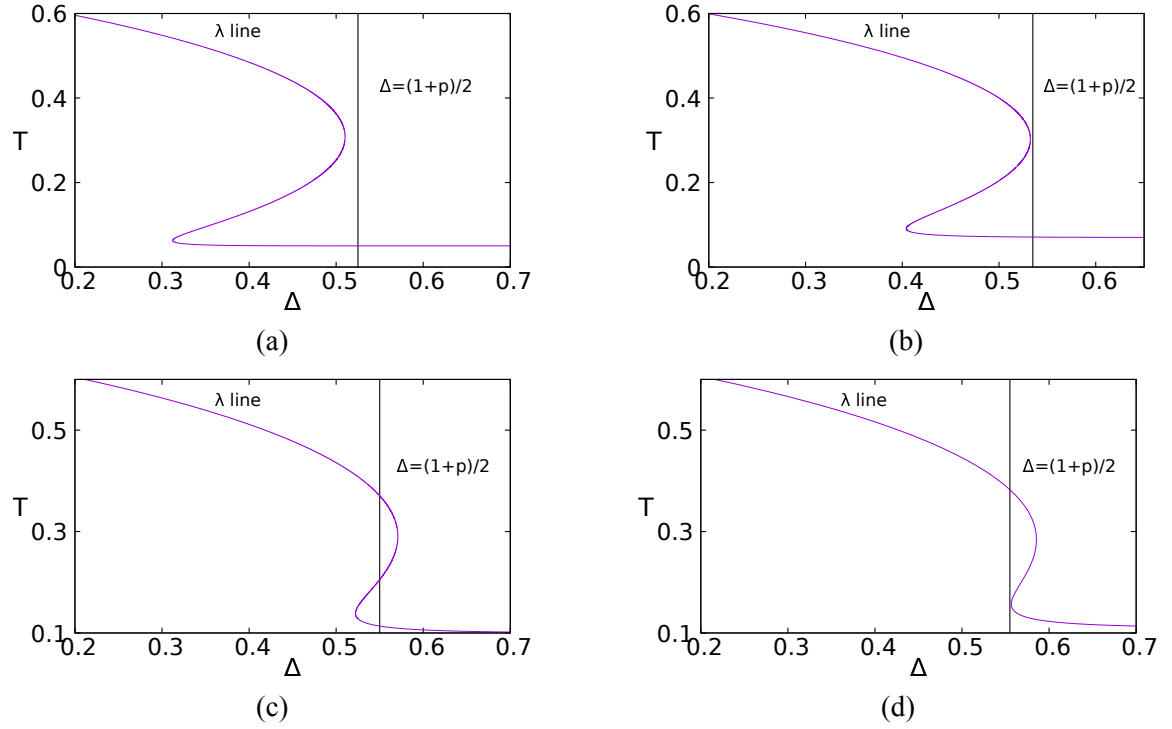
Figure 3.6: λ-line plotted along with $\Delta = (1 + p)/2$. For $p <= 0.07$ the $\Delta = (1 + p)/2$ line intersect the λ-curve only once. For $0.07 < p < 0.11$ it intersects it three times and only for $p >= 0.11$ it is fully on the left of the curve and hence doesn't intersect

In Fig.3.5, we plot the free energy functional along the first order line. The BEP and the CEP1 are connected by the quadrupole line, which separates two ferromagnetic phases shown by Fig. 3.5b. And then there is a usual triple line between CEP1 and CEP2, as shown in Fig. 3.5d. Between CEP2 and 0 temperature there is again a quadruple line as shown in Fig 3.5e.

In [185], Santos et al also reported the presence of CEP1 and CEP2 for $0.022 < p < 0.074$, by looking at the point of intersection of the λ-line with the first order line. We find that this topology extends till $p = 0.1078$. In order to understand the discrepancy, we have plotted λ-line given by Eq. 3.16 along with a line parallel to T-axis at $\Delta = (1+p)/2$ in Fig. 3.6. The line $\Delta = (1 + p)/2$ is a good approximation to the first order line in the (T, Δ) plane as we found that the first order line is almost parallel to T-axis. As shown in Fig. 3.6,

0.022 < p ≤ 0.107578					
p	T_{BEP}	$\triangle_{BEP}$	T_{CEP1}	$\triangle_{CEP1}$	T_{CEP2}	$\triangle_{CEP2}$
0.03	0.2961208	0.489187	0.295197	0.489166	0.03	0.4977229
0.044	0.28153	0.500195	0.27585	0.500186	0.04401	0.521585
0.07	0.26185	0.518896	0.24036	0.519398	0.07099	0.533953
0.107	0.24166	0.542	0.15972	0.547514	0.13975	0.549068

Table 3.2: Co-ordinates of the BEP and CEP's for $0.022 < p < 0.107$.

$\Delta = (1 + p)/2$ line crosses the λ-line once till $p \approx 0.07$ and thrice for $0.07 < p < 0.11$. For $p >= 0.11$ there is no intersection. More careful analysis using the full free energy functional, gives us the value to be around $p = 0.1078$. This matches with the value obtained by equating the free energy functional and its first derivative along the λ-line, as described in details in the Section 3.5.

In Table 2 we tabulate the location of BEP, CEP1 and CEP2 for different values of p. The first order line between CEP2 and Δ- axis is similar to the first order line reported in Sec 3.4.3, which separates the states with almost all ± 1 spins from a state with p fraction of ± 1 spins. The presence of CEP1 and a four phase co-existence line between BEP and CEP1 is due to the occurence of a new magnetic state. This state has more than p fraction of ± 1 spins, as it occurs at a higher temperature, very close to the λ line.

3.4.5 Weak disorder regime : $0 < p \leq 0.022$

Along the region $0 \leq p \leq 0.022$ the wings meet the λ-line at the TCP and the phase diagram is similar to the pure case. Along the first order line there is three phase coexistence. As p increases, the TCP shifts towards smaller T and larger Δ. At $p = 0.022$ the TCP becomes a fourth order critical point. Again, at very low temperature there is a CEP, similar to the case discussed (the CEP1) in the Subsection 3.4.4 for all $p > 0$, which is a state with p fraction of ± 1 spins and occurs at low temperatures on a complete graph. For $0.017 < p < 0.022$, there is re-entrance region in the phase diagram, as the TCP does not coincide with the
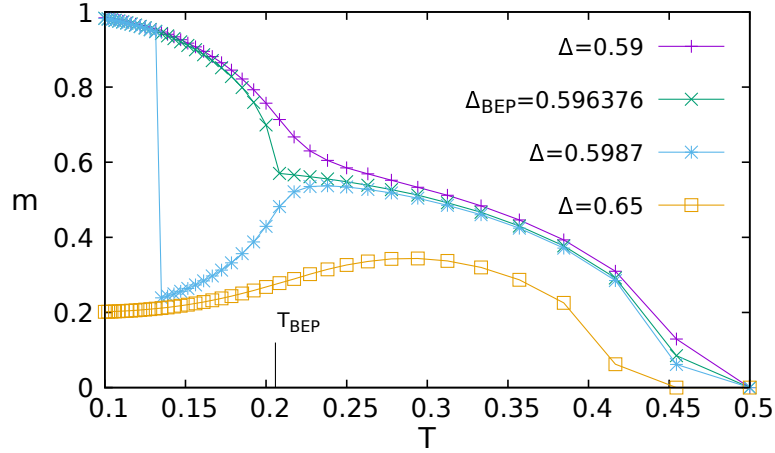
Figure 3.7: Magnetization(m) vs T plot for $p = 0.2$ for different values of Δ for $H = 0$. At BEP the first order jump vanishes and near $T = T_{BEP}$ one sees a change in slope for broad range of Δ.

maximum of λ-line given by Eq. 3.16. The phase diagram for this region has been shown in Fig. 3.2(a).

3.5 Bicritical end point (BEP) and critical end point (CEP)

In this section, we will give a detailed discussion about the emerging multicritical points in RCFBC model.

3.5.1 Bicritical end point (BEP)

Bicritical end points (BEP) are the multicritical points where two critical lines intersects at a first order surface [228, 229]. This point has been wrongly reported as an ordered critical point in earlier studies in (T, Δ) plane [185]. BEP has been comparatively less observed and studied in the literature. Few examples where BEP has been observed are : anisoptropic continuous spin systems as an end point of the spin flop line [230], spin 3/2 systems with crystal field [231, 232], metamagnet [233] FeBr$_2$ [234], binary and quasi-binary systems of trifluoromethane with n-alkanes, phenylalkanes and alkanols [235], antiferroelectric
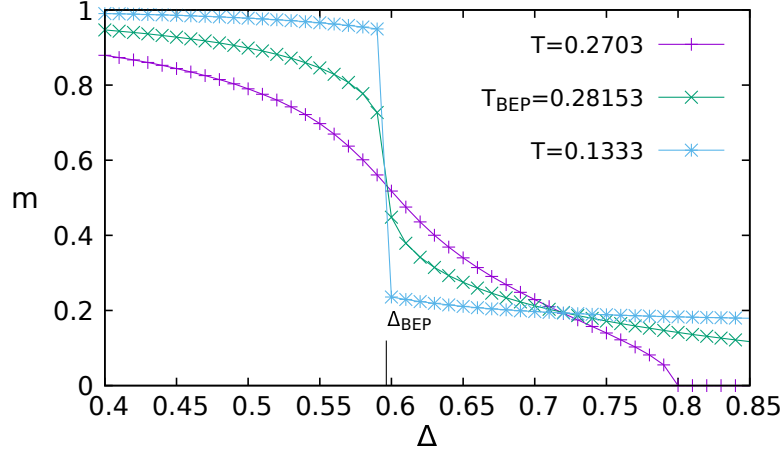
Figure 3.8: Magnetization(m) vs Δ plot for $p = 0.2$ for different values of T.

squaric acid [236] and so on. According to mean-field approximation, antiferromagnetic Ising model [228], metamagnets [237], RFIM [106] exhibits BEP, as in such systems the TCP spilts into a CEP and a BEP. Such splitting of TCP has also been verified using Monte-Carlo simulations in the antiferromagnet spin-1 Blume-Capel model for $d = 3$ [238, 239].

As shown in the plot of the free energy functional at the BEP, shown in Fig. 3.4c and Fig. 3.5a, BEPs are actually a point of coexistence of two critical phases. To understand the nature of transition especially at BEP, we looked at the magnetisation (m) and magnetic susceptibility $(\chi) = \frac{\partial m}{\partial H}|_{H \to 0}$. The expression of the susceptibility can be calculated as :

$$m = G(\beta, m, H, p, \Delta)$$

$$\Rightarrow \chi = G'\beta\chi + \beta G' \Rightarrow \chi = \frac{\beta G'}{1 - \beta G'} \tag{3.29}$$

where

$$G(\beta, m, H, p, \Delta) \equiv 2\sinh\beta(m+H)\left[\frac{pe^{\beta\Delta}}{1 + 2e^{\beta\Delta}\cosh\beta(m+H)} + \frac{(1-p)e^{-\beta\Delta}}{1 + 2e^{-\beta\Delta}\cosh\beta(m+H)}\right] \tag{3.30}$$

Let us first look at the magnetisation as a function of T in the $H = 0$ plane for different fixed values of Δ (see Fig. 3.7). We find that for $\Delta < \Delta_{BEP}$, the magnetisation changes
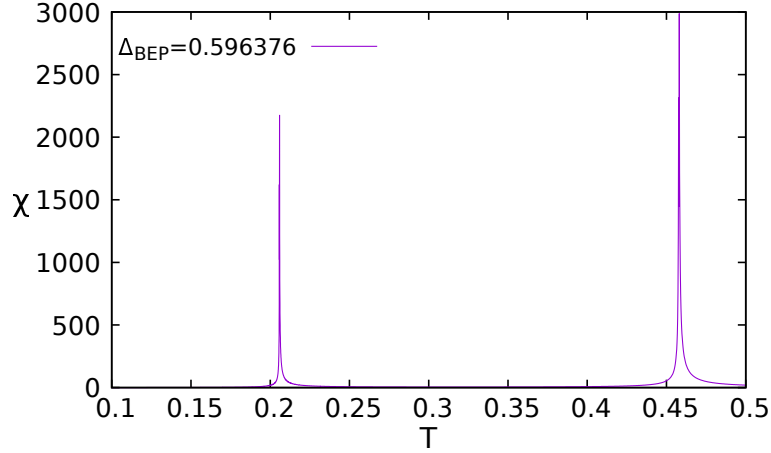
Figure 3.9: Magnetic susceptibility(χ) vs T plot at Δ_{BEP} for $p = 0.2$

its slope near $T = T_{BEP}$, the change becomes sharper as one approaches $\Delta = \Delta_{BEP}$. For $\Delta > \Delta_{BEP}$ (but close to Δ_{BEP}), the magnetisation undergoes a first order transition as it crosses the quadruple line and then changes slope near $T = T_{BEP}$. For Δ much larger than Δ_{BEP}, as we increase T there is no first order jump or change of slope around $T = T_{BEP}$. We also looked at m as a function of Δ for three different values of T (see Fig. 3.8). First order jump as one crosses the quadruple line is clear for $T < T_{BEP}$. For $T > T_{BEP}$ there is no signature of any transition.

It is hard to deduce the nature of transition at BEP by looking at the magnetisation alone. Hence we studied the magnetic susceptibility near BEP. First we look at it for fixed value of Δ. As we fix $\Delta = \Delta_{BEP}$ and vary T, we find that there is an infinite peak at the T of λ transition. There is another peak at $T = T_{BEP}$, but this peak is finite (see Fig. 3.9). This behaviour can be contrasted with the behaviour at $\Delta > \Delta_{BEP}$ as shown in Fig. 3.10. We find a discontinuity where it crosses the first order line and a finite peak near $T = T_{BEP}$.

We also studied magnetic susceptibility as we vary Δ at T_{BEP}, as shown in Fig. 3.11. As expected, we found that there is a finite peak at $\Delta = \Delta_{BEP}$. For $T < T_{BEP}$, there was instead a first order jump in magnetic susceptibility. We scanned a large region in (T, Δ) plane near BEP. We find that the effect of the presence of BEP is felt even far away
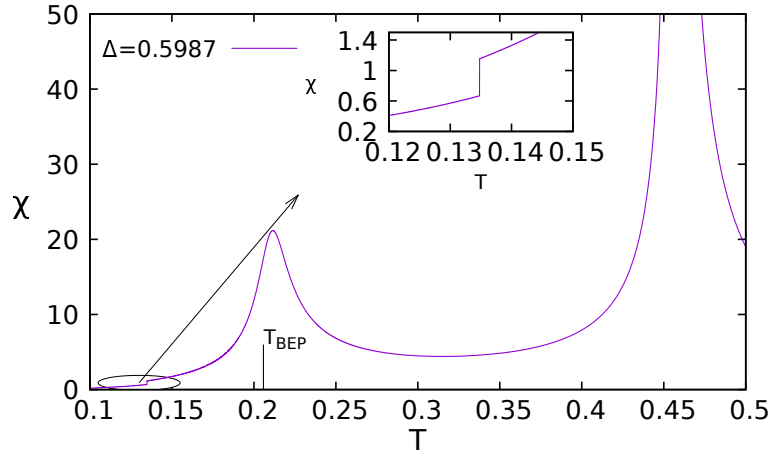
Figure 3.10: Magnetic susceptibility(χ) vs T plot for $p = 0.2$ for $\Delta > \Delta_{BEP}$

from the point. But the magnetisation and susceptibility plots are smooth near BEP (though susceptibility shows a cusp). It was shown via scaling arguments [240] that if the two critical lines meeting at BEP are in the same universality class and are symmetric, then the singular behaviour contribution to the phase boundary cancels out [240, 231]. In our case the two critical lines λ_+ and λ_- lie in the Ising universality class. Looking at the three dimensional phase diagram it is clear that there is only one phase in the system in the sense that there exist a path between any two non-singular points in the phase diagram which does not have to encounter a singularity. At BEP the first three derivatives of $\tilde{f}(m)$ w.r.t m are zero and hence the free energy is not analytic at this point. Hence, we conclude that BEP is a point of two phase co-existence and there is no critical transition from one phase to another at BEP.

3.5.2 Critical end point (CEP)

Critical end point (CEP) is a critical point where a line of second order transitions terminates at a line of first order transitions [241, 20]. Alternately, it can also be defined as a point where two phases become critical in the presence of one or more ordered phases, known as the spectator phases [242], in systems with multiple phases. There are a variety of physical systems which shows CEP. For example : superfluids [19], gel-fluid mixture
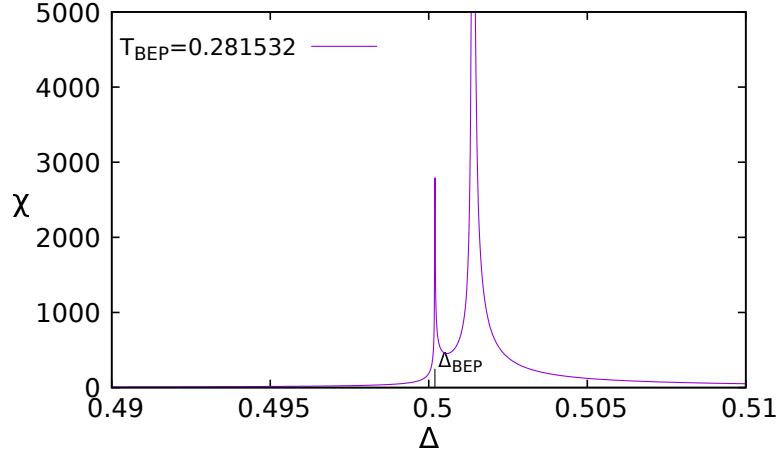
Figure 3.11: Magnetic susceptibility(χ) vs Δ plot for $p = 0.044$ at $T = T_{BEP}$

[243], metamagnets [244], ferroelectrics [245], liquid crystals [13], binary fluid mixtures [8, 9, 10], quantum chromodynamics [246] and so on.

The free energy functional at the CEP is shown in Fig. 3.5c, where two phases become critical in presence of two non-critical phases. At CEP, $\tilde{f}(m)$ for $m = 0$ and for $m \neq 0$ should be equal (i.e $\tilde{f}(m = 0) = \tilde{f}(m \neq 0)$) along with their derivative with respect to m ($\tilde{f}'(m = 0) = \tilde{f}'(m \neq 0)$). If this point lies on the λ line, then we get the condition for CEP. Hence to find CEP, we explore the λ-line for a point where $\tilde{f}(m = 0) = \tilde{f}(m \neq 0)$ along with $\tilde{f}'(m = 0) = \tilde{f}'(m \neq 0)$. We find that for $p > 0.1078$ the condition cannot be satisfied. For $0 < p \leq 0.022$, we observe that there the condition satisfied once and for $0.022 < p \leq 0.1078$ it satisfies twice, giving rise to two CEPs (CEP1 and CEP2).

Similar to the BEPs, we plot the magnetic susceptibility as a function of Δ for $T = T_{CEP}$ in $H = 0$ plane. In contrast to the BEP, the susceptibility near CEP shows an infinite peak at at the CEP1 (see Fig. 3.12).

The scaling arguments for the different multicritical points like the TCP, CEP and BEP are different from each other. We will give a detailed study of the scaling near the CEP and BEP in Chapter 6. In the next section we will discuss about the Landau theory near these multicritical points.
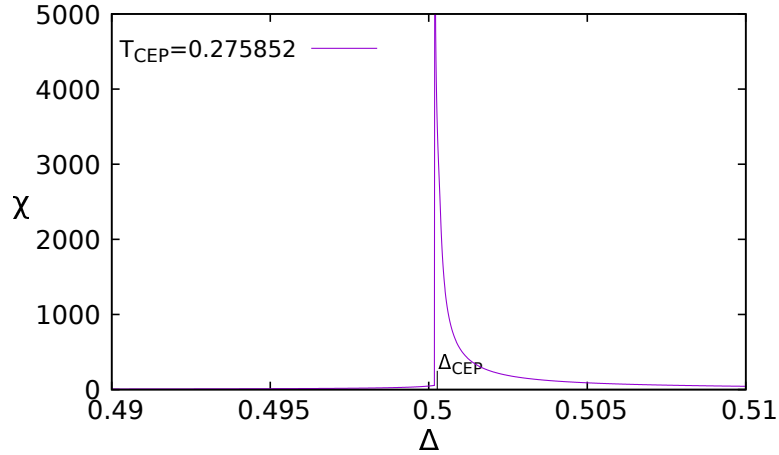
Figure 3.12: Magnetic susceptibility(χ) vs Δ plot for $p = 0.044$ at $T = T_{CEP}$

3.6 Landau theory

In the previous sections we studied the phase diagram by looking at the full free energy functional and its derivatives. Usually, Landau theory is a very useful tool to classify different kinds of transitions and even though it might not be accurate quantitatively, it helps in understanding different possible topologies of the phase diagram. But while very successful in explaining ordinary critical point, it is not always possible to find a Landau description for higher order critical point, i.e. it is perhaps possible to define a free functional always, but it might not always be Taylor expandable [247]. In this section we expand the free energy functional to check if we can explain the phase diagrams based on the coefficients of different powers of the order parameter. For example, the Ising universality class critical point can be determined easily by expanding upto fourth power in m, provided that the next higher order coefficient is positive. For TCP one needs to expand till sixth order. A sixth order Landau theory hence allows only for ordinary critical points and TCPs. We expect that we need to keep more terms in the expansion, if we expect to find higher order critical points like CEP and BEP . Hence we expanded the free energy functional till eighth power

of m. We get

$$\tilde{f}(m) = a_2 m^2 + a_4 m^4 + a_6 m^6 + a_8 m^8 \tag{3.31}$$

where a_i's are Landau coefficients, as follows:

$$a_2 = \frac{\beta}{2} \left(1 + \frac{2\beta(p-1)}{2+c} - \frac{2\beta pc}{1+2c} \right) \tag{3.32}$$

$$a_4 = \frac{\beta^4}{12} \left(\frac{(-4+c)(p-1)}{(2+c)^2} + \frac{p\ c(-1+4c)}{(1+2c)^2} \right) \tag{3.33}$$

$$a_6 = \frac{\beta^6}{360} \left(\frac{(64-26c+c^2)(p-1)}{(2+c)^3} - \frac{pc(1-26c+64c^2)}{(1+2c)^3} \right) \tag{3.34}$$

$$a_8 = \frac{\beta^8}{20160} \left(\frac{(1188c-2176-120c^2+e^{3\beta\Delta})(p-1)}{(2+c)^4} + \frac{pc(-1+120c-1188c^2+2176c^3)}{(1+2c)^4} \right) \tag{3.35}$$

where $c \equiv e^{\beta\Delta}$. The second order transition is given by $a_2 = 0$, provided $a_4 > 0$. Equating $a_2 = 0$ gives us:

$$1 + \frac{2\beta(p-1)}{2+e^{\beta\Delta}} = \frac{2\beta p e^{\beta\Delta}}{1+2e^{\beta\Delta}} \tag{3.36}$$

This equation is same as Eq. 3.16, obtained by linear expansion around $m = 0$. According to the Landau theory, a new universality class, namely the TCP occurs when a_4 becomes equal to 0, provided $a_6 > 0$. We find that the condition for $a_4 = 0$ along the λ-line is the same as given by substituting Eq. 3.16 into Eq. 3.18. For $p > p_c = 0.0454$,

a_4 is never 0 and hence beyond p_c the condition for occurrence of TCP cannot be satisfied. For $p > 0.022$, $a_6 < 0$ at the point where $a_4 = 0$. Hence sixth order Landau theory while sufficient for $p < 0.022$, is not enough for $p > 0.022$.

Hence for $a_6 < 0$, we consider the expansion till eighth order, since $a_8 > 0$ for all ranges of the parameters. CEP will be a point along the λ-line (given by Eq. 3.36) where the $\tilde{f}(T_c, m_c) = 0$ and $\tilde{f}'(T_c, m_c) = 0$ and $m_c \neq 0$. Solving these, we get the condition for the existence of CEP to be

$$\frac{a_6^2}{4a_4a_8} = 1 \tag{3.37}$$

We find that Eq. 3.37 can be satisfied only for $0.022 < p \leq 0.0454$, and that too at a point very close to the point where $a_4 = 0$. For example, for $p = 0.044$ from Eq. 3.37, we get $(T_{CEP1}, \Delta_{CEP1}) = (0.267, 0.497)$ and for $p = 0.03$ we get $(T_{CEP1}, \Delta_{CEP1}) = (0.294, 0.489)$. Hence we find that the value obtained via Eq. 3.37 are different from the ones obtained by looking at the full free energy functional in Section (see Table 3.2). The difference increases with increasing p. More importantly, in Section 3.4.3 we had found numerically that CEP is present for a much larger range of p: $0.022 < p \leq 0.1078$.

To estimate BEP using truncated $\tilde{f}(m)$, we equate the first three derivatives of the truncated $\tilde{f}(m)$ in Eq. 3.31 w.r.t m to 0. For $m \neq 0$, this gives the condition for BEP to be: $a_6 = -\sqrt{\frac{8a_4a_8}{3}}$. Again this condition gets satisfied only for $0.022 < p \leq 0.0454$. This gives a BEP very close to CEP and the actual location does not match with the numerical estimates of Section 3.4.3. Hence, a Landau description of this system predicts the phase diagram correctly for $p < 0.022$ (except for CEP present at very low temperatures for all $p > 0$) and gives qualitatively similar diagram for $0.022 < p < 0.0454$, though the location of BEP and CEPs does not match the actual value. For $p > 0.0454$ it is inadequate in predicting the phase diagram. We tried including more terms in the expansion of $\tilde{f}(m)$, but

we could not locate BEP using a truncated $\tilde{f}(m)$, suggesting that full $\tilde{f}(m)$ is needed for locating the BEP.

3.7   Summary and conclusion

The effect of disorder on first order transition has been less studied in literature. The spin-1 Blume-Capel model is the simplest model which exhibits a multicritical point and has a very rich phase diagram. The phase diagram of the Blume-Capel model on the $T - \Delta$ plane in the presence of random crystal field disorder has studied extensively using many different techniques [183]-[196]. And it was reported that the TCP as well as the first-order transition line of the model disappears as the strength of the disorder increases [194]. As the full phase diagram of the TCP is three dimensional, in this work we have investigated the effect of crystal field disorder on the $T - \Delta - H$ phase diagram of an infinite range Blume-Capel model [213]. This study has not been done earlier.

We observe that the presence of disorder is relevant and affects the system's critical behavior drastically. We found that as depending on the strength of the disorder, there can be three different types of phase diagrams. For small strength of disorder the TCP persists. As disorder strength increases, the TCP vanishes but the wings as well as the first order transition line persists. The TCP splits into a BEP and a CEP. And the two wings now meet at a BEP. For further increase in the strength of disorder, we observe that the CEP also disappears and the phase diagram is only consists of a BEP and the wings persist for all strength of disorder.

The emergence of the BEP as a consequence of the disorder was some new observation in this work. We showed that the BEP is actually a point of co-existence of two critical phases, where the magnetic susceptibility is finite. Hence in-spite of the three derivatives of the free energy being zero at BEP, it is not critical. This point was identified as an or-

dered critical point in earlier studies [185, 196]. Another important observation was that the Landau expansion of the free energy could not locate the multicritical points like BEP and CEP precisely. The origin of BEP in our model is different than that for the pure anisotropic continuous spin systems, where the BEP was seen as an end-point of spin flop transition line [230]. A two parameter Landau theory description exists for spin-flop [20]. Our free energy functional is a one parameter function which shows BEP. Due to this fact, despite of observing three different topologies of the phase diagram for bimodal RCFBC model [183, 185] , the authors couldn't identify the BEPs and CEPs correctly.

Chapter 4

Blume-Capel model with random field disorder

In this chapter we study the effect of random field disorder on the spin-1 Blume-Capel model in presence of two different symmetric distribution : discrete and continuous. We start with the introduction of the random field Blume-Capel (RFBC) model Hamiltonian and solve it using tilted LDP. We first discuss the ground state phase diagram and then go to the finite temperature phase diagrams for both the distributions. We show how the different symmetric distributions give rise to different phase diagrams. We also discuss many interesting features in the finite temperature phase diagram for the trimodal case.

4.1   Random field Blume-Capel model (RFBC)

The spin-1 random field Blume-Capel model (RFBC) has been studied in presence of bimodal random field distribution using the mean-field method [205, 206] in the $T - h$ and $T - \Delta$ plane respectively. It was reported that the phase diagrams in the $T - \Delta$ and $T - h$ plane are similar and there are five different phase diagrams depending on the values of h and Δ respectively. The RFBC model has also been studied on the Bethe lattice in presence of bimodal [207] and equal trimodal distribution [208]. Here the presence of two lines of first order transition and one continuous line of transition was reported. Another study of the RFBC model was in random network with finite connectivity in presence of bimodal distribution [209].

In this work [214] we have considered the following Hamiltonian for the RFBC model with N spins on a fully connected graph
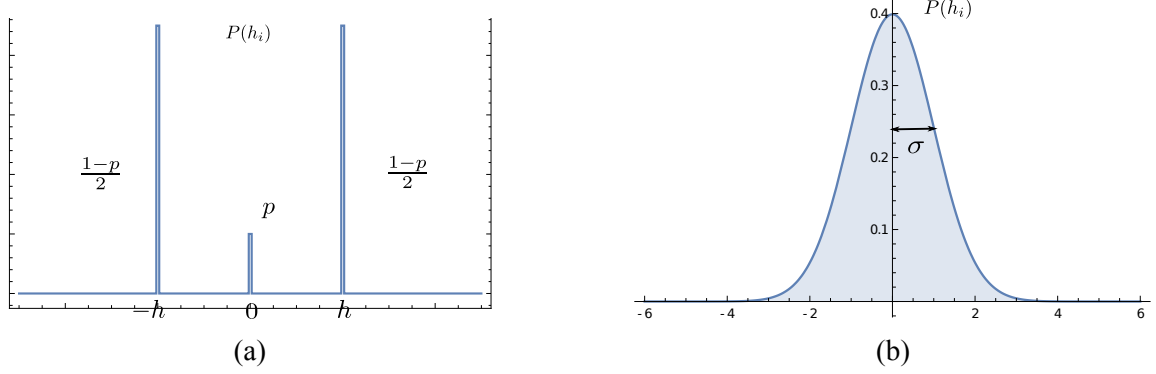
Figure 4.1: Different symmetric random field distributions. **(a)** Discrete symmetric distribution : Trimodal distribution, and **(b)** Continuous distribution : Gaussian distribution. Both the distributions has zero mean.

$$\mathcal{H} = -\frac{1}{2N}(\sum_i s_i)^2 + \Delta \sum_i s_i^2 - \sum_i (h_i + H)s_i \tag{4.1}$$

where s_i can take values $\pm 1, 0$, Δ is the crystal field of the system which controls the density of the magnetic and non-magnetic spins, H is the uniform external magnetic field and h_i is the quenched random field at site i. In this study we consider two different symmetric distribution. For discrete distribution we consider the trimodal distribution as follows (see Fig. 4.1a):

$$P(h_i) = p\delta(h_i) + \frac{1-p}{2}(\delta(h_i + h) + \delta(h_i - h)) \tag{4.2}$$

here $0 \leq p \leq 1$. The random field take values $\pm h$ with probability $\frac{1-p}{2}$, and p fraction of spins are free from the disorder. $p = 1$ is the pure Blume-Capel model and $p = 0$ is known as bimodal distribution. δ is the Dirac-delta function. The first two cumulants of this distribution are $\langle h \rangle = 0$ and $\langle h^2 \rangle = \sqrt{1-p}\; h$.

Whereas for continuous distribution we consider the following Gaussian distribution with zero mean and variance σ (see Fig. 4.1b):

$$P(h_i) = \frac{1}{\sqrt{2\pi\sigma^2}}\; e^{\frac{-h_i^2}{2\sigma^2}} \tag{4.3}$$

Trimodal RFIM is relevant in studying the diluted antiferromagnets in a uniform field,

where the field conjugate to the antiferromagnetic order parameter takes three values [82]. It can be shown that the low order cumulants like the second and the fourth cumulants of both the distributions are equal when $p = \frac{2}{3}$. So the trimodal distribution is a good approximation of the the Gaussian distribution when $p = \frac{2}{3}$. It was conjectured [76] that for random field $O(n)$ models in presence of symmetric distribution gives similar phase diagrams. It has been shown that for $n = 1$ i.e the RFIM the phase diagram becomes similar for trimodal and Gaussian distribution [100] for $\frac{1}{3} \leq p < 1$ [105, 106, 118, 119, 124]. Recently for $n = 2$ random field XY model similarity in the phase diagram in presence of cubic symmetric distribution has been reported [248].

We have studied the phase diagrams for both the symmetric distributions in the ground state as well as in the finite T. We have considered all the ranges of p and σ and investigated how the presence of different random field disorder affects the rich phase diagram of the higher spin model like the Blume-Capel model.

In the next section we will show the calculation of the free energy functional of the system using LDP.

4.2   Calculation of the rate function

We solve the Hamiltonian Eq. 4.1 using the tilted LDP as mentioned in Chapter 2. We first start with the calculation of the rate function $R(x_1, x_2)$ corresponding to the non-interacting part of the Hamiltonian $\mathcal{H}_{ni} = \Delta \sum_i s_i^2 - \sum_i (h_i + H)s_i$. Using the Gärtner-Ellis (GE) theorem the expression of $R(x_1, x_2)$ is

$$R(x_1, x_2) = \sup_{k_1, k_2} \left[x_1 k_1 + x_2 k_2 - \lambda(k_1, k_2) \right]$$

(4.4)

where the logarithmic cumulant generating function $\lambda(k_1, k_2)$ for the random variables x_1 and x_2 is given by
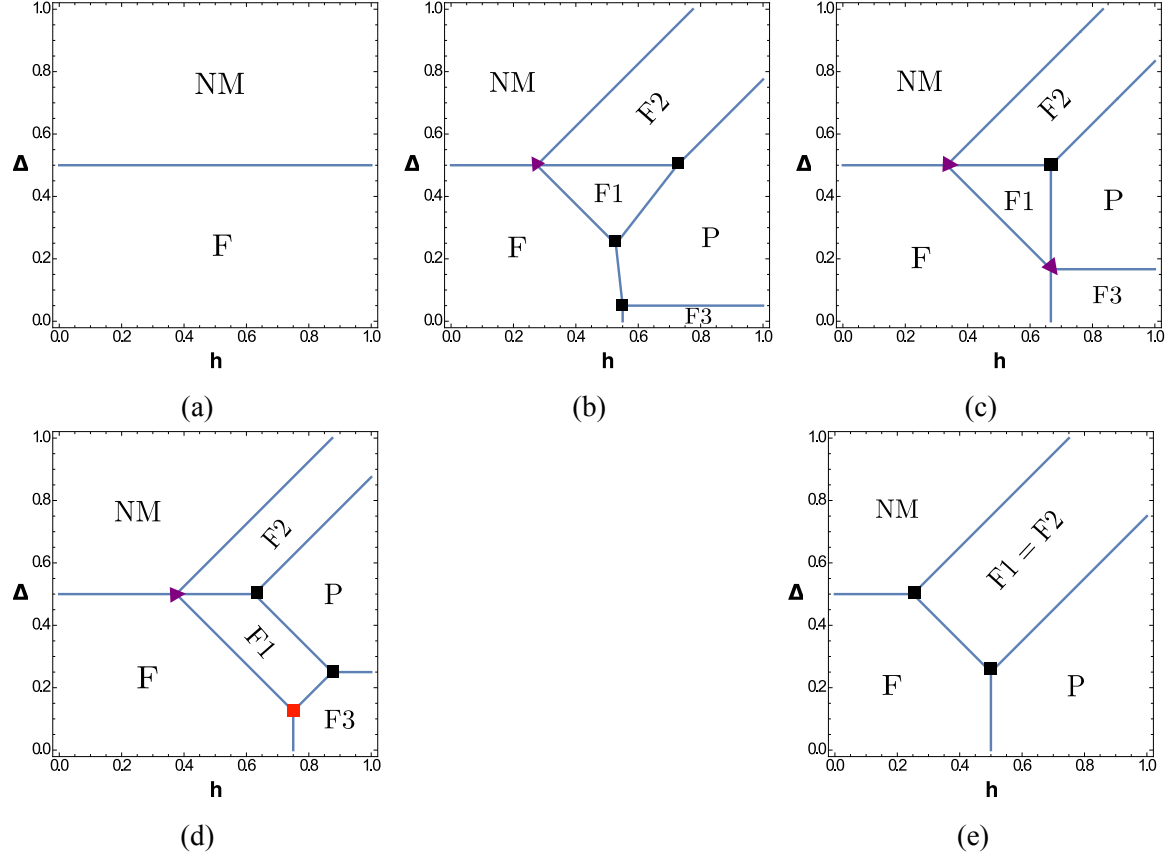
Figure 4.2: Ground state phase diagram for the trimodal distribution. Solid blue lines are the lines of first order transition. The purple triangles denote the A_7 points, black squares are the A_5 points and the red squares are the A_6 points. **(a)** Is the phase diagram for the pure Blume-Capel model ($p = 1$). In this case there is a first order transition from the **F** ($m = q = 1$) to the **NM** ($m = q = 0$) phase at $\Delta = 0.5$. **(b)**, **(c)** and **(d)** are the phase diagram for $0 < p < 1$. Each of the phase diagram contains six phases: **F**, **F1** ($m = q = \frac{1+p}{2}$), **F2** ($m = q = \frac{1-p}{2}$), **F3** ($m = p$, $q = 1$), **P** ($m = 0$, $q = 1 - p$), and, **NM**. All the phases are separated by first order transition lines. Fig.**(b)** shows the phase diagram for $p = \frac{1}{10}$. This qualitatively holds for all $0 < p < \frac{1}{3}$. Fig.**(c)** shows the phase diagram for $p = \frac{1}{3}$ and Fig.**(d)** shows the phase diagram for $p = \frac{1}{2}$, this qualitatively holds for all $\frac{1}{3} < p < 1$. Fig. **(e)** is the phase diagram for $p = 0$, the bimodal random field distribution. In this case, the phases **F1** and **F2** become equal and we call it **F1=F2** phase.

$$\lambda(k_1, k_2) = \left\langle \log\left(1 + 2e^{k_2 - \beta\triangle}\cosh(k_1 + \beta H + \beta h_i)\right) \right\rangle_h$$

(4.5)

$\langle\rangle_h$ represents the average over the random field distribution.

Minimization of the expression $x_1 k_1 + x_2 k_2 - \lambda(k_1, k_2)$ in w.r.t the k_1 and k_2 gives the following equations for the supremum (k_1^*, k_2^*) as a function of x_1 and x_2

$$x_1 = \left\langle \frac{2e^{k_2^* - \beta\triangle}\sinh(\beta h_i + \beta H + k_1^*)}{1 + 2e^{k_2^* - \beta\triangle}\cosh(\beta h_i + \beta H + k_1^*)} \right\rangle_h$$

(4.6)

$$x_2 = \left\langle \frac{2e^{k_2^* - \beta\triangle}\cosh(\beta h_i + \beta H + k_1^*)}{1 + 2e^{k_2^* - \beta\triangle}\cosh(\beta h_i + \beta H + k_1^*)} \right\rangle_h$$

(4.7)

We then calculate the full rate function of the interacting Hamiltonian $I(x_1, x_2)$ via tilted LDP. The full rate function $I(x_1, x_2)$ is given by

$$I(x_1, x_2) = R(x_1, x_2) - \frac{\beta x_1^2}{2} - \inf_{y_1, y_2}\left(R(y_1, y_2) - \frac{\beta y_1^2}{2}\right)$$

(4.8)

After substituting $R(x_1, x_2)$ we get

$$I(x_1, x_2) = x_1 k_1^* + x_2 k_2^* - \frac{\beta x_1^2}{2} - \left\langle \log\left(1 + 2e^{k_2^* - \beta\triangle}\cosh(k_1^* + \beta H + \beta h_i)\right) \right\rangle_h$$

(4.9)

here $(k_1^*,\ k_2^*)$ are given by the solutions of Eq. 4.6 and Eq. 3.1. Minimizing the full rate-function w.r.t the order parameters (x_1, x_2) we get $k_1^* = \beta m$ and $k_2^* = 0$. The variables m

and q represent the minimum of x_1 and x_2 respectively. On substituting k_1^* and k_2^* in we get the free energy functional to be

$$f(m) = \frac{\beta m^2}{2} - \left\langle \log\left(1 + 2e^{-\beta\Delta} \cosh \beta(m + H + h_i) \right) \right\rangle_h$$

(4.10)

$$m = \left\langle \frac{2e^{-\beta\Delta} \sinh \beta(h_i + H + m)}{1 + 2e^{-\beta\Delta} \cosh \beta(h_i + H + m)} \right\rangle_h$$

(4.11)

Another order parameter is the quadrupole moment (q). It is the expectation value of s_i^2, given by $q = \frac{1}{\beta} \frac{\partial f(m)}{\partial \Delta}$. Using that we get

$$q = \left\langle \frac{2e^{-\beta\Delta} \cosh \beta(h_i + H + m)}{1 + 2e^{-\beta\Delta} \cosh \beta(h_i + H + m)} \right\rangle_h$$

(4.12)

In the next part we solve the ground state phase diagram for both the distributions.

4.3 Ground state phase diagram

4.3.1 Trimodal distribution

Using the distribution $P(h_i)$ from Eq. 4.2 in Eq. 4.1, the free energy functional of the system at $H = 0$ becomes

$$\begin{aligned} f(m) &= \frac{\beta m^2}{2} - p \log\left(1 + 2e^{-\beta\Delta} \cosh \beta m\right) - \frac{1-p}{2} \log\left(1 + 2e^{-\beta\Delta} \cosh \beta(-h + m)\right) \\ &\quad - \frac{1-p}{2} \log\left(1 + 2e^{-\beta\Delta} \cosh \beta(h + m)\right) \end{aligned}$$

(4.13)

Phases	Ground state energy
NM $: m = q = 0$	$E(m) = 0$
F $: m = q = 1$	$E(m) = \Delta - \frac{1}{2}$
F1 $: m = q = \frac{1-p}{2}$	$E(m) = \frac{1-p}{2}\left(\Delta - h - \frac{1}{4}(1-p)\right)$
F2 $: m = q = \frac{1+p}{2}$	$E(m) = \frac{1+p}{2}\left(\Delta - \frac{1}{4}(1+p)\right) - \frac{1-p}{2}h$
P $: m = 0,\ q = 1 - p$	$E(m) = (1-p)(\Delta - h)$
F3 $: m = p,\ q = 1$	$E(m) = \Delta - (1-p)h - \frac{p^2}{2}$

Table 4.1: Ground state phases and their corresponding ground state energies for any general $0 \le p < 1$ in trimodal RFBC model. There are four ferromagnetic phases **F, F1, F2, F3**, one paramagnetic phase **P** and one non-magnetic phase **NM**.

For $\beta \to \infty$, the ground state rate function given by, $\Phi(m) = \lim\limits_{\beta \to \infty} \frac{1}{\beta} f(m)$ is

$$
\begin{aligned}
\Phi(m) \;=\; & \frac{m^2}{2} - p \mid m - \Delta \mid \Theta(m - \Delta) - \frac{1-p}{2} \mid m + h - \Delta \mid \Theta(m + h - \Delta) \\
& - \frac{1-p}{2} \mid h - \Delta - m \mid \Theta(h - \Delta - m) - \frac{1-p}{2} \mid m - h - \Delta \mid \Theta(m - h - \Delta)
\end{aligned}
$$

(4.14)

here $\Theta(x)$ is the Heaviside step function with $\Theta(x) = 1$ for $x > 0$, and $\Theta(x) = 0$ for $x \le 0$. The disorder averaged ground state energy is $E = \min\limits_{m} \Phi(m)$. As soon as the disorder is switched on, depending on the conditions on Δ and h we found that there are six phases in the ground state phase diagram for all $0 \le p < 1$.

- For $\Delta > m + h$ and $\Delta > m$: the phase is non-magnetic phase $m = q = 0$, denoted by **NM**.

- For $\Delta < m + h$ and $\Delta < m$: the phase is ferromagnetic phase $m = q = 1$, denoted by **F**.

- For $\Delta > m - h$ and $\Delta > m$: the phase is $m = q = \frac{1-p}{2}$, denoted by **F2**.
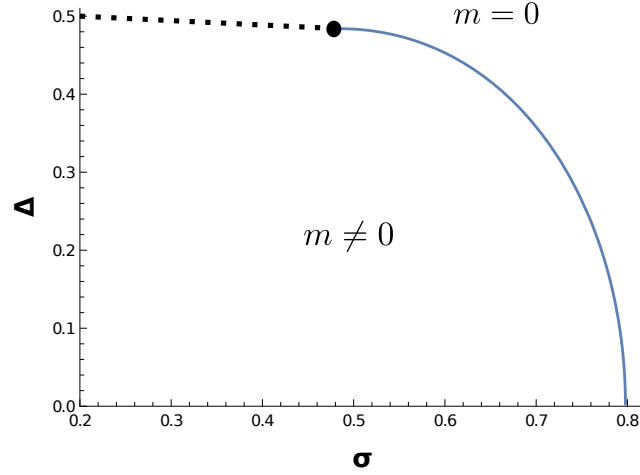
Figure 4.3: Ground state phase diagram for the Gaussian field distribution. Dotted line is the line of first order transitions and solid line is the line of second order transitions. Solid circle is the TCP. There is one ordered phase ($m \neq 0$) and one disordered phase ($m = 0$) in the phase diagram. The transition is first order for small σ. As σ increases, the transition changes to second order at a TCP with the coordinates $\sigma_{TCP} = \Delta_{TCP} = \sqrt{\frac{2}{e\pi}}$.

- For $\Delta > m - h$ and $\Delta < m$: the phase is $m = q = \frac{1+p}{2}$, denoted by **F1**.

- $h > m + \Delta$ and $\Delta > m$: the phase is paramagnetic phase $m = 0, q = 1 - p$, denoted by **P**.

- For $h > m + \Delta$ and $\Delta < m$: the phase is $m = p, q = 1$, denoted by **F3**.

All the six phases with their corresponding ground state energy are listed in Table 4.1.

For high values of h, the spins are more likely to be $s = \pm 1$ and distributed equally at the same time. So the phase becomes a paramagnetic phase (**P**). On the other hand, for large Δ and small h, the $s = 0$ spins dominate, hence the phase becomes non-magnetic (**NM**). An ordered phase **F3** exists for all large values of h and small Δ because of the p fraction of spins which are free from the disorder field. For both large values of Δ and h, the ordered phase **F2** appears and it continues to exist for all large values of $h \approx \Delta$. This phase appears due to the competition between the Δ and h.

In the next paragraphs we will discuss about the phase diagrams for all $0 \leq p < 1$.

$p = 1$ **: Pure Blume-Capel model**

The case $p = 1$ corresponds to pure Blume-Capel model. In this case there are two phases : one ordered **F** and one disordered phase **NM**, separated by a first order transition line at $\Delta = \frac{1}{2}$. The ground state phase diagram for $p = 1$ is shown in Fig. 4.2a.

General p : $0 < p < 1$

For all $0 < p < 1$, there six phases in the ground state state phase diagram. All the phases are separated by first order transition lines. These lines are computed by comparing the ground state energy of all the phases. For all $0 < p < 1$ there are six first order phase boundaries that are always present. These are : the **F3** phase is separated from the **F** phase by a first order transition line parallel to the Δ axis at $h = \frac{1+p}{2}$, phases **F1** and **F2** and phases **F** and **NM** are separated via a first order transition line parallel to h axis at $\Delta = \frac{1}{2}$, phases **P** and **F3** are separated by a first order transition line parallel to h axis at $\Delta = \frac{p}{2}$. The phase **F2** is separated from phase **NM** via the first order transition line $\Delta - h = \frac{1}{4}(1 - p)$. The phase **F2** is separated from the phase **P** via the first order transition line $h - \Delta = \frac{1}{4}(1 - p)$. The phases **F** and **F1** are separated by the first order transition line given by the solution of the equation $(1 - p)(\Delta + h) = \frac{1}{4}(3 - p^2 - 2p)$. Apart from these there are some other first order transition lines in the phase diagrams which depend on the range of p.

- **$0 < \mathbf{p} < \frac{1}{3}$:** For the range $0 < p < \frac{1}{3}$, there are two more first order phase boundaries apart from the ones mentioned above. The phases **F1** and **P** are separated by the first order transition line given by the equation : $(3p - 1)\Delta + (1 - p)h = \frac{1}{4}(1 + p)^2$. Another is the first order phase boundary between the phases **F** and **P** given by the equation : $p\Delta + (1 - p)h = \frac{1}{2}$. At the junction of these first order transition lines there are multi-phase coexistence points. There is one A_7 point at the junction of the **F-NM-F1-F2** phases located at ($\Delta = \frac{1}{2}$, $h = \frac{1+p}{4}$), and three A_5 points at the
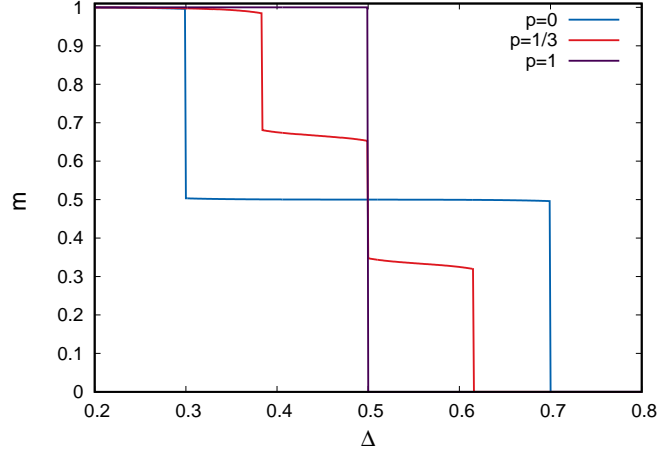
Figure 4.4: Plot of m vs Δ for $T = 0.05$ and field $h = 0.45$ for $p = 1$, $\frac{1}{3}$ and 0. The first order transition from the **F** to **NM** phase for the pure case ($p = 1$) gets replaced by two and three first order transitions for bimodal ($p = 0$) and trimodal (fixed at $p = \frac{1}{3}$) distributions respectively.

junction of **F-P-F1** phases at ($\Delta = \frac{1-p^2-2p}{4(1-2p)}$, $h = \frac{p^3+2p^2-5p+2}{4(1-2p)(1-p)}$), **F-P-F3** phases at ($\Delta = \frac{p}{2}$, $h = \frac{1+p}{2}$), and **P-F1-F2** phases at ($\Delta = \frac{1}{2}$, $h = \frac{3-p}{4}$). Fig. 4.2b shows the ground state phase diagram for $p = \frac{1}{10}$. The purple triangle represents the A_7 point and the solid black squares represent the A_5 points.

- **p = $\frac{1}{3}$** : For $0 < p < \frac{1}{3}$ regime we saw that there is always a first order transition line given by the equation $p\Delta + (1 - p)h = \frac{1}{2}$ from **F** to the **P** phase which was bounded by two A_5 points (at the junction of **P-F1-F** and **F-P-F3** phases). At exactly $p = \frac{1}{3}$, these two A_5 points coincide and become a A_7 point and the first order transition line between them vanishes. So instead of three A_5 points there are now two A_7 points and one A_5 point. The A_7 points are : one at the junction of **F-P-F1-F3** located at ($\Delta = \frac{p}{2}$, $h = \frac{1+p}{2}$) and the other at the junction of the **F-NM-F1-F2** phases located at ($\Delta = \frac{1}{2}$, $h = \frac{1+p}{4}$). The A_5 point is located at the junction of **P-F1-F2** at ($\Delta = \frac{1}{2}$, $h = \frac{3-p}{4}$). The phase boundary between the phase **F1** and phase **P** is given by the first order transition line with $h = \frac{1+p}{2}$ parallel to the Δ axis (see Fig. 4.2c).

- $\frac{1}{3} < \mathbf{p} < \mathbf{1}$: For $\frac{1}{3} < p < 1$, the **F1** phase penetrates in between the phases **F-F3** and **F3-P** and the new A_7 point now breaks into a A_6 and a A_5 point and a new first order transition line $(1 - p)(\Delta - h) = \frac{1}{4}(3p^2 - 2p - 1)$ emerges, separating the phases **F1** and **F3** as shown in Fig. 4.2d for $p = \frac{1}{2}$. The red square represents the A_6 point and it is located at $(\Delta = \frac{1-p}{4}, \ h = \frac{1+p}{2})$, at the junction of **F-F3-F1** phases and the new A_5 point is located at $(\Delta = \frac{p}{2}, \ h = \frac{1+5p}{4})$ at the junction of **P-F3-F1** phases. The phases **F1** and **P** are again separated by the first order transition line $(3p - 1)\Delta + (1 - p)h = \frac{1}{4}(1 + p)^2$.

$\underline{p = 0}$ **: Bimodal RFBC**

For the bimodal distribution $(p = 0)$ there are four phases in the ground state. One ordered **F**, one **NM** and one **P** phase. Another ordered phase emerges for high values of h and Δ. The phases **F1** and **F2** become equal and becomes a single phase. We call this **F1=F2** phase. The first order transition lines separating these phases are similar to the ones described in the Subsection 4.3.1. There are two A_5 points at $(\Delta = \frac{1}{2}, \ h = \frac{1}{4})$ and $(\Delta = \frac{1}{4}, \ h = \frac{1}{2})$ at the junction of **NM-F-(F1=F2)** and **F-P-(F1=F2)** phases respectively (see Fig. 4.2e).

4.3.2 Gaussian distribution

For the Gaussian distribution on the other hand the phase diagram is rather simpler. The $T = 0$ rate function for RFBC is :

$$
\begin{aligned}
\Phi(m) \ = \ & \frac{m^2}{2} - \frac{m}{2}\left(\text{erf}\left(\frac{m + \Delta}{\sqrt{2}\sigma}\right) - \text{erf}\left(\frac{-m + \Delta}{\sqrt{2}\sigma}\right) \right) \\
+ \ & \frac{\Delta}{2}\left(2 - \text{erf}\left(\frac{-m + \Delta}{\sqrt{2}\sigma}\right) - \text{erf}\left(\frac{m + \Delta}{\sqrt{2}\sigma}\right) \right) \\
- \ & \frac{\sigma}{\sqrt{2\pi}}\left(\exp\left[-\frac{(-m + \Delta)^2}{2\sigma^2}\right] + \exp\left[-\frac{(m + \Delta)^2}{2\sigma^2}\right] \right)
\end{aligned}
$$

$$(4.15)$$

Here erf$(x) = \frac{2}{\sqrt{\pi}} \int_0^x e^{-t^2} dt$ is the error function. The $\min_m \Phi(m)$ gives the disorder averaged ground state energy. The expression of magnetization (m) and quadrupole moment (q) from Eq. 4.11 and Eq. 4.12 after taking $\beta \to \infty$ limit are

$$m = \frac{1}{2} \left(\text{erf} \left(\frac{m + \Delta}{\sqrt{2}\sigma} \right) - \text{erf} \left(\frac{-m + \Delta}{\sqrt{2}\sigma} \right) \right) \tag{4.16}$$

$$q = \frac{1}{2} \left(2 - \text{erf} \left(\frac{m + \Delta}{\sqrt{2}\sigma} \right) - \text{erf} \left(\frac{-m + \Delta}{\sqrt{2}\sigma} \right) \right) \tag{4.17}$$

We find that there is one ordered phase with $m \neq 0$ and one disordered phase with $m = 0$. The quadrupole moment q changes continuously from $q = 1$ to $q = 0$ as Δ goes from 0 to ∞. Thus there is no transition in q. On expanding Eq. 4.15 around $m = 0$, we get

$$\Phi(m) = a_2^0 m^2 + a_4^0 m^4 + a_6^0 m^6 + a_8^0 m^8 + ... \tag{4.18}$$

where,

$$
\begin{aligned}
a_2^0 &= \frac{-\sqrt{2}e^{\frac{-\Delta^2}{2\sigma^2}} + \sqrt{\pi}\sigma}{2\sqrt{\pi}\sigma} \\
a_4^0 &= -e^{\frac{-\Delta^2}{2\sigma^2}} \frac{(\Delta^2 - \sigma^2)}{12\sqrt{2\pi}s^5} \\
a_6^0 &= -e^{\frac{-\Delta^2}{2\sigma^2}} \frac{(\Delta^4 - 6\Delta^2\sigma^2 + 3\sigma^4)}{360\sqrt{2\pi}s^9} \\
a_8^0 &= -e^{\frac{-\Delta^2}{2\sigma^2}} \frac{(\Delta^6 - 15\Delta^4\sigma^2 + 45\Delta^2\sigma^4 - 15\sigma^6)}{20160\sqrt{2\pi}s^{13}}
\end{aligned}
\tag{4.19}
$$

This expansion can be used to determine the continuous transitions in the system. The line of second order transition is given by $a_2^0 = 0$, provided $a_4^0 > 0$. This gives the line of

(a) $0 \leq h < 0.257$

(b) $0.257 \leq h < 0.275$

(c) $0.275 \leq h < 0.452$

(d) $0.452 \leq h < 0.476$

(e) $0.476 \leq h < 0.5275$

(f) $0.5275 \leq h < 0.5281$

(g) $0.5281 < h < 0.725$

(h) $h > 0.725$
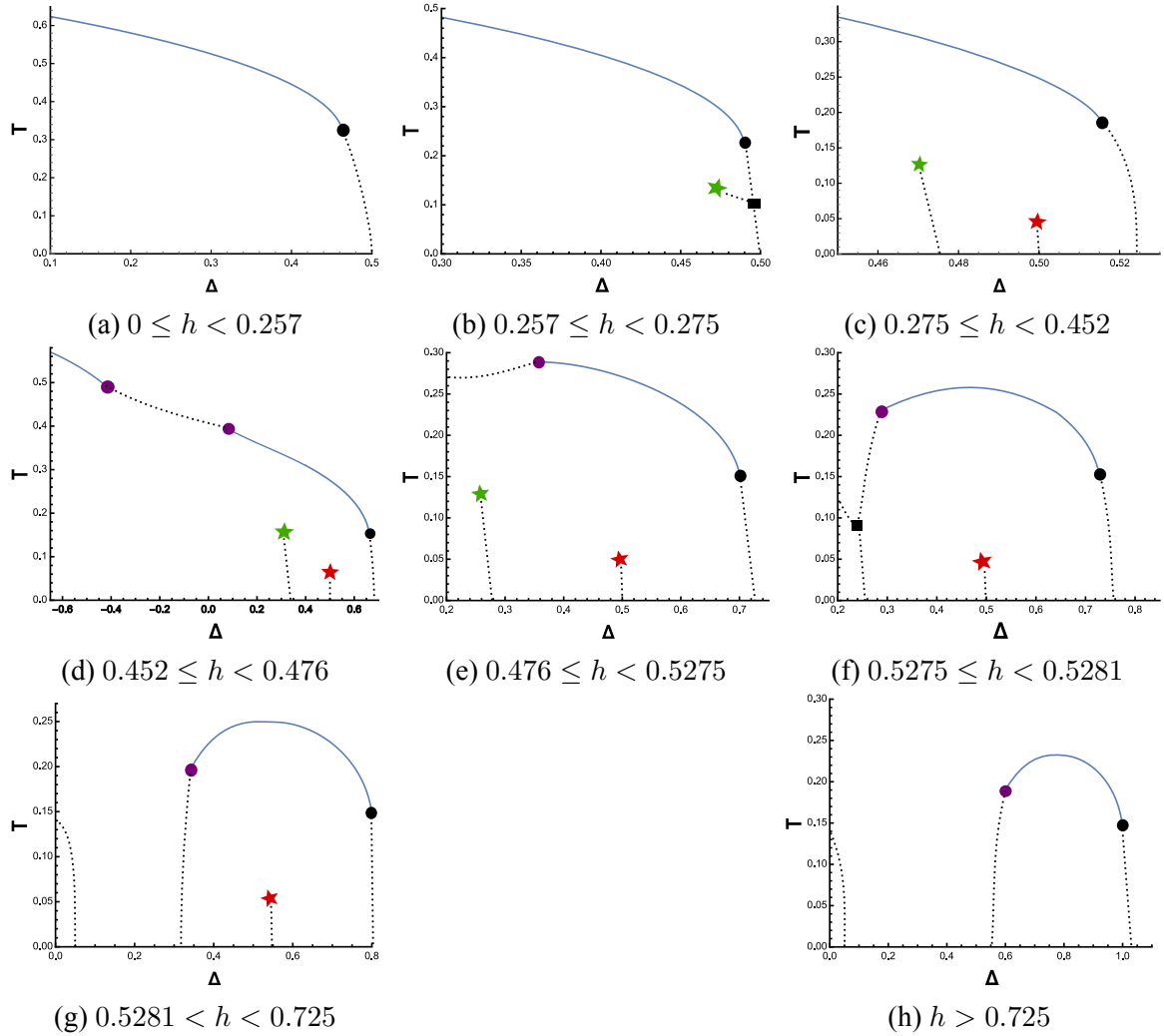
Figure 4.5: $T - \Delta$ phase diagram for different ranges of h for $p = \frac{1}{10}$. The solid line is the loci of continuous transitions and the dotted line is the loci of first order transitions, solid stars are the BEPs, solid circles are the TCPs, solid squares are the A_5 points. There are eight different phase diagrams depending on the range of h.
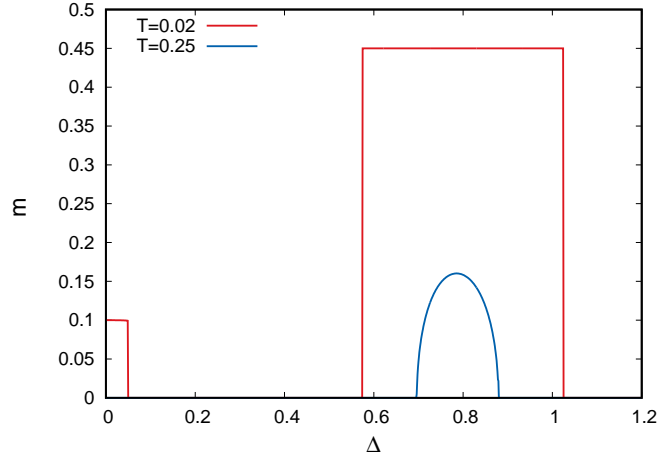
Figure 4.6: Plot of the magnetization (m) as a function of Δ corresponding to the Fig. for $p = \frac{1}{10}$ at a fixed $h = 0.8$ at two different temperatures. At $T = 0.25$ the magnetization shows two continuous transitions, first from **P** phase to **F2** and then to the **NM** phase. At $T = 0.02$, for low Δ there is an ordered phase (**F3**) due to the presence of p fraction of magnetic spins. As Δ increases, the phase undergoes a first order transition to **P** phase. The phase **P** again undergoes a first order transition to **F2** phase which is separated from the **NM** phase by another first order transition line.

continuous transition to be

$$\sigma_c = \sqrt{\frac{2}{\pi}} \exp\left(\frac{-\Delta_c^2}{2\sigma_c^2} \right) \tag{4.20}$$

This is valid as long as $a_4^0 > 0$. For $a_4^0 \leq 0$ we cannot ignore higher order terms in Eq. 4.18. We find $a_2^0 = a_4^0 = 0$ at $\sigma_{TCP} = \Delta_{TCP} = \sqrt{\frac{2}{e\pi}} = 0.483941$. Since $a_6^0 > 0$ at this point, this is a tricritical point(TCP). It is shown in Fig. 4.3 by a solid circle. So the transition is second order for $\sigma_{TCP} < \sigma \leq 1$. For $\sigma < \sigma_{TCP}$, $a_4^0 < 0$ and the three phases coexist. The transition becomes first order for $0 \leq \sigma < \sigma_{TCP}$ and the transition line can be found by equating the free energy and its first derivatives w.r.t m on both sides. For $\sigma \to 0$, the first order transition line cuts the Δ axis at $\Delta = \frac{1}{2}$. The phase diagram is shown in Fig. 4.3.

4.4 Finite temperature phase diagrams

We observed that the ground state phase diagram are completely different for different symmetric distribution. In this Section we discuss about the finite temperature phase diagram for both the distributions.

4.4.1 Trimodal distribution

We saw that for $T = 0$, there were five different phase diagrams depending on the value of p. One interesting and non-trivial part of the phase diagram was the presence of multiple ordered phases separated by first order transition lines. For finite temperature, the model exhibits phase diagrams which show re-entrance and multiple phase transitions between the ordered phases. We find that the phase diagrams can be classified into five categories just like for $T = 0$. At finite temperature, multiple first order transition lines emerge separating the different ordered phases discussed in Sec. 4.3.1. At low temperatures, the system undergoes two and three first order transitions as a function of both Δ and h for bimodal ($p = 0$) and trimodal ($0 < p < 1$) distributions respectively (see Fig. 4.4 as a function of Δ). Also, the system exhibits multiple TCPs. The origin of two of them is easy to understand. One corresponds to the TCP present in the pure Blume-Capel model and the second one is the $\Delta \to -\infty$ TCP present in the RFIM with bimodal distribution. Besides these two other TCPs appear in the model. It also has BEPs and CEPs and nth order coexistence points denoted by A_n.

The magnetization in the system satisfies the fixed point equation $\frac{\partial f(m)}{\partial m} = 0$, where $f(m)$ is the functional given by Eq. 4.13. This gives the following self-consistent equation for m

$$\frac{m}{a} = \frac{1-p}{2} \left(\frac{y^2 x^2 - 1}{yx + ay^2 x^2 + a} + \frac{x^2 - y^2}{xy + ax^2 + ay^2} \right) + p \frac{x^2 - 1}{x + ax^2 + a} \qquad (4.21)$$

(a) $-\infty < \Delta \leq 0.05$

(b) $0.05 < \Delta \leq 0.238$

(c) $0.238 < \Delta < 0.247$

(d) $0.247 \leq \Delta < \ln 4/3$

(e) $\ln 4/3 \leq \Delta \leq 0.493$

(f) $0.493 < \Delta < \frac{1}{2}$

(g) $\Delta > \frac{1}{2}$
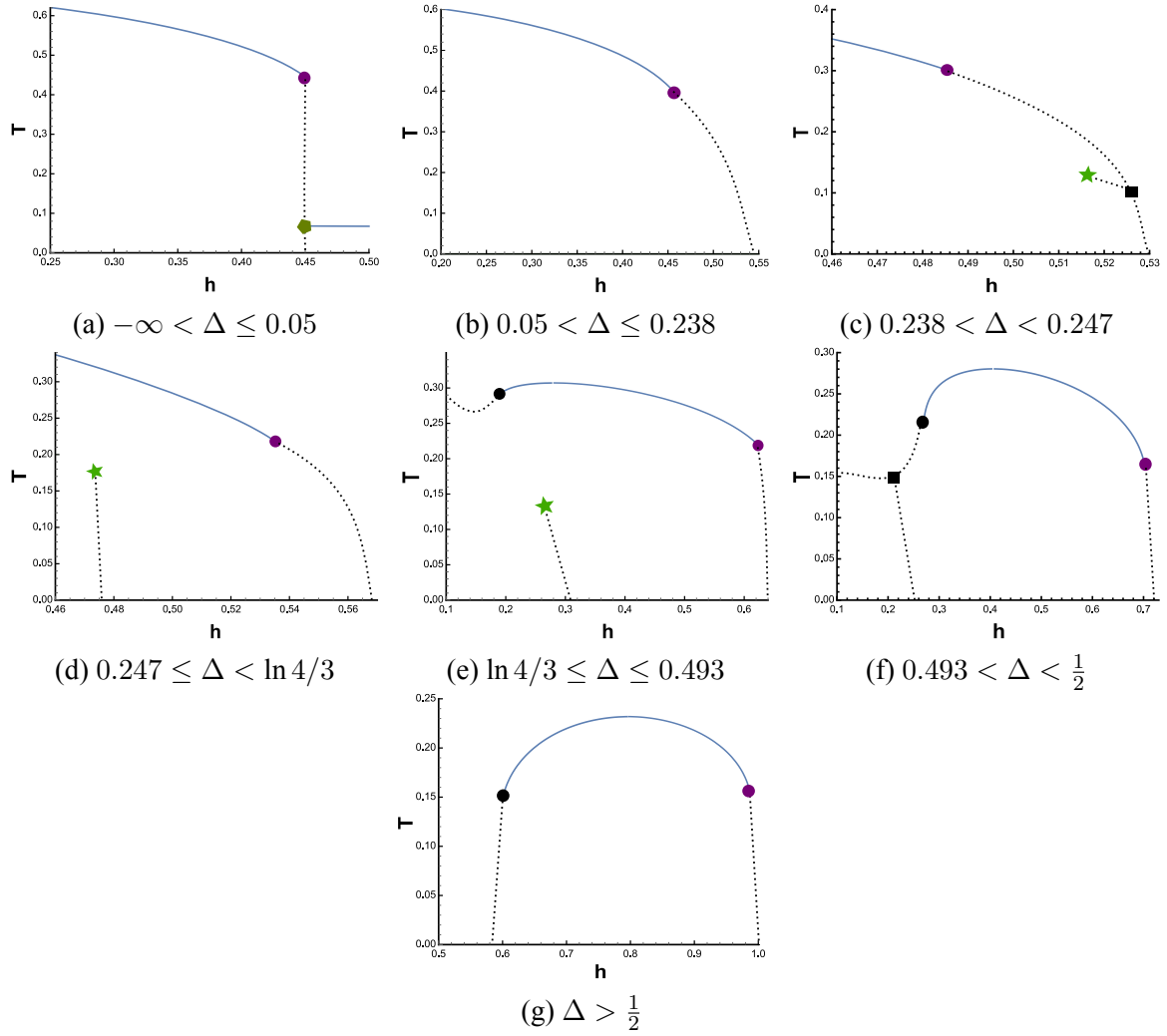
Figure 4.7: $T - h$ phase diagram for different regimes of Δ for $p = \frac{1}{10}$. The solid line is the line of second order transitions, the dotted lines are lines of first order transition, solid stars are the BEPs, solid circles are the TCPs, solid squares are the A_5 points and green circles are CEPs. There are seven different phase diagrams depending on the range of Δ.
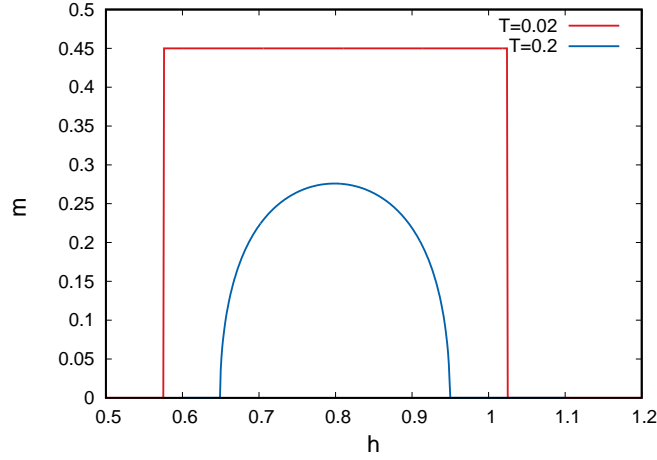
Figure 4.8: Plot of the magnetization (m) as a function of h corresponding to the Fig. at $\Delta = 0.8$ and $p = \frac{1}{10}$ at two different temperatures. At $T = 0.2$ the magnetization undergoes two second order transitions, **NM** to **F2** phase and **F2** to **P** phase. At $T = 0.02$, the magnetization shows two first order jumps.

here $a = e^{-\beta\Delta}$, $x = e^{\beta(m+H)}$ and $y = e^{\beta h}$.

Linearizing Eq. 4.21 around $m = 0$, we get the line of continuous transition as

$$\frac{1}{2\beta} = \frac{ap}{2a+1} + \frac{(1-p)a(2a+z_1)}{(1+2az_1)^2} \tag{4.22}$$

where $z_n = \cosh n\beta h$. This equation is valid only as long as the coefficients of the third order term in the expansion of Eq. 4.21 in powers of m is positive.

At TCP the line of continuous transitions (known as the λ line) given by Eq. 4.22 meets the two other lines of continuous transitions in the $T - \Delta - H$ space [162, 213]. These are the $\lambda_{\pm}$ lines. At a TCP the λ, λ_+ and λ_- lines meet in the $T - \Delta$ plane. TCP is also the end point of the λ line given by equating the second and fourth coefficient to zero in the power series expansion of $f(m)$ for $H = 0$. The BEP occurs when the λ_+ and λ_- lines do not meet the λ line, and instead meet at a point in the ordered region in the $T - \Delta$ plane. In order to locate the BEP we use the general condition of criticality by equating the first three derivatives of the free energy to zero ($f'(m) = f''(m) = f'''(m) = 0$) along with the condition, $f''''(m) > 0$. We get the following two equations by equating $f''(m) = 0$ and

$f'''(m) = 0$ respectively

$$\frac{1-p}{2}\left(\frac{4ayx+y^2x^2+1}{(yx+ay^2x^2+a)^2} + \frac{4axy+x^2+y^2}{(xy+ax^2+ay^2)^2}\right)y + p\,\frac{4ax+x^2+1}{(x+ax^2+a)^2} = \frac{1}{\beta ax}$$

$$(4.23)$$

$$\frac{1-p}{2}\left(\frac{(xy-8a^2yx-ay^2x^2-a)(x^2y^2-1)}{(yx+ay^2x^2+a)^3} + \frac{(xy-8a^2yx-ax^2-ay^2)(x^2-y^2)}{(yx+ax^2+ay^2)^3}\right)y$$
$$+p\,\frac{(x-8a^2x-ax^2-a)(x^2-1)}{(x+ax^2+a)^3} = 0$$

$$(4.24)$$

Numerically solving Eq.4.21, Eq.4.23 and Eq.4.24 simultaneously for T, Δ and h by taking $H = 0$ we find the coordinates of the point of intersection of the $\lambda_\pm$ lines. If $m = 0$ at the point of intersection, then it is a TCP, else it is a BEP.

We have studied the entire range of p and we find many different phases, depending on the values of T, Δ and h. We give the details of all possible phase diagrams in this section.

Phase diagram of pure Blume-Capel model : $p = 1$

The phase diagram of the pure Blume-Capel model in the $T - \Delta$ plane is well known . It is similar to Fig. 4.3 , with $x-$axis being the temperature T. There is a line of second order transition which meets the line of first order transition at a TCP ($T_{BC} = \frac{1}{3}, \ \Delta_{BC} = \frac{\ln 4}{3}$). The first order transition line continues till $T = 0$, with the first order transition at $\Delta = \frac{1}{2}$ for $T = 0$.

Phase diagrams for $p = \frac{1}{10}$

Fig. 4.5 shows different phase diagrams in the $T - \Delta$ plane for different ranges of h for $p = \frac{1}{10}$. There are eight different phase diagrams depending on the value of h. For $0 \leq$

(a) $0 \leq h < 0.325$

(b) $0.325 \leq h < 0.33$

(c) $0.33 \leq h < 0.333$

(d) $0.333 \leq h < 0.6079$

(e) $0.6079 \leq h \leq 0.63$

(f) $0.63 < h < 0.658$

(g) $0.658 \leq h < 0.66$

(h) $0.66 \leq h < 0.666$

(i) $h > 0.666$
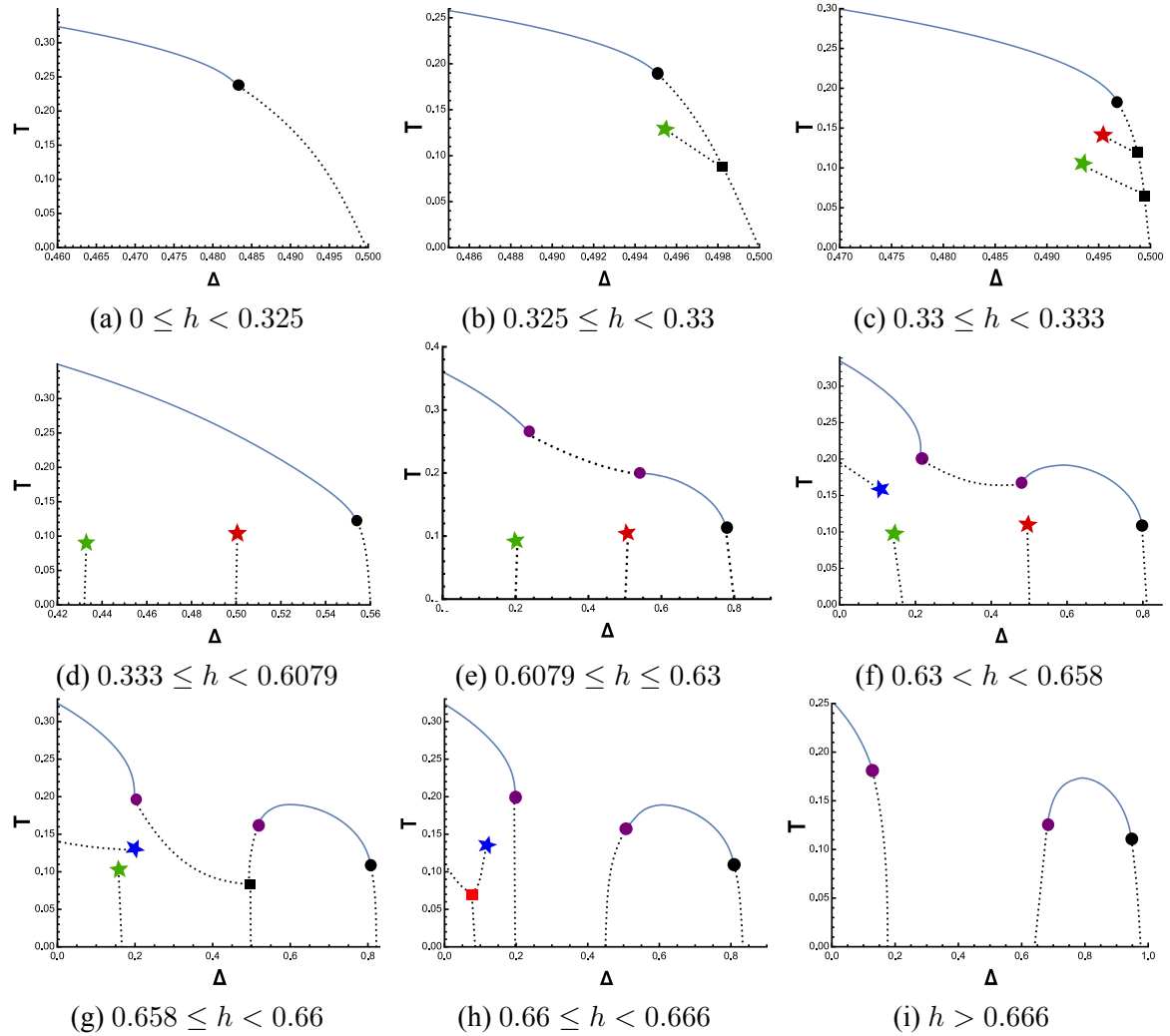
Figure 4.9: $T - \Delta$ phase diagram for different regions of h for $p = \frac{1}{3}$. The solid line are the lines of second order transitions, the dotted lines are the lines of first order transitions, solid stars are the BEPs, solid circles are the TCPs and solid squares are the A_5 points. There are nine different phase diagrams depending on the range of h.
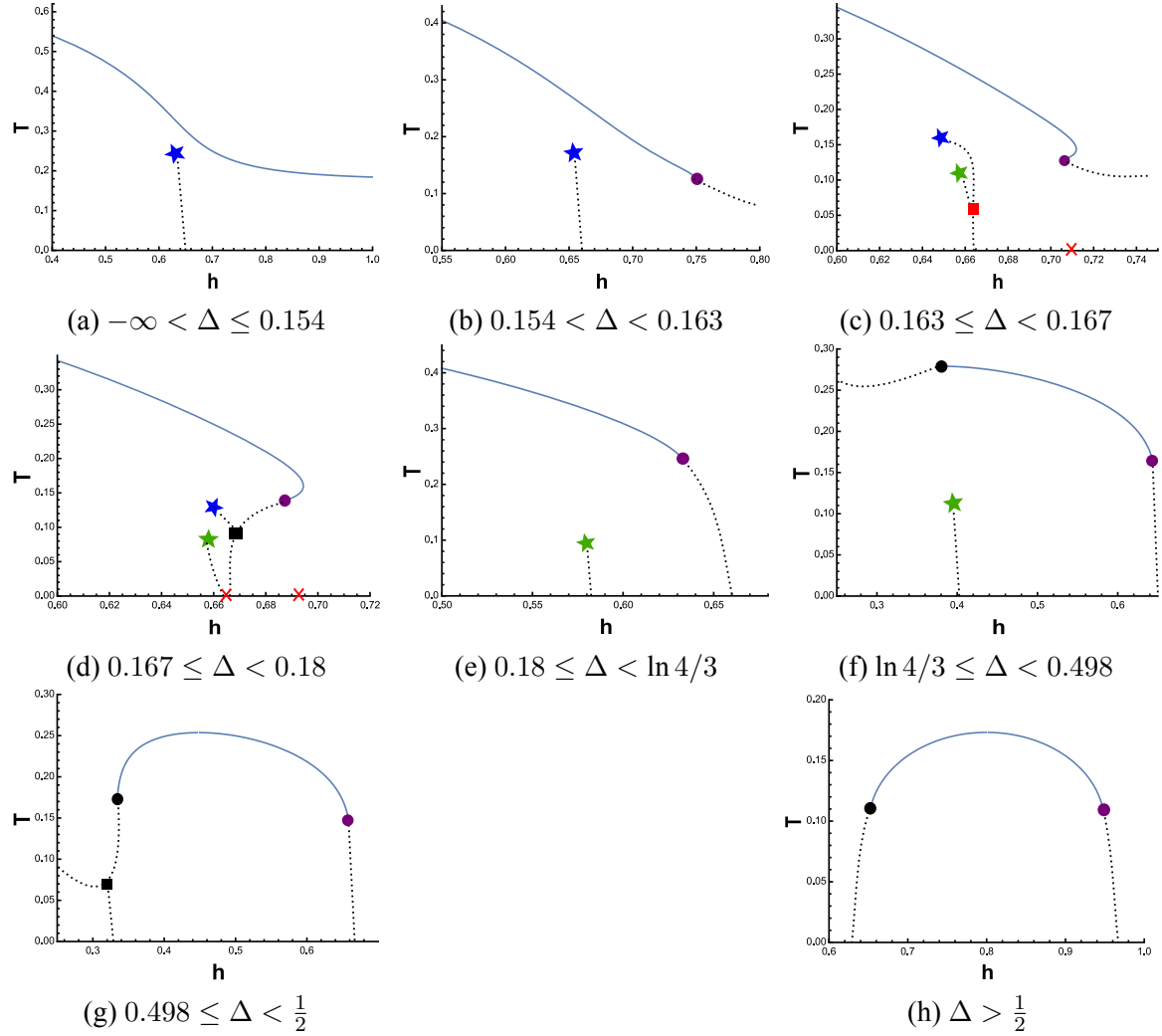
Figure 4.10: $T - h$ phase diagram for different regimes of Δ for $p = \frac{1}{3}$. The solid lines are the lines of second order transitions, the dotted lines are first order transitions, the solid stars are the BEPs, the solid circles are the TCPs, solid squares are the A_5 points and red squares are the A_6 points. There are eight different phase diagrams depending on the range of Δ.

$h < 0.257$, the phase diagram is similar to the pure model (see Fig. 4.5a). As h increases, new multicritical points arise. For $0.257 \le h < 0.275$, another first order transition line emerges (shown by dotted lines) separating **F-F1** phases, which ends at a BEP. The two first order transition lines meet at a A_5 point (Fig. 4.5b). For $0.275 \le h < 0.452$, the phase diagram consists of three first order transition lines separating **F-F1**, **F1-F2** and **F2-NM** phases respectively as Δ increases (see Fig. 4.5c). For $0.452 \le h < 0.476$ (shown in Fig. 4.5d), the λ line (shown by a continuous line) separates into two parts, which are connected by a first order transition line. This gives rise to three TCPs in the system. As we increase h further, one of the TCP vanishes and the phase diagram consists of two TCPs and two BEPs (see Fig. 4.5e). For $0.5275 \le h < 0.5281$ one of the BEP gets replaced by a A_5 point (Fig. 4.5f).

At $\Delta = 0.5281$ the A_5 point moves to $T = 0$ and the phase diagram divides into two parts. The ordered phase **F3** exists for small Δ. And for large Δ the phases **F1** and **F2** are separated by a first order transition line which ends at a BEP. These phases are bounded by the two disordered phases : for higher Δ the phase is **NM** and the intermediate disordered phase between the two parts is **P** (Fig. 4.5g). For $h > 0.725$, the BEP vanishes and the phase diagram contains two TCPs (see Fig. 4.5h). The plot of the magnetization for Fig. 4.5h is shown in Fig. 4.6.

The $T - h$ phase diagrams for different values of Δ are shown in Fig. 4.7. There are seven different phase diagrams depending on the value of Δ. For $-\infty < \Delta < 0.05$, the phase diagram consists two lines of continuous transition, a TCP and a CEP. The **F3** phase occurs at low T bounded by a line of second order transitions. This second order transition line meets the first order transition line at a CEP (shown in Fig. 4.7a). CEP is a point where a second order transition line abruptly terminates onto a first order transition line. As Δ increases, the CEP vanishes (Fig. 4.7b). On increasing Δ further, a first order transition line arises separating **F-F1** phases and ends at a BEP (Fig. 4.7c,). At exactly

(a) $0 \le h < 0.374$

(b) $0.374 \le h < 0.378$

(c) $0.378 \le h < 0.4$

(d) $0.4 \le h < 0.577$

(e) $0.577 \le h \le 0.6$

(f) $0.6 \le h < 0.625$

(g) $0.625 \le h < 0.875$

(h) $h > 0.875$
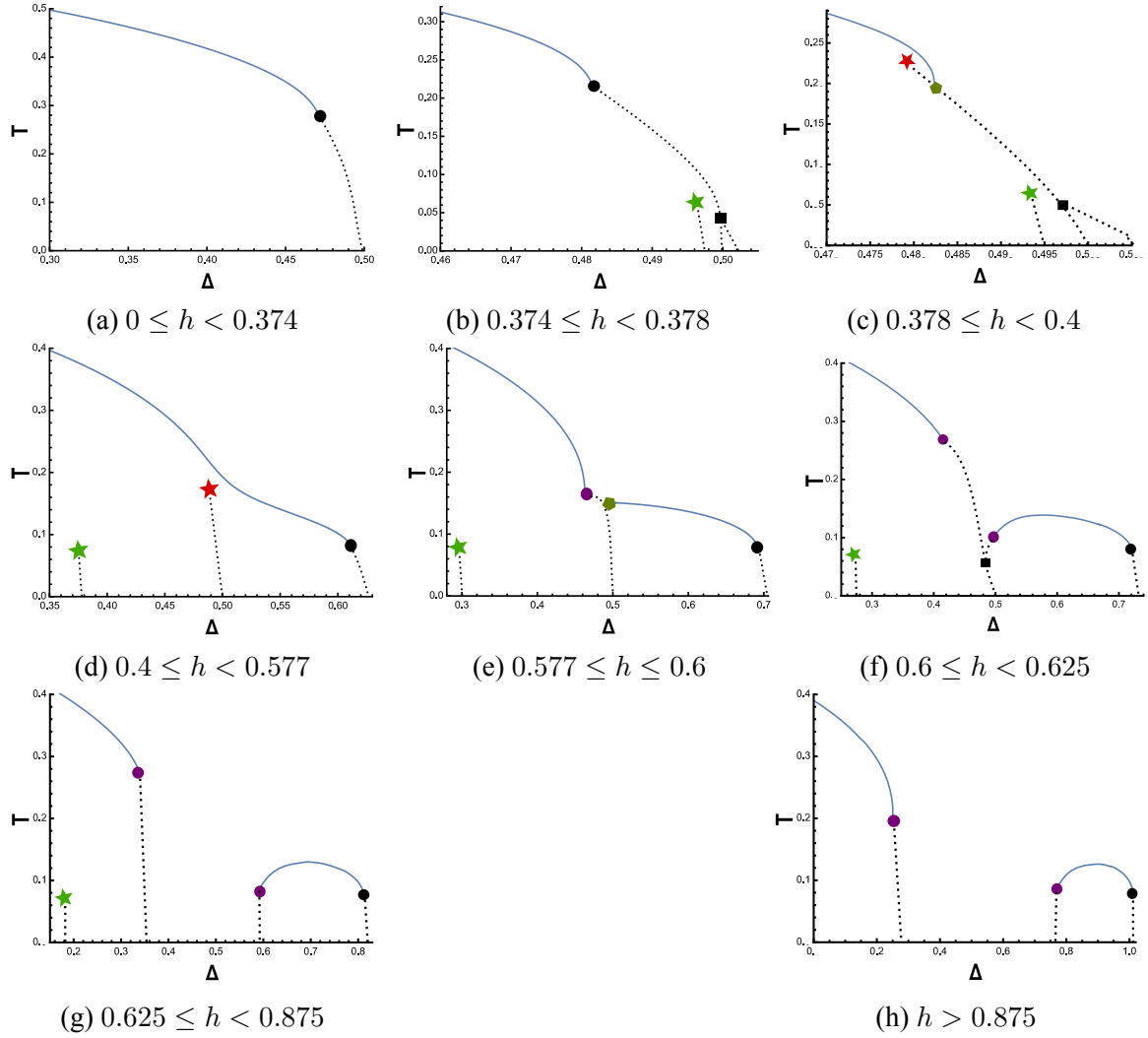
Figure 4.11: $T - \Delta$ phase diagram for different regimes of h for $p = \frac{1}{2}$. The solid line is the line of second order transition, the dotted lines are first order transitions, the solid stars are the BEPs, solid circles are the TCPs, black solid squares are the A_5 points and green circles are the CEPs. There are eight different phase diagrams depending on the range of h.

$\Delta = \Delta_{BC} = \ln 4/3$, another TCP emerges at $\beta = 3$ and $h = 0$, corresponding to the TCP of the pure model. For $\Delta_{BC} \leq \Delta \leq 0.493$, there are two TCPs and one BEP (see Fig. 4.7d). As Δ increases further, the BEP turns into a A_5 point (Fig. 4.7e).

Fig. 4.7f is the phase diagram for $\Delta > 0.5$. There is only one ordered phase **F2** which exists for high values of h. This phase is separated from the two disordered phases by two first order transition lines with **P** phase for higher h and **NM** phase for lower h. The behaviour of the magnetization for some fixed values of T along the h axis is shown in Fig. 4.8.

For all $p < \frac{1}{3}$ we find similar phase diagrams. Although, depending on p, the exact location of the transitions for different phase diagram changes.

Phase diagrams for $p = \frac{1}{3}$

Fig. 4.9 shows the different phase diagrams in the $T - \Delta$ plane for different ranges of h for $p = \frac{1}{3}$. There are now nine different phase diagrams. Four of the phase diagrams (Fig. 4.9a, Fig. 4.9b, Fig. 4.9d and Fig. 4.9e) are similar to the phase diagrams for $p = \frac{1}{10}$ (Fig. 4.5a - Fig. 4.5d). In the intermediate values of h between Fig. 4.9b and Fig. 4.9d, the phase diagram has three first order lines, two of them are inside the ordered region separating the phases **F-F1** and **F1-F2**. These two lines start at different A_5 points and end at two different BEPs (see Fig. 4.9c). For $0.63 < h < 0.658$, the phase diagram consists of three BEPs and two TCPs, see Fig. 4.9f. As h increases, one BEP turns into a A_5 point (Fig. 4.9g) and as h increases further another BEP turns into a A_6 point (Fig. 4.9h). Finally, for all $h > \frac{2}{3}$, there is always an ordered phase **F2** for large Δ separated from the disordered phases by two first order transition lines, and another ordered phase **F3** for small Δ. Thus there are three TCPs in this range of h (see Fig. 4.9i).

Similarly, the projection of the phase diagrams in the $T - h$ plane can be divided into eight categories depending on the ranges of Δ, shown in Fig. 4.10. Four of the phase
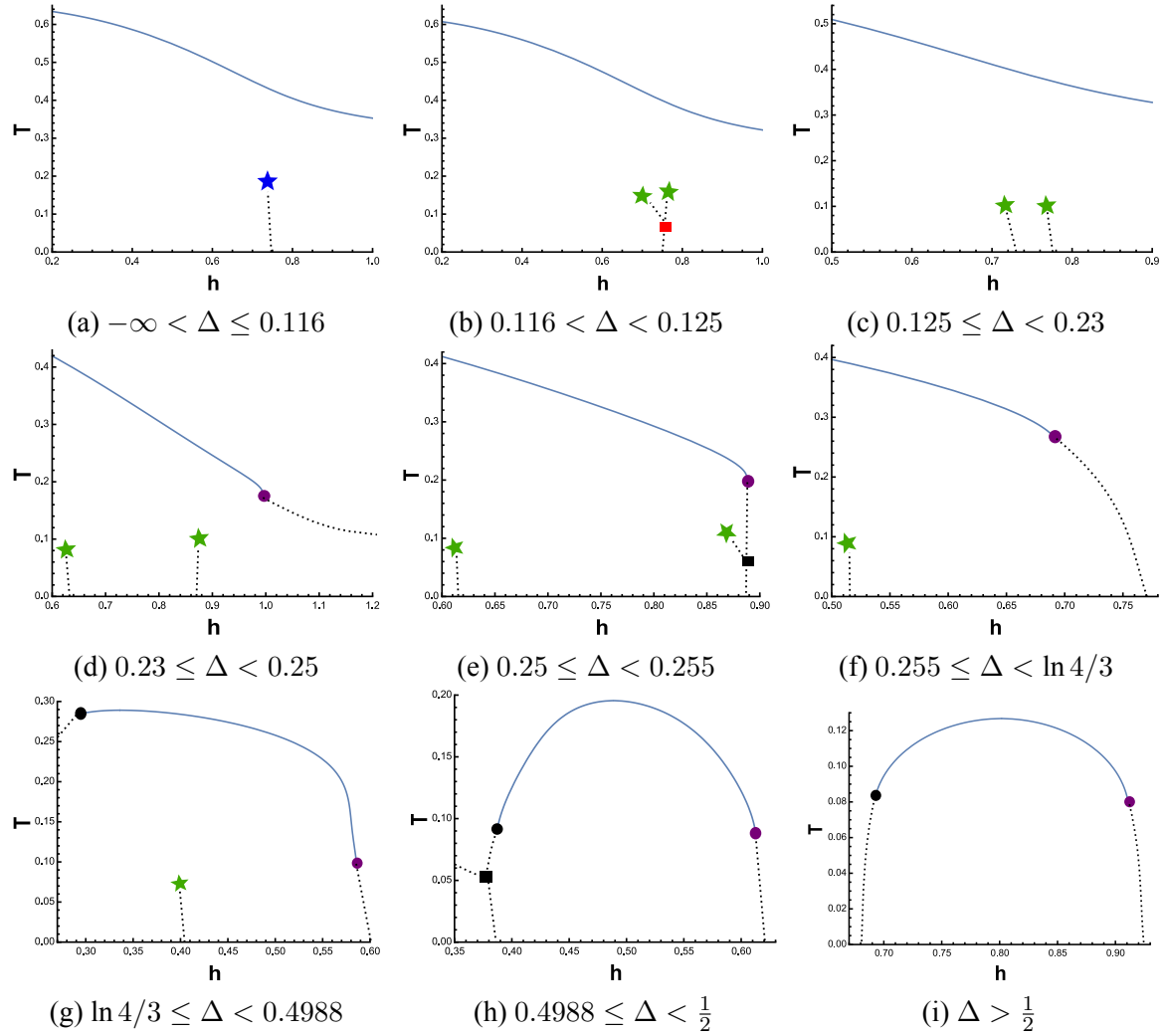
Figure 4.12: $T-h$ phase diagram for different regimes of h for $p = \frac{1}{2}$. The solid line is the line of second order transitions, dotted lines are the lines of first order transitions, solid stars are the BEPs, solid circles are the TCPs, black squares are the A_5 points and red squares are the A_6 points. There are nine different phase diagrams depending on the range of Δ.

(a) $0 \leq h < 0.2382$

(b) $0.2382 \leq h < 0.25$

(c) $0.25 \leq h < 0.414$

(d) $0.414 \leq h < 0.4389$

(e) $0.4389 \leq h < 0.4927$

(f) $0.4927 \leq h < 0.5$

(g) $h > 0.5$
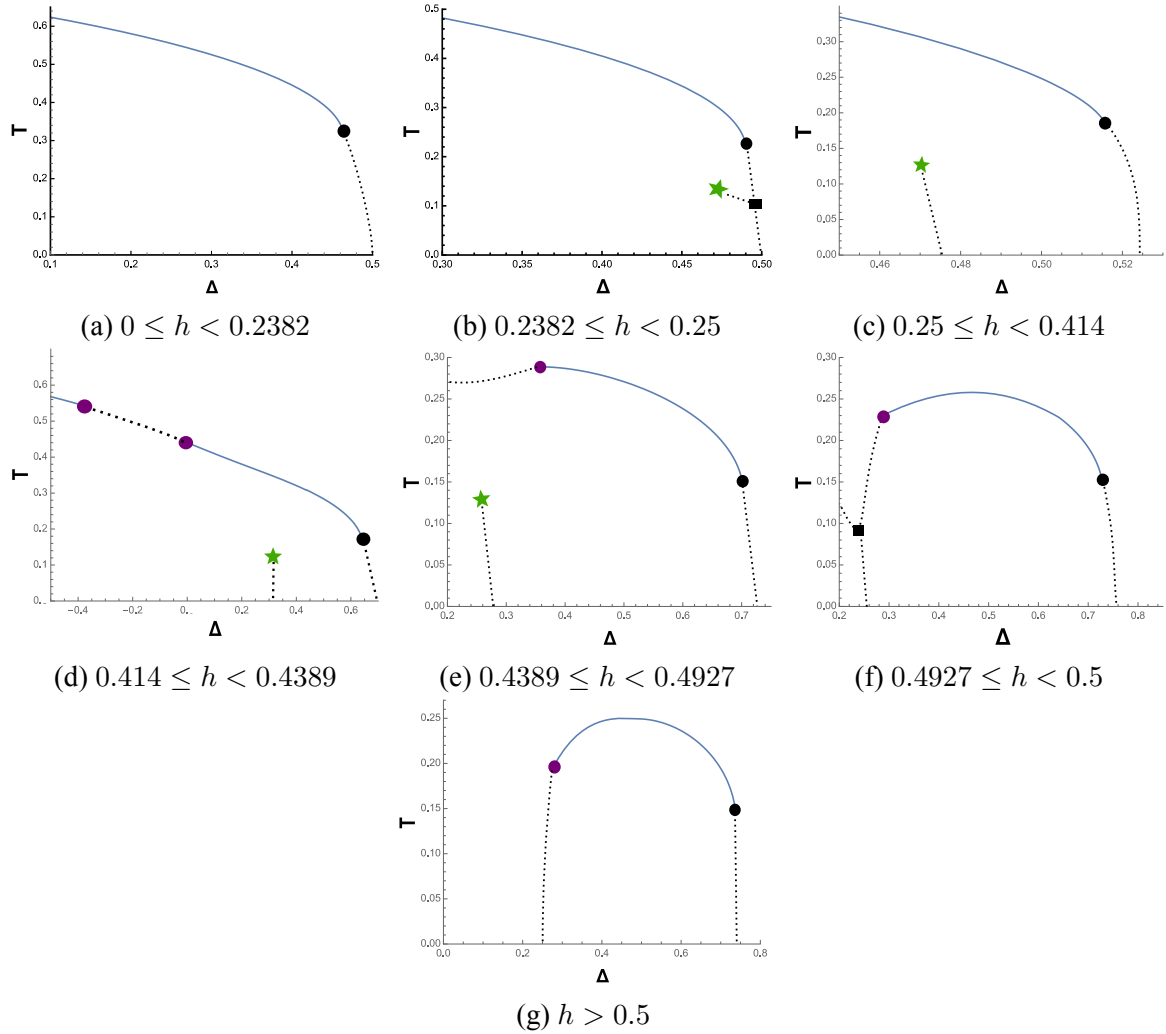
Figure 4.13: $T - \Delta$ phase diagram for different ranges of h for $p = 0$. The solid line is the loci of continuous transitions and the dotted line is the loci of first order transitions, solid stars are the BEPs, solid circles are the TCPs, solid square is the A_5 point. There are seven different phase diagrams depending on the range of h.

diagrams (Fig. 4.10e, Fig. 4.10f, Fig. 4.10g and Fig. 4.10h) are similar to the $T - h$ phase diagrams of the $p = \frac{1}{10}$ case (Fig. 4.7d, Fig. 4.7e, Fig. 4.7f and Fig. 4.7g). For $-\infty < \Delta \leq 0.154$, there is one first order transition line separating **F-F3** phases ending at a BEP. The **F3** phase exists for all values of h (Fig. 4.10a). For $0.154 < \Delta < 0.163$, a TCP arises (Fig. 4.10b). For $0.163 \leq \Delta < 0.167$ another first order transition line appears separating **F1-F3** phases, and the two first order transition lines meet at a A_6 point, see Fig. 4.10c. As Δ increases further, two of the first order transition lines meet at a A_5 point and the phase diagram now has no ordered phases at low T for high values of h (Fig. 4.10d).

We find re-entrance in the phase diagrams shown in Fig. 4.10c and Fig. 4.10d. We have studied the magnetization, susceptibility, free energy and specific heat in the re-entrance region. The details are given in Sec. 4.5.

Phase diagrams for $p = \frac{1}{2}$

The Fig. 4.11 shows the different phase diagrams in the $T - \Delta$ plane for different ranges of h for $p = \frac{1}{2}$. There are eight different phase diagrams depending on the ranges of h. Three of them, Fig. 4.11a, Fig. 4.11d and Fig. 4.11e are similar to the $T - \Delta$ phase diagrams of $p = \frac{1}{3}$ (Fig. 4.9a, Fig. 4.9d and Fig. 4.9i). For $0.375 < h < 0.378$, there are three first order transition lines separating **F-F1**, **F1-F2** and **F2-NM** phases. The phase diagram contains one BEP, one TCP and one A_5 point (Fig. 4.11b). As h increases, the TCP breaks into a CEP and a BEP. Thus there are two BEPs, one A_5 point and one CEP for $0.378 \leq h < 0.4$ (see Fig. 4.11c). For $0.4 \leq h < 0.577$, the CEP and the A_5 point vanish (Fig. 4.11f) and a TCP emerges. For $0.577 \leq h \leq 0.6$, the second order transition line breaks into two parts and one BEP turns into a new TCP and a CEP (Fig. 4.11g). For $0.6 \leq h < 0.625$, the CEP breaks up into another TCP and a A_5 point and there are three TCPs, one BEP and one A_5 point in the phase diagram (Fig. 4.11h).

In the $T - h$ plane projection (Fig. 4.12), there are nine different phase diagrams de-

pending on the ranges of Δ. Six of them (Fig. 4.12a and Fig. 4.12e - 4.12i) are similar to the $T - h$ phase diagrams for $p = \frac{1}{3}$ (Fig. 4.10a and Fig. 4.10d - Fig. 4.10h). For $0.116 < \Delta < 0.125$, another first order transition line appears and the phase diagram consists of two BEPs and one A_6 point, see Fig. 4.12c. For $0.23 \leq \Delta < 0.25$ one TCP emerges. Thus there are two BEPs and one TCP, see Fig. 4.12d.

Phase diagrams for $p = 0$

The bimodal distribution has been previously studied for the $T - h$ plane and the $T - \Delta$ plane in [205] and [206] respectively. In [206] the $T - \Delta$ plane phase diagram was reported for some distinct values of h. In Fig. 4.13 we show the $T - \Delta$ phase diagram for $p = 0$. There are seven different phase diagrams depending on the values of h. We re-obtain the five phase diagrams mentioned in [206] shown in Fig. 4.13a, Fig. 4.13c, Fig. 4.13e - 4.13g. We find two additional phase diagrams, one for $0.2382 \leq h < 0.25$ similar to Fig. 4.13b and another for $0.414 \leq h < 0.4389$ as shown in Fig. 4.13d, consist of three TCPs and one BEP. The phase diagram in Fig. 4.13d appears due to the non-monotonic behaviour of the locus of TCP. We will discuss this further in Sec. 4.6.

We find that, in the $T - h$ plane there are six different phase diagrams depending on the values of Δ shown in Fig. 4.14. Five of these phase diagrams Fig. 4.14a, Fig. 4.14c - 4.14f are similar as reported in [205]. In addition we find that for $0.244 < \Delta < 0.25$, there is a phase diagram shown in Fig. 4.14b. These phase diagrams are similar to Fig. 4.7b - 4.7g for $p = \frac{1}{10}$ in the $T - h$ plane.

4.4.2 Gaussian distribution

Unlike the trimodal case, the phase diagrams in $T - \Delta$ and $T - h$ plane for Gaussian distribution contain only one TCP.

Free energy functional for the Gaussian distribution at $H = 0$ is,

(a) $0.0 < \Delta \leq 0.244$

(b) $0.244 < \Delta < 0.25$

(c) $0.25 \leq \Delta < \ln 4/3$

(d) $\ln 4/3 \leq \Delta \leq 0.4929$

(e) $0.4929 < \Delta < \frac{1}{2}$

(f) $\Delta > \frac{1}{2}$
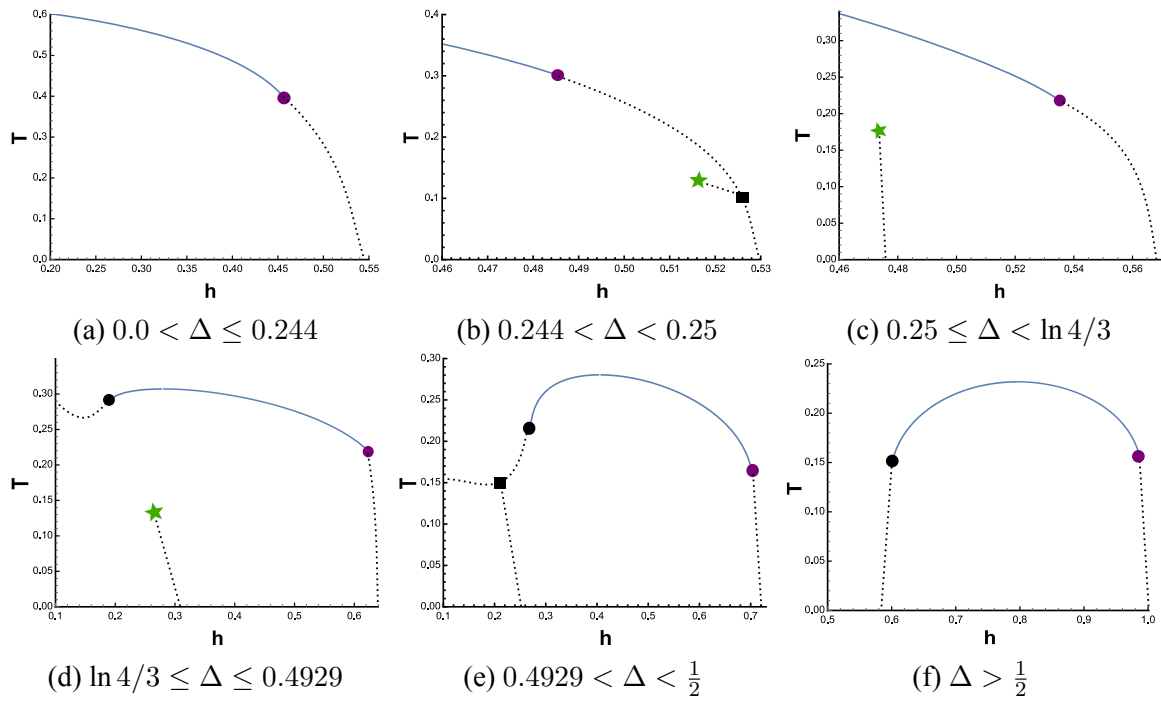
Figure 4.14: $T - h$ phase diagram for different regimes of Δ for $p = 0$. The solid line is the line of second order transitions, the dotted lines are lines of first order transition, solid stars are the BEPs, solid circles are the TCPs, and solid squares are the A_5 points. There are six different phase diagrams depending on the range of Δ.

(a) $\Delta = 0.3$ (b) $\Delta = 0.465$
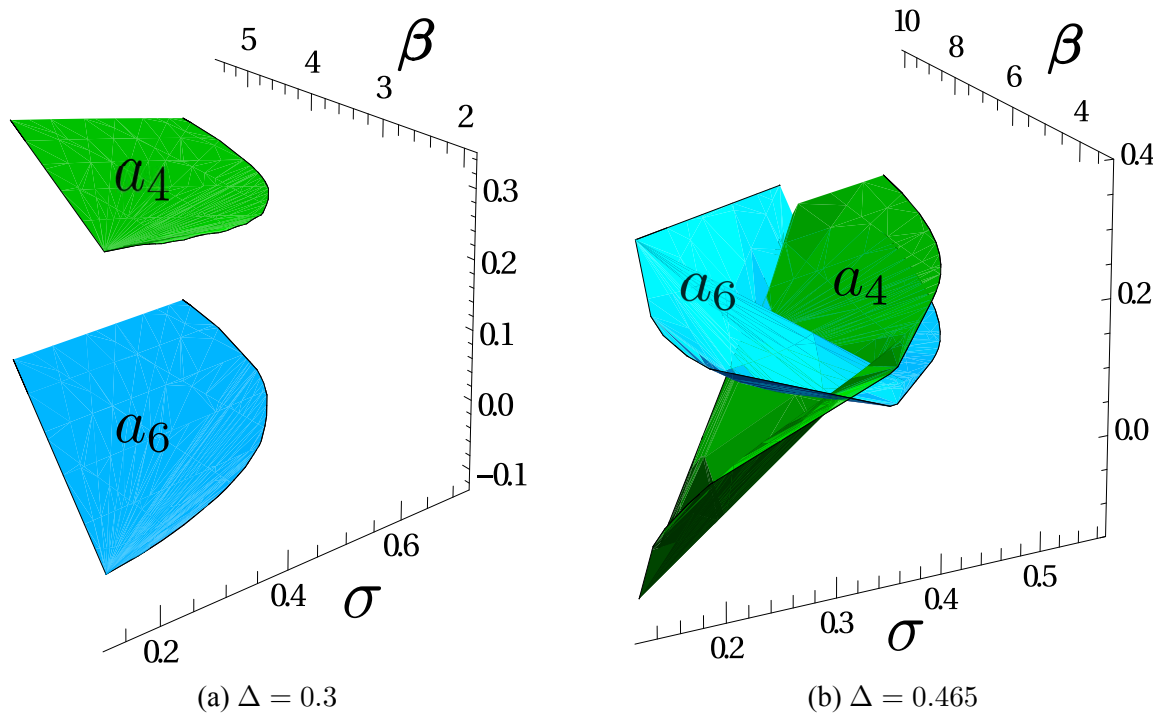
Figure 4.15: Plot of the Landau coefficients a_4 and a_6 when $a_2 = 0$ in the $\beta - \sigma$ plane. Fig. **(a)** shows the plot for $\Delta = 0.3$. Here a_4 is always positive at the coordinates of $a_2 = 0$. So the transition is always second order. Fig. **(b)** shows the plot for $\Delta = 0.465$. For high values of σ, the a_4 is positive. So the transition is second order for this range of σ. As σ decreases, a_4 crosses $a_4 = 0$ at $\sigma_{th} = 0.16$ and $\beta_{th} = 3.2499$ provided $a_6 > 0$. So the second order transition ends at a TCP and becomes first order transition for $0 \le \sigma < 0.16$.

$$f(m) = \frac{\beta m^2}{2} - \frac{1}{\sqrt{2\pi\sigma^2}} \int_{-\infty}^{\infty} \log\left(1 + 2e^{-\beta\triangle}\cosh\beta(m + h_i)\right) e^{\frac{-h_i^2}{2\sigma^2}} dh_i \qquad (4.25)$$

Expanding Eq. 4.25 around $m = 0$ upto 8th order we get the following Landau coefficients

$$a_2 = \frac{\beta}{2} - \frac{a\beta^2}{\sqrt{2\pi\sigma^2}} \int_{-\infty}^{\infty} \frac{z_1 + 2a}{\left(1 + 2az_1\right)^2} e^{-\frac{h^2}{2\sigma^2}} dh \qquad (4.26)$$

$$a_4 = \frac{a\beta^4}{12\sqrt{2\pi\sigma^2}} \int_{-\infty}^{\infty} \frac{4a(4a^2 - 1)(1 - z_2) - a^2(z_3 - 16a) + (13a^2 - 1)z_1}{\left(1 + 2az_1\right)^4} e^{-\frac{h^2}{2\sigma^2}} dh$$

$$(4.27)$$

$$\begin{aligned}
a_6 = -\frac{a\beta^6}{360\sqrt{2\pi\sigma^2}} \int_{-\infty}^{\infty} &\bigg(6a(352a^4 - 69a^2 + 1) + (898a^4 - 146a^2 + 1)z_1 \\
&- 26a(64a^4 - 20a^2 + 1)z_2 - 3a^2(113a^2 - 33)z_3 \\
&+ 2a^3(32a^2 - 13)z_4 + a^4 z_5\bigg)\left(1 + 2az_1\right)^{-6} e^{-\frac{h^2}{2\sigma^2}} dh
\end{aligned}$$

$$(4.28)$$

where $a = e^{-\beta\triangle}$ and $z_n = \cosh n\beta h$.

Integrating a_2 numerically and then equating it to zero, we get the line of continuous transition, provided that $a_4 > 0$ at those coordinates. Similarly, integrating a_4 at the coordinates of $a_2 = 0$ and then equating it to zero gives the location of the TCP, provided $a_6 > 0$. In order to obtain the coordinates of the λ line and the TCP in the $T - \sigma$ plane and $T - \triangle$ plane we plot the values of the a_4 and a_6 coefficients after substituting the coordinates for which $a_2 = 0$ for different values of $\triangle$ and σ respectively.

(a)

(b)
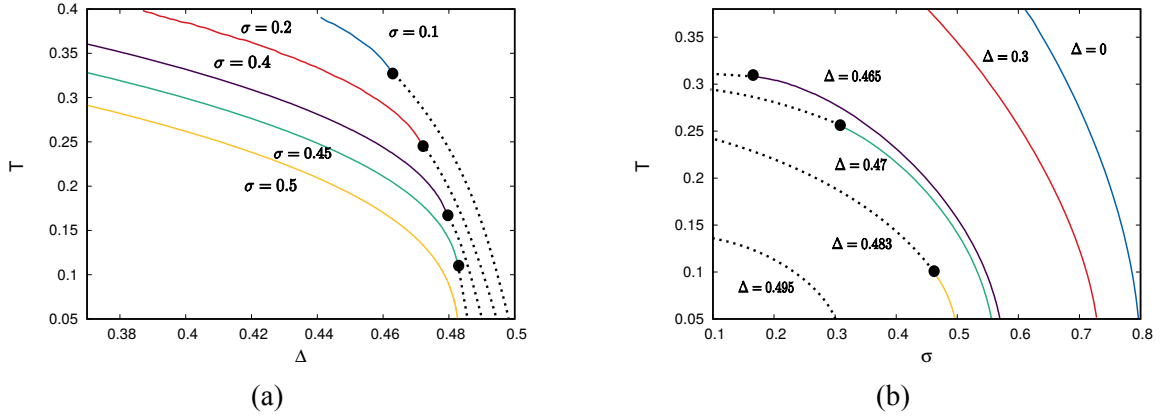
Figure 4.16: Phase diagrams of the Gaussian RFBC model. The solid lines are the lines of second order transition and the dotted lines are the first order transition lines. Solid circles are the TCPs. **(a)** Is the $T - \Delta$ phase diagram for different values of σ. For $\sigma < \sigma_{TCP} \approx 0.4839$ the phase diagram exhibits a TCP. This TCP moves to $T = 0$ at σ_{TCP}. For $\sigma > \sigma_{TCP}$ there is only a line of continuous transition in the phase diagram. **(b)** Denotes the $T - \sigma$ phase diagram for different values of Δ. Below $\Delta = \Delta_{BC} = \frac{\ln 4}{3} \approx 0.462098$, there is only a line of second order transition. For $\Delta > \Delta_{BC}$, TCP emerges and moves to $T = 0$ at $\Delta_{TCP} = \sigma_{TCP} \simeq 0.4839$. There are only first order transition lines for $0.5 \geq \Delta > \Delta_{TCP}$. For $\Delta > 0.5$, there is no ordered state and hence no transition.

To illustrate the procedure, in Fig. 4.15 we plot the a_4 and a_6 values for the condition $a_2 = 0$ at two values of Δ. Fig. 4.15a shows the plot of a_4 and a_6 for fixed $\Delta = 0.3$. In this case $a_4 > 0$ and the transition is always second order. Fig. 4.15b shows the plot for $\Delta = 0.465$. Here we find $a_4 > 0$ for $\sigma > 0.16$. At $\sigma_{th} = 0.16$ and $\beta_{th} = 3.2499$, $a_4 = 0$ with $a_6 > 0$. This hence is the locus of the TCP. For $\sigma < \sigma_{th}$ the transition is always first order. The coordinates of the first order transition can be found by equating the free energies ($f(m = 0) = f(m \neq 0)$) and also their first order derivative on both side. We use this method to obtain the phase diagram in the entire $T - \sigma$ and $T - \Delta$ planes by fixing the values of Δ and σ respectively.

We find that for small values of σ, the transition in the $T - \Delta$ plane is second order at high temperature and first order at low temperature. These two transition lines meet at a TCP. As σ increases, the first order transition line decreases and above $\sigma_c = \sqrt{\frac{2}{e\pi}} \sim 0.483941..$,

(a) (b) (c)
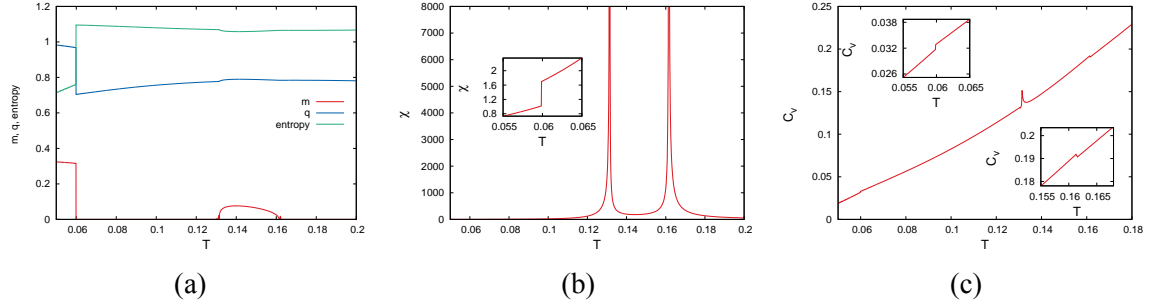
Figure 4.17: Thermodynamic quantities near the re-entrance regime of Fig. for $p = \frac{1}{3}$ at $\Delta = 0.165$. Fig. **(a)** shows the magnetization (m), spin density (q) and entropy as a function of T for $h = 0.708$. The magnetization at the second order transition at $T_c = 0.131407$ fits with the scaling function $2.008 \mid T - T_c \mid^{0.5}$ and the second transition at $T_c = 0.1615509$ fits with the scaling function $0.628833 \mid T - T_c \mid^{0.5}$. Fig. **(b)** is the susceptibility (χ) plot. χ shows two divergences at the two continuous transition points and the inset shows the discontinuity in χ at the low T due to the first order transition. Fig. **(c)** is the plot of the specific heat (C_v). There are three jumps in the C_v plot at the three transition points.

the transition becomes second order. This is same as the value of σ_{TCP} in Sec. 4.3.2. There σ_{TCP} was the TCP value of σ for $T = 0$, below which the transition is always first order. For $\sigma < \sigma_c$, there is always a TCP in the $T - \Delta$ phase diagram shown in Fig. 4.16a.

Similarly in the $T - \sigma$ plane, the phase diagram consists of a second order transition for $\Delta < \Delta_{BC} (= \frac{\ln 4}{3})$, which is the value of Δ at the TCP of pure BC model. For $\Delta \geq \Delta_{BC}$, one TCP emerges in the phase diagram and the phase diagram consists of first and a second order transition lines meeting at a TCP. The TCP moves to lower temperature with the increasing Δ. At exactly $\Delta = \Delta_{TCP} = \sqrt{\frac{2}{e\pi}} \sim 0.483941..$ (TCP value at $T = 0$), the TCP moves to zero and there is only a first order transition line in the phase diagram (shown in Fig. 4.16b). For $\Delta_{TCP} < \Delta \leq \frac{1}{2}$, the transition is always first order and for $\Delta > \frac{1}{2}$, there is no transition in the $T - \sigma$ plane.

In a recent study of spin-s random field Blume Capel model using the Gaussian distribution using effective field theory only continuous transition lines were reported [249]. They did not find the lines of first order transition and the TCP.

Interestingly, it can be seen that similar to the ground state phase diagram, the finite
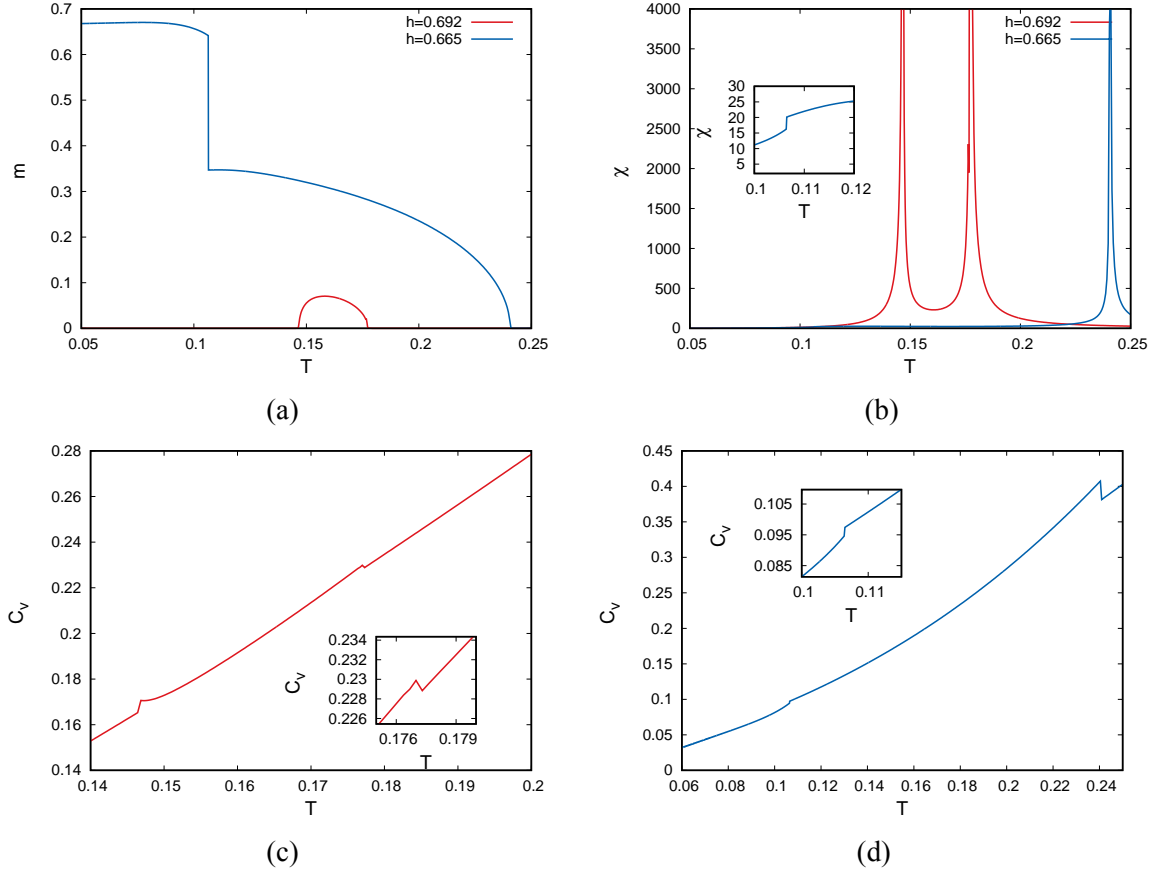
Figure 4.18: Thermodynamic quantities near the re-entrance regime of Fig. for $p = \frac{1}{3}$ at $\Delta = 0.17$. The blue solid line is for $h = 0.692$ and red solid line is for $h = 0.665$. Fig. **(a)** shows the magnetization (m). At $h = 0.692$, the phase diagram shows re-entrance in m and for $h = 0.665$ m has two transitions : a first order transition at lower temperature and a continuous transition at higher temperature. Fig. **(b)** the susceptibility (χ) is plotted for both the values of h. It confirms the nature of transition in m. Fig. **(c)** and Fig. **(d)** are the plot of the specific heat (C_v) for $h = 0.692$ and $h = 0.665$ respectively. C_v is discontinuous at all transition points.

121

temperature phase diagrams are also different for different distributions. This behavior of the spin-1 RFBC model contradicts the conjecture for the random field $O(n)$ models. Apart from this there are some other novel features that emerge for the trimodal RFBC model. In the following sections we will discuss about them in details.

4.5 Re-entrance for equal peak trimodal RFBC model ($p = \frac{1}{3}$)

Re-entrance is a phenomena where a more ordered phase becomes stable than a less ordered phase as temperature increases. Usually it is expected that as temperature increases, the ordered state of a system like crystalline or ferromagnetic state should transform to a disordered state like fluid or paramagnetic state respectively. But for re-entrance phenomena for some values of the thermodynamic parameter the disordered phase transforms to an ordered state as temperature increases. Due to this reason it is also known as inverse melting or inverse freezing transition. This behaviour happens when the entropy of the ordered state becomes more than the disordered phase, as temperature increases. Re-entrance has been observed experimentally in different systems. Some of the examples where such inverse transitions can be seen are : ferroelectricity in Rochelle salt [250], high T superconductors [251], polymer solutions [252, 253, 254, 255], colloidal mixtures [256], cold denaturation in proteins [257, 258] and so on. There are some theoretical models which has been studied to explain such behaviors observed experimentally in the above examples [259, 260, 261]. Spin models in presence of random interactions has been shown to incorporate all the feature of inverse melting transitions [262, 155, 156, 157]. Such models are beneficial because of their simplicity and yet gives a broad insight about the inverse transitions. The mean-field Blume-Capel model are known to show re-entrance in the presence of strong degeneracy of the $s = \pm 1$ spins [155, 156].

In our case the RFBC model shows re-entrance in presence of trimodal distribution.
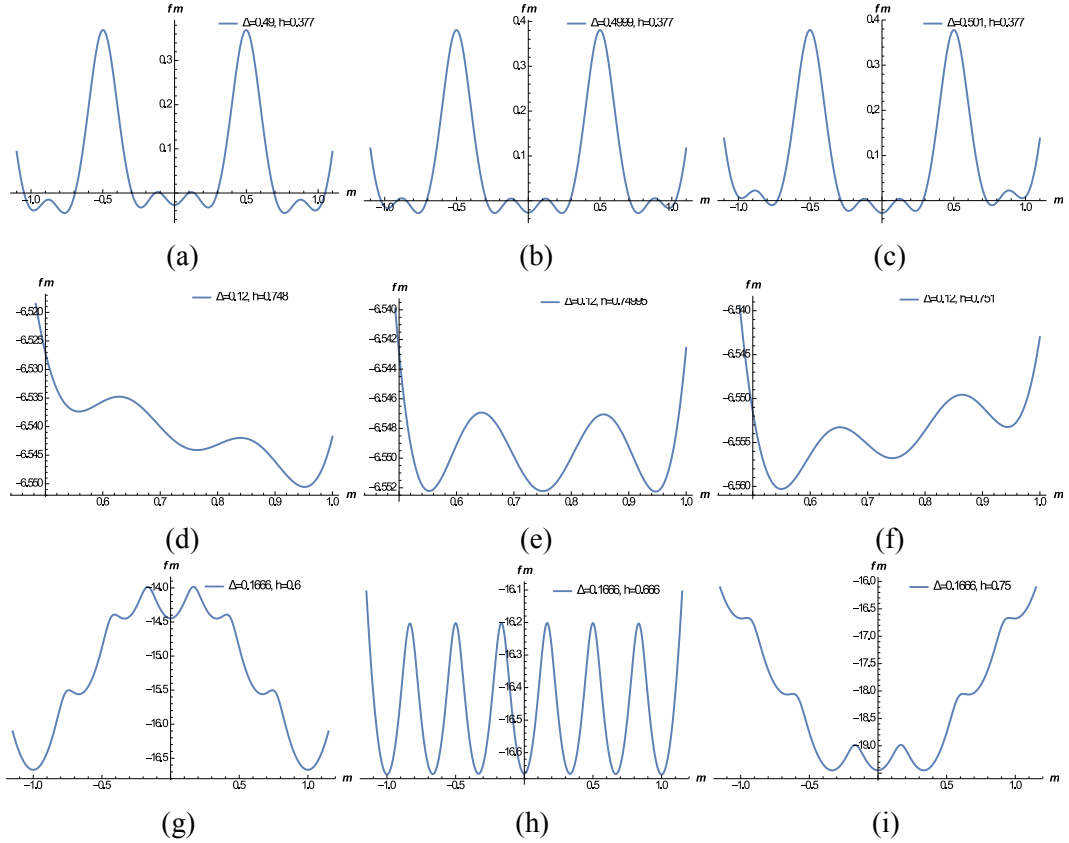
Figure 4.19: The plot of the free energy functional around the multi-phase coexistence points. **(a) - (c)** Shows the plot of the free energy functional around and at the A_5 points for $p = \frac{1}{2}$. The A_5 point is situated at $\Delta_{A5} = 0.4999$, $\beta_{A_5} = 23.66$ and $h_{A5} = 0.377$. **(a)** Shows the plot at h_{A5}, β_{A_5} $\Delta < \Delta_{A5}$, **(b)** is at the A_5 point, and **(c)** for h_{A5}, β_{A_5}, $\Delta > \Delta_{A5}$. **(d) - (f)** Shows the plot of the free energy functional around and at the A_6 points for $p = \frac{1}{2}$ (only the positive m side is shown here). The A_6 point is situated at $\Delta_{A6} = 0.12$, $\beta_{A_6} = 17.15$ and $h_{A6} = 0.74996$. **(d)** Shows the plot for β_{A_6}, Δ_{A6}, $h < h_{A6}$, **(e)** is at the A_6 point, and **(f)** for $h > h_{A6}$, β_{A_6}, Δ_{A6}. **(g) - (i)** Shows the plot of the free energy functional around and at the A_7 points for $p = \frac{1}{3}$. The A_7 point is at $\Delta_{A7} = 0.1666$ and $h_{A7} = 0.6666$. **(g)** Shows the plot for $h < h_{A7}$, Δ_{A7}, **(h)** at the A_7 point, and **(i)** for $h > h_{A7}$, Δ_{A7}.

For the $p = \frac{1}{3}$, the $T - h$ plane phase diagram shows re-entrance of the ordered phase for certain values of Δ. For example, in Fig. 4.10c and Fig. 4.10d the phase diagram shows re-entrance.

We study some thermodynamic quantities near the re-entrance regions (marked with red cross in 4.10c and Fig. 4.10d) in order to understand the underlying mechanism. The 4.10c shows the double re-entrance phenomena of the phases ordered-disordered-ordered-disordered as T increases. In Fig. 4.17, we plot of the two order parameters : magnetization (m) and spin density q, entropy, susceptibility (χ) and specific heat (C_v) for $h = 0.708$ and $\Delta = 0.165$ (see Fig. 4.10c). In 4.17a the m shows a first order jump at low T from **F3** to **P** then a small ordered region **F3** appears for higher T (shown by solid red line). Similarly q shows a first order jump for low T. As T increases the q increases and shows a maxima near the re-entrant **F3** phase, then again decreases with increasing T (shown by solid blue line). From the corresponding entropy plot (shown by solid green line) it can be explained that as T decreases, the $s = \pm 1$ increases and thus entropy decreases. For further decrease in T, the energy gain due to $s = \pm 1$ spins is unable to compensate the entropy loss and thus the system chooses to increase the entropy by increasing the density of $s = 0$ spins. And thus the system becomes paramagnetic. Near the two continuous transition the m can be fitted with the scaling function $2.008 \mid T - T_c \mid^{0.5}$ with $T_c = 0.131407$ and $0.628833 \mid T - T_c \mid^{0.5}$ with $T_c = 0.1615509$ respectively. Both continuous transitions lie in the mean-field Ising universality class.

In Fig. 4.18 we plot the magnetization(m), susceptibility(χ) and specific heat plot(C_v) for two fixed values of $h = 0.692$, 0.695 at $\Delta = 0.17$ (see Fig. 4.10d). The red and blue curves show the thermodynamic quantities for $h = 0.692$ and $h = 0.665$ respectively. For $h = 0.692$ a small ordered region **F3** appears for higher T, showing re-entrance. Whereas for $h = 0.665$, the magnetization (m) undergoes two transitions, a first order at low T and a continuous transition at higher T as shown in Fig. 4.18a. There is no re-entrance in the
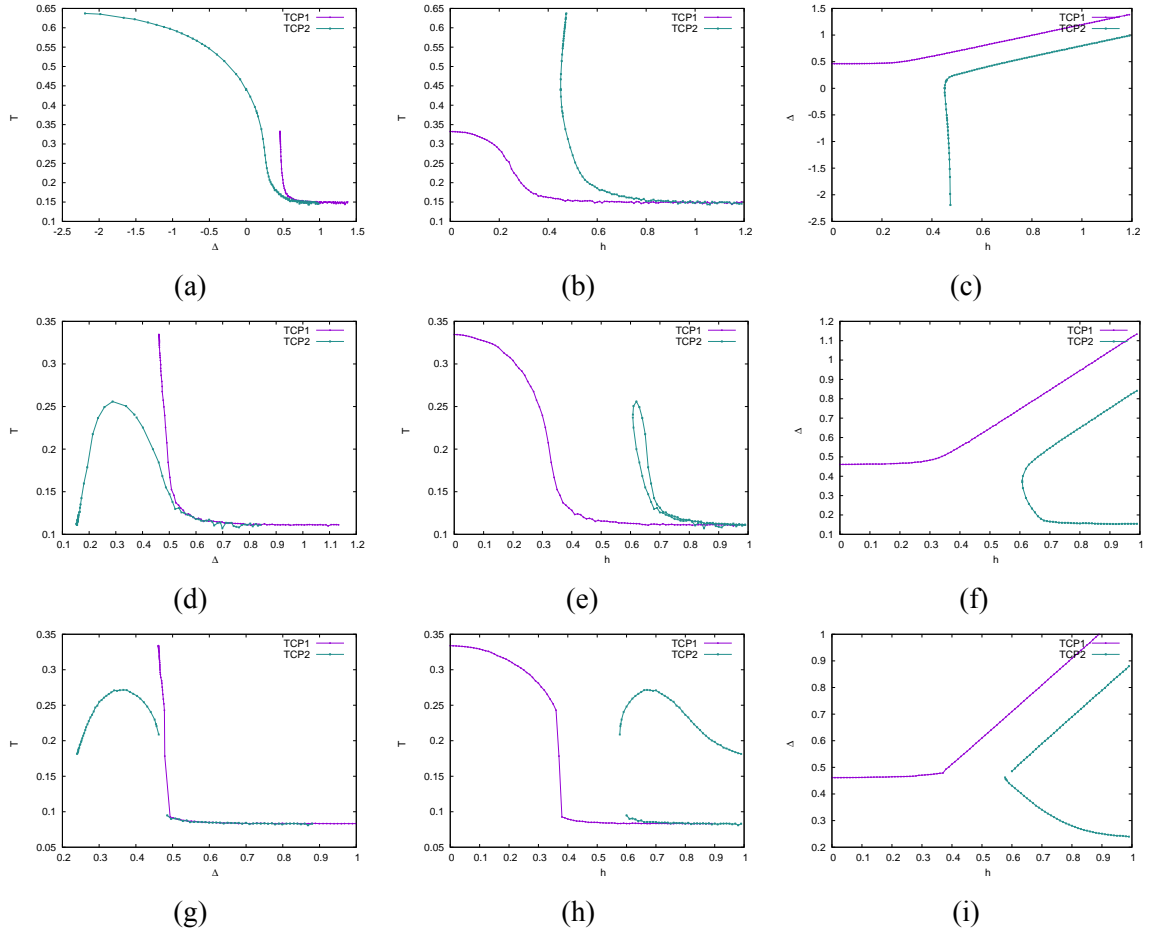
Figure 4.20: Projection of the coordinates of the TCPs in the $T - \Delta$, $T - h$ and $\Delta - h$ plane respectively for different values of p. **(a)**, **(b)** and **(c)** shows the projections for $p = \frac{1}{10}$. **(d)**, **(e)** and **(f)** shows the projections for $p = \frac{1}{3}$. **(g)**, **(h)** and **(i)** shows the projecions for $p = \frac{1}{2}$.

magnetization in this case.

4.6 Multicritical points and multi-phase coexistence points for trimodal RFBC model

For the trimodal random field distribution, the RFBC model exhibits six phases, multicritical points like BEP, CEP and multi-phase coexistence points like A_5, A_6 and A_7 along with the TCPs.

4.6.1 Multi-phase co-existence points

Fig. 4.19 shows the plot of the free energy functional around the multi-phase coexistance points. $A5$ point is a five phase coexisting point : two ordered and one disordered, shown in Fig. 4.19a - 4.19c. At the A_5 point the Landau co-efficients are: a_4 is negative, and all the other coefficients (a_2, a_6, and a_8) are positive. This point exists for all $0 \leq p < 1$. The existence of this multi-phase coexistence point was reported earlier in [205] and [206]. On the other hand, A_6 point is a six phase coexisting point : three ordered phase, shown in Fig. 4.19d-4.19f. This point persists for all $\frac{1}{3} \leq p < 1$. And A_7 point is a seven phase coexisting point: three ordered and one disordered, shown in 4.19g-4.19i. At the A_7 point the Landau co-efficients are: a_2 is positive, and all the other coefficients (a_4, a_6, and a_8) are negative. This is observed for all $0 < p < 1$. For only $p = \frac{1}{3}$ the A_7 point emerges twice.

4.6.2 TCPs and BEPs

The multicritical points like BEP and TCPs emerges in multiple number depending on the values of p. In Fig. 4.20 we plot the projection of the co-ordinates of the TCPs for different values of p on the $T - \Delta$, $T - h$, and $\Delta - h$ plane respectively. We have not shown the pure case ($p = 1$) as there is only one TCP which appears at $T = \frac{1}{3}$, $\Delta = 0.462098$, $h = 0$. As we switch on disorder by taking p less than 1, the coordinate of this TCP (we call it as TCP1) increases monotonically in Δ as h increases, shown by solid purple lines. Another line of TCP emerges for all $0 \leq p < 1$ (we call it as TCP2) represented by the solid green line. Fig. 4.20a- 4.20c shows the projections for $p = \frac{1}{10}$, Fig. 4.20d- 4.20f shows the projections for $p = \frac{1}{3}$, and Fig. 4.20g- 4.20i shows the projections for $p = \frac{1}{2}$. For all values of p the trajectories of the TCP2 co-ordinate shows non-monotonicity. The non-monotonicity of the TCP2 lines are more sensitive to the Δ and h than T.

In order to understand the origin of the multiple BEP and TCPs we projected the coor-

dinates of TCPs and BEPs on the ground state phase diagram in the $\Delta - h$ plane (Fig. 4.21). The solid blue line shows the phase boundaries in the ground state, black and purple dashed lines are the projections of the coordinates of the TCP1 and TCP2s and red, blue and green dotted lines are the projections of the coordinates of the BEPs. Fig. 4.21a is the plot for the projection of the TCP and BEP coordinates for $p = \frac{1}{2}$. The TCP1 line moves along the phase boundaries of **F1 - NM** , **F1 - NM** and **F2 - NM** . And the TCP2 line moves along the phase boundaries of **F2 - P** , **F1 - P** and **F3 - P** . Along with the TCP2 line, three BEP lines also emerge along the separation of the phases **F-F3**, **F-F2**, **F-F1**, **F1-F3** denoted by blue, red and green dotted lines respectively.

On further decreasing p, the BEP line along the phase separations of **F3-F1** vanishes and there are now three BEP lines along the phase separation lines of **F1-F2** and **F-F3** and **F-F1**. The TCP1 behaves similarly to the $p = \frac{1}{2}$ case. And the TCP2 starts from $(\Delta \simeq \frac{p}{2}, \ h \to \infty)$. As h decreases, the TCP2 line remains close to $\Delta \simeq \frac{p}{2}$ until $h \simeq \frac{1+p}{2}$. Below $h \simeq \frac{1+p}{2}$, the TCP2 line shows an extrema at $\Delta \approx 0.375, h \approx 0.607, T \approx 0.24$ and then increases in Δ as h increases. Due to this extrema the TCP2 line shows non-monotonic behaviour. Fig. 4.21b shows the projection of the BEPs and TCPs for $p = \frac{1}{3}$.

For p moving towards the bimodal value $p = 0$, the line of BEPs along the **F-F3** phase separation vanishes and the phase diagram now consist of two lines of BEP along the phase boundaries of **F1-F2** and **F-F1**. The TCP1 behaves similar to as for $p = \frac{1}{3}$. The TCP2 line starts from $\Delta \to -\infty$ instead of $\Delta \simeq \frac{p}{2}$ and then Δ increases as h increases (shown in Fig. 4.21c for $p = \frac{1}{10}$).

At exactly $p = 0$, we get back the two TCP lines (TCP1 and TCP2) of the bimodal distribution (shown in Fig. 4.21d). TCP1 starts from the pure Blume-Capel model TCP and then increases monotonically with increasing Δ and h. The TCP2 starts at the TCP of the RFIM $\Delta \to -\infty$, $T = \frac{2}{3}$, $h \sim 0.43899$ and increases non-monotonically in Δ as h increases. The phase diagram also exhibits one BEP line along the phase separation of
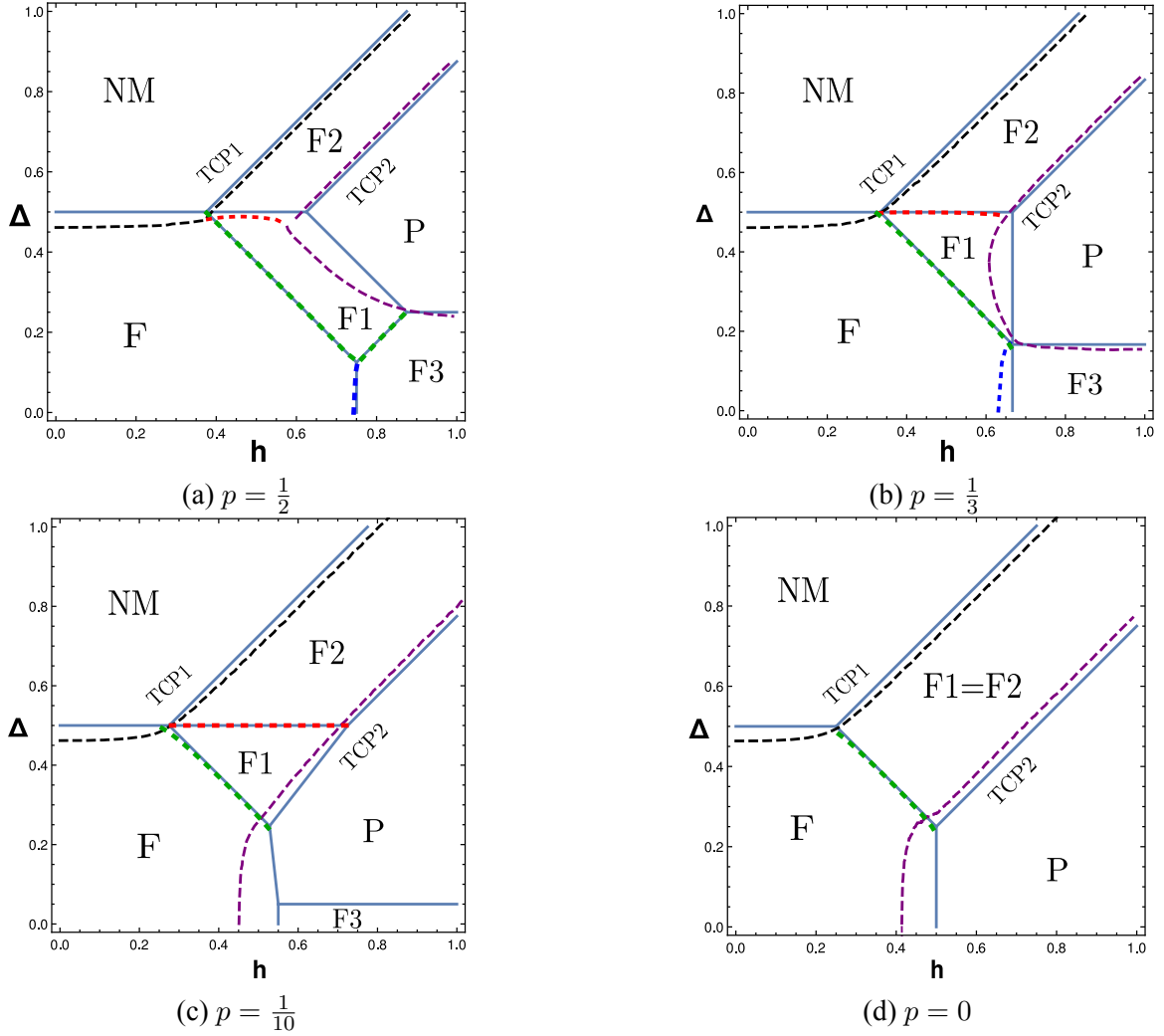
Figure 4.21: Projection of the TCP and BEP coordinates at different T onto the ground state phase diagram for **(a)** $p = \frac{1}{2}$, **(b)** $p = \frac{1}{3}$, **(c)** $p = \frac{1}{10}$, and **(d)** $p = 0$. The solid blue lines are the ground state phase boundaries, the black dashed lines are the projection of the TCP1 coordinates, the purple dashed lines are the projection of the TCP2 coordinates, and the red, green and blue dashed lines are the projection of the BEP coordinates along the phase boundaries of the different phases. The TCP2 coordinate is non-monotonic depending on the value of p.

(a) $h = 0.603$ (b) $h = h_c = 0.6079$ (c) $h = 0.615$
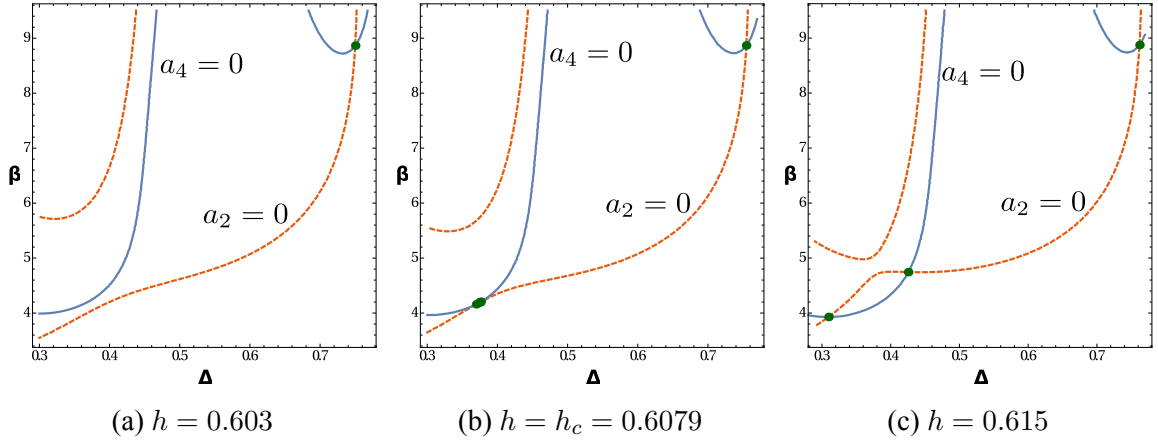
Figure 4.22: Contour plot of the λ line (Eq. 4.22) shown by dashed lines and the solutions for $a_4 = 0$ given by Eq. 4.29 (solid blue line) for $p = \frac{1}{3}$ in the $\beta - \Delta$ plane for h close to h_c. Here h_c is the value of the random field at which the double TCP emerges. **(a)** For $h = 0.603$, the two curves intersect only once (shown by solid green circle), hence the phase diagram Fig. shows only one TCP (which is TCP1). **(b)** For $h = h_c = 0.6079$, the two curves intersect at TCP1 for higher Δ and for low Δ the two curves are tangential to each other. **(c)** For $h = 0.615$, the two curves intersect at three points giving rise to one TCP1 and two TCP2s in the phase diagram Fig. .

F-(F1=F2).

By studying the projection of TCPs and BEPs on the ground state phase diagram, we find that their coordinates closely follow the phase boundaries present in the $T = 0$ phase diagrams. We hence show that the multicritical points arise due to the presence of first order transition lines in $T = 0$ phase diagram.

Non-monotonicity of the TCP co-ordinates

The TCP2 line shows a non-monotonic dependence of Δ on H for all $0 \leq p < 1$. As a result as we cross the TCP2 line along Δ axis near the non-monotonic regime, we get three TCPs in the phase diagrams of $T - \Delta$ plane for some values of h (i.e Fig. 4.5d for $p = \frac{1}{10}$, Fig. 4.9e and Fig. 4.9f for $p = \frac{1}{3}$, Fig. 4.11f for $p = \frac{1}{2}$ and Fig. 4.13d for $p = 0$). Two intercepts come from the TCP2 line and the other comes from the TCP1 line. These two TCP2 points emerge in the phase diagram as a pair. For example in Fig. 4.22 we plot the

(a)   (b)
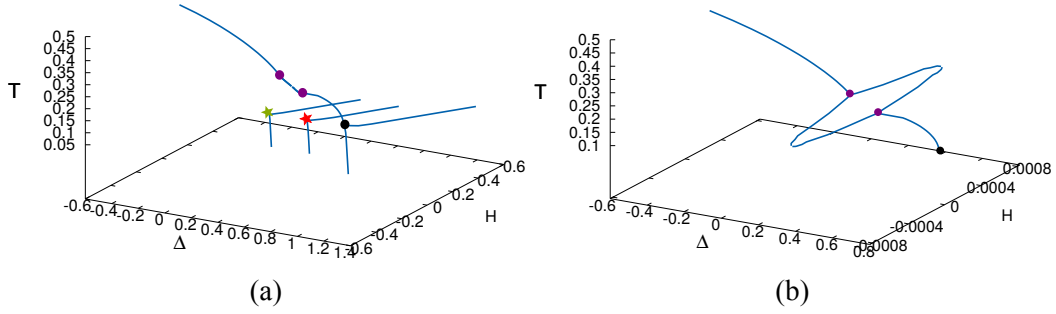
Figure 4.23: $T - \Delta - H$ phase diagram for $p = \frac{1}{3}$ at a fixed $h = 0.63$. It only shows the wings originated from the TCPs and BEPs of the Fig. 4.9e in the finite and uniform external field H. Blue solid lines depicts lines of continuous transitions. Solid circels are TCPs, stars are BEPs. **(a)** Shows there are four wing surfaces. two originating from two BEPs, one coming from the TCP1, and the last one is generated by the paired TCP2s. **(b)** Shows the zoomed in region of the wings existing between the paired TCP2s. Here the critical line bounding the first order surface form a loop like structure and it exists only for very small values of H.

values of (β, Δ) at which the second order term (a_2) equals zero. These are the coordinates of the λ line (Eq. 4.22). We also plot the values of (β, Δ) at which the third order term (a_4) equals zero in the expansion of Eq. 4.13. The equation for $a_4 = 0$ is

$$\frac{\beta^4 a}{12} \left(\frac{p(4a - 1)}{(2a + 1)^2} - \frac{(1 - p)(a^2(z_3 - 13) - 16a^3(2 + z_1) + 4a(1 - z_2) + z_1)}{(1 + 2az_1)^4} \right) = 0 \tag{4.29}$$

We plot the solutions of Eq. 4.22 (shown by red dashed line) and Eq. 4.29 (shown by solid blue line) in the $\beta - \Delta$ plane for h values very close to the value h_c at which two TCP2 emerge for $p = \frac{1}{3}$. Fig. 4.22a shows for $h < h_c$, the two curves intersect only at one point and the phase diagram (Fig. 4.9d) consists of only TCP1. Near $h \approx h_c$, the two curves almost become tangential, see Fig. 4.22b. For $h \geq h_c$ the curves intersect thrice giving rise to two TCP2s and one TCP1 in the phase diagram (Fig. 4.9e), see Fig. 4.22c.

The first order wings that emerges due to the paired TCP2s in the $T - \Delta$ phase diagrams in Fig. 4.5d, Fig. 4.9e, Fig. 4.9f, Fig. 4.11f, and Fig. 4.13d can be seen by applying
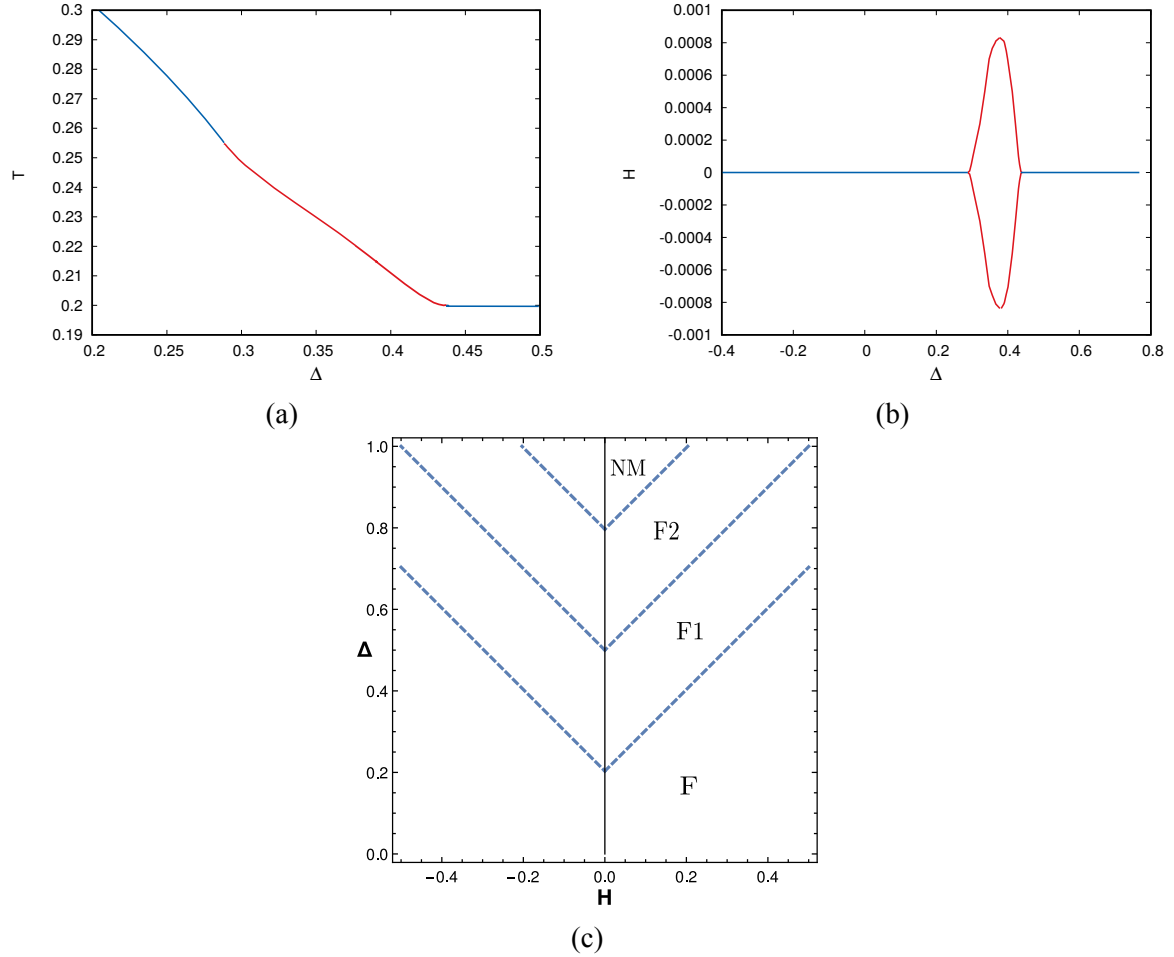
Figure 4.24: Projection of the lines of second order transition near the paired TCP2s of Fig. 4.23 in the **(a)** $T - \Delta$ and **(b)** $H - \Delta$ plane. The solid blue lines represent the λ line and the solid red lines represent the second order transition lines in the finite H plane generated from the paired TCP2s. These lines form a loop-like structure and exists only for a very small ranges of H and T. **(c)** Shows the ground state phase diagram in the $\Delta - H$ plane for Fig. 4.23. The blue dashed lines represent the lines of first order transition which are generated from the two BEPs and the TCP1 of Fig. 4.23. There are no first order transition lines for the paired TCP2s.

a uniform non-zero external magnetic field H (similar to [213]). Fig. 4.23a shows the $T - \Delta - H$ phase diagram for $p = \frac{1}{3}$ for $h = 0.63$, corresponding to the $T - \Delta$ phase diagram of Fig. 4.9e. We zoomed in the region of the first order surface generated due to the pair TCP2s in Fig. 4.23b. It shows that the second order transition lines which bounds the first order surfaces form a loop-like structure and this loop exists for very small ranges of H and T. Fig. 4.24c and 4.24a shows the projection of the second order transition lines near the paired TCP2s on the $T - \Delta$ and $\Delta - H$ plane respectively. The blue solid line represents the λ line near the paired TCP2s and the solid red lines are the loop generated from the paired TCP2s. These loop-like second order transition lines are not similar to the usual "wings" which extends till $T = 0$. As h increases, the TCP2s get detached from each other and so does the loop formed by the lines of second order transition. The wings generated by the TCP2s has no projection in the $T = 0$ plane. For example Fig. 4.24b the ground state phase diagram of Fig. 4.23 on the $\Delta - H$ plane. The first order transition lines separating the phases are present due to the existence of the wings generated by the two BEPs and one TCP1.

4.7 Summary and conclusion

Effect of random-field disorder with different distributions on spin $-\frac{1}{2}$ Ising model (RFIM) has been studied earlier using various techniques. It was reported that the phase topology of the system depends on the form of the distribution function. Effect of the random-field disorder on the spin-1 Blume-Capel model has been studied less. In the earlier work [205, 206] presence of the bimodal random-field distribution in the RFBC model has been discussed. It was shown that a novel phase emerges at sufficiently strong random field.

In the present work we try to address the question of how the different form of distribution functions affect the phase topology of the pure Blume-Capel model on a fully

connected graph [214]. In order to answer that question, we consider two types of symmetric random-field distribution: trimodal and Gaussian. We have reproduced the results of the bimodal case which is just a special case of the trimodal distribution. We have studied the phase diagrams for both the distribution in the ground state as well as in the finite T. We observed that the presence of the crystal field interaction plays an important role. Due to the interplay of the random field disorder and the crystal field interaction new phases arises for the trimodal random field disorder and an ordered state always persists for strong field disorder. The presence of these new phases make the first order transition gets divided into many small jumps. Whereas, in the Gaussian case, no such new phase exists. The phase diagram is rather simpler for the Gaussian distribution. The first order transition gets destroyed as disorder increases. Also, the TCP in the Gaussian case vanishes as the disorder strength increases. On the other hand in the trimodal case, the TCP never vanishes. Instead new multicritical point emerges in the system.

It was shown in the RFIM case that for $p = \frac{1}{3}$, the trimodal distribution and the Gaussian distribution becomes equivalent [105, 263, 118, 119, 124]. Interestingly, in our work we couldn't find any resemblance in the phase diagram of the two distributions. The phase topology of the above distributions are entirely different. This behavior contradicts the earlier conjecture given by Aharony for $O(n)$ models in presence of symmetric random field distribution [76]. The possibility of such contradiction could be due to the artefact of the mean-field nature of the solutions, or the argument that was given based on ϵ expansion study of the $O(n)$ models might not hold for higher spin models like the Blume-Capel model.

The trimodal random-field Blume-Capel model shows very rich phase topologies depending on the strength of the field. For some values of the parameter the phase diagram shows re-entrance phenomenon. Also the trimodal RFBC model exhibits multiple number of multicritical points. We observed the TCPs and BEPs that observed at the finite T closely

follows the ground state phase boundaries in the $\Delta - h$ plane. This indicates how the random field dominates the low temperature behavior and therefore all the critical properties in finite T can be understood just by studying the $T = 0$ phase diagram. Another interesting behavior is that for some values of the parameters, two paired TCPs emerge in the phase diagram simultaneously and as the parameter changes they get shifted from each other via a first order line. This unique behavior has not been reported earlier. Recently, this kind of behavior has been observed in non-equilibrium transitions in resetting problems [264]. This suggests that such phase diagrams are not only limited to equilibrium systems but can also be seen for non-equilibrium systems. We also studied the lines of second order transition generated by these paired TCPs by switching on the external magnetic field. We observed that they kind of form a loop-like structure and exists only for a small parameter values. The behavior of this first order surface generated by the paired TCPs are interestingly different from the usual wings which extends till $T = 0$.

Chapter 5

Spin-1 model with higher order interactions

In this section we will discuss about the effect of biquadratic excahnge interactions in the spin-1 Blume-Capel model. We will consider a infinite range generalized Blume-Emery-Griffiths model. We will discuss about the behavior of the phase diagrams in two ensembles : canonical and microcanonical. We will then show the ensemble inequivalence that arises from the long-range interactions.

5.1   Blume-Emery-Griffiths model

As shown in the previous chapters, the multicritical points emerge in the presence of the disorder. These points are also seen in fluid mixtures containing three or more components [265, 241]. The phase diagram of such systems can be described using spin models in presence of some higher order interactions [266, 158, 267, 268, 269]. Some of the higher order interactions are : biquadratic exchange interactions, crossed quadrupolar-dipolar interactions and so on. Presence of biquadratic exchange interaction is known to be relevant to understand the properties of the rare-earth compounds. The biquadratic exchange was first suggested by Kittel in the theory of magnetoelastic effect in NiAs type structures [270], and by Anderson in the superexchange interaction of iron group oxides and flurides [271]. In rare-earth compounds, the unpaired $4f$ electrons lie deep inside the $5d$ and $5s$ orbital. So these electrons do not experience the strong crystal field generated by other ions in the crystal. Hence their spherically symmetric potential is not completely destroyed. As a result the orbital angular momentum is not entirely quenched. The super-exchange between

these unquenched orbital momentum gives rise to a biquadratic exchange interaction term in the Hamiltonian [272]. Other interactions such as phonon exchange between ions [273] and the Schrodinger's spin-one exchange operator[274] can also result in the inclusion of such interaction. Both attractive and repulsive biquadratic interactions are of interest. The requirement of small repulsive exchange interaction in a Hamiltonian was first mentioned by Harris and Owen [275] and Rodbell *et.al* [276] in order to explain the paramagnetic resonance of the Mn ion pairs which are present as an impurity in the crystals of MgO.

Biquadratic exchange interaction is represented by a term that is fourth order in spin operators. The Blume-Emery-Griffiths (BEG) model is the simplest model which incorporates biquadratic interactions [266]. The Hamiltonian of the BEG model on a complete graph in the presence of external magnetic field is given by:

$$\mathcal{H} = -\frac{1}{2N}(\sum_i s_i)^2 - \frac{K}{2N}(\sum_i s_i^2)^2 + \triangle \sum_i s_i^2 - H \sum_i s_i \tag{5.1}$$

where K is the biquadratic interaction coefficient. Here the spins $s_i = \pm 1,\ 0$ represents thethree components of a fluid mixtures. The K represents the mean interactions b. The BEG model is the generalization of the Blume-Capel model ($K = 0$). At finite temperature, when $K < 0$, both the biquadratic term and the crystal field term prefer 0 spins. Hence the λ transition occurs at a lower $\triangle$ as K decreases. On the other hand, for positive K the magnetic spins are more likely to be chosen. Hence, when $K > 0$ there is a competition between the biquadratic and crystal field term in the Hamiltonian and the λ transition occurs at a higher $\triangle$ for positive K.

The attractive biquadratic exchange interaction($K > 0$) BEG model has been extensively studied. Its phase diagram changes with the value of K. For small K, there is a transition from a ferromagnetic to paramagnetic phase in the $(T - \triangle)$ plane. This transition line changes from a continuous to a first order transition line at a tricritical point (TCP). As

K increases further, another paramagnetic state emerges and the two paramagnetic states are separated by another first order line. The two first order lines meet at a triple point. For larger value of K, the continuous transition line terminates on the first order line at a critical end point (CEP), and the TCP disappears. The phase diagram has been well studied using various techniques like mean-field [266, 277, 278, 158, 279], cluster variation [280], Bethe lattice [281], high-temperature series expansion [282] etc. Apart from the mean-field, the phase diagram has also been studied in the finite dimensions using renormalization group [283, 284], Monte-Carlo simulations in two and three dimensions [285, 286, 168]. However, the simulations have been done mostly on the Blume-Capel model to study the continuous transition line and the TCP. The other multicritical points have not been studied as they are hard to locate in the simulations.

For repulsive biquadratic interaction ($K < 0$) the competition between the biquadratic and the bilinear interactions gives rise to a very different behaviour from the behaviour for positive K. The negative K term chooses the non-magnetic spins over the magnetic ones. This creates a competition between the magnetic and non-magnetic spins. In a recent study on a complete graph [287] in the $(T - \Delta)$ plane it was shown that as K becomes more negative, the TCP changes to a quadrupolar point at $K = -0.0828$ and $K = -0.1838$ in microcanonical and canonical ensembles respectively. They studied the system for small negative values of K upto $K = -0.4$.

In this work [288] we will first discuss about the phase diagram of pure BEG model for both attractive and repulsive K in canonical as well as in the microcanonical ensemble, with emphasis on large negative K regime in the $(T - \Delta - H)$ space. Since the multicritical points occur in systems described by three or more thermodynamic fields, it is useful to study them in $(T - \Delta - H)$ space. We will also discuss about the ensemble inequivalence that appears due to the infinite-range interactions.

In the next section we will discuss about the ground state phase diagram of the BEG
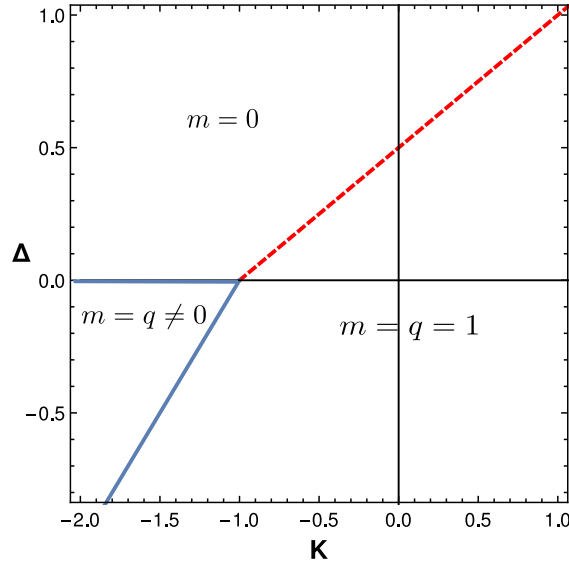
Figure 5.1: Ground state phase diagram of the BEG model in the $\Delta - K$ plane. There are three stable phases : two ferromagnetic and one paramagnetic. The red dashed lines depict the co-ordinate of the first order transition and the solid blue line represents the second order transition.

model for all ranges of K.

5.2 Ground state phase diagram of the BEG model

First let us look at the zero temperature phase diagram of the system. The ground state energy per particle can be written as (from the Hamiltonian Eq. 5.1):

$$\epsilon = -\frac{1}{2}(m^2 + Kq^2) + \Delta q - Hm \qquad (5.2)$$

For $H = 0$ depending on the values and signs of K, there are three phases in the ground state phase diagram. Fig. 5.1 shows the ground state phase diagram of the BEG model for all values of K. When all the spins are zero the energy is $\epsilon = 0$. Apart from this paramagnetic phase (which is $m = 0$), there are other states which are possible depending on the parameter values. For $-1 \leq K \leq \infty$, the ferromagnetic state, $m = \pm 1$ and $q = 1$

dominates. Energy of this state is $\epsilon = -\frac{1}{2}(1 + K) + \Delta$. If $2\Delta > 1 + K$, then the phase is paramagnetic, for $2\Delta < 1 + K$, the phase is ferromagnetic. At exactly $2\Delta = 1 + K$ there is a first order phase transition, shown by the red dashed line. For $H \neq 0$, the phases $m = 0$ and $m = 1$ are separated by the first order transition line : $H = \Delta - \frac{1}{2}(1 + K)$. Similarly, the phases $m = 0$ and $m = -1$ are separated by the first order transition line : $H = -\Delta + \frac{1}{2}(1 + K)$. And the $m = \pm 1$ phases are separated by $H = 0$. Fig. 5.2a shows the ground state phase diagram in the $\Delta - H$ plane for all $-1 \leq K < \infty$.

For $K < -1$, the term $-\frac{1}{2}(1 + K)$ in the energy contributes a positive value. So for any $\Delta \geq H$, the ϵ has a minima at $m = 0$. So the paramagnetic phase is the stable state for $\Delta \geq H$. When $\Delta < H$, there is another ferromagnetic state emerges with $|m| = q < 1$: $m^* = \frac{\Delta - H}{1 + K}$. It becomes stable when $\Delta - H < 1 + K$. The phases $\pm m^*$ and $m = 0$ are separated by a second order transition line $H = \pm \Delta$. For $\Delta - H > (1 + K)$, the phase m^* changes continuous to $m = 1$ phase and thus there is a second order transition line now between these two ferromagnetic states $\pm m^*$ and $m = 1$ at $\Delta = \pm H \mp (1 + K)$ respectively. The solid blue lines in Fig. 5.1 represent the lines of continuous transition in the $\Delta - K$ plane for all $K < -1$. And the Fig. 5.2b shows the ground state phase diagram in the $\Delta - H$ plane for all $K < -1$.

In the next sections, we will discuss about the finite temperature phase diagram for all ranges of K for both canonical and microcanonical ensemble.

5.3 Canonical ensemble

Given the Hamiltonian (Eq. 5.1), we solve it using the large deviation principle (LDP) [215] similar to the previous chapters. We find the scaled cumulant generating function (CGF) is:

$$\Lambda(k_1, k_2) = \log\big(1 + 2e^{k_2 - \beta\triangle}\cosh(k_1 + \beta H)\big) - \log\big(1 + 2e^{-\beta\triangle}\cosh\beta H\big) \qquad (5.3)$$

(a)　　　　　　　　　　　(b)
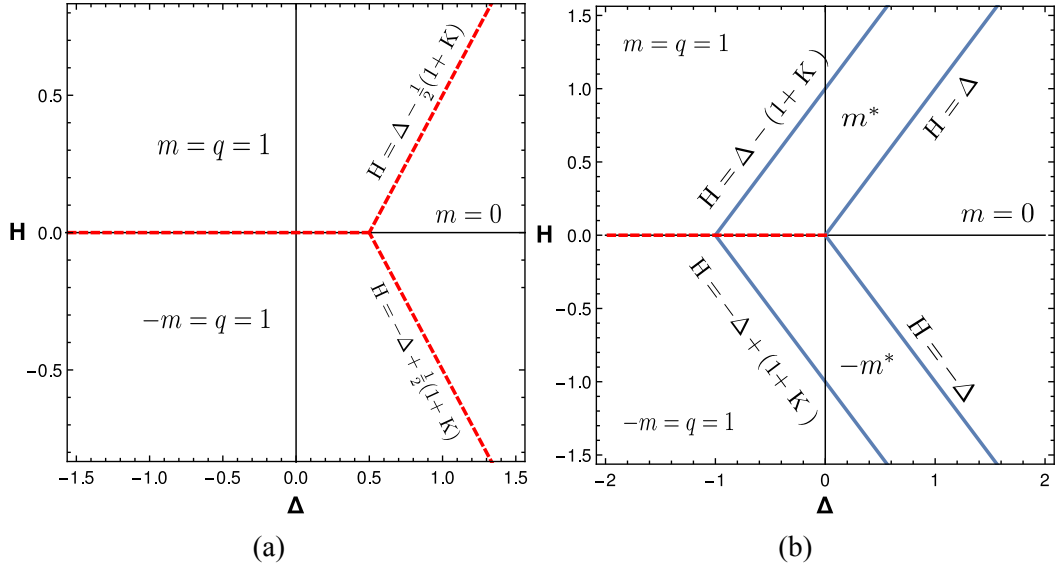
Figure 5.2: Ground state phase diagram of the BEG model in the $\Delta - H$ plane. The red dashed lines denote first order transition lines and the solid blue line denotes lines of continuous transition. for **(a)** $-1 \leq K < \infty$ and, **(b)** $K < -1$.

The rate function $R(x_1, x_2)$ for the non interacting Hamiltonian then can be evaluated using Gärtner Ellis theorem [215] and is given by :

$$R(x_1, x_2) = \sup_{k_1, k_2} \left[x_1 k_1 + x_2 k_2 \quad - \quad \log\left(1 + 2e^{k_2 - \beta\triangle} \cosh(k_1 + \beta H)\right)\right]$$
$$+ \quad \log\left(1 + 2e^{-\beta\triangle} \cosh \beta H\right)] \tag{5.4}$$

Minimizing the above equation w.r.t k_1 and k_2 gives the following relations between the order parameters and the minimas of k_1 and k_2 :

$$x_1 = \frac{2e^{k_2^* - \beta\triangle} \sinh k_1^*}{1 + 2e^{k_2^* - \beta\triangle} \cosh k_1^*} \tag{5.5}$$

$$x_1 = \frac{2e^{k_2^* - \beta\triangle} \cosh k_1^*}{1 + 2e^{k_2^* - \beta\triangle} \cosh k_1^*} \tag{5.6}$$
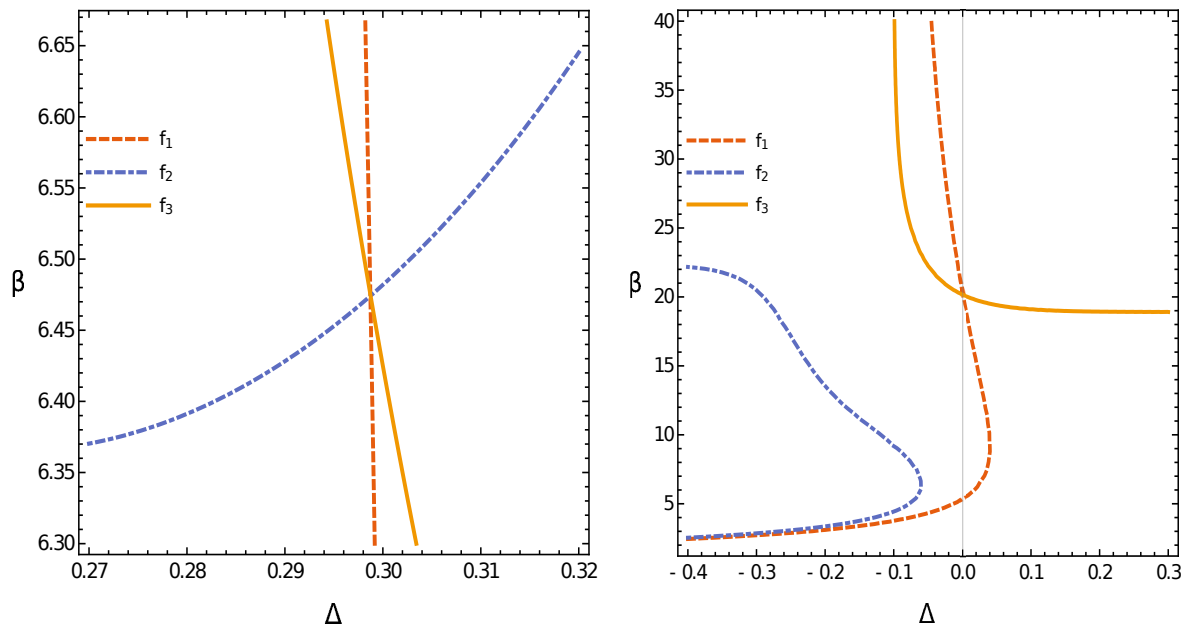
Figure 5.3: Plot of f_1, f_2 and f_3 in $\beta - \Delta$ plane. **(a)** $K = -0.4$ at $H = 0$. The intersection of the three derivative lines give the critical point at a non-zero value of m, which gives the locus of the BEP at which the $\lambda_{\pm}$ lines meet in the $H = 0$ plane. **(b)** $K = -2$ at $H = 0$. The three lines never intersect simultaneously for any value of m, which shows that there are no critical points.

Using tilted LDP we generate a new large deviation principle (LDP) from an old LDP by a change of measure and we find the full rate function to be :

$$I(x_1, x_2) = x_1 k_1^* + x_2 k_2^* - \Lambda(k_1^*, k_2^*) - \frac{\beta x_1^2}{2} - \frac{\beta K x_2^2}{2} - \inf_{k_1, k_2}[R(k_1, k_2) - \frac{\beta k_1^2}{2} - \frac{\beta K k_2^2}{2}]$$

(5.7)

Minimization of the rate function w.r.t x_1 and x_2 gives the following two coupled equations for the two order parameters:

$$m = \frac{2e^{\beta(Kq-\Delta)}\sinh\beta(m+H)}{1 + 2e^{\beta(Kq-\Delta)}\cosh\beta(m+H)}$$

(5.8)

$$q = \frac{2e^{\beta(Kq-\Delta)}\cosh\beta(m+H)}{1 + 2e^{\beta(Kq-\Delta)}\cosh\beta(m+H)}$$

(5.9)

where m and q are the extremums of x_1 and x_2. For $m \neq 0$, the two fixed point equations are connected via:

$$q = m\coth\beta(m+H)$$

(5.10)

and the minima of the rate function $I(x_1, x_2)$ gives the free energy functional at the fixed point and can be written as (using Eq. 5.10);

$$
\begin{aligned}
f(m) &= \frac{\beta m^2}{2} + \frac{\beta K m^2 \coth^2 \beta m}{2} + \log\left(1 + 2e^{-\beta\Delta}\cosh\beta H\right) \\
&- \log\left(1 + 2e^{\beta(Km\coth\beta m - \Delta)}\cosh\beta(m+H)\right)
\end{aligned}
$$

(5.11)

For $H = 0$, the system has a line of continuous transition (λ line) in the $(T - \Delta)$ plane. The equation of this line can be obtained by linearizing Eq. 6.3. On linearizing we get the equation of the λ line to be:

$$2(\beta - 1) = e^{\beta(\Delta - K)}$$

(5.12)

For $H \neq 0$, we calculate the $\lambda_\pm$ lines using the condition mentioned in Chapter 3 : $f'(m) = f''(m) = f'''(m) = 0$ and $f''''(m) > 0$. This gives the following equations:
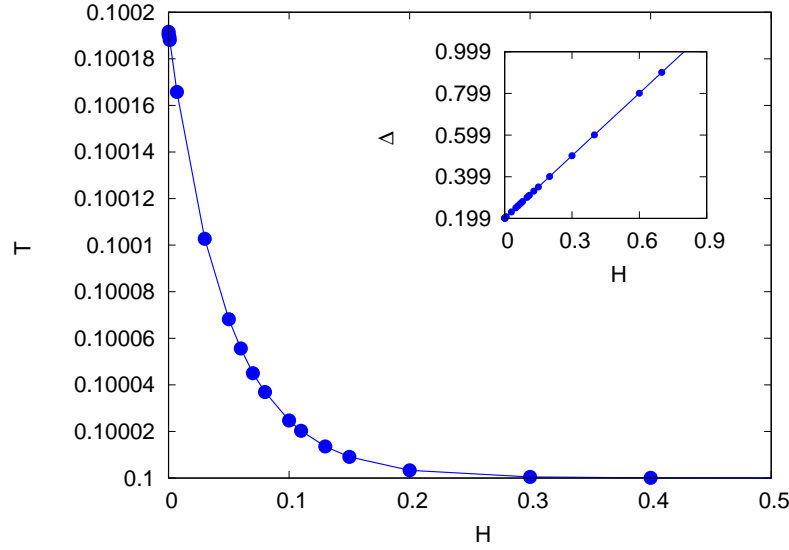
Figure 5.4: The value of temperature (T) and the crystal field (Δ) as a function of H along the λ_+ line in canonical ensemble for $K = -0.6$. The main plot shows that the temperature decreases exponentially with H and it saturates towards a certain temperature (T_{sat}) for high magnetic field. The inset shows how Δ increases linearly with H.

$$f_1 \equiv m - \frac{az}{C} = 0 \tag{5.13}$$

$$f_2 \equiv \frac{1}{za\beta} - \frac{azy^2 + \sqrt{y^2 + 1}\,y + yK(\sqrt{y^2 + 1} - \beta my^2)}{C^2} = 0 \tag{5.14}$$

$$f_3 \equiv \frac{\beta^3 z}{C^3} \left(azK^2 \sqrt[3]{y^2 + 1} - K(y^2 + 1)y\left[(2 + K) + 2az(1 + K)my\beta\right]\right.$$

$$+\sqrt{y^2 + 1}\left[az(1 + 2K) + 2\beta K^2 my^3 + \beta^2 azK^2m^2y^4\right]$$

$$-y\left[1 - 2a^2z^2 + 2\beta Kazym - 2Ky^2 - 2\beta azKmy^3 + \beta^2 K^2m^2y^4\right] \right) = 0 \tag{5.15}$$

where $a = e^{-\beta\Delta}$, $y = cosech\,\beta(H + m)$, $z = 2e^{\beta Km\coth\beta(H+m)}$, and $C = \sqrt{y^2 + 1}za + y$. For $K = 0$, the above equations reduce to the equations for pure Blume-Capel model (shown in Chapter 3 given by Eqs. 3.22, 3.23, 3.24, 3.26, 3.27):

For $K \neq 0$ solving Eq. 5.13- 5.15 is not possible analytically. Hence we use graphical methods to get the co-ordinates of the critical points in the $(T - \Delta - H)$ space for a given

K. We plot f_1, f_2 and f_3 in $(\beta - \Delta)$ plane for m, fixing K and changing different values of H. The value of m for a fixed value of H and K at which three equations meet gives the co-ordinates of the critical point. If we now take $H = 0$ in Eq. 5.13, 5.14 and 5.15, then we will get the co-ordinates of the point of intersection of the $\lambda_\pm$ lines in the $(T - \Delta)$ plane. We can hence use this to locate the multicritical points (TCP and BEP) in the $(T - \Delta)$ plane. We use this to obtain the phase diagram for various values of K. For example: Fig. 5.3(a) is the contour plot of f_1, f_2 and f_3 in the $(\beta - \Delta)$ plane at $K = -0.4$ and $H = 0$. The intersection of the three functions gives the co-ordinates of the critical point. We find that for $K > -0.1838$ the functions intersect only for $m = 0$, which is the point where the $\lambda_\pm$ lines meet the λ line. Hence this point is the TCP. For the range $-0.1838 > K > -1$ we find that the intersection occurs for $m \neq 0$. This $m \neq 0$ solution gives the locus of the BEP where the $\lambda_\pm$ lines meet the $H = 0$ plane in this regime of K. Interestingly, we find that for $K < -1$ the three functions never intersect at the same point for any m. For example in Fig. 5.3(b) we plot three functions for $K = -2$. We will discuss these results in detail in the next section (Sec. 5.3.1).

5.3.1 Repulsive Blume-Emery-Griffiths model

In this section we analyze the results of the repulsive BEG model. We find that for $0 \geq K \geq -0.1838$ two critical lines ($\lambda_\pm$) at $H \neq 0$ meets the λ line (at $H = 0$) at the TCP. Temperature decreases exponentially and Δ increases linearly with increasing H along the $\lambda_\pm$ lines, as shown in Fig. 5.4. As K becomes more negative (for $-0.1838 > K > -1$), the ($\lambda_\pm$) lines no longer meet the λ line, instead they enter into the ordered region and meet at the first order surface ($H = 0$) at a BEP. The λ line in this case terminates on the first order line at a CEP.

As K approaches -1, the wing width in temperature (which is the difference between the temperature at the BEP (T_{BEP}) and the saturation value of the temperature (T_{sat}) at
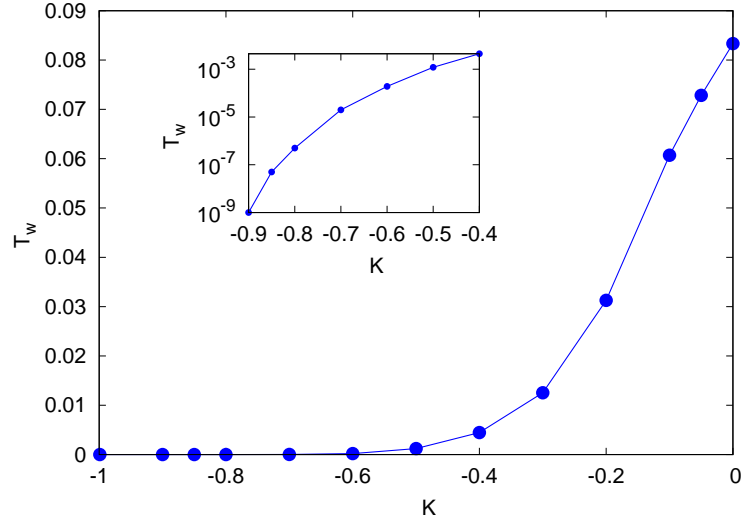
Figure 5.5: The width of the wings in temperature (T_w) as a function of K for the repulsive BEG model. The main plot shows that as K decreases, the width in temperature goes to zero. The inset is the semi-log plot for the same.

which both the Δ, $H \to \infty$) denoted as T_w, starts to shrink. At exactly $K = -1$ the BEP, CEP, and the T_w reach zero. As we decrease K further, we find that there are no transitions in the H plane. This is also supported by the fact that now there are no multicritical points in the ($T - \Delta$) plane. Hence we conclude that for $K < -1$ the wing surfaces completely disappear. The phase diagram consists of only a continuous transition line (λ line) from ferromagnetic phase to paramagnetic phase in the $H = 0$ plane. For large negative K, the area enclosed by the λ line in the ($T - \Delta$) plane shrinks. At $K \to -\infty$, there is no phase transition, only the $s = 0$ state dominates. The decreasing width of the wings with decreasing K is shown in Fig. 5.5. We also observe that the T_{sat} can be approximated numerically as $T_{sat} \simeq (K + 1)/4$. This will be discussed in more detail in Sec. 5.4.1, where we obtain the similar results in the microcanonical ensemble. The values of the T_w, T_{sat} and the co-ordinates of the multicritical points (TCP, BEP) for the repulsive BEG model are listed in Table 5.1.

Absence of phase transition for $K < -1$ in the H plane can also be seen by looking

145
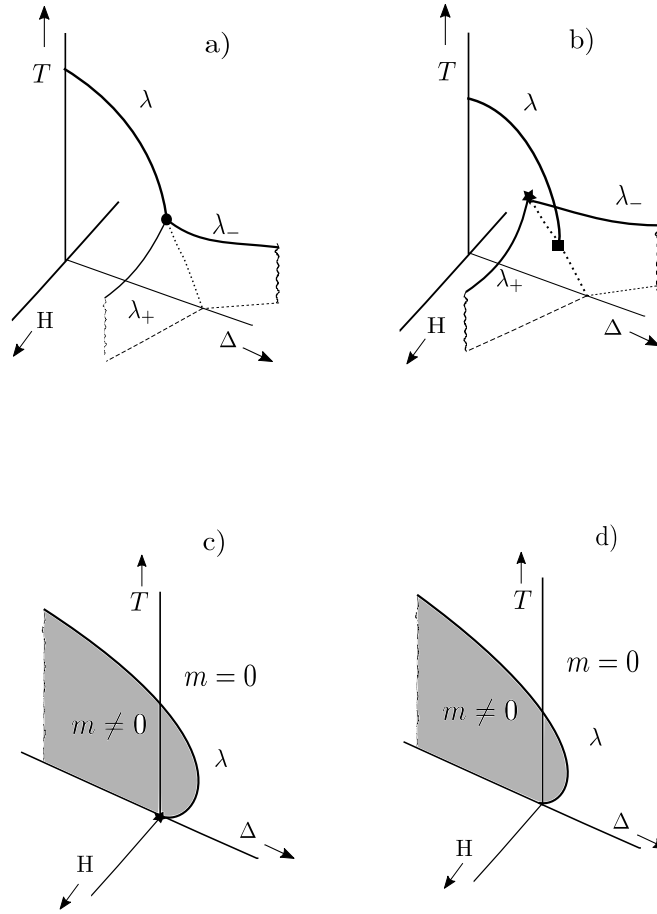
Figure 5.6: Schematic phase diagram of the repulsive BEG model in the $(T - \Delta - H)$ space for both canonical and microcanonical ensembles. Solid lines represent the critical lines (λ, $\lambda_{\pm}$) and the dashed lines represent the lines of first order transition. The λ line is the line of continuous transition between the ferromagnetic phase ($m \neq 0$) and the paramagnetic phase ($m = 0$) in the $H = 0$ plane, whereas the $\lambda_{\pm}$ lines are the line of continuous transition in the $\pm H$ planes respectively. The solid circle represents the tricritical point (TCP), where the λ and $\lambda_{\pm}$ lines meet. The star symbol represents the bicritical end point (BEP), where the $\lambda_{\pm}$ lines meet inside the ordered region. The square symbol represents the critical end point (CEP), where the λ line terminates on the first order line. **(a)** Shows the phase topology in the *Canonical ensemble*, for the range: $-0.1838 \leq K \leq 0$ and in the, *Microcanonical ensemble* for: $-0.0828 \leq K \leq 0$. In this regime the critical lines ($\lambda_{\pm}$) meet the λ line at the TCP. **(b)** Is the phase topology in the *Canonical ensemble* for the range: $-1 < K < -0.1838$ and, in the *Microcanonical ensemble* for the range: $-1 < K < -0.0828$. Here the $\lambda_{\pm}$ lines move inside the ordered region and meet at the BEP. The λ line terminates on the first order line at a CEP. **(c)** Shows the phase topology for both *Canonical* and, *Microcanonical ensembles* at $K = -1$. In both the ensemble the wings as well as the BEP and CEP reaches $T = \Delta = 0$. **(d)** Topology of the phase diagram for $K < -1$ for both the *Canonical* and, *Microcanonical ensembles*. Only the λ transition remains. The only transition is from the ferromagnetic state to the paramagnetic state in the $H = 0$ plane.

Canonical: $-1 \leq K \leq 0$				
K	TCP / BEP		T_{sat}	T_w
	T	Δ	$\simeq (K+1)/4$	$(= T_{TCP/BEP} - T_{sat})$
0	0.33333	0.462098	0.25	0.0833333
-0.05	0.3103448	0.44741	0.237501	0.072843316
-0.1	0.2857142	0.431268	0.2250124	0.0607018
-0.2	0.2312737	0.391831	0.2	0.03127376
-0.3	0.1875335	0.346377	0.17499956	0.01253394
-0.4	0.15446222	0.298727	0.14999925	0.00446297
-0.6	0.100192068	0.199958	0.1	0.000192068
-0.7	0.075009189	0.149998	0.07500018	0.000009009
-0.8	$\simeq 0.05000025$	$\simeq 0.1$	$\simeq 0.049999875$	$\simeq 0.000000375$
-0.9	$\simeq 0.024999969$	$\simeq 0.05$	$\simeq 0.024999968$	$\simeq 0.000000001$
-0.999	$\simeq 0.00025$	$\simeq 0.0005$	$\simeq 0.00025$	$\simeq 0.00$

Table 5.1: Co-ordinates of the TCP and BEP for different K's. T_{sat} is the saturation value of the temperature at which both the Δ and $H \to \infty$. T_w is the width of the wing lines for different K

at the magnetization and susceptibility. We find that the magnetic susceptibility diverges around the expected critical point for $K > -1$. On the other hand for $K \leq -1$ magnetic susceptibility is finite in the entire H plane. We plot the magnetization and the susceptibility for $H = 0.5$ at $K = -0.6$ and $K = -1.2$. In Fig. 5.7(a) we plot them as a function of Δ for $K = -0.6$, by fixing $T = 0.1$. The susceptibility shows singular behaviour at $\Delta = 0.7$. The point of divergence matches with the co-ordinates of the transition obtained from Eq. 5.13, 5.14 and 5.15. On the other hand for $K = -1.2$, we find no such divergence. In Fig. 5.7(b) for $K = -1.2$ by fixing $T = 0.025$ we plot the magnetization and find that it changes continuously along Δ and the susceptibility shows a cusp but does not diverge. Though we plot only for a fixed T, we have checked the entire plane by changing the values of T. Magnetic susceptibility has no divergence for any T.

The vanishing of the wings can also be anticipated from the ground state phase diagram of the BEG model in Sec. 5.2. For any $-1 \leq K < \infty$, the $\Delta - H$ phase diagram at

147

the ground state shows first order transition lines separating the different phases (see Fig. 5.2a). These lines of first order transition extend to the finite temperature and gives rise to the wings. Whereas, the ground state phase diagram in the finite H plane consist only of lines of second order transition (shown in Fig. 5.2b) which might not extend to finite temperatures.

5.3.2 Attractive Blume-Emery-Griffiths model

The attractive BEG model has been extensively studied earlier by various authors [266, 270, 271, 272, 273, 274, 275, 276, 147, 148, 289, 277, 278, 158] and the topology of the phase diagram is known as a function of K in the $(T - \Delta)$ plane. We observe the similar topology of the phase diagram. We study the $(T - \Delta - H)$ phase diagram and find that the topology of the phase diagram for different K's are similar to [158]. To recap we find : For $0 < K \leq 2.78$, the phase diagram is similar to what we find for $0 \geq K \geq -0.1838$. The $\lambda_{\pm}$ meets at the TCP. For $2.78 < K < 3$ a new first order surface appears separating two paramagnetic states: P2 ($m = 0$, $q_- < 0.5$) and P1 ($m = 0$, $q_+ > 0.5$). This surface meets the first order line (at $H = 0$) at a triple point. This new first order surface terminates on a line of critical points(at $H \neq 0$ plane). As K changes from $K = 2.78$, this line of critical points in the paramagnetic region moves higher in temperature and at exactly $K = 3$ it intersects the $\lambda_{\pm}$ lines and then extends to infinity. For $3 < K \leq 3.8$, the $\lambda_{\pm}$ lines terminates at the first order surface which separates the P1 and P2 phase, and becomes finite. For $K > 3.8$, the λ line terminates at a CEP, and thus the wings vanish.

We observe that for $K > 1$, the wings show non-monotonic behaviour in temperature in contrast to what happens in the range of $-1 < K < 1$(Fig. 5.4). For small values of H, the $\lambda_{\pm}$ lines go towards lower T and higher Δ. As H becomes larger, these lines start moving towards higher Δ and higher T as shown in Fig. 5.8. This non-monotonic behaviour observed in the wings for all $K \geq 1$ values can be interpreted as follows : For any positive

(a)

(b)
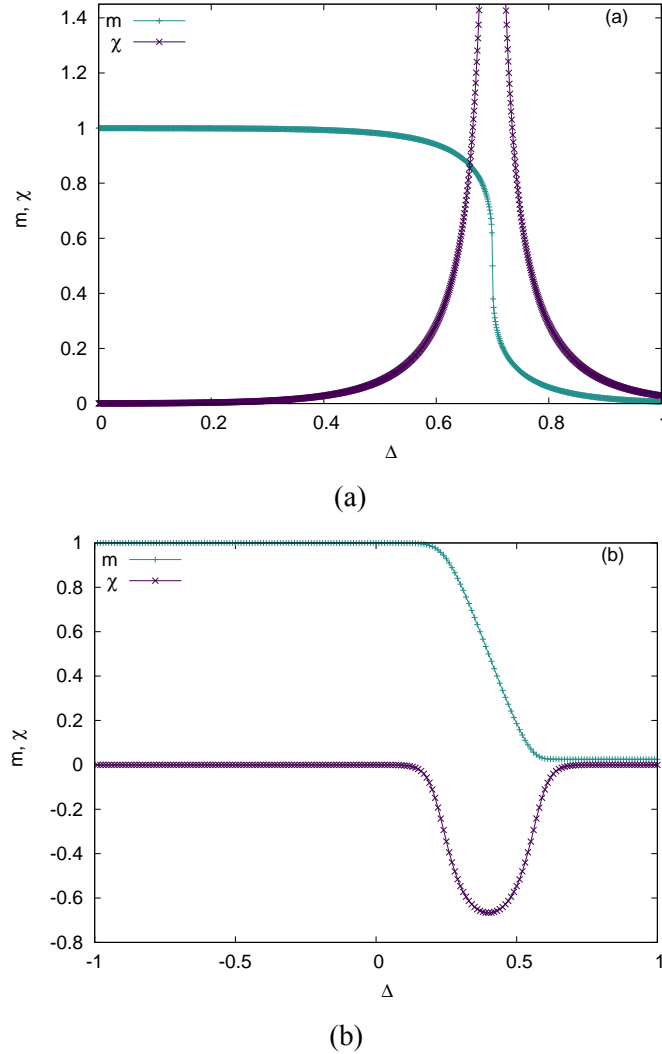
Figure 5.7: Magnetization (m) and magnetic susceptibility (χ) as a function of Δ for **(a)** $K = -0.6$, $T = 0.1$ and $H = 0.5$. This shows that the m goes to zero continuously around $\Delta = 0.7$. Also the χ has a singularity at the same Δ which suggests that there is a second order transition in the $H \neq 0$ plane, **(b)** $K = -1.2$, $T = 0.025$ and $H = 0.5$. Both the m and χ changes continuously as a function of Δ. Magnetic susceptibility (χ) shows no singularity or discontinuity and there is no phase transition in the finite H plane.
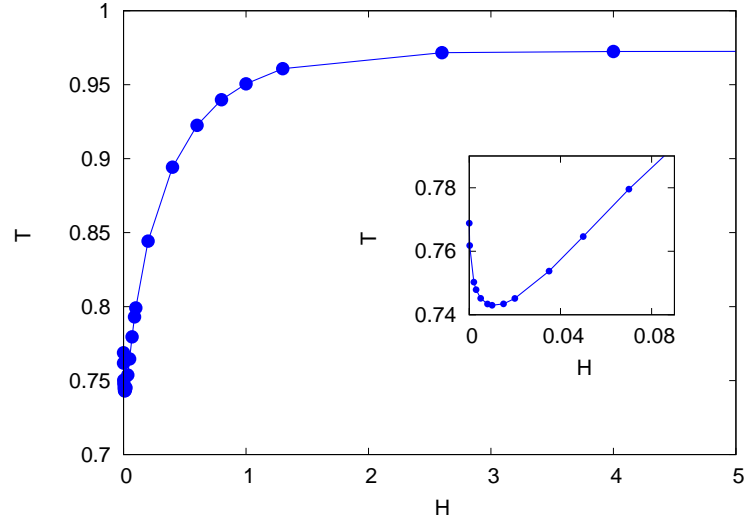
Figure 5.8: Plot for the non-monotonic behaviour of temperature (T) as a function of magnetic field (H) along the λ_+ line for $K = 2.89$. The inset shows that for lower H, T decreases with H like before, but for higher H it increases and saturates to a higher value (T_{sat}) shown in the main plot.

K, there are two possible solution of q for a fixed value of energy, $q_\pm$ (more details are in Sec. 3.6) with $q_+ > q_-$. When $K \geq 1$, the first term in the energy ϵ (mentioned in Sec. 5.1) dominates over the crystal field term and the density of $s = \pm 1$ spin increases. For smaller values of H the q_- solution dominates in the system and the wings show monotonic behaviour like before. As H increases further the q_+ solution becomes favorable which in turn lowers the energy. Thus the energy-entropy balance occurs at a higher temperature.

5.4 Microcanonical ensemble

In order to analyze the system in the microcanonical ensemble, we need to express the energy in terms of the number of particles with spin ± 1 and 0. Let us assume the number of particles with ± 1 spin are $N_\pm$ and the number of particles with zero spins are N_0, such that $N = N_+ + N_- + N_0$, where N is the total number of particles in the system. The energy

of the system can thus be written as,

$$E = \Delta Q - \frac{1}{2N}M^2 - \frac{K}{2N}Q^2 - HM \tag{5.16}$$

where $M = N_+ - N_-$ is the total magnetization and $Q = N_+ + N_-$ is the spin density of the system. In terms of $m\,(= M/N)$ and $q\,(= Q/N)$, the expression for the energy will be,

$$\epsilon = \Delta q - \frac{1}{2}m^2 - \frac{K}{2}q^2 - Hm \tag{5.17}$$

where, $\epsilon = \frac{E}{N}$ is the energy per particle, m and q are the single site magnetization and density(as mentioned in Sec. 5.1). The total number of microstates of the system can be written in terms of N, N_+, N_- and N_0 as,

$$\Omega = \frac{N!}{N_+!N_-!N_0!} \tag{5.18}$$

In the limit when N_+, N_-, N_0 are large, the expression for entropy, i.e., $S = k_B\,ln(\Omega)$ can be written by using Stirling approximation as,

$$s = \frac{S}{k_B N} = q\,ln(2) - (1-q)ln(1-q) - \frac{1}{2}(q+m)ln(q+m) - \frac{1}{2}(q-m)ln(q-m) \tag{5.19}$$

where, s is the entropy per particle of the system. The equilibrium entropy can be obtained by maximizing the entropy of Eq. 5.19 with respect to m and q. We can express q in terms of m and the other variables as,

$$q_\pm = \frac{\Delta}{K} \pm \gamma^{1/2} \tag{5.20}$$

where, $\gamma = \left(\frac{\Delta}{K}\right)^2 - \frac{2\epsilon}{K} - \frac{m^2}{K} - \frac{2Hm}{K}$. For $K = 0$, the expression has a much simpler form, $q = \frac{1}{\Delta}\left(\epsilon + \frac{1}{2}m^2 + Hm\right)$.

Since, there are two values of q, the one which is in the range $[0, 1]$ will be accepted. There is also a possibility that both the q values are in the range $[0, 1]$, then the equilibrium

entropy will be the one with maximum value at its corresponding equilibrium m. We find that for $K < 0$, only q_- is acceptable, however, for $K > 0$, both the $q_\pm$ solutions are acceptable.

Next, we aim to find the second order transition line in the $(T - \Delta - H)$ space. In the $H = 0$ plane, the value of the magnetization m on the line of continuous transition is zero, however, for any nonzero H, the magnetization m will have a nonzero value on the continuous transition line. In order to obtain this continuous transition line, we need to equate the first three derivatives of s (with respect to m) to zero, with the constraint that the fourth derivative will be negative. The first four derivatives of the entropy s are:

$$\frac{\partial s}{\partial m} = q' \, ln\left\{ \frac{2(1-q)}{\sqrt{q^2 - m^2}} \right\} - ln\sqrt{\frac{q+m}{q-m}} \tag{5.21}$$

$$\frac{\partial^2 s}{\partial m^2} = q'' \, ln\left\{ \frac{2(1-q)}{\sqrt{q^2 - m^2}} \right\} - \frac{q'^2}{1-q} - \frac{1}{2}\left\{ \frac{(q'+1)^2}{q+m} + \frac{(q'-1)^2}{q-m} \right\} \tag{5.22}$$

$$\frac{\partial^3 s}{\partial m^3} = q''' \, ln\left\{ \frac{2(1-q)}{\sqrt{q^2 - m^2}} \right\} - \frac{q'^3}{(1-q)^2} + \frac{1}{2}\left\{ \frac{(q'+1)^3}{(q+m)^2} + \frac{(q'-1)^3}{(q-m)^2} \right\}$$
$$- \frac{3}{2}\left\{ \frac{2q'q''}{1-q} + \frac{q''(q'+1)}{q+m} + \frac{q''(q'-1)}{q-m} \right\} \tag{5.23}$$

$$\frac{\partial^4 s}{\partial m^4} = q'''' \, ln\left\{ \frac{2(1-q)}{\sqrt{q^2 - m^2}} \right\} - 2q'''\left\{ \frac{q'+1}{q+m} + \frac{q'-1}{q-m} + \frac{2q'}{1-q} \right\}$$
$$+ 3q''\left\{ \frac{(q'+1)^2}{(q+m)^2} + \frac{(q'-1)^2}{(q+m)^2} - \frac{2q'^2}{(1-q)^2} \right\} - \frac{3}{2}q''^2\left\{ \frac{2}{1-q} + \frac{1}{q+m} + \frac{1}{q-m} \right\}$$
$$- \frac{(q'+1)^4}{(q+m)^3} - \frac{(q'-1)^4}{(q-m)^3} - \frac{2q'^4}{(1-q)^3} \tag{5.24}$$

where, q', q'' ...... are partial derivatives of q w.r.t. m. We solve the above first three equations numerically and obtain a set of physical solutions (Δ, ϵ, m), such that the fourth derivative is negative. We then calculate the temperature, using the relation $\beta = \frac{\partial s}{\partial \epsilon}$,
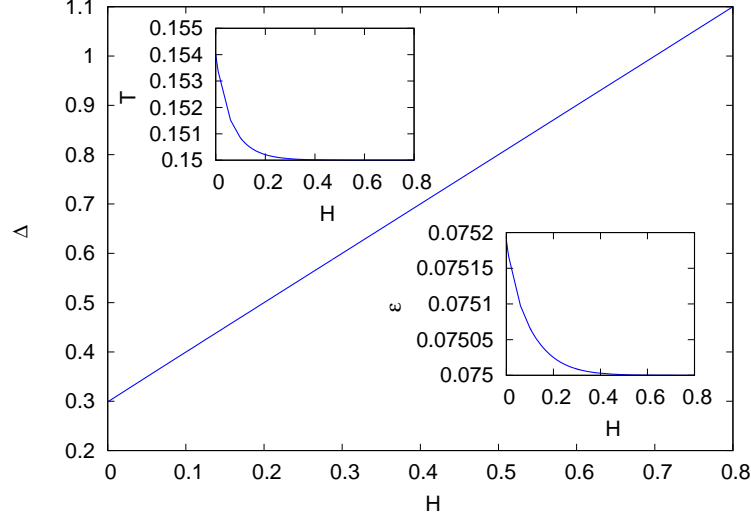
Figure 5.9: The value of crystal field (Δ) and temperature (T) along the λ_+ line at $K = -0.4$ in the microcanonical ensemble. The main plot shows the λ_+ line in the $\Delta - H$ plane, where the value of Δ increases almost linearly with H. From our numerical data, the variation of this line comes out to be $\Delta \simeq (K+1)/2 + H$. **Bottom Inset**: The λ_+ line in the $\epsilon - H$ plane. The value of ϵ decreases and finally saturates at ϵ_{sat}, which is numerically predicted to be $(K+1)/8$. **Top Inset**: The λ_+ line in the $T - H$ plane, showing similar qualitative behaviour as in the $\epsilon - H$ plot. The value of T saturates for large H at $(K+1)/4$.

$$\beta = \mp \frac{1}{K\gamma^{1/2}} ln \left\{ \frac{2(1-q_\pm)}{\sqrt{q_\pm^2 - m^2}} \right\} \tag{5.25}$$

which gives the equivalent phase diagram in the $(T - \Delta - H)$ space.

5.4.1 Repulsive Blume-Emery-Griffiths Model

In this section, we show our results for repulsive BEG model in the microcanonical ensemble in the $(T - \Delta - H)$ space. In the absence of magnetic field, this model has been recently studied in [277, 287]. We find that for $-0.0828 \leq K \leq 0$ the phase diagram consists of a TCP where the $\lambda_\pm$ lines meet the λ line in the $H = 0$ plane. As the K decreases further, for $-1 < K < -0.0828$, it was reported earlier in [287] that a critical point (CP) appears in the ordered region of the system along with a CEP. In this topology, as we switch on the field H, we note that the $\lambda_\pm$ lines meet at the proposed CP. Thus, the CP is actually a BEP.

We show our results for $K = -0.4$ in the (Δ, H), (ϵ, H) and (T, H) plane in Fig. 5.9. Here, we show the behaviour of the λ_+ line for positive H. We note that the value of Δ on the λ_+ line increases with H almost linearly in the large H limit. The values of ϵ and the T decreases with H and saturates for large H. We note that the variation of Δ in the large H limit is of the type, $\Delta \simeq (K+1)/2 + H$. Also, the saturation values are, $\epsilon_{sat} \simeq (K+1)/8$ and $T_{sat} \simeq (K+1)/4$. The values of (Δ, ϵ, T) for BEP and the saturation values of ϵ and T are listed in Table 5.2.

On the $\lambda_{\pm}$ line, the variation of Δ and ϵ (or T) in the limit $H \to \infty$ can be explained in a simple way. In the limit $H \to \infty$, we can safely assume that there are no particles with spin -1, or in other words, $N_- = 0$. Thus, q will be equal to m. In this limit, the entropy of the system (per particle) can be written as, $s = -(1-m)ln(1-m) - mln(m)$, having a maximum at $m = 1/2$. Now, the energy per particle, in this limit, turns out to be, $\epsilon \to \{(\Delta - H)/2 - (K+1)/8\}$. In order for the energy (per particle) to be finite on the transition line, Δ should also increase linearly with H. We indeed get the linear variation of Δ with H on the $\lambda_{\pm}$ line. If we use the variation of Δ as approximated numerically, i.e., $\Delta \simeq (K+1)/2 + H$, we can estimate the saturation value of $\epsilon \to \epsilon_{sat} \simeq (K+1)/8$. Using these values in the expression for calculating the temperature (Eq. 5.25), it can be easily shown that the saturation of T will be $T_{sat} \simeq (K+1)/4$. Hence, the saturation values of ϵ and T will become zero for $K = -1$.

We measure the width of the wings in energy(and temperature). We denote it by ϵ_w (and T_w). We also list the saturation values of ϵ and T and the width of the wings (ϵ_w and T_w) in Table 5.2. We plot the BEP and the width of the wings (ϵ_w and T_w) in Fig. 5.10. We note that the BEP tends to $\epsilon = T = 0$ as $K \to -1$. The width of the wings are also found to decrease exponentially and tends to zero as K tends to -1. From all the above observations, it is clear that at $K = -1$ the width of the wings vanish and BEP reaches $\epsilon = T = 0$. Thus, for $K \leq -1$, there is no phase transition in the non-zero H plane for a finite T.

K	TCP / BEP			Microcanonical: $-1 \leq K \leq 0$			
	Δ	ϵ	T	ϵ_{sat} $\simeq (K+1)/8$	T_{sat} $\simeq (K+1)/4$	ϵ_w $(= \epsilon_{TCP/BEP} - \epsilon_{sat})$	T_w $(= T_{TCP/BEP} - T_{sat})$
0	0.46240	0.15275	0.33033	0.12502	0.25007	0.02773	0.08026
-0.05	0.44741	0.14125	0.31032	0.11875	0.23750	0.0225	0.07282
-0.1	0.43079	0.12556	0.27964	0.11250	0.22500	0.01306	0.05464
-0.2	0.39100	0.10343	0.22454	0.10000	0.20000	0.00343	0.02454
-0.3	0.34624	0.08837	0.18564	0.08750	0.17500	0.00087	0.01064
-0.4	0.29871	0.07519	0.15401	0.07500	0.15000	0.00019	0.00401
-0.5	0.24968	0.062529	0.126145	0.06250	0.12500	0.000029	0.001145
-0.6	0.19996	0.05000025	0.10001879	0.050000000	0.1000000000	0.0000025	0.0001879
-0.7	0.15	0.0375000615	0.075009205	00.03750000	0.0750000	0.000000061	0.0000092
-0.75	0.125	0.0312500035	0.06250078	0.031250000	0.0625000	0.0000000035	0.00000078
-0.8	$\simeq 0.1$	$\simeq 0.0250000000103$	$\simeq 0.0500000192$	$\simeq 0.025$	$\simeq 0.05$	$\simeq 0.0000000000103$	$\simeq 0.0000000000192$

Table 5.2: Co-ordinates of the multicritical points (TCP, BEP), saturation values of ϵ, T and the width of the wings for $-1 < K \leq 0$.
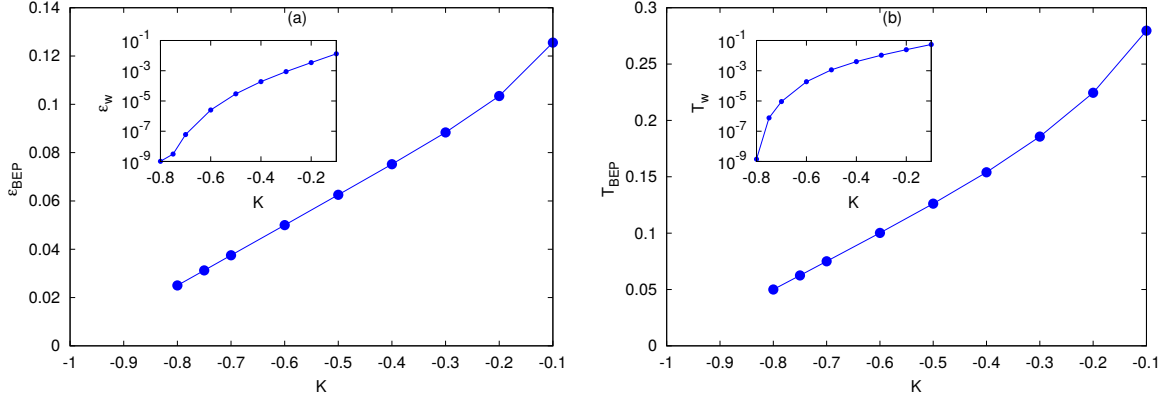
Figure 5.10: Variation of BEP and the width of the wings (ϵ_w and T_w) with K. (a) ϵ_{BEP} decreases as K tends to -1, and appears to meet at $\epsilon = 0$ at $K = -1$. Inset show the variation of the width of wings in ϵ. We note that the width decreases exponentially as K tends to -1. (b) T_{BEP} with K showing similar qualitative behaviour as ϵ_{BEP}. Inset show the width of the wings in temperature T_w, which also decreases exponentially as K tends to -1.

5.4.2   Attractive Blume-Emery-Griffiths model

The attractive BEG model has been studied earlier in microcanonical ensemble in [277], in the $(T - \Delta)$ plane. The full phase diagram$(T - \Delta - H)$ was not studied before for the microcanonical ensemble as of our knowledge. In this section, we present results for the attractive BEG model in the $(T - \Delta - H)$ space. We find that, in the range $0 < K < 3$, the phase diagram is similar to the case $0 > K \geq -0.0828$. For $K > 3$, the λ line truncates on the first order line at a CEP. The first order line continues to exist in the paramagnetic region and becomes a surface in the $(T - \Delta - H)$ space which separates two paramagnetic phases P1 and P2(discussed before in Sec.5.3.2) and the wings no longer exist.

For small positive K, the variation of ϵ is monotonic with H on the $\lambda_{\pm}$ lines, similar to negative K. For large positive $K (\geq 1)$, however, the variation in ϵ is non-monotonic on the transition line as shown in Fig.5.11(a). This can be understood by separating the expression of ϵ into two parts: $\epsilon = \epsilon_1 + \epsilon_2$, where, $\epsilon_1 = \Delta q - \frac{1}{2}m^2 - Hm$ and $\epsilon_2 = -\frac{K}{2}q^2$. We note that the variation of ϵ_1 remains similar for small as well as large K, however, the variation of
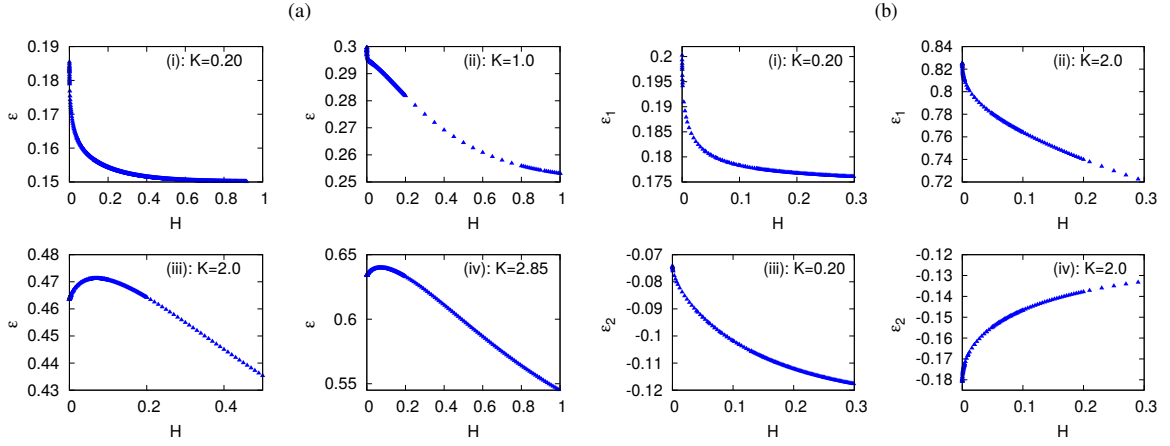
Figure 5.11: Non-monotonic variation of the ϵ as a function of H along the λ_+ line for positive K. (a) The variation of ϵ along the λ_+ line for various K. For small K, the curve is monotonic; ϵ decreases with H and then saturates. For large K, ϵ varies non-monotonically with H. (b) Variation of ϵ_1 and ϵ_2 for $K = 0.20$ and $K = 2.0$. The variation of ϵ_1 is similar for small and large K values, however, the qualitative nature in the variation of ϵ_2 is different for small and large K. This is the cause of the non-monotonic variation in ϵ.

ϵ_2 is different for small and large K. It decreases with H for small K while increases with H for large K (see Fig. 5.11(b)). The variation in ϵ_2 is mainly due to the variable q, which itself shows such behaviour. In ϵ_1 also, we have the variable q, but it appears with other terms. ϵ_1 does not change its qualitative behaviour when we change K. For small K, since both the ϵ_1 and ϵ_2 decreases with H, the sum also decreases with H. For large K, there is a competition between ϵ_1 and ϵ_2. In the small H regime, the variation in ϵ_2 dominates, which gives rise to an increase in ϵ with H. For large H, the variation in ϵ_1 starts dominating and ϵ decreases with H. For very large H, ϵ_1, ϵ_2 and ϵ will all finally saturate. The saturation values of ϵ follow similar relationship with K as obtained for the negative K. The variation of T also shows similar non-monotonic behaviour in the same range of K. We made similar observations in the canonical ensemble in Sec.5.3.2.

5.5 Ensemble inequivalence

Systems with long-range interactions shows some unusual characteristics compared to the short-range systems. For such systems the energy and other thermodynamic potentials (entropy, free energy, etc.) are non-additive, means the system cannot be divided into independent macroscopic parts which is the case for short range systems. Due to the non-additive nature of the interactions, it shows ensemble inequivalence. That means the phase diagrams can be different for different ensembles. There are numerous examples of long-range systems which shows ensemble inequivalence like : 2D geophysical flows [290], plasmas [291, 292], mean-field spin models [293, 294, 295, 296, 297] (where every spins interacts with other spins equally) and so on.

The inequivalence of different ensembles in the mean-field Blume-Emery-Griffiths model has been reported earlier in [277, 287] in the absence of magnetic field. In the $(T-\Delta)$ plane, while the λ line equation is same in both the ensembles, the first order line and the multicritical points are known to be located differently [298, 299, 293, 300]. It was reported that the TCP and other multicritical points are different for canonical and microcanonical ensembles for a given value of K [277, 287].

In this work, we have looked at all the three continuous transition lines($\lambda, \lambda_+, \lambda_-$) and the first order surfaces. We find that not just the multicritical points, the continuous transition lines λ_+ and λ_- are also different in the two ensembles. In fact, the ensemble inequivalence of the two ensembles can be seen as a consequence of this inequivalence. For $K = 0$, which corresponds to the Blume-Capel model, in Fig. 5.12, we plot the locus of the λ_+ line in two ensembles and one can see that they are different (λ_- line also behaves in a similar way). We plot the product of $\beta\Delta$ on the λ_+ line as a function of H for both the ensembles, and note that for $H \to 0$, these lines meet at different points, which is the TCP of their corresponding ensembles. For canonical ensemble, these $\lambda_\pm$ lines meet at $(\beta\Delta)_{TCP} \simeq 1.3863$,
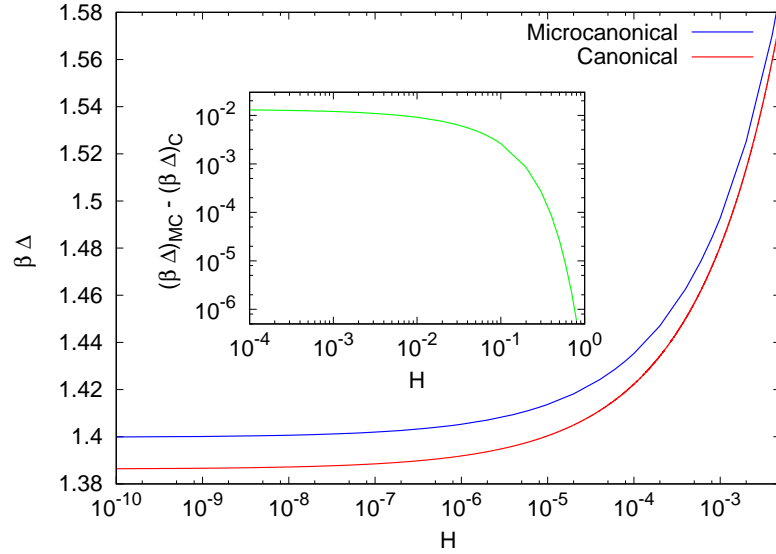
Figure 5.12: Ensemble inequivalence in the Blume-Capel model ($K = 0$). We show the locus of the λ_+ line (product of $\beta\Delta$) as a function of H, which is different for the two ensembles. In the inset, we plot the difference in the value of $\beta\Delta$ for the two ensembles, as a function of H. This value decreases to zero almost exponentially.

while for microcanonical ensemble, these lines meet at $(\beta\Delta)_{TCP} \simeq 1.3998$ (see Fig. 5.12). We also note that the λ_+ lines for the two ensembles become close to each other for large H. We plot the difference in the value of $\beta\Delta$ for the two ensembles for a given K, and plot it as a function of H in the inset of Fig. 5.12. We note that this value decreases exponentially to zero as H becomes large.

For non-zero K, the $\lambda_\pm$ lines meet the λ line at the TCP. This topology persists for $0 \geq K \geq -0.1838$ in the canonical ensemble, whereas for microcanonical ensemble this topology occurs for $0 \geq K \geq -0.0828$. As K decreases further (for canonical ensemble $-0.1838 < K < -1$ and for microcanonical ensemble $-0.0828 < K < -1$), the $\lambda_\pm$ lines move inside the ordered region and meet at BEP in the $H = 0$ plane. Interestingly, we find that the difference in the position of BEP and CEP in the two ensembles decreases with decreasing K and for $K = -1$ the two ensembles become equivalent. In Fig. 5.13(a), we plot the value of $\beta\Delta$ at the BEP for both the ensembles. We note that the value of

159

$\beta_{BEP}\Delta_{BEP}$ for the two ensembles becomes closer as $K \rightarrow -1$. In the inset of Fig. 5.13(a), we also plot the difference in the value of $\beta_{BEP}\Delta_{BEP}$ for microcanonical and canonical ensembles, and note that this difference decreases exponentially as $K \rightarrow -1$. Thus, for $K \leq -1$, we find that there is no ensemble inequivalence in the $H = 0$ plane.

We have shown in Sec. 5.3.1 and Sec. 5.4.1 that for $K \leq -1$, there is no phase transition for finite magnetic field in either of the ensembles and hence there are no wings. Thus there is no inequivalence in the $H \neq 0$ plane as well. For $K > -1$, however, we do have wings and the continuous transition lines λ_+ and λ_-, meet at its corresponding TCP or BEP for canonical and microcanonical ensembles in the limit $H \rightarrow 0$. Thus, the critical lines in the H plane are different for the two ensembles for $K > -1$. In Fig. 5.13(b), we plot the value of $\beta\Delta$ on the continuous transition line for $K = -0.3$, as a function of H for both the ensembles. We note that the two lines are different for small H, however, these lines tend to meet each other for large H. We measure the difference between the value of $\beta\Delta$ for the two ensembles for a given K, and plot it as a function of H in Fig. 5.13(b) inset. We note that this difference reaches zero almost exponentially as H increases. Thus, in the limit $H \rightarrow \infty$, these critical lines for both the ensembles become equivalent.

From the above discussion, it is clear that the ensemble inequivalence is observed for $K > -1$ with small H values, however, for $K \leq -1$, the phase diagrams in the two ensembles become equivalent. In previous literature [301, 302, 299, 303], where ensemble inequivalence with long-range interactions are studied, it was found that whenever the two ensembles (either micro-canonical/canonical or canonical/grand-canonical) have a continuous transition, the transition occurs at the same point. The phase diagrams of the two ensembles can however be different from each other when the phase transition becomes first order in one of the ensembles. This kind of behaviour is observed in many systems such as the spin-1 Blume-Emery-Griffiths (BEG) model [301, 302], the ABC model [299, 303] etc.

160
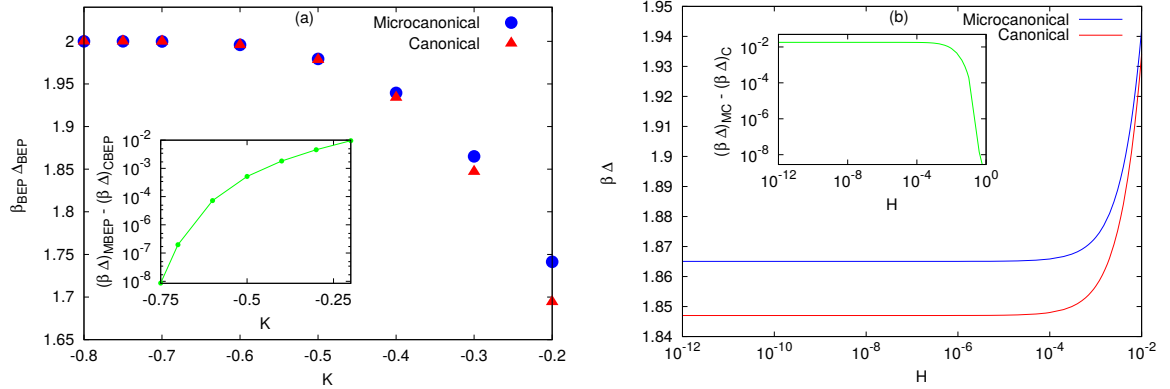
Figure 5.13: Ensemble inequivalence in the Blume-Emery-Griffiths model ($K \neq 0$). (a) The product of $\beta\Delta$ at the BEP, as a function of K. We note that the difference in the $\beta_{BEP}\Delta_{BEP}$ decreases to zero as $K \to -1$. (b) The locus of λ_+ line (product of $\beta\Delta$) for $K = -0.3$, for the two ensembles. These lines are different in the two ensembles in the small H regime, however, the lines tend to become closer as H increases. In the inset, we plot the difference in the value of $\beta\Delta$ as a function of H, for the two ensembles. The difference decreases with increasing H.

However, this is not always true. Even the continuous transition point can be different in the two ensembles. For example in a generalized ABC model in Ref. [304], the canonical and grand-canonical ensembles are found to exhibit a second-order phase transition at different points in the phase space. In [298], a general statement is provided to check the possibility of ensemble inequivalence for continuous transition using Landau theory. The transition is observed for a system undergoing phase transition governed by some order parameter, 'μ_1' (say) in a given ensemble. This parameter can be the average magnetization in the case of a magnetic transition, or the difference in the density of the two phases for a liquid-gas phase transition. Then the model is considered within a 'higher' ensemble, where a certain thermodynamic variable, denoted by 'μ_2', is allowed to fluctuate, (within the 'lower' ensemble, 'μ_2' was kept at a fixed value). In the case where μ_2 is the energy, the two ensembles would correspond to the canonical and micro canonical ensembles, while in the case when μ_2 is the particle density, they would correspond to the grand-canonical and canonical ensembles. The system is thus described by the Landau free

energy denoted by $f(\mu_1, \mu_2)$. They found that [298] if $f(\mu_1, \mu_2) = f(-\mu_1, \mu_2)$, the two ensembles will be equivalent, when any of them shows a continuous transition. If on the other hand, $f(\mu_1, \mu_2) = f(-\mu_1, -\mu_2)$, the system will show ensemble inequivalence even for continuous transition.

In our case, μ_1 is the magnetization m, and μ_2 is the energy ϵ of the system. The lower ensemble in our case is thus the microcanonical ensemble and the higher one is the canonical. If we check the above symmetries, we note that neither of the conditions studied in [298] is satisfied. When we add a magnetic field term, the symmetry of the problem is broken and we find that we have ensemble inequivalence even when the two ensembles show second order transition.

5.6 Summary and conclusion

Spin-1 BEG model has been shown to successfully capture the physics of some higher order interactions and has been widely studied. The interplay between the different interaction terms gives rise to very interesting phase diagrams. We have studied the effect of K on an infinite range BEG model for both all the ranges of $-\infty < K < \infty$ in the $T - \Delta - H$ space. We have considered the canonical and microcanonical ensemble. The repulsive and attractive BEG model in both the ensemble has been studied earlier. This model is known to exhibit many multicritical points along with the first and second order line of transition.

The attractive BEG model has been well studied and we find results similar to as reported in the earlier studies in the $(T - \Delta)$ plane [266, 277, 278, 279, 283, 284, 285, 280, 281, 282]. The full phase diagram in the $(T - \Delta - H)$ space was studied only for the attractive BEG model in the presence of external field in the canonical ensemble [158]. We revisited the model and in our study of the $(T - \Delta - H)$ space, we found a non-monotonic behaviour of the wings in terms of temperature as K becomes greater than $K = 1$. This as

far as we know has not been reported earlier.

Though we have explored the phase diagram for the entire range of K, we mainly focused on the repulsive BEG model. We found that the competition introduced by the repulsive biquadratic interaction makes it a very interesting model to study. For small and intermediate negative K ($-1 < K \leq 0$), the model exhibits phase diagram similar to the topology of the phase diagram for the RCFBC model shown in Chapter 3 for the intermediate and weak disorder regime [213]. For the canonical ensemble the range of K for the first topology is $0 \geq K \geq -0.1838$, whereas for microcanonical ensemble it is $0 \geq K \geq -0.0828$. And for the second topology the range of K for canonical is $-0.1838 > K > -1$ and for microcanonical $-0.0828 > K > -1$. We also observed that as $K \to -1$, the width of the wings decreases. At exactly $K = -1$, the wing width in temperature becomes zero along with the CEP and BEP reaching $T = \Delta = 0$ in both canonical and microcanonical ensemble. And for all $K < -1$ there is no phase transition in the $H \neq 0$ plane. Interestingly for $K > -1$, we observe that the $\lambda_{\pm}$ lines are different in the two ensembles and they meet at different multicritical points in the $H = 0$ plane. For $K \leq -1$, we find that there is no phase transition in the H plane for both the ensembles. This indicates that the the ensemble inequivalence that are being observed in the $T - \Delta$ plane are actually the consequence of the ensemble inequivalence that occurs in the finite H plane.

Absence of transition in the finite H plane for $K \leq -1$ can be argued by looking at the ground state phase diagram shown in Sec. 5.2. The $\Delta - H$ phase diagram for the finite H values are first order only for $K \leq -1$, which extends in the finite temperature and terminates at the wings. Whereas, the phase diagram for all $K < -1$ consists of only second order line of transition for the $H \neq 0$ values which does not extend till finite T.

Chapter 6

Scaling behavior near different multicritical points

In this section we will study behaviour near different multicritical points that we encountered in our study of the disordered spin models. We will verify all the scaling arguments that has been reported earlier for TCP, CEP and BEP using the disordered spin-1 Blume-Capel model.

6.1   Multicritcal points

Multicritical points are ubiquitous in nature. There are many physical systems which exhibits multicritical point. Multicomponent fluid mixtures [7, 8, 9, 10], binary alloys [11], liquid crystals [12, 13], semiconducting alloys [14], metamagnets [15, 16, 17], super-fluidity [18, 19] etc to name a few. Multicritical points are critical points in a thermodynamic parameter space which can only be reached after tuning two or more thermodynamic parameters. In other way it can be said that the full phase diagram of a multicritical point is multidimensional [4, 6, 5].

An ordinary critical point (CP) is defined by an end of a coexistence region, where the two phases become a single phase. The signature of a CP is that it shows singularities in some of the thermodynamic observables. These singularities are expressed in terms of universal critical exponents, critical amplitude, critical amplitude ratio, scaling function etc. Depending on the dimensionality and symmetry of the system the CP falls into a universality class. The scaling relations near the CP are well studied and well understood [1, 2].

Tricritical point (TCP) is one of the most widely studied and well understood multicrit-
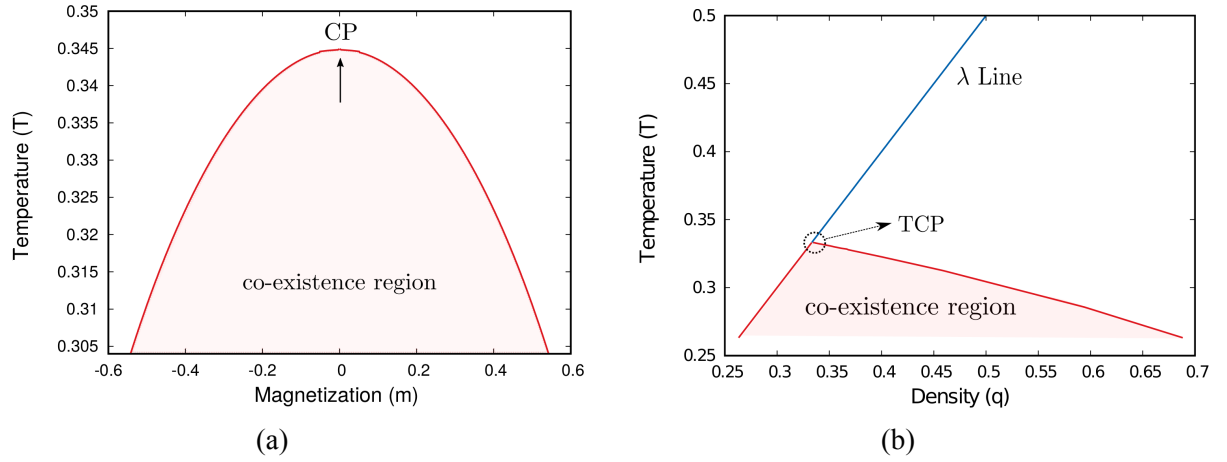
Figure 6.1: **(a)** Temperature(T) vs. magnetization (m) plot for Blume-Capel model. The red line is the magnetization coexistence region. The peak of the coexistence region ends at a critical point (CP). **(b)** Temperature(T) vs. density(q) plot for Blume-Capel model. The blue line denotes the co-ordinates of the λ line and the area under the red line is the density coexistence region. The λ line truncates at the peak of the coexistence region at a TCP.

ical points [6, 4]. As discussed in Chapter 1, TCP is an example of a multicritical point where three critical lines meet in the space of three fields (T, Δ, H in our model). Alternatively it can also be defined as a multicritical point at which a λ line meets at the peak of a phase separation curve. We also encountered other multicritical points in our study of disordered Blume-Capel model namely the critical end point (CEP) and bicritical end point (BEP). The CEPs are points where two phases become critical in presence of one or more non-critical phases, known as spectator phases [20]. On the other hand a BEP is a point of coexistence of two critical phases [213]. Presence of disorder or higher order interaction in a Hamiltonian can cause the emergence of such multicritical points in a system [213, 288].

The scaling hypothesis and universality class near the TCPs are well understood and have been verified in many models [305, 306, 307, 4]. In the $T - \Delta$ plane, both TCP and CEP separate line of CPs from a triple line of first order transition. It is generally accepted that the bulk critical exponents near a CEP are same as that of a CP [308]. Field-theoretic renormalization group theory has confirmed this realization on continuum models [309,

310]. Though there are further singularities that arise near a CEP in the bulk [311, 312, 313, 314, 5, 9, 10] and interfacial or surface tensions [242, 315, 316, 317]. The singularities in the bulk thermodynamics has been pointed out to be characterized by universal parameters [311, 312, 313, 314, 5, 9, 10], which is in contrast with the behaviour of the interfacial singularity [242, 315]. It was argued by Fisher [311] using scaling arguments that the non-analyticities of the first order surface near a CEP is related to the singularities of the critical line. This prediction was verified using spherical models [312, 313, 314, 5] and using eighth order Landau free energy expansion for isomorphous transitions [318, 240] and two order parameter Landau free energy expansion for ferroelectric materials [319]. Later, using an extensive Monte-Carlo simulation Wilding provided the first evidence of the singular behaviour on the first order phase boundary near CEP for a symmetrical binary fluid [9, 10]. Both the Fisher and the Wilding conjecture was verified for an asymmetric Ising model using Wang-Landau study on a triangular lattice [320, 321].

BEP is expected to fall in the Ising universality class [228, 322, 323]. Using the eighth order Landau expansion for isomophous transition it was asserted that near the BEP the phase boundary is analytic if the $\lambda_{\pm}$ lines that meet at the BEP are symmetric in nature and under same universality class [240]. And the critical exponents lies in the same universality class of the mean-field values of a critical point. Later, using extensive Monte-Carlo simulation this argument was proved by Plascak *et. al* [231] for spin 3/2 Blume Capel model.

The analysis of the above mentioned scaling relations has been done only on pure models. The emergence of a CEP and a BEP is completely different than that of a pure model as we observed in Chapter 3, 5. In such cases the TCP splits into a CEP and a BEP. We have studied the scaling hypothesis of these multicritical points for the spin-1 Blume-Capel model in presence of disorder (considering RCFBC model) and in presence of higher order interactions (the BEG model). Both of these models exhibits TCP as well as CEP depend-
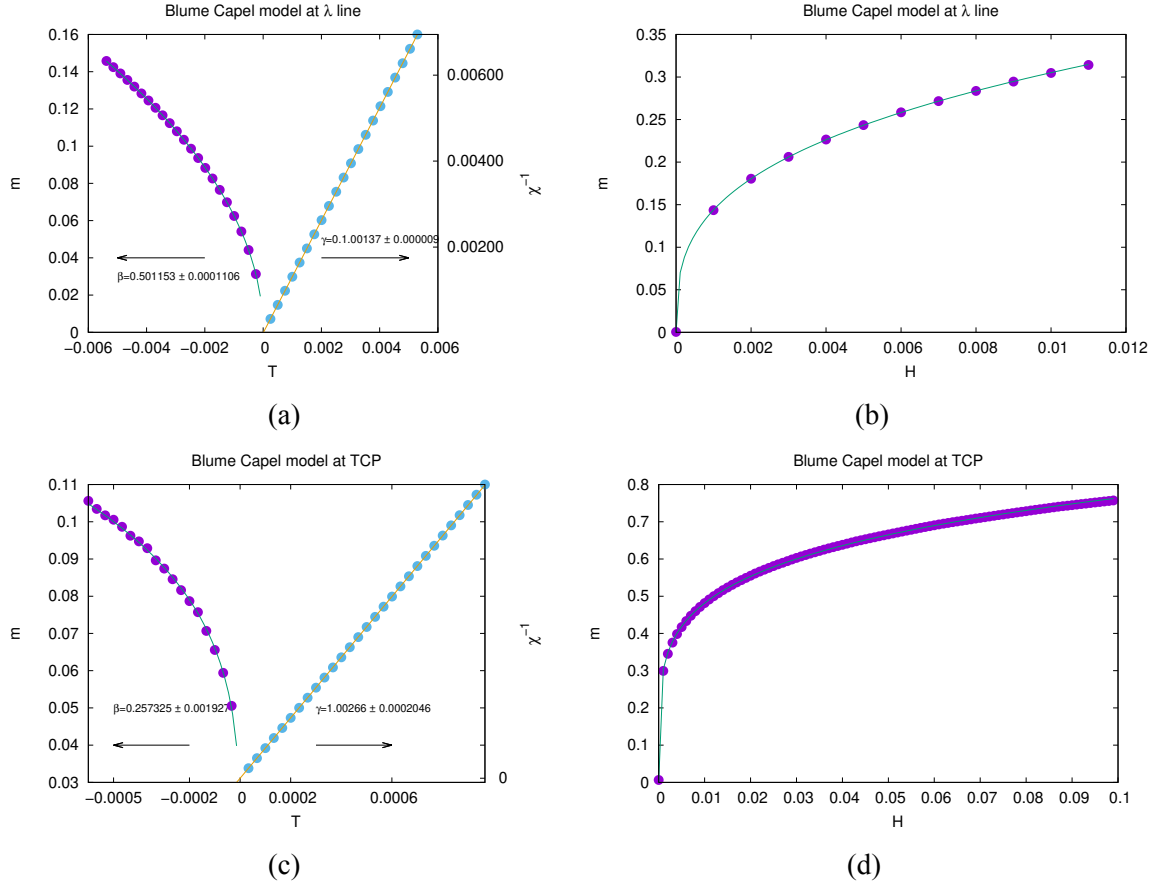
Figure 6.2: Blume capel model exponents (β, γ, δ) of the λ line and near the TCP. The solid circle shows the data points and the solid lines depicts the power law fitting functions. **(a)** and **(c)** Shows the plot of the magnetisation (m) and the inverse of the magnetic susceptibility (χ^{-1}) w.r.t reduced temperature (T) fitted using power law fitting for λ line and TCP respectively. Exponents β and γ are mentioned in the plot with errorbars. **(b)** and **(d)** Shows the plot of the magnetisation (m) w.r.t the external magnetic field H fitted with the scaling exponent $\delta = 3.063547 \pm 0.0005584$ and $\delta = 4.98611 \pm 0.000415$ for λ line and TCP respectively.

ing on the strength of the disorder or higher order interactions. So it is easier to verify the scaling hypothesis near the multicritical points and distinguish the behaviour of the phase boundary near a TCP and a CEP.

The plan of the chapter is as follows. In section 2 we briefly discuss about the scaling relations near a CP and TCP and verify them for the Blume-Capel model. In section 3, we discuss about the scaling relations near CEP. We revisit the Fisher-Barbosa argument for the scaling hypothesis near a CEP and the Wilding's argument briefly. In section 4, we show our observations near the CEP for RCFBC and for BEG model and compare them with the corresponding quantities near a TCP. In section 5, we show the scaling near a BEP. We then summarize the conclusions briefly in section 6.

6.2 Scaling near a CP and a TCP

6.2.1 Critical point (CP)

An ordinary critical point (CP) is a point where the magnetization coexistence region ends (shown in Fig. 6.1a). Near a CP the measurable thermodynamic quantities such as the magnetisation M, magnetic susceptibility χ, specific heat C_v etc shows a power law behaviour. Close to the CP, the free energy can be expressed as the sum of a analytic boundary term and a singular term.

$$f(T,h) \sim f_{ns}(T,h) - Q \ |t|^{2-\alpha} \ W_{\pm} \left[\frac{Uh}{|t|^{\Delta}} \right] \tag{6.1}$$

where $+(-)$ sign refers to $T > T_c$ $(T < T_c)$ and t is the scaled temperature : $t = \frac{T-T_c}{T_c}$. The singularities near a CP are expressed in terms of some universal critical exponents and critical amplitudes as the following
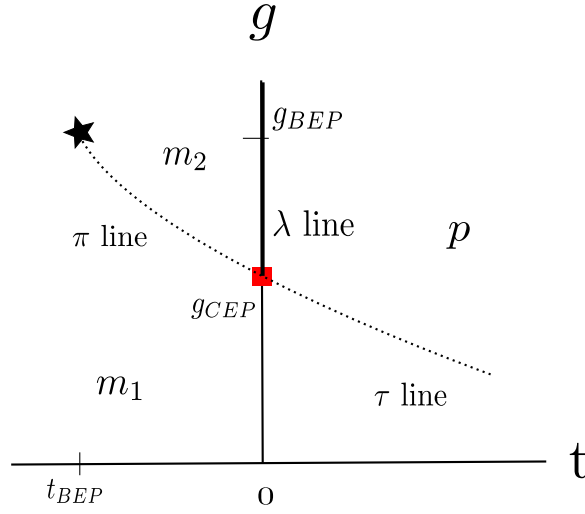
Figure 6.3: Schematic phase diagram of the spin-1 ferromagnets in the $g - t$ plane, where the scaled fields are $t = \frac{T - T_c(g)}{T_c(g)}$ and $g = -\Delta$. Solid line depicts lines of second order transition and dotted lines are lines of first order transition. The first order phase boundary π separates the two ordered phases m_1 and m_2 and the τ separates the phase m_1 and the disordered phase p. Solid star represents BEP and the solid red square is CEP. Figure taken from [240].

$$M \approx B|t|^{\beta} \tag{6.2}$$

$$M \approx B_{\pm} h^{1/\delta} \tag{6.3}$$

$$\chi \approx C_{\pm}|t|^{-\gamma} \tag{6.4}$$

$$C_v \approx A_{\pm}|t|^{-\alpha} \tag{6.5}$$

The $\alpha, \beta, \gamma, \delta$ are the critical exponents of the system. And these exponents are related to each other by

$$\alpha + 2\beta + \gamma = 2 \tag{6.6}$$

$$\beta\gamma = \beta + \gamma \tag{6.7}$$

known as the Rushbrooke and the Widom identity respectively [1]. The coefficients $A_{\pm}$, $B_{\pm}$, $C_{\pm}$ are called critical amplitudes, they itself are non-universal but their ratio is an

universal quantity. For example, $\frac{C_+}{C_-} = 2$ for mean-field Ising model. Systems under the same universality class show same values of the critical exponents. For example, Fig. 6.2a and 6.2b shows the values of the exponents β, γ and δ for the λ line of the mean-field pure Blume-Capel model by plotting the magnetisation m and susceptibility χ as a function of the reduced temperature T and m as a function of the external magnetic field H. It shows that the exponents of the λ line fall under the mean-field Ising universality class, where $\beta = \frac{1}{2}, \gamma = 1$ and $\delta = 3$.

6.2.2 Tricritical point (TCP)

The tricritical point (TCP), on the other hand are the multicritical points where a λ line terminates on the peak of the coexistence curve in the temperature (T) vs density (q) plane (shown in Fig. 6.1b). At the TCP the λ line meets the peak of the coexistence region at a finite angle [4].

The universality class of TCP is different than the ordinary critical point [4]. For the TCP at the pure Blume-Capel model located at ($H = 0, T = 1/3, \Delta = 0.46209812$), we get the following critical exponents near TCP by fitting : $\beta = 0.257325 \pm 0.001927$, $\gamma = 1.00266 \pm 0.0002046$ and $\delta = 4.98611 \pm 0.000415$ from the power law fitting (Fig. 6.2c , 6.2d) consistent with the mean-field values of : $\beta = 0.25$, $\gamma = 1$ and $\delta = 5$. The solid blue line denotes the λ line and the red shaded region is the co-existence region of the densities of the magnetic and non-magnetic spins.

6.3 Scaling hypothesis near a CEP

Critical end points (CEP) are the multicritical points where the λ line is truncated by a first order transition line [20]. CEPs are present in systems with more than two thermodynamic parameter. For spin-1 ferromagnets, there are three thermodynamic fields : temperature (T), crystal field (Δ) and external magnetic field (H). Fig. 6.3 shows the schematic plot
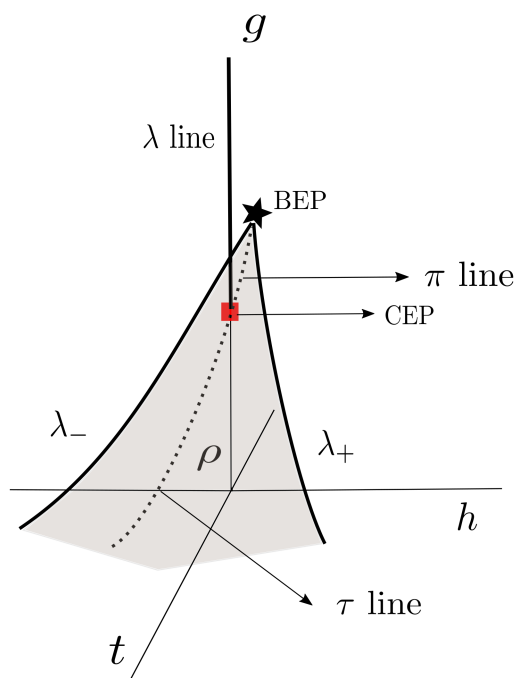
Figure 6.4: Schematic phase diagram of the spin-1 ferromagnets in presence of the external magnetic field h, in the $g - t - h$ plane. Solid lines represent the lines of second order transition (λ and $\lambda_{\pm}$), dotted line represents line of first order transition, red square is the CEP and black star is the BEP. ρ is the spectator phase boundary. Figure taken from [240].

in the the scaled fields $t = \frac{T - T_c(g)}{T_c(g)}$ and $g \equiv -\Delta$. Here t is a function of g. The π line is the coexistence of two ferromagnetic states: m_1 and m_2 and the τ line is the coexistence of a disordered phase (p) and the ordered state m_1. The p phase and the m_2 phase becomes critical in presence of a non-critical phase m_1 at the CEP. m_1 is the spectator phase here. The separation between the two ordered phase (m_1, m_2) becomes zero at the BEP, shown by a black star in Fig. 6.3.

In presence of H, the three dimensional diagram is shown in Fig: 6.4. In the $g - t - H$ plane the lines of first order transition π and τ becomes a surface ρ. The first order phase boundary ρ, specified by the function $g_\rho(T, h)$ shows non-analyticity as a function of T and h as we approach the CEP. It was shown by Fisher *et.al* [311, 312] that the curvature of the first order surface ρ shows singularity and the singularities can be expressed by the universal critical exponent and the critical amplitude ratios of the λ line. In the next subsection we will discuss about the scaling argument given by Fisher near the vicinity of CEP.

6.3.1 Derivation of the scaling argument near CEP by Fisher *et.al*

The critical temperature T_c of the λ line is a function of the non-ordering field g, i.e. $T_c(g)$. The free energy near the λ line can be written as :

$$f_p(T, h, g) \sim f_0(T, h, g) - Q|t|^{2-\alpha} W_\pm \left[\frac{Uh}{|t|^\Delta} \right] \tag{6.8}$$

The f_0 is the non-singular part of the free energy. The spectator phase m_1 boundary can be expressed as the Taylor expansion around the CEP $(T_e, 0, g_e)$:

$$f_{m_1}(T, h, g) = f_e + f_1^{m_1} \Delta g + f_2^{m_1} \Delta \hat{t} + f_3^{m_1} h + \dots \dots \tag{6.9}$$

where $\hat{t} = \frac{T - T_e}{T_e}$ and $\Delta g = g - g_e$. Similarly the f_0 can be expanded near the CEP:

$$f_0(T, h, g) = f_e + f_1^0 \Delta g + f_2^0 \Delta \hat{t} + f_3^0 h + \dots \dots \tag{6.10}$$

Also t, U, and Q can be expanded as the following

$$t = \hat{t} + q_1 \Delta g + q_2 \Delta g^2 + q_3 \hat{t} \Delta g + q_4 \hat{t}^2 + q_5 h^2 + \ldots \tag{6.11}$$

$$U(T, h, g) = U_e + U_1 \Delta g + U_2 \hat{t} + U_3 h + \ldots \tag{6.12}$$

$$Q(T, h, g) = Q_e + Q_1 \Delta g + Q_2 \hat{t} + Q_3 h + \ldots \tag{6.13}$$

here q_1 is the slope of the λ line at the CEP

$$q_1 = \frac{1}{T_e} \left. \frac{\partial T_c(g)}{\partial g} \right|_e \tag{6.14}$$

The first order phase boundary can be calculated by equating and solving the free energies of p and m_1 : $f_{m_1}(T, h, g) = f_p(T, h, g)$, which in turn gives

$$
\begin{aligned}
f_e + f_1^{m_1} \Delta g + f_2^{m_1} \Delta \hat{t} \quad &+ \quad f_3^{m_1} h + \ldots \\
&= \quad f_e + f_1^0 \, \Delta g + f_2^0 \, \Delta \hat{t} + f_3^0 \, h + \ldots - Q \, |t|^{2-\alpha} \, W_\pm \left[\frac{Uh}{|t|^\Delta} \right]
\end{aligned}
\tag{6.15}
$$

Defining $D_i = f_i^{m_1} - f_i^0$ and $g_i = -\frac{D_{i+1}}{D_i}$, the above equation for the phase boundary of ρ can be rewritten as

$$g_\rho(T, h) \approx g_e + g_1 \hat{t} + g_2 h + \ldots - R(T, h) \, |t|^{2-\alpha} \, W_\pm \left[\frac{Uh}{|t|^\Delta} \right] \tag{6.16}$$

where

$$R(T, h) \equiv \frac{Q[T, h, g_\rho(T, h)]}{(D_1 + D_2' \hat{t} + D_3' h + \ldots)} = R_e + R_1 \hat{t} + R_2 h + \ldots \tag{6.17}$$

where the D_2', D_3', R_1, R_2 etc are the coefficients which can be expressed in terms of the coefficients in Eq. 6.11 - 6.3.1 . The slope of the phase boundary $g_\rho(T, h)$ at the CEP

$\{g_\rho(T,0),\ h=0\}$ is given by

$$g_1 = T_e \left.\frac{\partial g_\rho(T,h)}{\partial T}\right|_e \tag{6.18}$$

For h= 0

$Q[T, h, g_\rho(T,h)]$ also contains t and h which is are functions of $g_\rho(T,h)$. So the spectator phase boundary at $h = 0$ can be found by considering only the leading order terms when $\hat{t} \longrightarrow \pm 0$:

$$
\begin{aligned}
g_\rho(T) - g_0(T) &= -R_e \ |\hat{t} + q_1 g_\rho(T) - q_1 g_e|^{2-\alpha} \ W_\pm[0] \\
&= -X_\pm \ |\hat{t}|^{2-\alpha} \left(1 + O(|\hat{t}|^{1-\alpha})\right)
\end{aligned}
\tag{6.19}
$$

where $g_0(T) = g_e + g_1\hat{t} + g_2 h + ...$

The singularity in the phase boundary is expressed by the term $X_\pm \ |\hat{t}|^{2-\alpha}$ of the above equation. The amplitude of the singular term $X_\pm$ is related to the curvature of the phase boundary as

$$X_\pm = R_e \ W_\pm(0) \ |e_0|^{2-\alpha} \tag{6.20}$$

with the parameter e_0 related to the curvature of the phase boundary to be

$$e_0 = 1 + g_1 q_1 = 1 - \left[\frac{\partial g_\rho}{\partial T}\right]_e \left[\frac{\partial T_c}{\partial g}\right]_e \tag{6.21}$$

Now from the scaling function of the free energy Eq. 6.8, the critical amplitudes in Eq. 6.2 - 6.5 can be expressed as

$$A_\pm = (2-\alpha) \ (1-\alpha) \ W_\pm(0) \ Q[T_c(g), 0, g_\rho] \tag{6.22}$$

$$B = W'_-(0) \ Q[T_c(g), 0, g_\rho] \ U[T_c(g), 0, g_\rho] \tag{6.23}$$

$$C_\pm = W_\pm(0) \ Q[T_c(g), 0, g_\rho] \ U^2[T_c(g), 0, g_\rho] \tag{6.24}$$

and the ratio of the critical amplitudes can be expressed in terms of the scaling function $W_\pm$

as

$$\frac{A_+}{A_-} = \frac{W_+}{W_-} \quad \text{and} \quad \frac{C_+}{C_-} = \frac{W''_+}{W''_-} \tag{6.25}$$

Comparing the ratio of the critical amplitude $A_\pm$ in Eq. 6.25 and the ratio of the amplitudes of the curvature of the phase boundary ρ $X_\pm$ in Eq. 6.20, it turns out that

$$\frac{X_+}{X_-} = \frac{A_+}{A_-} \tag{6.26}$$

As the critical amplitude ratios $\frac{A_+}{A_-}$ are universal, $\frac{X_+}{X_-}$ which is related to the curvature of the phase boundary is also universal.

For h$\neq 0$

Now for small and $h \neq 0$, the scaling function can be Taylor expanded around $h = 0$,

$$g_\rho(T, h) - g_0(T, h) = -R_e \ |\hat{t} + q_1 g_\rho(T) - q_1 g_e|^{2-\alpha} \left(W_\pm[0] + \frac{hU_e}{|t|^\Delta} \ W'_\pm[0] + \frac{1}{2}\left(\frac{hU_e}{|t|^\Delta}\right)^2 W''_\pm[0] + ... \right) \tag{6.27}$$

As $B = 0$ for $\hat{t} \longrightarrow 0^+$, thus $W'_+ = 0$. So only for $\hat{t} \longrightarrow 0^+$ Eq. 6.27 can be written as

$$g_\rho(T) - g_0(T) \approx -X_+|\hat{t}|^{2-\alpha} - \frac{1}{2}Z_+ h^2|\hat{t}|^{-\gamma} + ... \tag{6.28}$$

Similarly for $\hat{t} \longrightarrow 0^-$, the expression Eq. 6.27 becomes

$$g_\rho(T) - g_0(T) \approx -X_-|\hat{t}|^{2-\alpha} - Y|h||\hat{t}|^\beta - \frac{1}{2}Z_- h^2|\hat{t}|^{-\gamma} + ... \tag{6.29}$$

where the amplitudes $Z_\pm, \ Y$ related to the phase boundary ρ can be shown be

$$Z_\pm = R_e \ W''_\pm(0) \ |e_0|^{2-\alpha-2\Delta} = R_e \ W''_\pm(0) \ |e_0|^{-\gamma} \tag{6.30}$$

$$Y = R_e \ W'_-(0) \ |e_0|^{2-\alpha-\Delta} = R_e \ W'_-(0) \ |e_0|^\beta \tag{6.31}$$

using the scaling relations Eq. 6.6. Similar to the ratio $\frac{X_+}{X_-}$, the other amplitude ratios can also be expressed in terms of the critical amplitude ratios by comparing Eq. 6.23, 6.24, 6.25 to Eq. 6.30, Eq. 6.31. This can be expressed as

$$\frac{Z_+}{Z_-} = \frac{C_+}{C_-} \tag{6.32}$$

$$\zeta_1 \equiv \frac{X_+ Z_+}{Y^2} = \frac{A_+ C_+}{(1-\alpha)(2-\alpha)B^2} \tag{6.33}$$

So near the vicinity of the CEP the equation of the phase boundary ρ is expressed as

$$g_\rho(T,h) = g_e + g_1\,\hat{t} + g_2\,h + ... - X_\pm\,|\hat{t}|^{2-\alpha} - Y\,|h|\,|\hat{t}|^\beta - \frac{1}{2}Z_\pm\,h^2\,|\hat{t}|^{-\gamma} + ... \tag{6.34}$$

This is the argument which was given by Fisher [311] using the phenomenological theory of scaling and thermodynamic arguments. It states that the divergent curvature of the phase boundary ρ near the CEP is expressed in terms of the amplitudes $X_\pm$, Y, $Z_\pm$. The ratio of these amplitudes are related to the universal critical amplitude ratio of the critical phase boundary λ. Therefore, the singularity in $g_\rho(T,h)$ of the phase boundary ρ can be verified by calculating the derivatives $\frac{\partial\,g_\rho(T,h)}{\partial T}$, $\frac{\partial^2\,g_\rho(T,h)}{\partial T^2}$, $\frac{\partial\,g_\rho(T,h)}{\partial h}$, $\frac{\partial^2\,g_\rho(T,h)}{\partial h^2}$ near the CEP.

This predictions were verified using the spherical models [312, 313, 314, 5] and using eighth order Landau free energy expansion for isomorphous transitions [318, 240] and two order parameter Landau free energy expansion for ferroelectric materials [319].

6.3.2 Wilding's scaling theory around CEP

A straightforward extension of the Fisher's scaling argument was done by B. Wilding [9, 10] in order to study the singularities in the thermodynamic density q conjugate to g (or $-\Delta$). It was first shown using Monte-Carlo simulation for a binary fluid mixture that additional to the singularity of the phase boundary $g_\rho(T,h)$ proposed by Fisher *et al* there are another singularities in the diameter of the coexistence curve. It showed that the temperature

(a)   (b)
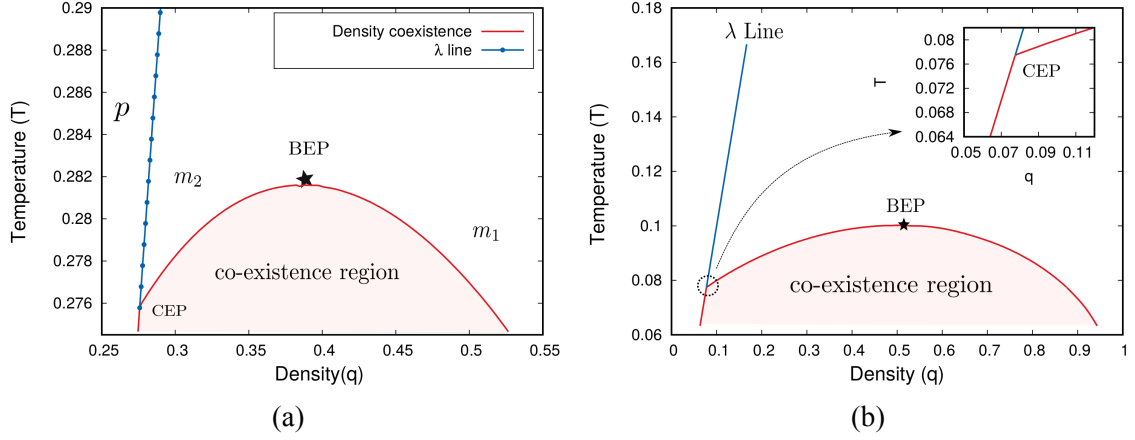
Figure 6.5: Temperature (T) vs. density (q) plot for **(a)** RCFBC model at $p = 0.044$ and **(b)** BEG model at $K = -0.6$. The blue line denotes the co-ordinates of the λ line and the area under the red line is the density coexistence region. The coexistence region ends at a BEP and the λ line truncates at the coexistence region at a CEP shown above.

derivative of the coexistence diameter diverges at the CEP and this divergence occurs in first derivative of the coexistence diameter. The diameter of the coexistence curve is defined as

$$q_d(T) \equiv \frac{1}{2}\Big(q_{p/m_2}(g_\rho(T)) + q_{m_1}(g_\rho(T))\Big) \tag{6.35}$$

where the density q can be obtainable from the free energy as

$$q = -\frac{1}{V}\left(\frac{\partial f(T, h, g)}{\partial g}\right)_{T,h} \tag{6.36}$$

and q_{m_1}, q_{p/m_2} are the densities of the spectator phase m_1 and the phases p and m_2 which becomes critical at the λ line respectively shown in Fig. 6.5. Using the Eq. 6.8, 6.9, 6.35 and 6.36, the singular behaviour of the diameter q_d can be written as

$$q_d(T) \approx U_\pm |\hat{t}|^{1-\alpha} + \text{terms analytic at } T_e \tag{6.37}$$

where the non-universal amplitudes $U_\pm$ can be expressed in terms of the scaling function $W_\pm$ of Eq. 6.8.

Thus the scaling argument shows that the coexistence curve diameter $q_d(T)$ exhibits a

177

divergence near the CEP and it can be verified by plotting the derivative of the $q_d(T)$

$$\frac{\partial q_d(T)}{\partial T} \approx \tilde{U}_{\pm}|\hat{t}|^{-\alpha} \tag{6.38}$$

near the vicinity of a CEP. As the divergence occurs in the first derivative of observable $q_d(T)$, it is more visible experimentally rather than the second derivative of the phase boundary $g_\rho(T, h)$.

6.4 Our observation near CEP

In our work, we verify the scaling arguments of the Fisher *et al* and Wilding for disordered spin-1 ferromagnets. We have considered RCFBC model and BEG model in presence of repulsive biquadratic exchange interaction (K).

6.4.1 Scaling argument verification by Fisher *et al*

For the spin-1 model, the phase boundary $g_\rho(T, h)$ is the function $-\Delta(T, h)$. In order to observe the singularity in the phase boundary ρ, we plot the in the co-ordinates of the first order phase boundary $\Delta_\rho(T, 0)$ and the second order derivative $\frac{\partial^2 \Delta_\rho(T,0)}{\partial T^2}$ in Fig. 6.6 for RCFBC model for the strength of disorder $p = 0.044$, $p = 0.07$ and for BEG model at $K = -0.6$. In all the cases, the phase diagram exhibits a CEP and a BEP.

In Fig. 6.6a, 6.6c, 6.6e we plot the co-ordinates of the phase boundary Δ as a function of temperature (T). In this case the Δ continuously decreases with T. In Fig. 6.6b, 6.6d, 6.6f we plot the second derivative of the phase boundary $\frac{\partial^2 \Delta}{\partial T^2}$ as a function of T. It shows that the phase boundary shows a discontinuity at the T_{CEP}. The discontinuity observed in the $\frac{\partial^2 \Delta}{\partial T^2}$ is similar to the jump in the specific heat plot (C_v) as a function of temperature T at the λ line, shown in Fig. 6.7.

Thus according to the Eq. 6.34 of the phase boundary ρ near the CEP in absence of
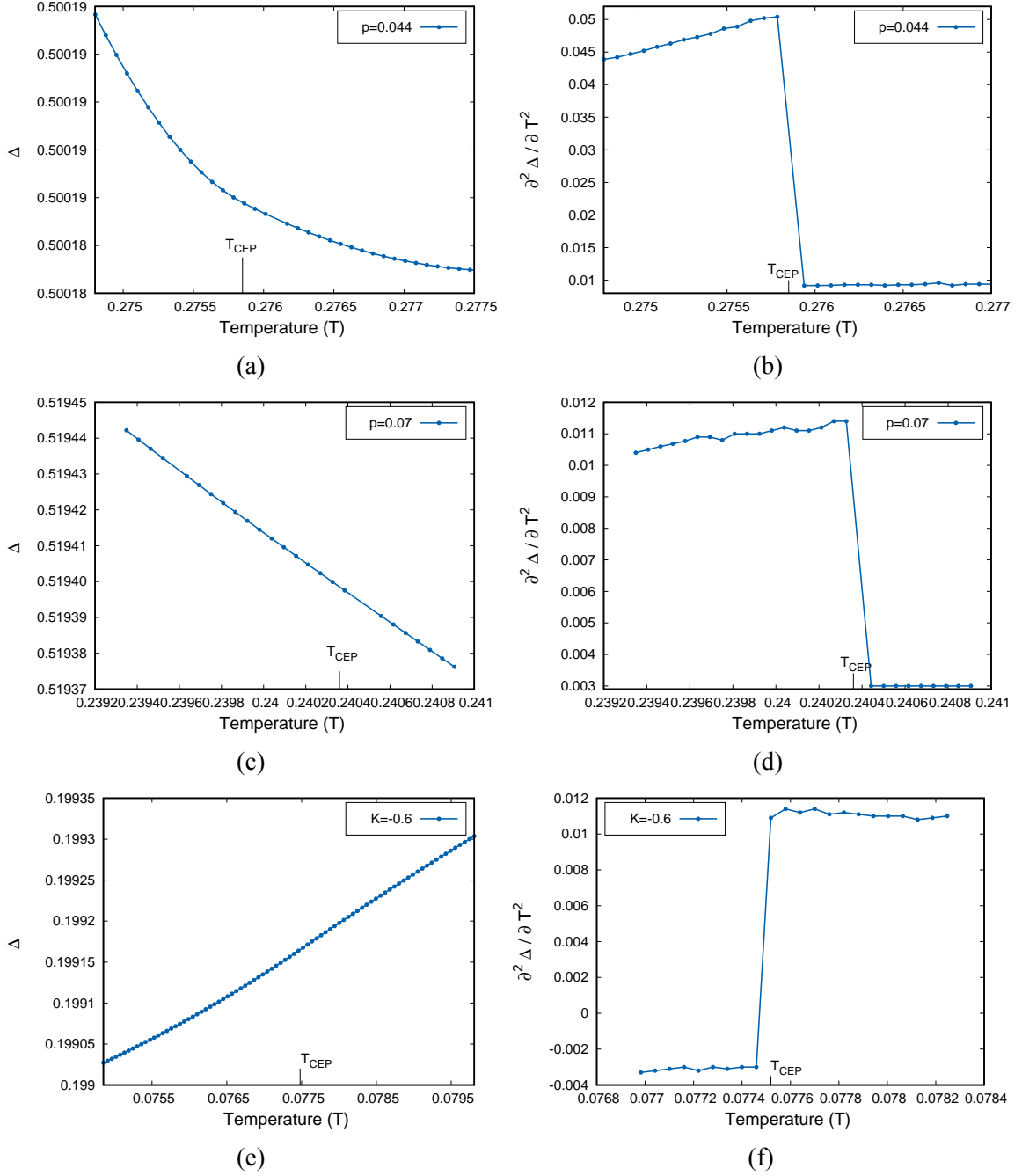
Figure 6.6: Fisher-Barbosa scaling argument verification for RCFBC model at $p = 0.044$ and $p = 0.07$. And for BEG model at $K = -0.6$. Fig. **(a)**, **(c)** and **(e)** shows the plot of the spectator phase boundary $\Delta_\rho(T, 0)$ as a function of temperature (T). Fig. **(b)**, **(d)** and **(f)** shows the plot of the second derivative of the phase boundary $\frac{\partial^2 \Delta}{\partial T^2}$ as a function of temperature (T).
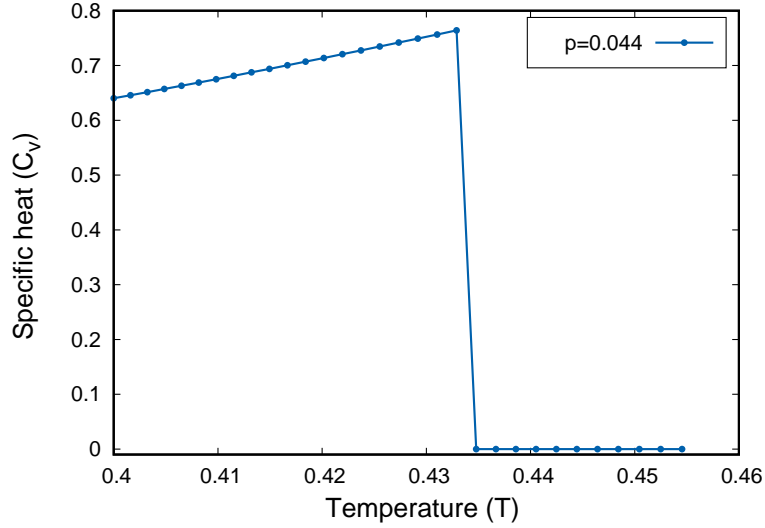
Figure 6.7: Specific heat (C_v) vs temperature (T) plot for RCFBC model along the λ line, keeping Δ fixed at $\Delta = 0.45$. The critical exponent is $\alpha = 0$. The discontinuity shown in the phase boundary and the phase co-existence curve near a CEP shows similar jump like the C_v.

external field h, the curvature of the phase boundary $\Delta_\rho(T,0)$ diverges as

$$\frac{\partial^2 \Delta_\rho(T,0)}{\partial T^2} = X_\pm |\hat{t}|^{-\alpha} \quad \text{with } \alpha = 0 \tag{6.39}$$

and $X_\pm$ is given by the jump of $\frac{\partial^2 \Delta_\rho(T,0)}{\partial T^2}$ at T_{CEP}.

6.4.2 Scaling argument verification by Wilding

In order to verify the Wilding's scaling argument we first plot the density coexistence curve as a function of temperature (T) for RCFBC model at $p = 0.044$ in Fig. 6.5a and for BEG model at $K = -0.6$ in Fig. 6.5b. The coexistence curve (shown in red line) ends at a BEP and the λ line (shown by blue line) truncates on the coexistence curve at a CEP. The co-existence curve near the CEP shows a kink (shown in the inset of Fig. 6.5b).

In Fig. 6.8, we plot the the co-ordinates of the diameter q_d and the first derivative $\frac{\partial q_d}{\partial T}$ of the co-existence curve of Fig. 6.5 as a function of temperature (T). We consider the RCFBC model for $p = 0.044$, $p = 0.07$ and BEG model for $K = -0.6$. In Fig. 6.8a,
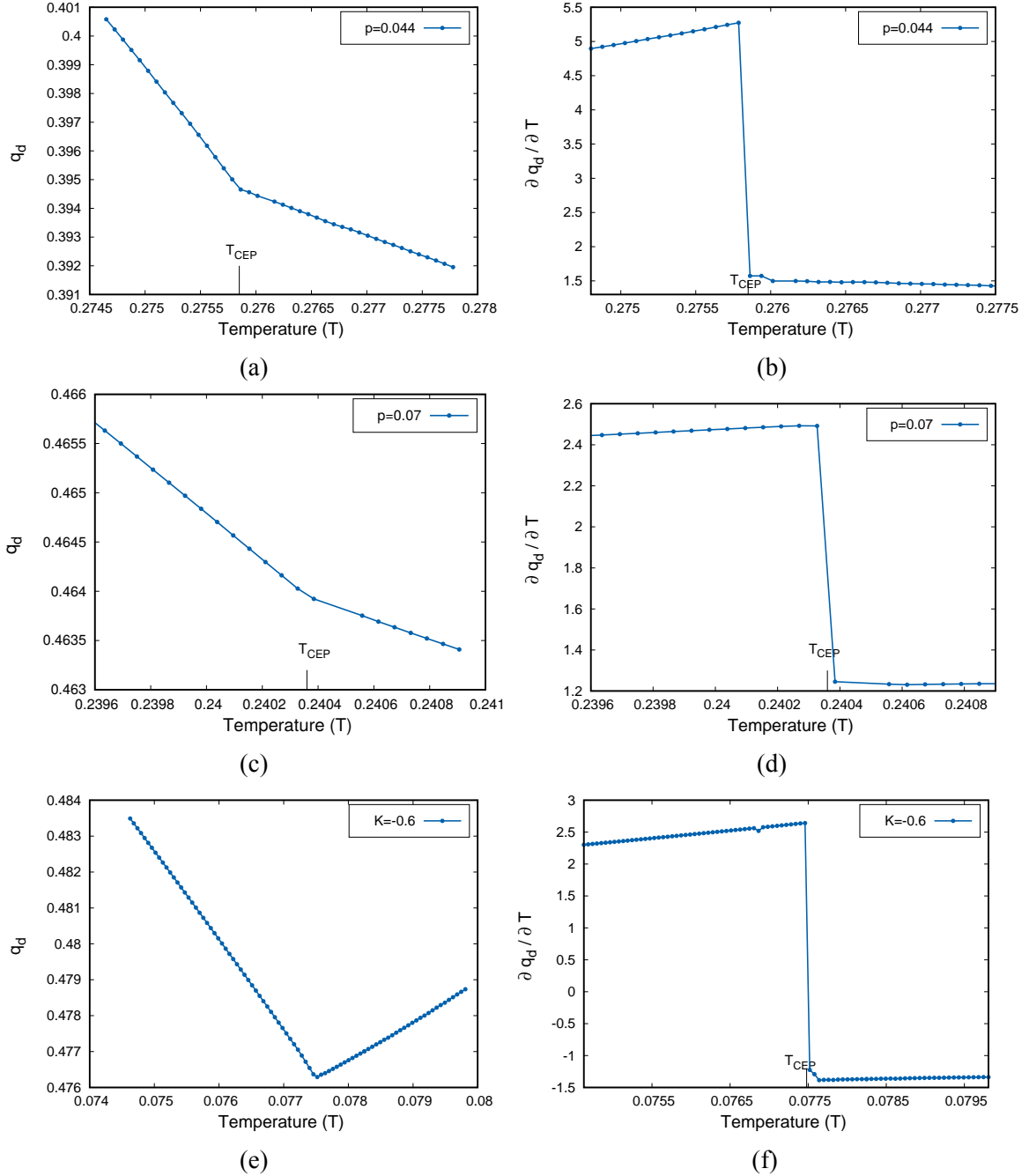
Figure 6.8: Wilding scaling argument verification for RCFBC model at $p = 0.044$ and $p = 0.07$. And for BEG model at $K = -0.6$. Fig. **(a)**, **(c)** and **(e)** shows the plot of the co-existence diameter (q_d) as a function of temperature (T). Fig. **(b)**, **(d)** and **(f)** shows the plot of the derivative of the diameter $\frac{\partial q_q}{\partial T}$ as a function of temperature (T).
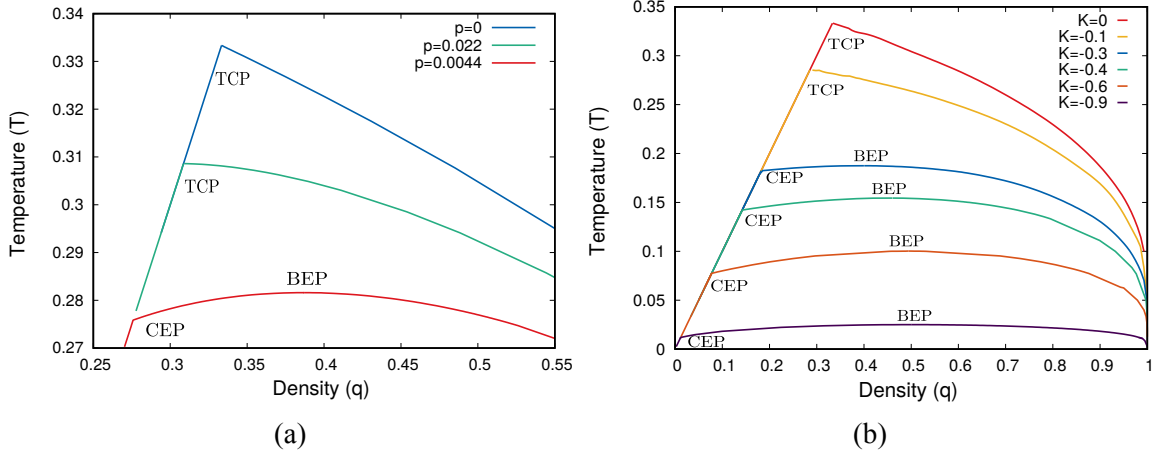
Figure 6.9: The behaviour of the phase co-existence region near a CEP and a TCP. Plot of the temperature (T) vs. density (q) **(a)** for RCFBC model for a range of p and **(b)** for BEG model for a range of K.

6.8c and 6.8e we plot the diameter q_d of the density coexistence region as a function the temperature (T). We observe that at the T_{CEP} it shows a kink in q_d. In Fig. 6.8b, 6.8d and 6.8f we plot the corresponding derivative $\frac{\partial q_q}{\partial T}$ as a function of T. It shows a discontinuity at the CEP. This discontinuity is again similar to the jump of C_v vs T (Fig. 6.7) plot with the critical exponent $\alpha = 0$.

6.4.3 Comparison of the scaling arguments near a CEP and a TCP

Both the TCP and CEP are points where a λ line meets at the phase coexistence region. In order to distinguish between these two multicritical points one can compare the behaviour phase boundaries near these points. For example, the shape of the phase coexistence curve is different for a CEP and a TCP. In Fig. 6.9 we plot the phase coexistence curve for the RCFBC model and BEG model for a range of p and K respectively. We observe that, for all the ranges of parameter ($0 \leq p \leq 0.022$ for RCFBC model shown in Fig. 6.9a and $-0.1838 \leq K \leq 0$ for BEG model shown in Fig. 6.9b) for which the TCP exists, the λ line meets at the peak of the coexistence region, where the phase coexistence continuously goes to zero. For the rest of the parameters the λ line does not terminates at the peak of the
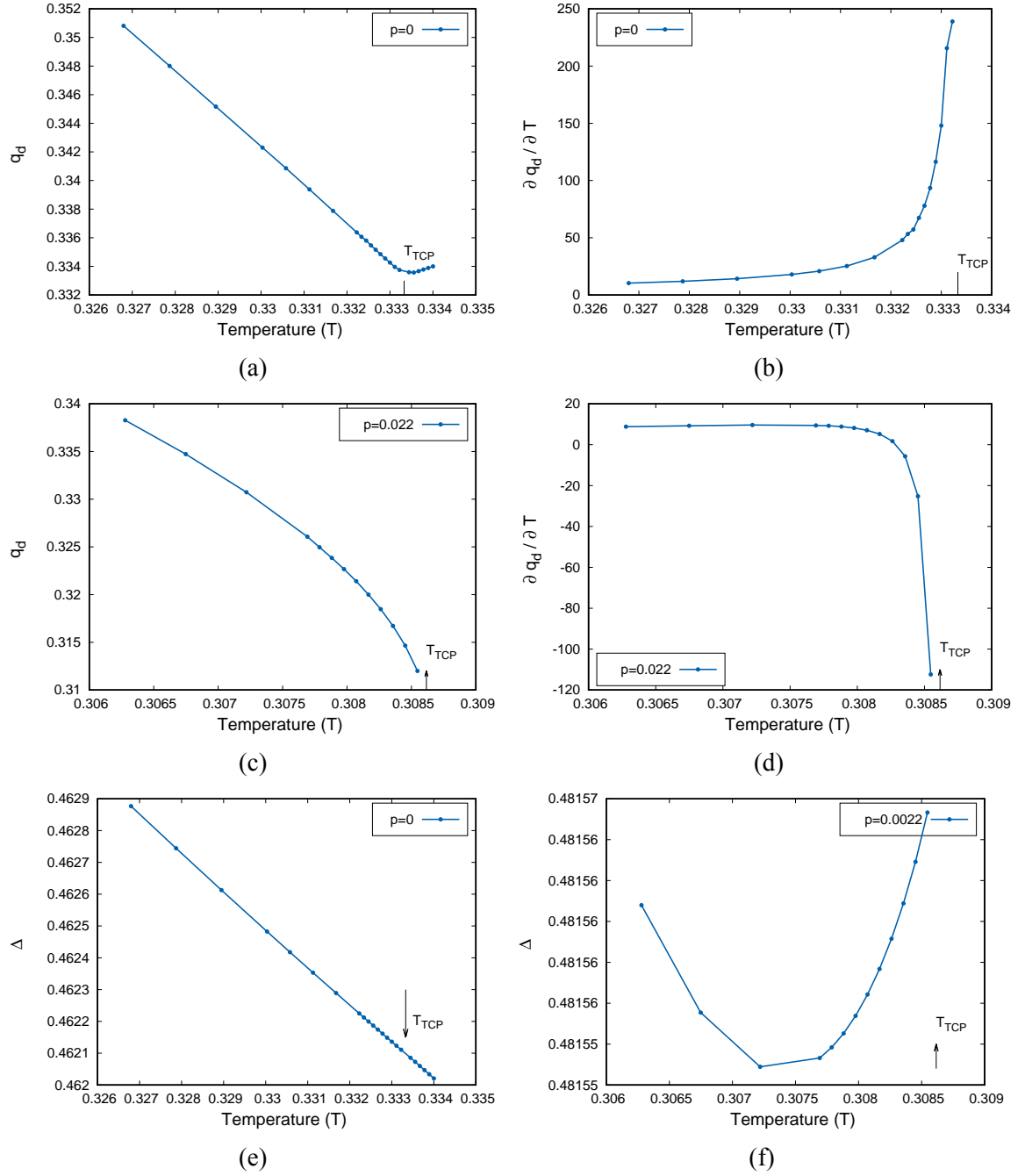
Figure 6.10: Plot of the coexistence diameter q_d, the derivative of the diameter $\frac{\partial q_q}{\partial T}$ and phase boundary $\Delta_\rho(T, 0)$ as a function of temperature T in order to compare the scaling arguments near a TCP for RCFBC model at $p = 0$ and $p = 0.022$. **(a)** and **(c)** Shows the plot of q_d as a function of T. **(b)** and **(d)** Shows the plot of $\frac{\partial q_q}{\partial T}$ as a function of T. The derivative shows a divergence at the TCP. We plot the co-ordinate of $\Delta_\rho(T, 0)$ for **(e)** $p = 0$ and **(f)** $p = 0.022$. Near the TCP, the $\Delta_\rho(T, 0)$ decreases linearly with T and thus the $\frac{\partial^2 \Delta}{\partial T^2}$ is zero for both the values of p.

coexistence region. The peak is now becomes a BEP and the λ line truncates on either side of the coexistence region giving rise to a kink at the CEP.

The distinction between these two multicritical points can also be done quantitatively by plotting the quantities related to the scaling arguments of the CEP and compare them. In order to compare the Wilding's scaling argument, we plot the diameter of the coexistence region q_d and it's derivative $\frac{\partial q_q}{\partial T}$ as a fuction of T for the RCFBC model at $p = 0$ and $p = 0.022$ in Fig. 6.10a - 6.10d. We observe that the q_d decreases continuously as a function of T, shown in Fig. 6.10a and Fig. 6.10c for $p = 0$ and $p = 0.022$ respectively. The derivative of the diameter q_d shows a divergence at the TCP shown in Fig. 6.10b and Fig. 6.10d for $p = 0$ and $p = 0.022$ respectively. Which is in contrast with the behaviour of q_d and $\frac{\partial q_q}{\partial T}$ shows a jump near a CEP.

Similarly, in order to check the Fisher's scaling argument, we plot the similar quantities near the TCP (Δ as a function of the T). In Fig. 6.10e and Fig. 6.10f we plot them for $p = 0$ and $p = 0.022$ respectively. In Fig. 6.10f, the Δ along the coexistence region changes linearly for $p = 0$. For $p = 0.022$, the Δ shows a non-monotonicity. But in both cases, the second derivative of the Δ as a function of T gives zero near the TCP. Which is in contrast with Fig. 6.6b, 6.6d for the similar quantities near a CEP, where the second derivative shows a jump.

6.5   Scaling near BEP

Bicritical end point (BEP) is a point of coexistence of two critical phases. This point is where two critical lines meet. It a point of finite magnetisation. We first try to get an idea of the behaviour of BEP in mean field theory. Using Landau free energy functional expanding upto 6th order in presence of an external magnetic field:

$$f(m) = mh + a_2 m^2 + a_4 m^4 + a_6 m^6 + a_8 m^8 \tag{6.40}$$

$a_2 \propto (T - T_c)$. Taking first derivative of $f(m)$ to be zero:

$$h = 2m(a_2 + 2a_4 m^2 + 3a_6 m^4 + 4a_8 m^6) \tag{6.41}$$

Now to know the behaviour around the BEP, we take $h = 0$, and define $m' \equiv m^2$. Eq:6.41 has a form for $m \neq 0$, with $\alpha = a_2, \beta = 2a_4, \gamma = 3a_6, \delta = 4a_8$:

$$\alpha + \beta m' + \gamma m'^2 + \delta m'^3 = 0 \tag{6.42}$$

This cubic equation has a double root and one simple root. The solutions are:

Simple root:

$$m' = \frac{4\beta\gamma\delta - 9\delta^2\alpha - \gamma^3}{\delta(\gamma^2 - 3\delta\beta)} \tag{6.43}$$

Double root:

$$m' = \frac{9\delta\alpha - \beta\gamma}{2(\gamma^2 - 3\delta\beta)} \tag{6.44}$$

So the magnetisation m, from the above equations can be scaled as:

$$m^2 \sim a_2 \rightarrow m \sim (T - T_c)^{\frac{1}{2}} \tag{6.45}$$

To get the susceptibility we take derivative of Eq:6.41 w.r.t h:

$$1 = 2(a_2 + 6a_4 m^2 + 15a_6 m^4 + 28a_8 m^6)\chi$$
$$\chi = \frac{1}{2(a_2 + 6a_4 m^2 + 15a_6 m^4 + 28a_8 m^6)} \sim \frac{1}{T - T_c} \tag{6.46}$$

At the critical point $T = T_c$, $a_2 = 0$. Eq:6.41 can now be written as:
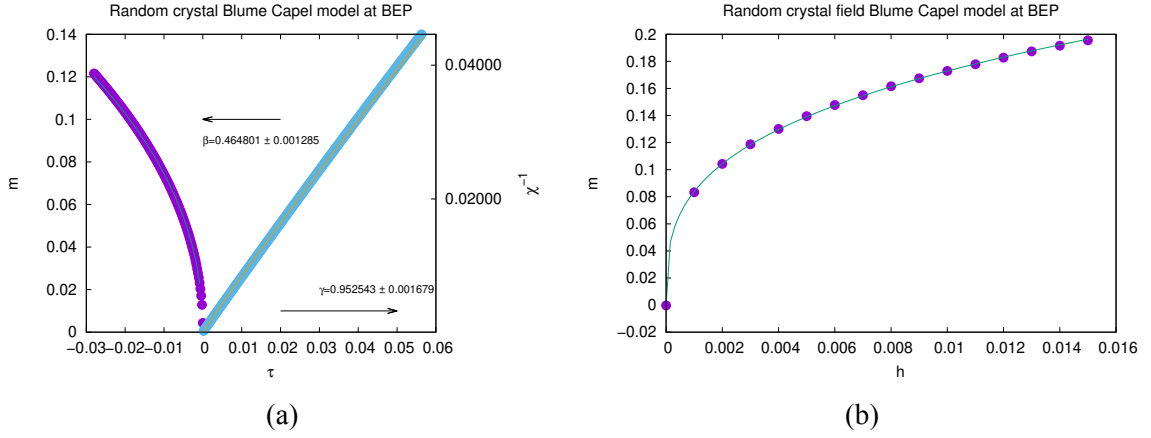
Figure 6.11: Calculation of the critical exponents β, γ and δ at the BEP using power law fitting for RCFBC model at $p = 0.2$. The solid circles are the data plots and the solid lines are the fitting function. **(a)** Shows the m and χ^{-1} plot as a function of the reduced temperature τ. Exponents β and γ are mentioned in the plot with error bars. **(b)** Shows the $m - H$ plot with scaling exponent $\delta = 3.184013704 \pm 001052$. This shows that the critical exponents of a BEP falls under the mean-field Ising universality class.

$$h = 2(2a_4 m^3 + 3a_6 m^5 + 4a_8 m^7) \qquad (6.47)$$

The leading term of m gives the dependence in h to be: $m \sim h^{\frac{1}{3}}$. which implies the BEP to be in the mean-field Ising universality class.

Next in order to observe the behaviour near the BEP from the full free energy, we plot the magnetisation and the susceptibility at the BEP of RCFBC model for $p = 0.2$. In Fig. 6.11 we plot the rescaled magnetisation $m \equiv M - M_0$ and rescaled susceptibility $\chi \equiv \chi - \chi_0$ near the BEP co-ordinate : $\beta = 4.8589227251599$, $\Delta = 0.596375976333334$ for $p = 0.2$. Where the values of the constants are $M_0 = 0.577133329708503$, and $\chi_0 = 3.752999689475423 \times 10^{14}$. We then do a power law fitting for the observables. We get the exponents near the BEP similar to the mean-field Ising universality class.

6.6 Summary and conclusion

The scaling hypothesis has been done earlier near the multicritical points like TCP and CEP. The scaling near the TCP is well studied [305, 306, 307, 4]. On the other hand the scaling hypothesis for the singularities near a CEP has been conjectured and has been proved in some examples [312, 313, 240, 9].

In this work [324] we have revisited the scaling hypothesis for the spin-1 RCFBC model and the BEG model. We have determined the first order phase boundaries near the CEP and studied the behaviour of the phase co-existence diameter and the their derivatives. The phase boundary curvature and it's double derivative shows a jump at the CEP which confirms the predictions by Fisher *et al* [311, 312]. This jump is similar to the specific heat (C_v) plot as a function of T with the critical exponent $\alpha = 0$. We also checked the Wilding's arguments near the CEP separately [9]. We observed that the diameter of the coexistence curve shows a kink and it's derivative shows a jump at the CEP similar to $C_v - T$ plot as predicted by Wilding [9].

We have done a comparative study between the TCP and CEP in order to distinguish between the two multicritical points just by observing the behaviour of the phase boundaries near these multicritical points. We observed that the phase coexistence diameter shows a kink near the CEP whereas the diameter continuously goes to zero near a TCP.

We have also studied the scaling behavior near the BEP both using the Landau free energy expansion and also by plotting the observables near the BEP. We observed that the critical exponents belongs to the same universality class as the mean-field Ising universality class.

Chapter 7

Summary and Conclusions

Quenched randomness has a significant impact on a system's critical behaviour, particularly at first order transitions and multicritical points. Spin models with random field disorder are a good representation of many systems with quenched randomness [97]. While there have been a lot of work on effect of disorder on Ising spins, effect on spin-1 has been studied less. The spin-1 model has a richer phase diagram than the spin-$\frac{1}{2}$ model. They have many applications in modelling of different physical systems like : $^3He - ^4He$ mixtures [149], inverse melting [155, 156], semiconducting alloys [160], and so on. In this thesis, we have focused on the study of the effect of random crystal field and random field disorder on a infinite-ranged spin-1 Blume-Capel model using large deviation techniques [215]. It is the simplest spin model which exhibits multicritical behavior.

In **Chapter 3** we investigated the effect of bimodal random crystal field disorder on a infinite-ranged Blume-Capel model (RCFBC) [213]. We observed that the disorder is always relevant and the phase diagrams can be divided into three categories depending on the value of p. Weak ($0 < p \le 0.022$), intermediate ($0.022 < p \le 0.107875$), and strong ($0.107875 < p \le 0.5$) disorder regime. However, the wings never disappear, even though the TCP of the system vanishes for $p > 0.022$. Instead different multicritical points like CEP and BEP emerges. We observed that the BEP is a point of coexistence of two critical phases. This was earlier reported as an ordered critical point [185] in the $T - \Delta$ plane. One interesting observation was that the one-parameter 8th order Landau theory cannot locate the co-ordinates of the CEP and BEPs accurately.

In **Chapter 4** we investigated the effect of different symmetric random field distribu-

tions on the infinite-ranged Blume-Capel model (RFBC) [214]. We found that the effect of the random field disorder is very different than the effect of random crystal-field disorder. In presence of the random crystal-field disorder the system consists of a TCP which vanishes as disorder increases and a BEP emerges [213]. Whereas, in the random-field disorder multiple new phases emerge which are separated by multiple first order transition lines. As a result, first order transition of the pure model gets replaced by two or more small jumps in magnetization. We considered a trimodal and a Gaussian distribution. We studied both the $T = 0$ and finite T phase diagram for both the distributions. We observed that for the trimodal distribution, three new ordered phases emerge. The phase diagram consists of 4 ordered and 2 disordered phases for all $0 < p < 1$. We classified the phase diagram into five categories depending on p : $p = 0$, $0 < p < \frac{1}{3}$, $p = \frac{1}{3}$, $\frac{1}{3} < p < 1$ and $p = 1$. We found that the phase diagrams consist of multiple numbers of first order transition lines along with multiple numbers of multicritical points like TCPs, BEPs, and multi-phase co-existence points which we designate as A_n points. On the other hand we found that the phase diagram for Gaussian distribution is rather simpler. It has one ordered phase and one disordered phase, and its phase diagram resembles that of the pure Blume-Capel model. Interestingly, we discovered that the phase diagrams are not similar for different symmetric distributions. This contradicts the earlier conjecture by Aharony for $O(n)$ models in presence of symmetric random field distribution [76].

In **Chapter 5** we studied the effect of higher order interactions on infinite range spin-1 BEG model in the $T - \Delta - H$ space [288]. We solved the system in both canonical and microcanonical ensembles. We found that the phase diagrams can be divided into four categories. The presence of negative K creates a frustration in this pure model which we find affects the phase diagram in a similar way like the random crystal field disorder [213] and for small negative values of K, the first two phase diagrams are similar to the phase diagrams of the RCFBC model for weak and intermediate regimes respectively. As K

decreases further, the co-ordinates of the CEP and BEP move towards $T = 0$ and exactly at $K = -1$ they reach $T = 0$. For $K < -1$, the multicritical points as well as the wings vanish and the phase diagram becomes two dimensional in the $T - \Delta - H$ space. Interestingly, we found that the model exhibits ensemble inequivalence only for $K > -1$. The co-ordinates of the $\lambda_\pm$ lines are different for different ensembles which in $H = 0$ plane meet at different multicritical points. For $K < -1$ the wings vanish and hence the ensemble inequivalence also disappears.

In conclusion, we studied the effect of disorder and higher order interaction on infinite range spin-1 models. We observed that even in presence of an infinitesimal amount of disorder changes the system's critical behavior. A plethora of different phase diagrams emerge. We also observed that the BEG model being a pure model in presence of repulsive biquadratic exchange interaction creates the similar frustration in the system like the random crystal field disorder. In presence of disorder and as well as in presence of frustration we observed that many multicritical points like TCP, BEP and CEP emerges. In order to get more insight near the multicritical points a proper scaling theory near these points is required to differentiate between different multicritical points. The scaling theory near a TCP shows that it has a different universality class than the ordinary critical point [4]. A scaling theory near the CEP has been proposed earlier by Fisher *et al* [311, 312, 313] and later by Wilding [10]. In **Chapter 6** we revisited these scaling theories and verified the scaling behavior around the CEP and TCP for the disordered spin-1 Blume-Capel model both for the RCFBC and BEG model [324].

Our investigations has been focused on the effects of different random field disorder in the spin-1 Blume-Capel model on a fully connected graph. Study on the fully connected graph is relevant because the upper critical dimension of the TCP is $d_u = 3$ and also the simulations are challenging. It will be interesting to study the system in finite dimensions to check if such interesting behavior arises or not. For example : emergence of different

190

multicritical points, existence of an ordered state even for strong random field disorder, differences in phase diagrams for different symmetric random field distributions. The method used in this thesis can be straightforwardly applied to study other spin models as well, like the Potts model, BEG model, Ashkin Teller model in presence of disorder.

References

[1] Nigel Goldenfeld. *Lectures on phase transitions and the renormalization group*. CRC Press, 2018.

[2] Leo P. Kadanoff. Scaling laws for ising models near T_c. *Physics Physique Fizika*, 2:263–272, Jun 1966.

[3] Ernst Ising. Beitrag zur theorie des ferromagnetismus. *Zeitschrift für Physik*, 31:253–258, Feb 1925.

[4] C. Domb, M.S. Green, and J.L. Lebowitz. *Phase Transitions and Critical Phenomena*. Number v. 9 in Phase Transitions and Critical Phenomena. Academic Press, 1984.

[5] Michael E. Fisher. Critical endpoints, interfaces, and walls. *Physica A: Statistical Mechanics and its Applications*, 172(1):77–86, 1991.

[6] Robert B. Griffiths. Phase diagrams and higher-order critical points. *Phys. Rev. B*, 12:345–355, Jul 1975.

[7] Carl W Garland and Bruce B Weiner. Changes in the thermodynamic character of the n h 4 cl order-disorder transition at high pressures. *Physical Review B*, 3(5):1634, 1971.

[8] Bruce M. Law. Surface amplitude ratios near a critical end point. *Phys. Rev. Lett.*, 67:1555–1558, Sep 1991.

[9] Nigel B. Wilding. Coexistence curve singularities at critical end points. *Phys. Rev. Lett.*, 78:1488–1491, Feb 1997.

[10] Nigel B. Wilding. Critical end point behavior in a binary fluid mixture. *Phys. Rev. E*, 55:6624–6631, Jun 1997.

[11] D. Peña Lara, G. A. Pérez Alcázar, Ligia E. Zamora, and J. A. Plascak. Blume-capel model for $(Fe_{0.65}Ni_{0.35})_{1-x}mn_x$ and $fe_pal_qmn_x$ alloys. *Phys. Rev. B*, 80:014427, Jul 2009.

[12] R Shashidhar and S Chandrasekhar. Pressure studies on liquid crystalline materials. *Le Journal de Physique Colloques*, 36(C1):C1–49, 1975.

[13] Yoshinori Takikawa, Keisuke Katagiri, Makoto Iwata, and Hiroshi Orihara. Dielectric study of the electric-field-induced critical endpoint in a nematic liquid crystal with positive dielectric anisotropy. *Journal of the Physical Society of Japan*, 91(2):024002, 2022.

[14] A. M. Goldman. Tricritical points of thin superconducting films. *Phys. Rev. Lett.*, 30:1038–1041, May 1973.

[15] V. A. Schmidt and S. A. Friedberg. Metamagnetism of ni$(NO_3)_2$.2h$_2$o. *Phys. Rev. B*, 1:2250–2256, Mar 1970.

[16] BE Keen, D Landau, B Schneider, and WP Wolf. First-and higher-order magnetic phase transitions in dysprosium aluminum garnet. *Journal of Applied Physics*, 37(3):1120–1121, 1966.

[17] I. S. Jacobs and P. E. Lawrence. Metamagnetic phase transitions and hysteresis in fecl$_2$. *Phys. Rev.*, 164:866–878, Dec 1967.

[18] Gregory Goellner and Horst Meyer. Chemical potential of he^3 - he^4 solutions near the tricritical point. *Phys. Rev. Lett.*, 26:1534–1537, Jun 1971.

[19] Takeshi Mizushima, Shigehiro Yasui, and Muneto Nitta. Critical end point and universality class of neutron $^3p_2$ superfluids in neutron stars. *Phys. Rev. Research*, 2:013194, Feb 2020.

[20] P. M. Chaikin and T. C. Lubensky. *Principles of Condensed Matter Physics*. Cambridge University Press, 1995.

[21] Patrick A. Lee and T. V. Ramakrishnan. Disordered electronic systems. *Rev. Mod. Phys.*, 57:287–337, Apr 1985.

[22] D. Belitz and T. R. Kirkpatrick. The anderson-mott transition. *Rev. Mod. Phys.*, 66:261–380, Apr 1994.

[23] Anatoly I Larkin. Effect of inhomogeneties on the structure of the mixed state of superconductors. *Soviet Journal of Experimental and Theoretical Physics*, 31:784, 1970.

[24] AI Larkin and Yu N Ovchinnikov. Pinning in type ii superconductors. *Journal of Low Temperature Physics*, 34(3):409–428, 1979.

[25] Yoshitake Yamazaki, Arno Holz, Moyuru Ochiai, and Yoshiichi Fukuda. Static and dynamic critical behavior of extended-defect n-component systems in cubic anisotropic crystals. *Phys. Rev. B*, 33:3460–3473, Mar 1986.

[26] Markus Spanner, Felix Höfling, Sebastian C. Kapfer, Klaus R. Mecke, Gerd E. Schröder-Turk, and Thomas Franosch. Splitting of the universality class of anomalous transport in crowded media. *Phys. Rev. Lett.*, 116:060601, Feb 2016.

[27] Thomas O. E. Skinner, Simon K. Schnyder, Dirk G. A. L. Aarts, Jürgen Horbach, and Roel P. A. Dullens. Localization dynamics of fluids in random confinement. *Phys. Rev. Lett.*, 111:128301, Sep 2013.

[28] D. E. Moncton, F. J. DiSalvo, J. D. Axe, L. J. Sham, and Bruce R. Patton. Charge-density wave stacking order in $1t - \text{ta}_{1-x}\text{zr}_x\text{se}_2$: Interlayer interactions and impurity (zr) effects. *Phys. Rev. B*, 14:3432–3437, Oct 1976.

[29] H. Fukuyama and P. A. Lee. Dynamics of the charge-density wave. i. impurity pinning in a single chain. *Phys. Rev. B*, 17:535–541, Jan 1978.

[30] M. Mézard, G. Parisi, and R. Zecchina. Analytic and algorithmic solution of random satisfiability problems. *Science*, 297(5582):812–815, 2002.

[31] S. M. A. Tabei, M. J. P. Gingras, Y.-J. Kao, P. Stasiak, and J.-Y. Fortin. Induced random fields in the liho$_x$y$_{1-x}$f$_4$ quantum ising magnet in a transverse magnetic field. *Phys. Rev. Lett.*, 97:237203, Dec 2006.

[32] Hatem Barghathi and Thomas Vojta. Random fields at a nonequilibrium phase transition. *Phys. Rev. Lett.*, 109:170603, Oct 2012.

[33] Paul Robustelli, Stefano Piana, and David E. Shaw. Developing a molecular dynamics force field for both folded and disordered protein states. *Proceedings of the National Academy of Sciences*, 115(21):E4758–E4766, 2018.

[34] Felix Höfling and Thomas Franosch. Anomalous transport in the crowded world of biological cells. *Reports on Progress in Physics*, 76(4):046602, 2013.

[35] Aurelien Bancaud, Christophe Lavelle, Sebastien Huet, and Jan Ellenberg. A fractal model for nuclear organization: current evidence and biological implications. *Nucleic acids research*, 40(18):8783–8792, 2012.

[36] Viktor Dotsenko. *Introduction to the Replica Theory of Disordered Statistical Systems*. Collection Alea-Saclay: Monographs and Texts in Statistical Physics. Cambridge University Press, 2000.

[37] Leticia F. Cugliandolo. Advanced statistical physics: Quenched disordered systems. 2017.

[38] A. P. (A. Peter) Young. *Spin glasses and random fields / editor A.P. Young.* Directions in condensed matter physics ; vol. 12. World Scientific, Singapore : River Edge, N.J., 1998.

[39] Barry M. McCoy and Tai Tsun Wu. Theory of a two-dimensional ising model with random impurities. i. thermodynamics. *Phys. Rev.*, 176:631–643, Dec 1968.

[40] S F Edwards and P W Anderson. Theory of spin glasses. *Journal of Physics F: Metal Physics*, 5(5):965–974, may 1975.

[41] David Sherrington and Scott Kirkpatrick. Solvable model of a spin-glass. *Phys. Rev. Lett.*, 35:1792–1796, Dec 1975.

[42] R. B. Stinchcombe. Theory of dilute anisotropic magnets. In Claudio Castellani, Carlo Di Castro, and Luca Peliti, editors, *Disordered Systems and Localization*, pages 41–45, Berlin, Heidelberg, 1981. Springer Berlin Heidelberg.

[43] R. Harris, M. Plischke, and M. J. Zuckermann. New model for amorphous magnetism. *Phys. Rev. Lett.*, 31:160–162, Jul 1973.

[44] C. Domb, J. L. Lebowitz, D.R. Nelson, F.W. Wiegel, and R. B. Stinchcombe. *Phase Transitions and Critical Phenomena*. Number v. 7 in Phase Transitions and Critical Phenomena. Academic Press, 1983.

[45] Wolfhard Janke, Bertrand Berche, Christophe Chatelain, Pierre-Emmanuel Berche, and Meik Hellmund. Quenched Disordered Ferromagnets. *PoS*, LAT2005:018, 2005.

[46] Yoseph Imry and Shang-keng Ma. Random-field instability of the ordered state of continuous symmetry. *Phys. Rev. Lett.*, 35:1399–1401, Nov 1975.

[47] G S Rushbrooke, R A Muse, R L Stephenson, and K Pirnie. On randomly dilute ferromagnetic models. *Journal of Physics C: Solid State Physics*, 5(23):3371–3386, nov 1972.

[48] Robert B. Griffiths. Nonanalytic behavior above the critical point in a random ising ferromagnet. *Phys. Rev. Lett.*, 23:17–19, Jul 1969.

[49] A B Harris. Effect of random defects on the critical behaviour of ising models. *Journal of Physics C: Solid State Physics*, 7(9):1671–1692, may 1974.

[50] A. Brooks Harris and T. C. Lubensky. Renormalization-group approach to the critical behavior of random-spin models. *Phys. Rev. Lett.*, 33:1540–1543, Dec 1974.

[51] Kenneth Hui and A. Nihat Berker. Random-field mechanism in random-bond multicritical systems. *Phys. Rev. Lett.*, 62:2507–2510, May 1989.

[52] Yoseph Imry and Michael Wortis. Influence of quenched impurities on first-order phase transitions. *Phys. Rev. B*, 19:3580–3585, Apr 1979.

[53] Michael Aizenman and Jan Wehr. Rounding of first-order phase transitions in systems with quenched disorder. *Phys. Rev. Lett.*, 62:2503–2506, May 1989.

[54] Michael Aizenman and Jan Wehr. Rounding effects of quenched randomness on first-order phase transitions. *Communications in mathematical physics*, 130(3):489–528, 1990.

[55] A. Nihat Berker and Kenneth Hui. *Absence of Temperature-Driven First-Order Phase Transitions in Systems with Random Bonds*, pages 411–417. Springer US, Boston, MA, 1991.

[56] G. Grinstein and A. Luther. Application of the renormalization group to phase transitions in disordered systems. *Phys. Rev. B*, 13:1329–1343, Feb 1976.

[57] Amnon Aharony, Yoseph Imry, and Shang-keng Ma. Comments on the critical behavior of random systems. *Phys. Rev. B*, 13:466–473, Jan 1976.

[58] Amnon Aharony. Critical phenomena in disordered systems. *Journal of Magnetism and Magnetic Materials*, 7(1-4):198–206, 1978.

[59] Viktor S. Dotsenko and Vladimir S. Dotsenko. Critical behaviour of the phase transition in the 2d ising model with impurities. *Advances in Physics*, 32(2):129–172, 1983.

[60] K. Ziegler. Quenched thermodynamics of the random bond ising model on the square lattice. *Nuclear Physics B*, 344(3):499–530, 1990.

[61] Abel Weinrib and B. I. Halperin. Critical phenomena in systems with long-range-correlated quenched disorder. *Phys. Rev. B*, 27:413–427, Jan 1983.

[62] Wolfhard Janke and Martin Weigel. Harris-luck criterion for random lattices. *Phys. Rev. B*, 69:144208, Apr 2004.

[63] Johannes Zierenberg, Niklas Fricke, Martin Marenz, F. P. Spitzner, Viktoria Blavatska, and Wolfhard Janke. Percolation thresholds and fractal dimensions for square and cubic lattices with long-range correlated defects. *Phys. Rev. E*, 96:062125, Dec 2017.

[64] John Cardy. Quenched randomness at first-order transitions. *Physica A: Statistical Mechanics and its Applications*, 263(1):215–221, 1999. Proceedings of the 20th IUPAP International Conference on Statistical Physics.

[65] S. Chen, Alan M. Ferrenberg, and D. P. Landau. Monte carlo simulation of phase transitions in a two-dimensional random-bond potts model. *Phys. Rev. E*, 52:1377–1386, Aug 1995.

[66] S. Chen, Alan M. Ferrenberg, and D. P. Landau. Randomness-induced second-order transition in the two-dimensional eight-state potts model: A monte carlo study. *Phys. Rev. Lett.*, 69:1213–1215, Aug 1992.

[67] Shai Wiseman and Eytan Domany. Critical behavior of the random-bond ashkin-teller model: A monte carlo study. *Phys. Rev. E*, 51:3074–3086, Apr 1995.

[68] A. Nihat Berker. Critical behavior induced by quenched disorder. *Physica A: Statistical Mechanics and its Applications*, 194(1):72–76, 1993.

[69] John Cardy and Jesper Lykke Jacobsen. Critical behavior of random-bond potts models. *Phys. Rev. Lett.*, 79:4063–4066, Nov 1997.

[70] Christophe Chatelain and Bertrand Berche. Finite-size scaling study of the surface and bulk critical behavior in the random-bond eight-state potts model. *Phys. Rev. Lett.*, 80:1670–1673, Feb 1998.

[71] Christophe Chatelain, Bertrand Berche, Wolfhard Janke, and Pierre Emmanuel Berche. Softening of first-order transition in three-dimensions by quenched disorder. *Phys. Rev. E*, 64:036120, Aug 2001.

[72] Christophe Chatelain, Bertrand Berche, Wolfhard Janke, and Pierre-Emmanuel Berche. Monte carlo study of phase transitions in the bond-diluted 3d 4-state potts model. *Nuclear Physics B*, 719(3):275–311, 2005.

[73] Ganpathy N. Murthy. Critical behavior of the n-component ashkin-teller model with bond impurities. *Phys. Rev. B*, 36:7166–7168, Nov 1987.

[74] U. J. Cox, A. Gibaud, and R. A. Cowley. Effect of impurities on the first-order phase transition of kmnf$_3$. *Phys. Rev. Lett.*, 61:982–985, Aug 1988.

[75] H. G. Ballesteros, L. A. Fernández, V. Martín-Mayor, A. Muñoz Sudupe, G. Parisi, and J. J. Ruiz-Lorenzo. Critical behavior in the site-diluted three-dimensional three-state potts model. *Phys. Rev. B*, 61:3215–3218, Feb 2000.

[76] Amnon Aharony. Tricritical points in systems with random fields. *Phys. Rev. B*, 18:3318–3327, Oct 1978.

[77] G. Grinstein. Ferromagnetic phase transitions in random fields: The breakdown of scaling laws. *Phys. Rev. Lett.*, 37:944–947, Oct 1976.

[78] G. Grinstein and Shang-keng Ma. Roughening and lower critical dimension in the random-field ising model. *Phys. Rev. Lett.*, 49:685–688, Aug 1982.

[79] A. Nihat Berker. Ordering under random fields: Renormalization-group arguments. *Phys. Rev. B*, 29:5243–5245, May 1984.

[80] S Fishman and A Aharony. Random field effects in disordered anisotropic antiferro-magnets. *Journal of Physics C: Solid State Physics*, 12(18):L729–L733, sep 1979.

[81] John L. Cardy. Random-field effects in site-disordered ising antiferromagnets. *Phys. Rev. B*, 29:505–507, Jan 1984.

[82] Po☐Zen Wong, S. von Molnar, and P. Dimon. Random☐field effects in fe1−xmgxcl2. *Journal of Applied Physics*, 53:7954–7956, November 1982.

[83] R. Blossey, T. Kinoshita, and J. Dupont-Roc. Random-field ising model for the hysteresis of the prewetting transition on a disordered substrate. *Physica A: Statistical Mechanics and its Applications*, 248(3):247–272, 1998.

[84] R. L. C. Vink, K. Binder, and H. Löwen. Critical behavior of colloid-polymer mixtures in random porous media. *Phys. Rev. Lett.*, 97:230603, Dec 2006.

[85] C. Domb, M.S. Green, and J.L. Lebowitz. *Phase Transitions and Critical Phenomena*. Number v. 14 in Phase Transitions and Critical Phenomena. Academic Press, 1991.

[86] J. V. Maher, W. I. Goldburg, D. W. Pohl, and M. Lanz. Critical behavior in gels saturated with binary liquid mixtures. *Phys. Rev. Lett.*, 53:60–63, Jul 1984.

[87] S. K. Sinha, J. Huang, and S. K. Satija. *Binary Fluid Phase Separation in Gels: A Neutron Scattering Study*, pages 157–162. Springer US, Boston, MA, 1991.

[88] Q. Michard and J.-P. Bouchaud. Theory of collective opinion shifts: from smooth trends to abrupt swings. *The European Physical Journal B - Condensed Matter and Complex Systems*, 47:151–159, September 2005.

[89] AM Gutin, VI Abkevich, and EI Shakhnovich. Cooperativity of protein folding and the random-field ising model. *arXiv preprint cond-mat/9606136*, 1996.

[90] M. Shadaydeh, Y. Guanche, and J. Denzler. Classification of Spatiotemporal Marine Climate Patterns using Wavelet Coherence and Markov Random Field. In *AGU Fall Meeting Abstracts*, volume 2018, pages IN31C–0824, December 2018.

[91] Hui Wang, Florian Wellmann, Elizabeth Verweij, Christian von Hebel, and Jan van der Kruk. Identification and Simulation of Subsurface Soil patterns using hidden Markov random fields and remote sensing and geophysical EMI data sets. In *EGU General Assembly Conference Abstracts*, EGU General Assembly Conference Abstracts, page 6530, April 2017.

[92] Maxim Ziatdinov, Artem Maksov, and Sergei V. Kalinin. Learning surface molecular structures via machine vision. *npj Computational Materials*, 3:31, 8 2017.

[93] Farhad Ghazvinian Zanjani, Svitlana Zinger, and Peter H. N. de With. Cancer detection in histopathology whole-slide images using conditional random fields on deep embedded spaces. In John E. Tomaszewski and Metin N. Gurcan, editors, *Medical Imaging 2018: Digital Pathology*, volume 10581, pages 143 – 149. International Society for Optics and Photonics, SPIE, 2018.

[94] Huazhu Fu, Yanwu Xu, Stephen Lin, Damon Wing Kee Wong, and Jiang Liu. Deepvessel: Retinal vessel segmentation via deep learning and conditional random field. In Sebastien Ourselin, Leo Joskowicz, Mert R. Sabuncu, Gozde Unal, and William Wells, editors, *Medical Image Computing and Computer-Assisted Intervention – MICCAI 2016*, pages 132–139, Cham, 2016. Springer International Publishing.

[95] Olivier François, Sophie Ancelet, and Gilles Guillot. Bayesian Clustering Using Hidden Markov Random Fields in Spatial Population Genetics. *Genetics*, 174(2):805–816, 10 2006.

[96] Jinyuan Jia, Binghui Wang, Le Zhang, and Neil Zhenqiang Gong. Attriinfer: Inferring user attributes in online social networks using markov random fields. In *Proceedings of the 26th International Conference on World Wide Web*, WWW '17, page 1561–1569, Republic and Canton of Geneva, CHE, 2017. International World Wide Web Conferences Steering Committee.

[97] Enrique Hernández-Lemus. Random fields in physics, biology and data science. *Frontiers in Physics*, 9, 2021.

[98] Daniel S Fisher, Geoffrey M Grinstein, and Anil Khurana. Theory of random magnets. *Physics Today*, 41(12):56–67, 1988.

[99] Thomas Nattermann. Theory of the random field ising model. In *Spin glasses and random fields*, pages 277–298. World Scientific, 1998.

[100] T. Schneider and E. Pytte. Random-field instability of the ferromagnetic state. *Phys. Rev. B*, 15:1519–1522, Feb 1977.

[101] Serge Galam and Joseph L. Birman. Random-field distributions and tricritical points. *Phys. Rev. B*, 28:5322–5322, Nov 1983.

[102] David Andelman. First- and second-order phase transitions with random fields at low temperatures. *Phys. Rev. B*, 27:3079–3080, Mar 1983.

[103] N G Fytas, A Malakis, and K Eftaxias. First-order transition features of the 3d bimodal random-field ising model. *Journal of Statistical Mechanics: Theory and Experiment*, 2008(03):P03015, mar 2008.

[104] Nikolaos G. Fytas and Víctor Martín-Mayor. Universality in the three-dimensional random-field ising model. *Phys. Rev. Lett.*, 110:227201, May 2013.

[105] Daniel C. Mattis. Tricritical point in random-field ising model. *Phys. Rev. Lett.*, 55:3009–3009, Dec 1985.

[106] Miron Kaufman, Philip E. Klunzinger, and A. Khurana. Multicritical points in an ising random-field model. *Phys. Rev. B*, 34:4766–4770, Oct 1986.

[107] Thomas Vojta. Phases and phase transitions in disordered quantum systems. *AIP Conference Proceedings*, 1550(1):188–247, 2013.

[108] G. Parisi and N. Sourlas. Random magnetic fields, supersymmetry, and negative dimensions. *Phys. Rev. Lett.*, 43:744–745, Sep 1979.

[109] Amnon Aharony, Yoseph Imry, and Shang-keng Ma. Lowering of dimensionality in phase transitions with random fields. *Phys. Rev. Lett.*, 37:1364–1367, Nov 1976.

[110] A P Young. On the lowering of dimensionality in phase transitions with random fields. *Journal of Physics C: Solid State Physics*, 10(9):L257–L256, may 1977.

[111] Susan R McKay and A Nihat Berker. Equimagnetization lines in the hybrid-order phase diagram of the d= 3 random-field ising model. *Journal of Applied Physics*, 64(10):5785–5786, 1988.

[112] John Z. Imbrie. Lower critical dimension of the random-field ising model. *Phys. Rev. Lett.*, 53:1747–1750, Oct 1984.

[113] K Binder. Random-field induced interface widths in ising systems. *Zeitschrift für Physik B Condensed Matter*, 50(4):343–352, 1983.

[114] J. Bricmont and A. Kupiainen. Lower critical dimension for the random-field ising model. *Phys. Rev. Lett.*, 59:1829–1832, Oct 1987.

[115] David Andelman, H. Orland, and L. C. R. Wijewardhana. Lower critical dimension of the random-field ising model: A monte carlo study. *Phys. Rev. Lett.*, 52:145–148, Jan 1984.

[116] Amnon Aharony and E. Pytte. Low-temperature scaling for systems with random fields and anisotropies. *Phys. Rev. B*, 27:5872–5874, May 1983.

[117] T Nattermann. Instabilities in ising systems with short-and long-range-correlated quenched random fields. *Journal of Physics C: Solid State Physics*, 16(33):6407, 1983.

[118] V. K. Saxena. Trimodal random-field ising model on a bethe lattice and the tricritical point. *Phys. Rev. B*, 35:2055–2057, Feb 1987.

[119] Rafael M. Sebastianes and V. K. Saxena. Phase diagram of the random-field ising model with a trimodal distribution. *Phys. Rev. B*, 35:2058–2060, Feb 1987.

[120] Nuno Crokidakis and Fernando D Nobre. Destruction of first-order phase transition in a random-field ising model. *Journal of Physics: Condensed Matter*, 20(14):145211, mar 2008.

[121] Octavio R Salmon, Nuno Crokidakis, and Fernando D Nobre. Multicritical behavior in a random-field ising model under a continuous-field probability distribution. *Journal of Physics: Condensed Matter*, 21(5):056005, jan 2009.

[122] I.A. Hadjiagapiou. The random field ising model with an asymmetric trimodal probability distribution. *Physica A: Statistical Mechanics and its Applications*, 390(12):2229–2239, 2011.

[123] I.A. Hadjiagapiou. The random-field ising model with asymmetric bimodal probability distribution. *Physica A: Statistical Mechanics and its Applications*, 389(19):3945–3955, 2010.

[124] Theodorakis P.E. Fytas N.G. and Georgiou I. Universality aspects of the trimodal random-field ising model. *The European Physical Journal B*, 85:349, Oct 2012.

[125] M. Picco and N. Sourlas. Diluted antiferromagnetic 3d ising model in a field. *EPL (Europhysics Letters)*, 109(3):37001, feb 2015.

[126] Nikolaos G. Fytas, Víctor Martín-Mayor, Marco Picco, and Nicolas Sourlas. Phase transitions in disordered systems: The example of the random-field ising model in four dimensions. *Phys. Rev. Lett.*, 116:227201, Jun 2016.

[127] N G Fytas, V Martín-Mayor, M Picco, and N Sourlas. Specific-heat exponent and modified hyperscaling in the 4d random-field ising model. *Journal of Statistical Mechanics: Theory and Experiment*, 2017(3):033302, mar 2017.

[128] Laura Hernández and H. T. Diep. Existence of a tricritical point at finite field in the three-dimensional random-field ising model. *Phys. Rev. B*, 55:14080–14083, Jun 1997.

[129] Nicolas Sourlas. Universality in random systems: the case of the 3d random field ising model. *Computer Physics Communications*, 121-122:183–187, 1999. Proceedings of the Europhysics Conference on Computational Physics CCP 1998.

[130] Giorgio Parisi and Nicolas Sourlas. Scale invariance in disordered systems: The example of the random-field ising model. *Phys. Rev. Lett.*, 89:257204, Dec 2002.

[131] Anastasios Malakis and Nikolaos G. Fytas. Lack of self-averaging of the specific heat in the three-dimensional random-field ising model. *Phys. Rev. E*, 73:016109, Jan 2006.

[132] Shai Wiseman and Eytan Domany. Finite-size scaling and lack of self-averaging in critical disordered systems. *Phys. Rev. Lett.*, 81:22–25, Jul 1998.

[133] Pierre-Emmanuel Berche, Christophe Chatelain, Bertrand Berche, and Wolfhard Janke. Bond dilution in the 3d ising model: a monte carlo study. *The European Physical Journal B-Condensed Matter and Complex Systems*, 38(3):463–474, 2004.

[134] Marc Mézard and Giorgio Parisi. Replica field theory for random manifolds. *Journal de Physique I*, 1(6):809–836, 1991.

[135] M Mezard, G Parisi, and M Virasoro. *Spin Glass Theory and Beyond*. WORLD SCIENTIFIC, 1986.

[136] D. J. Thouless, P. W. Anderson, and R. G. Palmer. Solution of 'solvable model of a spin glass'. *The Philosophical Magazine: A Journal of Theoretical Experimental and Applied Physics*, 35(3):593–601, 1977.

[137] Marc MEZARD, Giorgio PARISI, and Miguel Angel VIRASORO. *THE TAP AP-PROACH*, pages 15–22.

[138] Cirano De Dominicis and Irene Giardina. *Mean field via TAP equations*, page 127–140. Cambridge University Press, 2006.

[139] C. De Dominicis. Dynamics as a substitute for replicas in systems with quenched random impurities. *Phys. Rev. B*, 18:4913–4919, Nov 1978.

[140] Cirano De Dominicis and Irene Giardina. *The dynamical approach*, page 35–56. Cambridge University Press, 2006.

[141] B. F. Svaiter and N. F. Svaiter. The distributional zeta-function in disordered field theory. *International Journal of Modern Physics A*, 31(25):1650144, 2016.

[142] Matthias Löwe, Raphael Meiners, and Felipe Torres. Large deviations principle for curie–weiss models with random fields. *Journal of Physics A: Mathematical and Theoretical*, 46(12):125004, mar 2013.

[143] Sumedha and Sushant K. Singh. Effect of random field disorder on the first order transition in p-spin interaction model. *Physica A: Statistical Mechanics and its Applications*, 442:276–283, 2016.

[144] G. Parisi. Infinite number of order parameters for spin-glasses. *Phys. Rev. Lett.*, 43:1754–1756, Dec 1979.

[145] G Parisi. A sequence of approximated solutions to the s-k model for spin glasses. *Journal of Physics A: Mathematical and General*, 13(4):L115–L121, apr 1980.

[146] G Parisi. The order parameter for spin glasses: a function on the interval 0-1. *Journal of Physics A: Mathematical and General*, 13(3):1101–1112, mar 1980.

[147] M Blume. Theory of the first-order magnetic phase change in u o 2. *Physical Review*, 141(2):517, 1966.

[148] H.W. Capel. On the possibility of first-order transitions in ising systems of triplet ions with zero-field splitting ii. *Physica*, 33(2):295 – 331, 1967.

[149] M. Blume, V. J. Emery, and Robert B. Griffiths. Ising model for the λ transition and phase separation in he^3-he^4 mixtures. *Phys. Rev. A*, 4:1071–1077, Sep 1971.

[150] Miron Kaufman, Robert B. Griffiths, Julia M. Yeomans, and Michael E. Fisher. Three-component model and tricritical points: A renormalization-group study. two dimensions. *Phys. Rev. B*, 23:3448–3459, Apr 1981.

[151] A. K. Jain and D. P. Landau. Monte carlo study of the fcc blume-capel model. *Phys. Rev. B*, 22:445–452, Jul 1980.

[152] D. P. Landau and R. H. Swendsen. Tricritical universality in two dimensions. *Phys. Rev. Lett.*, 46:1437–1440, Jun 1981.

[153] D. M. Saul, Michael Wortis, and D. Stauffer. Tricritical behavior of the blume-capel model. *Phys. Rev. B*, 9:4964–4980, Jun 1974.

[154] Fredric Harbus and H. Eugene Stanley. Ising-model "metamagnet" and tricritical susceptibility exponent. *Phys. Rev. Lett.*, 29:58–62, Jul 1972.

[155] Nurith Schupper and Nadav M. Shnerb. Spin model for inverse melting and inverse glass transition. *Phys. Rev. Lett.*, 93:037202, Jul 2004.

[156] Andrea Crisanti and Luca Leuzzi. Stable solution of the simplest spin model for inverse freezing. *Phys. Rev. Lett.*, 95:087201, Aug 2005.

[157] R. Erichsen, W. K. Theumann, and S. G. Magalhaes. Inverse melting and inverse freezing in a three-state spin-glass model with finite connectivity. *Phys. Rev. E*, 87:012139, Jan 2013.

[158] D. Mukamel and M. Blume. Ising model for tricritical points in ternary mixtures. *Phys. Rev. A*, 10:610–617, Aug 1974.

[159] N. B. Wilding and P. Nielaba. Tricritical universality in a two-dimensional spin fluid. *Phys. Rev. E*, 53:926–934, Jan 1996.

[160] Kathie E. Newman and John D. Dow. Zinc-blende—diamond order-disorder transition in metastable crystalline $(GaAs)_{1-x}ge_{2x}$ alloys. *Phys. Rev. B*, 27:7495–7508, Jun 1983.

[161] Amnon Aharony. Multicritical points. In F. J. W. Hahne, editor, *Critical Phenomena*, pages 209–258, Berlin, Heidelberg, 1983. Springer Berlin Heidelberg.

[162] C. Domb and M.S. Green. *Phase Transitions and Critical Phenomena*. Number v. 14 in Phase Transitions and Critical Phenomena. Academic Press, 1972.

[163] G. D. Mahan and S. M. Girvin. Blume-capel model for plane-triangular and fcc lattices. *Phys. Rev. B*, 17:4411–4415, Jun 1978.

[164] S. Grollau, E. Kierlik, M. L. Rosinberg, and G. Tarjus. Thermodynamically self-consistent theory for the blume-capel model. *Phys. Rev. E*, 63:041111, Mar 2001.

[165] Paul D. Beale. Finite-size scaling study of the two-dimensional blume-capel model. *Phys. Rev. B*, 33:1717–1720, Feb 1986.

[166] C. J. Silva, A. A. Caparica, and J. A. Plascak. Wang-landau monte carlo simulation of the blume-capel model. *Phys. Rev. E*, 73:036702, Mar 2006.

[167] CM Care. Microcanonical monte carlo study of a two-dimensional blume-capel model. *Journal of Physics A: Mathematical and General*, 26(7):1481, 1993.

[168] Johannes Zierenberg, Nikolaos G Fytas, Martin Weigel, Wolfhard Janke, and Anastasios Malakis. Scaling and universality in the phase diagram of the 2d blume-capel model. *The European Physical Journal Special Topics*, 226(4):789–804, 2017.

[169] Robert B. Griffiths. Proposal for notation at tricritical points. *Phys. Rev. B*, 7:545–551, Jan 1973.

[170] V. Taufour, D. Aoki, G. Knebel, and J. Flouquet. Tricritical point and wing structure in the itinerant ferromagnet uge_2. *Phys. Rev. Lett.*, 105:217201, Nov 2010.

[171] Hisashi Kotegawa, Valentin Taufour, Dai Aoki, Georg Knebel, and Jacques Flouquet. Evolution toward quantum critical end point in uge2. *Journal of the Physical Society of Japan*, 80(8):083703, 2011.

[172] Noriyuki Kabeya, Hirotaka Maekawa, Kazuhiko Deguchi, Noriaki Kimura, Haruyoshi Aoki, and Noriaki K. Sato. Non-fermi liquid state bounded by a possible electronic topological transition in zrzn2. *Journal of the Physical Society of Japan*, 81(7):073706, 2012.

[173] Udhara S. Kaluarachchi, Sergey L. Bud'ko, Paul C. Canfield, and Valentin Taufour. Tricritical wings and modulated magnetic phases in lacrge3 under pressure. *Nature Communications*, 8:546, 2017.

[174] Robert B. Griffiths. Thermodynamics near the two-fluid critical mixing point in he^3 - he^4. *Phys. Rev. Lett.*, 24:715–717, Mar 1970.

[175] D. Belitz, T. R. Kirkpatrick, and Jörg Rollbühler. Tricritical behavior in itinerant quantum ferromagnets. *Phys. Rev. Lett.*, 94:247205, Jun 2005.

[176] PG d De Gennes. Collapse of a polymer chain in poor solvents. *Journal de Physique Lettres*, 36(3):55–57, 1975.

[177] Kay Jörg Wiese and François David. Self-avoiding tethered membranes at the tricritical point. *Nuclear Physics B*, 450(3):495–557, 1995.

[178] I.N. Flerov, M.V. Gorev, M.S. Molokeev, and N.M. Laptash. 16 - ferroelastic and ferroelectric phase transitions in fluoro- and oxyfluorometallates. In Alain Tressaud and Kenneth Poeppelmeier, editors, *Photonic and Electronic Properties of Fluoride Materials*, pages 355–381. Elsevier, Boston, 2016.

[179] Wenfeng Liu and Xiaobing Ren. Large piezoelectric effect in pb-free ceramics. *Phys. Rev. Lett.*, 103:257602, Dec 2009.

[180] JP Straley and Michael E Fisher. Three-state potts model and anomalous tricritical points. *Journal of Physics A: Mathematical, Nuclear and General*, 6(9):1310, 1973.

[181] Stéphane Sarbach and Michael E. Fisher. Tricriticality and the failure of scaling in the many-component limit. *Phys. Rev. B*, 18:2350–2363, Sep 1978.

[182] George A. Baker and John W. Essam. Effects of lattice compressibility on critical behavior. *Phys. Rev. Lett.*, 24:447–449, Mar 1970.

[183] A Benyoussef, T Biaz, M Saber, and M Touzani. The spin-1 ising model with a random crystal field: the mean-field solution. *Journal of Physics C: Solid State Physics*, 20(32):5349–5354, nov 1987.

[184] C E I Carneiro, V B Henriques, and S R Salinas. Comment on the mean-field phase diagram of the spin-1 ising model in a random crystal field. *Journal of Physics: Condensed Matter*, 1(23):3687–3689, jun 1989.

[185] P.V. Santos, F.A. da Costa, and J.M. de Araújo. Mean-field solution of the blume–capel model under a random crystal field. *Physics Letters A*, 379(22):1397–1401, 2015.

[186] Hamid Ez-Zahraouy and Ahmed Kassou-Ou-Ali. Phase diagrams of the spin-1 blume-capel film with an alternating crystal field. *Phys. Rev. B*, 69:064415, Feb 2004.

[187] T Kaneyoshi and J Mielnicki. Comparison of effective-field and mean-field theories for the spin-one ising model with a random crystal field. *Journal of Physics: Condensed Matter*, 2(44):8773–8777, nov 1990.

[188] Yusuf Yüksel, Ümit Akıncı, and Hamza Polat. Critical behavior and phase diagrams of a spin-1 blume–capel model with random crystal field interactions: An effective field theory analysis. *Physica A: Statistical Mechanics and its Applications*, 391(9):2819–2832, 2012.

[189] Gul Gulpinar and Fadil Iyikanat. Dynamics of the blume-capel model with quenched diluted single-ion anisotropy in the neighborhood of equilibrium states. *Phys. Rev. E*, 83:041101, Apr 2011.

[190] C Buzano, A Maritan, and A Pelizzola. A cluster variation approach to the random-anisotropy blume-emery-griffiths model. *Journal of Physics: Condensed Matter*, 6(2):327–338, jan 1994.

[191] N. S. Branco and Beatriz M. Boechat. Real-space renormalization-group study of the two-dimensional blume-capel model with a random crystal field. *Phys. Rev. B*, 56:11673–11677, Nov 1997.

[192] D.Peña Lara and J.A. Plascak. General spin ising model with diluted and random crystal field in the pair approximation. *Physica A: Statistical Mechanics and its Applications*, 260(3):443–454, 1998.

[193] Erhan Albayrak. The spin-1 blume–capel model with random crystal field on the bethe lattice. *Physica A: Statistical Mechanics and its Applications*, 390(9):1529–1533, 2011.

[194] Sumedha and Nabin Kumar Jana. Absence of first order transition in the random crystal field blume–capel model on a fully connected graph. *Journal of Physics A: Mathematical and Theoretical*, 50(1):015003, nov 2016.

[195] C E I Carneiro, V B Henriques, and S R Salinas. Mean-field phase diagram of the spin-1 ising ferromagnet in a gaussian random crystal field. *Journal of Physics A: Mathematical and General*, 23(14):3383–3388, jul 1990.

[196] Octavio D Rodriguez Salmon and Justo Rojas Tapia. Multicriticality in the blume–capel model under a continuous-field probability distribution. *Journal of Physics A: Mathematical and Theoretical*, 43(12):125003, mar 2010.

[197] A. Malakis, A. Nihat Berker, I. A. Hadjiagapiou, and N. G. Fytas. Strong violation of critical phenomena universality: Wang-landau study of the two-dimensional blume-capel model under bond randomness. *Phys. Rev. E*, 79:011125, Jan 2009.

[198] A. Malakis, A. Nihat Berker, I. A. Hadjiagapiou, N. G. Fytas, and T. Papakonstanti-nou. Multicritical points and crossover mediating the strong violation of universality: Wang-landau determinations in the random-bond $d = 2$ blume-capel model. *Phys. Rev. E*, 81:041113, Apr 2010.

[199] Panagiotis E. Theodorakis and Nikolaos G. Fytas. Monte carlo study of the triangular blume-capel model under bond randomness. *Phys. Rev. E*, 86:011140, Jul 2012.

[200] A. Malakis, A. Nihat Berker, N. G. Fytas, and T. Papakonstantinou. Universality aspects of the $d = 3$ random-bond blume-capel model. *Phys. Rev. E*, 85:061106, Jun 2012.

[201] Alexis Falicov and A. Nihat Berker. Tricritical and critical end-point phenomena under random bonds. *Phys. Rev. Lett.*, 76:4380–4383, Jun 1996.

[202] N. G. Fytas, J. Zierenberg, P. E. Theodorakis, M. Weigel, W. Janke, and A. Malakis. Universality from disorder in the random-bond blume-capel model. *Phys. Rev. E*, 97:040102, Apr 2018.

[203] I. Puha and H.T. Diep. Random-bond and random-anisotropy effects in the phase diagram of the blume–capel model. *Journal of Magnetism and Magnetic Materials*, 224(1):85–92, 2001.

[204] V. Ongun Özçelik and A. Nihat Berker. Blume-emery-griffiths spin glass and inverted tricritical points. *Phys. Rev. E*, 78:031104, Sep 2008.

[205] Miron Kaufman and Michael Kanner. Random-field blume-capel model: Mean-field theory. *Phys. Rev. B*, 42:2378–2382, Aug 1990.

[206] P.V. Santos, F.A. da Costa, and J.M. de Araújo. The random field blume-capel model revisited. *Journal of Magnetism and Magnetic Materials*, 451:737–740, 2018.

[207] Erhan Albayrak. The random field blume-capel model on the bethe lattice. *Chinese Journal of Physics*, 68:100–105, 2020.

[208] Erhan Albayrak. Trimodal-random field blume-capel model. *Modern Physics Letters B*, 35(16):2150270, 2021.

[209] R. Erichsen, Amanda Azevedo Lopes, and S. G. Magalhaes. Multicritical points and topology-induced inverse transition in the random-field blume-capel model in a random network. *Phys. Rev. E*, 95:062113, Jun 2017.

[210] Victor Pereyra, Peter Nielaba, and Kurt Binder. Spin-one-ising model for (co)1−x(n2)xmixtures: A finite size scaling study of random-field-type critical phenomena. *Zeitschrift für Physik B Condensed Matter*, 97:179–187, June 1995.

[211] A. Benyoussef, H. Ez-Zahraouy, and M. Saber. Magnetic properties of a transverse spin-1 ising model with random longitudinal field. *Physica A: Statistical Mechanics and its Applications*, 198(3):593–605, 1993.

[212] A Benyoussef and H Ez-zahraouy. The bond-diluted spin-1 transverse ising model with random longitudinal field. *physica status solidi (b)*, 179(2):521–530, 1993.

[213] Sumedha and Soheli Mukherjee. Emergence of a bicritical end point in the random-crystal-field blume-capel model. *Physical Review E*, 101(4):042125, 2020.

[214] Soheli Mukherjee and Sumedha. Phase transitions in the blume-capel model with trimodal and gaussian random fields. *Journal of Statistical Physics*, 188:22, 2022.

[215] Hugo Touchette. The large deviation approach to statistical mechanics. *Physics Reports*, 478(1):1 − 69, 2009.

[216] Harald Cramér. On a new limit theorem of the theory of probability. *Uspekhi Matematicheskikh Nauk*, (10):166–178, 1944.

[217] SR Srinivasa Varadhan. Asymptotic probabilities and differential equations. *Communications on Pure and Applied Mathematics*, 19(3):261–286, 1966.

[218] Richard S Ellis, Peter T Otto, and Hugo Touchette. Analysis of phase transitions in the mean-field blume–emery–griffiths model. *The Annals of Applied Probability*, 15(3):2203–2254, 2005.

[219] Amir Dembo, Ofer Zeitouni, and IH Dinwoodie. Large deviations techniques and applications. *SIAM Review*, 36(2):303–303, 1994.

[220] Frank Hollander. *Large deviations*, volume 14. American Mathematical Soc., 2000.

[221] Yoshitsugu Oono. Large deviation and statistical physics. *Progress of Theoretical Physics Supplement*, 99:165–205, 1989.

[222] R. Tyrrell Rockafellar. *Convex Analysis*. Princeton University Press, 1997.

[223] Jan van Tiel. *Convex Analysis: An Introductory Text*. John Wiley, 1984.

[224] Carl M Bender, Steven Orszag, and Steven A Orszag. *Advanced mathematical methods for scientists and engineers I: Asymptotic methods and perturbation theory*, volume 1. Springer Science & Business Media, 1999.

[225] Richard S Ellis. *Entropy, large deviations, and statistical mechanics*, volume 1431. Taylor & Francis, 2006.

[226] Amos Maritan, Marek Cieplak, Michael R Swift, Flavio Toigo, and Jayanth R Banavar. Random-anisotropy blume-emery-griffiths model. In *AIP Conference Proceedings*, volume 286, pages 231–236. American Institute of Physics, 1992.

[227] Wolfram Research, Inc. Wolfram programming lab, Version 12.2. Champaign, IL, 2021.

[228] J.M. Kincaid and E.G.D. Cohen. Phase diagrams of liquid helium mixtures and metamagnets: Experiment and mean field theory. *Physics Reports*, 22(2):57–143, 1975.

[229] Kenkichi Okada and Ikuo Suzuki. Classical calculations on the phase transition i. phase diagram in four-dimensional space for the system with one order parameter. *Journal of the Physical Society of Japan*, 51(10):3250–3257, 1982.

[230] Michael E. Fisher and David R. Nelson. Spin flop, supersolids, and bicritical and tetracritical points. *Phys. Rev. Lett.*, 32:1350–1353, Jun 1974.

[231] J. A. Plascak and D. P. Landau. Universality and double critical end points. *Phys. Rev. E*, 67:015103, Jan 2003.

[232] P. Butera and M. Pernici. The blume–capel model for spins s=1 and 3⁄2 in dimensions d=2 and 3. *Physica A: Statistical Mechanics and its Applications*, 507:22–66, 2018.

[233] M Kerszberg, D Mukamel, H Rohrer, and H Thomas. *Novel multicritical points of "weak metamagnets"*. PhD thesis, American Institute of Physics, 1979.

[234] K. Katsumata, H. Aruga Katori, S. M. Shapiro, and G. Shirane. Neutron-scattering studies of a phase transition in the metamagnet febr$_2$ under external magnetic fields. *Phys. Rev. B*, 55:11466–11470, May 1997.

[235] W Poot and Th W De Loos. Liquid–liquid–vapour equilibria in binary and quasi-binary systems of chf 3 with n-alkanes, phenylalkanes and alkanols. *Physical Chemistry Chemical Physics*, 1(18):4293–4297, 1999.

[236] AP Moina. Influence of external field direction on polarization rotation in antiferro-electric squaric acid h _2 c _4 o _4. *arXiv preprint arXiv:2112.09942*, 2021.

[237] E. Stryjewski and N. Giordano. Metamagnetism. *Advances in Physics*, 26(5):487–650, 1977.

[238] HJ Herrmann, EB Rasmussen, and DP Landau. Computer simulation studies of three-dimensional tricritical behavior. *Journal of Applied Physics*, 53(11):7994–7996, 1982.

[239] Yung-Li Wang and JD Kimel. Multicritical behavior in the antiferromagnetic blume–capel model. *Journal of applied physics*, 69(8):6176–6178, 1991.

[240] E.L. de Santa Helena and Marcia C. Barbosa. Singularities near critical and bicritical end points: applications to an isomorphous transition. *Physica A: Statistical Mechanics and its Applications*, 208(3):479–492, 1994.

[241] B Widom. Tricritical points in three-and four-component fluid mixtures. *The Journal of Physical Chemistry*, 77(18):2196–2200, 1973.

[242] Michael E. Fisher and Paul J. Upton. Universality and interfaces at critical end points. *Phys. Rev. Lett.*, 65:2402–2405, Nov 1990.

[243] Toyoichi Tanaka. Collapse of gels and the critical endpoint. *Phys. Rev. Lett.*, 40:820–823, Mar 1978.

[244] Hiroki Nohara, Hisashi Kotegawa, Hideki Tou, Tatsuma D. Matsuda, Etsuji Yamamoto, Yoshinori Haga, Zachary Fisk, Yoshichika Ōnuki, Dai Aoki, and Jacques Flouquet. Strong longitudinal magnetic fluctuations near critical end point in ucoal: A 59co-nmr study. *Journal of the Physical Society of Japan*, 80(9):093707, 2011.

[245] Makoto Iwata, Keigo Yamashita, Soma Suzuki, Yoshinori Takikawa, and Yoshihito Tachi. *Japanese Journal of Applied Physics*, 60(SF):SFFA03, jul 2021.

[246] Alejandro Ayala, Adnan Bashir, J.J. Cobos-Martínez, Saúl Hernández-Ortiz, and Alfredo Raya. The effective qcd phase diagram and the critical end point. *Nuclear Physics B*, 897:77–86, 2015.

[247] N. Vigneshwar, Dipanjan Mandal, Kedar Damle, Deepak Dhar, and R. Rajesh. Phase diagram of a system of hard cubes on the cubic lattice. *Phys. Rev. E*, 99:052129, May 2019.

[248] Sumedha and Mustansir Barma. Solution of the random field XY magnet on a fully connected graph. *Journal of Physics A: Mathematical and Theoretical*, 55(9):095001, feb 2022.

[249] Ümit Akıncı. On the spin – s random field ising model. *Journal of Magnetism and Magnetic Materials*, 488:165368, 2019.

[250] RR Levitskii, IR Zachek, AP Moina, and A Ya Andrusyk. Isotopic effects in partially deuterated piezoelectric crystals of rochelle salt. *Condensed Matter Physics*, 2004.

[251] Nurit Avraham, Boris Khaykovich, Yuri Myasoedov, Michael Rappaport, Hadas Shtrikman, Dima E Feldman, Tsuyoshi Tamegai, Peter H Kes, Ming Li, Marcin Konczykowski, et al. 'inverse'melting of a vortex lattice. *Nature*, 411(6836):451–454, 2001.

[252] S. Rastogi, G. W. H. Höhne, and A. Keller. Unusual pressure-induced phase behavior in crystalline poly(4-methylpentene-1): calorimetric and spectroscopic results and further implications. *Macromolecules*, 32(26):8897–8909, 1999.

[253] C. Chevillard, M. A. V. Axelos, P. N. Pusey, and W. C. K. Poon. Phase separation of aqueous solution of methylcellulose. *Colloid and Polymer Science*, 275:537–545, June 1997.

[254] M Hirrien, C Chevillard, J Desbrières, M.A.V Axelos, and M Rinaudo. Thermogelation of methylcelluloses: new evidence for understanding the gelation mechanism. *Polymer*, 39(25):6251–6259, 1998.

[255] Kell Mortensen, Wyn Brown, and Bengt Nordén. Inverse melting transition and evidence of three-dimensional cubatic structure in a block-copolymer micellar system. *Phys. Rev. Lett.*, 68:2340–2343, Apr 1992.

[256] K. N. Pham, S. U. Egelhaaf, P. N. Pusey, and W. C. K. Poon. Glasses in hard spheres with short-range attraction. *Phys. Rev. E*, 69:011503, Jan 2004.

[257] Manuel I. Marqués, Jose M. Borreguero, H. Eugene Stanley, and Nikolay V. Dokholyan. Possible mechanism for cold denaturation of proteins at high pressure. *Phys. Rev. Lett.*, 91:138103, Sep 2003.

[258] S. A. Hawley. Reversible pressure-temperature denaturation of chymotrypsinogen. *Biochemistry*, 10(13):2436–2442, 1971. PMID: 5557794.

[259] Hans Mueller. Properties of rochelle salt. *Phys. Rev.*, 47:175–191, Jan 1935.

[260] Arup K Chakraborty and EI Shakhnovich. Phase behavior of random copolymers in quenched random media. *The Journal of chemical physics*, 103(24):10751–10763, 1995.

[261] Melissa R Feeney, Pablo G Debenedetti, and Frank H Stillinger. A statistical mechanical model for inverse melting. *The Journal of chemical physics*, 119(8):4582–4591, 2003.

[262] Creighton K. Thomas and Helmut G. Katzgraber. Simplest model to study reentrance in physical systems. *Phys. Rev. E*, 84:040101, Oct 2011.

[263] M. Schick and Wei-Heng Shih. Spin-1 model of a microemulsion. *Phys. Rev. B*, 34:1797–1801, Aug 1986.

[264] Saeed Ahmad, Krishna Rijal, and Dibyendu Das. First passage in the presence of stochastic resetting and a potential barrier. *Phys. Rev. E*, 105:044134, Apr 2022.

[265] Robert B. Griffiths and Benjamin Widom. Multicomponent-fluid tricritical points. *Phys. Rev. A*, 8:2173–2175, Oct 1973.

[266] M Blume, VJ Emery, and Robert B Griffiths. Ising model for the λ transition and phase separation in he 3-he 4 mixtures. *Physical review A*, 4(3):1071, 1971.

[267] Jean Sivardière and Joseph Lajzerowicz. Spin-1 lattice-gas model. ii. condensation and phase separation in a binary fluid. *Phys. Rev. A*, 11:2090–2100, Jun 1975.

[268] S. Krinsky and D. Mukamel. Spin-$\frac{3}{2}$ ising model for tricritical points in ternary fluid mixtures. *Phys. Rev. B*, 11:399–410, Jan 1975.

[269] Jean Sivardière and Joseph Lajzerowicz. Spin-1 lattice-gas model. iii. tricritical points in binary and ternary fluids. *Phys. Rev. A*, 11:2101–2110, Jun 1975.

[270] C. Kittel. Model of exchange-inversion magnetization. *Phys. Rev.*, 120:335–342, Oct 1960.

[271] P. W. Anderson. New approach to the theory of superexchange interactions. *Phys. Rev.*, 115:2–13, Jul 1959.

[272] R. J. Birgeneau, M. T. Hutchings, J. M. Baker, and J. D. Riley. High‐degree electrostatic and exchange interactions in rare‐earth compounds. *Journal of Applied Physics*, 40(3):1070–1079, 1969.

[273] O. Vatamaniuk and Yu. Rudavskii. Spin-one ising model with biquadratic exchange interaction within functional integration method. *physica status solidi (b)*, 197(1):199–210, 1996.

[274] G A T Allan and D D Betts. Spin one exchange interaction model of ferromagnetism. *Proceedings of the Physical Society*, 91(2):341, 1967.

[275] E A Harris and J Owen. Biquadratic exchange between mn 2+ ions in mgo. *Physical review letters*, 11(1):9, 1963.

[276] D S Rodbell, I S Jacobs, J Owen, and E A Harris. Biquadratic exchange and the behavior of some antiferromagnetic substances. *Physical Review Letters*, 11(1):10, 1963.

[277] V V Hovhannisyan, N S Ananikian, Alessandro Campa, and S Ruffo. Complete analysis of ensemble inequivalence in the blume-emery-griffiths model. *Physical Review E*, 96(6):062103, 2017.

[278] Joseph Lajzerowicz and Jean Sivardière. Spin-1 lattice-gas model. i. condensation and solidification of a simple fluid. *Phys. Rev. A*, 11:2079–2089, Jun 1975.

[279] D. Furman, S. Dattagupta, and Robert B. Griffiths. Global phase diagram for a three-component model. *Phys. Rev. B*, 15:441–464, Jan 1977.

[280] Carla Buzano and Alessandro Pelizzola. Surface reentrance in the semi-infinite spin-1 ising models. *Physica A: Statistical Mechanics and its Applications*, 195(1-2):197–214, 1993.

[281] K G Chakraborty and J W Tucker. A spin-one ising model with single-ion anisotropy and biquadratic exchange on a bethe lattice. *Journal of Magnetism and Magnetic Materials*, 54:1349–1350, 1986.

[282] D M Saul, Michael Wortis, and Dietrich Stauffer. Tricritical behavior of the blume-capel model. *Physical Review B*, 9(11):4964, 1974.

[283] A Nihat Berker and Michael Wortis. Blume-emery-griffiths-potts model in two dimensions: Phase diagram and critical properties from a position-space renormalization group. *Physical Review B*, 14(11):4946, 1976.

[284] A. Bakchich, A. Benyoussef, and M. Touzani. Phase diagrams of the blume-emery-griffiths model: real-space renormalization group investigation and finite size scaling analysis. *Physica A: Statistical Mechanics and its Applications*, 186(3):524 – 533, 1992.

[285] Motoyuki Tanaka and Takeshi Kawabe. Spin-one ising model including biquadratic interaction with positive coupling constant. *Journal of the Physical Society of Japan*, 54(6):2194–2203, 1985.

[286] Youjin Deng and Henk W. J. Blöte. Constrained tricritical blume-capel model in three dimensions. *Phys. Rev. E*, 70:046111, Oct 2004.

[287] V V Prasad, Alessandro Campa, David Mukamel, and Stefano Ruffo. Ensemble inequivalence in the blume-emery-griffiths model near a fourth-order critical point. *Physical Review E*, 100(5):052135, 2019.

[288] Soheli Mukherjee, Raj Kumar Sadhu, and Sumedha. Phase diagram of the repulsive blume–emery–griffiths model in the presence of an external magnetic field on a complete graph. *Journal of Statistical Mechanics: Theory and Experiment*, 2021(4):043209, apr 2021.

[289] R. B. Griffiths. First-order phase transitions in spin-one ising systems. *Physica*, 33(3):689 – 690, 1967.

[290] Freddy Bouchet and Antoine Venaille. Statistical mechanics of two-dimensional and geophysical flows. *Physics Reports*, 515(5):227–295, 2012. Statistical mechanics of two-dimensional and geophysical flows.

[291] Michael K.-H. Kiessling and Thomas Neukirch. Negative specific heat of a magnetically self-confined plasma torus. *Proceedings of the National Academy of Sciences*, 100(4):1510–1514, 2003.

[292] Ralph A. Smith and Thomas M. O'Neil. Nonaxisymmetric thermal equilibria of a cylindrically bounded guiding☐center plasma or discrete vortex system. *Physics of Fluids B: Plasma Physics*, 2(12):2961–2975, 1990.

[293] Julien Barré, David Mukamel, and Stefano Ruffo. Inequivalence of ensembles in a system with long-range interactions. *Phys. Rev. Lett.*, 87:030601, Jun 2001.

[294] Julien Barré, David Mukamel, and Stefano Ruffo. *Ensemble Inequivalence in Mean-Field Models of Magnetism*, pages 45–67. Springer Berlin Heidelberg, Berlin, Heidelberg, 2002.

[295] I. Ispolatov and E. G. D. Cohen. Phase transitions in systems with $1/r^\alpha$ attractive interactions. *Phys. Rev. E*, 64:056103, Oct 2001.

[296] Pierre de Buyl, David Mukamel, and Stefano Ruffo. Ensemble inequivalence in a xy model with long☐range interactions. *AIP Conference Proceedings*, 800(1):533–538, 2005.

[297] Alessandro Campa, Andrea Giansanti, David Mukamel, and Stefano Ruffo. Dynamics and thermodynamics of rotators interacting with both long- and short-range couplings. *Physica A: Statistical Mechanics and its Applications*, 365(1):120–127, 2006. Fundamental Problems of Modern Statistical Mechanics.

[298] O Cohen and D Mukamel. Ensemble inequivalence: Landau theory and the ABC model. *Journal of Statistical Mechanics: Theory and Experiment*, 2012(12):P12017, dec 2012.

[299] A. Lederhendler and D. Mukamel. Long-range correlations and ensemble inequivalence in a generalized *abc* model. *Phys. Rev. Lett.*, 105:150602, Oct 2010.

[300] O. Cohen and D. Mukamel. Nonequilibrium ensemble inequivalence and large deviations of the density in the *abc* model. *Phys. Rev. E*, 90:012107, Jul 2014.

[301] D. Mukamel, S. Ruffo, and N. Schreiber. Breaking of ergodicity and long relaxation times in systems with long-range interactions. *Phys. Rev. Lett.*, 95:240604, Dec 2005.

[302] Hugo Touchette, Richard S. Ellis, and Bruce Turkington. An introduction to the thermodynamic and macrostate levels of nonequivalent ensembles. *Physica A: Statistical Mechanics and its Applications*, 340(1):138 – 146, 2004. News and Expectations in Thermostatistics.

[303] A Lederhendler, O Cohen, and D Mukamel. Phase diagram of the ABC model with nonconserving processes. *Journal of Statistical Mechanics: Theory and Experiment*, 2010(11):P11016, nov 2010.

[304] J Barton, J L Lebowitz, and E R Speer. The grand canonicalABCmodel: a reflection asymmetric mean-field potts model. *Journal of Physics A: Mathematical and Theoretical*, 44(6):065005, jan 2011.

[305] Eberhard K. Riedel. Scaling approach to tricritical phase transitions. *Phys. Rev. Lett.*, 28:675–678, Mar 1972.

[306] Eberhard K. Riedel and Franz J. Wegner. Tricritical exponents and scaling fields. *Phys. Rev. Lett.*, 29:349–352, Aug 1972.

[307] Alex Hankey, H. Eugene Stanley, and T. S. Chang. Geometric predictions of scaling at tricritical points. *Phys. Rev. Lett.*, 29:278–281, Jul 1972.

[308] Robert B. Griffiths. Thermodynamic model for tricritical points in ternary and quaternary fluid mixtures. *The Journal of Chemical Physics*, 60(1):195–206, 1974.

[309] H.W. Diehl and M. Smock. Field-theoretical analysis of singularities at critical end points. *Physica A: Statistical Mechanics and its Applications*, 281(1):268–275, 2000.

[310] HW Diehl and M Smock. Bulk singularities at critical end points: a field-theory analysis. *The European Physical Journal B-Condensed Matter and Complex Systems*, 21(4):567–587, 2001.

[311] Michael E Fisher. Phases and phase diagrams: Gibbs's legacy today. In *the Proceeding of the Gibbs Symposium (Yale University)*, page 39, 1990.

[312] Michael E. Fisher and Marcia C. Barbosa. Phase boundaries near critical end points. i. thermodynamics and universality. *Phys. Rev. B*, 43:11177–11184, May 1991.

[313] Marcia C. Barbosa and Michael E. Fisher. Phase boundaries near critical end points. ii. general spherical models. *Phys. Rev. B*, 43:10635–10646, May 1991.

[314] Marcia C. Barbosa. Phase boundaries near critical end points. iii. corrections to scaling and spherical models. *Phys. Rev. B*, 45:5199–5208, Mar 1992.

215

[315] Michael E. Fisher and Paul J. Upton. Fluid interface tensions near critical end points. *Phys. Rev. Lett.*, 65:3405–3408, Dec 1990.

[316] Shun-Yong Zinn and Michael E. Fisher *. Interfacial tensions near critical endpoints: experimental checks of edgf theory. *Molecular Physics*, 103(21-23):2927–2942, 2005.

[317] Shun-yong Zinn and Michael E. Fisher. Scaling for interfacial tensions near critical endpoints. *Phys. Rev. E*, 71:011601, Jan 2005.

[318] Yoshihiro Ishibashi and Yoshiki Hidaka. On an isomorphous transition. *Journal of the Physical Society of Japan*, 60(5):1634–1637, 1991.

[319] E.L. de Santa Helena and Marcia C. Barbosa. Singularities near critical and tricritical end points: thermodynamics and applications. *Physica A: Statistical Mechanics and its Applications*, 219(3):408–422, 1995.

[320] Shan-Ho Tsai, Fugao Wang, and D. P. Landau. Critical endpoint behavior in an asymmetric ising model: Application of wang-landau sampling to calculate the density of states. *Phys. Rev. E*, 75:061108, Jun 2007.

[321] DP Landau, Fugao Wang, and Shan-Ho Tsai. Critical endpoint behavior: A wang–landau study. *Computer Physics Communications*, 179(1-3):8–12, 2008.

[322] H. J. Herrmann and D. P. Landau. Stability of the tricritical point in a three-dimensional next-nearest-neighbor ising antiferromagnet: A monte carlo simulation. *Phys. Rev. B*, 48:239–242, Jul 1993.

[323] M. Žukovič and T. Idogaki. Monte carlo investigation of the tricritical point stability in a three-dimensional ising metamagnet. *Phys. Rev. B*, 61:50–53, Jan 2000.

[324] Soheli Mukherjee and Sumedha. Critical behaviour near the critical end point and tricritical point in disordered spin-1 ferromagnets. *Submitted, 2023*.